SCUOLA DI DOTTORATO

UNIVERSITÀ DEGLI STUDI DI MILANO-BICOCCA

Dipartimento di / Department of

Fisica/Physics

Dottorato di Ricerca in / PhD program Fisica ed Astronomia Ciclo / Cycle XXX

Curriculum in Fisica della materia condensata, Fisica dei plasmi e biofisica

GEM BASED DETECTORS FOR FAST AND THERMAL NEUTRONS

Cognome / Surname Muraro Nome / Name Andrea

Matricola / Registration number 798498

Tutore / Tutor: Dr. Marco Tardocchi

Coordinatore / Coordinator: Prof. Marta Calvi

ANNO ACCADEMICO / ACADEMIC YEAR 2017/2018

Contents

Abstract

This PhD thesis concerns the development of GEM (Gas Electron Multiplier) based detectors for fast and thermal neutrons.

The first detector developed during my PhD, is a tripleGEM equipped with a three-dimensional cathode (3D-C) coated with $^{10}B_4C$, designed to detect thermal neutrons with a good efficiency, good spatial resolution and able to sustain the high rate foreseen in the new neutron spallation sources actually under construction, such as the European Spallation Source (ESS). The developed detector is called BAND-GEM (Boron Array Neutron Detector) and exploits the $^{10}B(n,\alpha)^7Li$ nuclear reaction to convert the thermal neutrons into secondary charged particles. During my PhD, several BAND-GEM prototypes were developed based on a series of numerical simulations whose goal was the optimization of the 3D-C geometry. The prototypes were tested under neutron irradiation at the EMMA beam line at ISIS (UK), where the efficiency and spatial resolution were measured, at the ORPHEE reactor in Saclay (France), where the high rate capabilities were tested, and finally at the TREFF beam line at the FRMII reactor (Munich) where the efficiency and the spatial resolution were measured using a 4.73 Å mono-chromatic beam. The last BAND-GEM prototype has an efficiency of about 45% at 4 Å, a spatial resolution of about 6 mm and is able to sustain rate in excess of 1 MHz/cm^2. These features make it an attractive candidate for installation - after further optimization - on LoKI, a Small Angle Neutron Scattering (SANS) instrument actually under construction at ESS. In this thesis I present the design for the realization of a full-scale detector for LoKI.

The second detector developed during my PhD is a tripleGEM equipped with a plastic converter cathode (nGEM) that will be able to provide the neutron intensity map of the neutron emitted from the beam dump surface of the two NBI (Neutral Beam Injector) prototypes for ITER under development in Padova (Italy) at Consorzio RFX, in the framework of the PRIMA project. The ITER neutral beam test facility (PRIMA) will host two experimental devices: SPIDER, a 100 keV negative hydrogen/deuterium beam, and MITICA, a full scale, 1 MeV deuterium beam. The diagnostic system developed in this thesis is called CNESM (acronym for Close-contact Neutron Emission Surface Mapping) and it is a neutron diagnostic installed in the SPIDER beam dump. The SPIDER beam

dump is two rectangular panels (made of CuCrZr-alloy, with an elemental composition of about 99% Cu) water-cooled with the hypervapotrons technique, that are used to stop the incoming beam. During deuterium operation, a significant amount of fast neutrons ($E_n \approx 2.45MeV$) will be produced due to the fusion reactions between the incoming deuterons of the beam and the deuterons previously implanted on the beam dump surface. The detector used by the CNESM diagnostic system is called nGEM and its heart is constituted by a tripleGEM equipped with a cathode composed of a polypropylene layer (2mm thick) that serves as neutron-proton converter followed by an aluminium layer (50 μm thick) that is used to stop all protons emitted from the polypropylene at an angle higher than 40° relative to the normal to the cathode surface. The nGEM is installed on the back of the beam dump and its cathode is positioned at about 30 mm from the beam dump front surface. The small distance of the detector from the neutron source (the beam dump surface), together with the presence of the Al foil, improves the spatial resolution of the detector, that will be able to provide the neutron intensity map with a spatial resolution approaching the size of the single SPIDER beamlet (40x22 mm^2). This thesis describes the nGEM detector development and tests. The directional response of the detector to neutrons was verified at FNG (Frascati Neutron Generator). The uniformity, stability and the gamma background rejection capabilities of the detector were tested at the ROTAX beam line at ISIS (UK). Also the engineering design for the integration of the CNESM diagnostic system inside the SPIDER vacuum vessel is presented in the thesis.

1 Chapter 1: Gaseous detectors

This thesis is about the development of gas detectors for fast and slow (thermal) neutrons. Two kinds of neutron detectors have been developed during this thesis, both based on the Gas Electron Multiplier (GEM) technology.

This Chapter describes the different operating modes of gas-based detectors with particular attention to the GEM, and the way of operation of neutron detectors in general.

1.1 Operational Regimes

A gas-based detector can operate mainly in three different operational modes: the ionization mode, the proportional mode, and the Geiger-Muller mode [1]. The parameters that define the operational mode are the geometry, the electric field configuration and the amplification process. Based on the operational mode, gas-based detectors can be divided into three categories: ionization chambers, proportional chambers, and Geiger-Mueller detectors.

Figure 1-1 shows the different operating regions as a function of the applied voltage (and thus of the electric field configuration). In the next paragraphs, the different operational modes will be described.

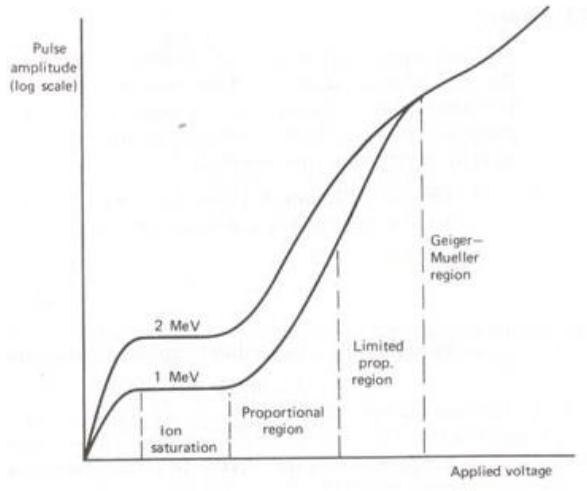

Figure 1-1: Gas detectors gain as a function of applied voltage [1]

1.1.1 Ionization mode

When a charged particle interacts with the gas, it can ionize it producing ions and free electrons pairs. There are three main types of interaction between the produced free electrons and ions and the neutral gas molecules, namely [1]:

- Charge transfer: an electron is transferred from a neutral molecule to an ion, reversing the two initial states;
- Electron attachment: a free electron is kept by a neutral molecule, that becomes a negative ion;
- Recombination: an electron is absorbed by a positive ion, giving rise to a neutral molecule.

The simplest gas-based detector is composed of a gaseous medium encapsulated between an anode and a cathode. When a suitable voltage ΔV is applied between the two electrodes, the produced pairs drift towards the anode (electrons) and the cathode (ions). The motion of the primary charges inside the gas volume produces a detectable signal, the amplitude of which is directly proportional to the energy deposited by the particle in the gas, given that no multiplication process is present. For this reason, highly ionizing particles, such as α-particles or heavy ions, are more easily detectable with ionization chambers since their energy loss in the gas and consequent signal is large with respect to the noise usually present in the read-out electronics.

1.1.2 Proportional mode

By increasing the electric field in the gas, the detector enters in the proportional operational mode. If the electric field is sufficiently high, the free electrons created in the gas by the ionizing particle, can be accelerated. If the electrons are accelerated enough (i. e. over a certain threshold typical of every gas and gas pressure), secondary ionisation can occur. For instance, the threshold value is about 1 MV/m for atmospheric pressure. The produced secondary electrons are further accelerated by the electric field and give rise to other pairs. This kind of cascade process is known as the Townsend Avalanche. The increase in the number of the electrons *n* per unit path length is described by the corresponding Townsend Equation [1]:

$$dn = n\alpha dx \qquad \text{Eq. 1-1}$$

where α is the First Townsend Coefficient for the gas, i.e. the inverse of the mean free path for ionization. α is zero below the threshold field and linearly increases with the electric field. For a uniform field the Townsend Equation predicts that n grows exponentially with distance during the avalanche:

$$n(x) = n(0)e^{\alpha x} \quad \text{Eq. 1-2}$$

Proportional chambers are then detectors that amplify the charge of the original electrons released within the gas. For this reason, they are used in the detection of X-Rays or Minimum Ionising Particles (MIPs), that produce only a few pairs. The initial energy of the ionizing particle can be measured because the amount of charges produced in the avalanche is still proportional to the number of the original pairs created by the radiation and, therefore, to the energy release in the gas.

1.1.3 Geiger-Mueller Multiplication Mode

If the field configuration is changed by substantially increasing the value of the electric field, the charge created by the positive ions can become completely dominant in determining the subsequent history of the pulse. In this condition, an avalanche may trigger a second avalanche in a different position due to the emission of a UV photon. This process, known as *Geiger Discharge*, suddenly becomes divergent and an exponentially growing number of avalanches can be reached in a very short time. The *Geiger Discharge* continues until the number of ion pairs created is sufficient to reduce the electric field below the threshold at which additional gas multiplication can take place. The process is then self-limiting and will terminate when a specific number of positive ions have been formed, regardless of the number of initial pairs. Each output pulse from a detector operating in this mode is of the same amplitude and no longer reflects any properties of the incident radiation.

1.2 Gas Electron Multiplier

The GEM [2] was invented by Sauli in 1997. GEM detectors belong to the family of the Micro Pattern Gaseous Detectors (MPGDs) together with the Micro Strip Gas Chamber (MSGC) [4] and the Micromegas [5]. A GEM consists in a thin (thickness ≈ 50 μm) insulating foil (typically kapton [6]) clad on each side with a copper layer (thickness ≈ 5

µm). Using conventional photolithographic methods, the foil is chemically perforated in order to obtain a high-density matrix of holes. Figure 1-2 shows a microscopic view of a standard GEM foil: every hole is bi-conical with an outer diameter of 70 µm and an inner diameter of 50 µm. The pitch between the holes is 140 µm and the holes are arranged in a hexagonal shape.

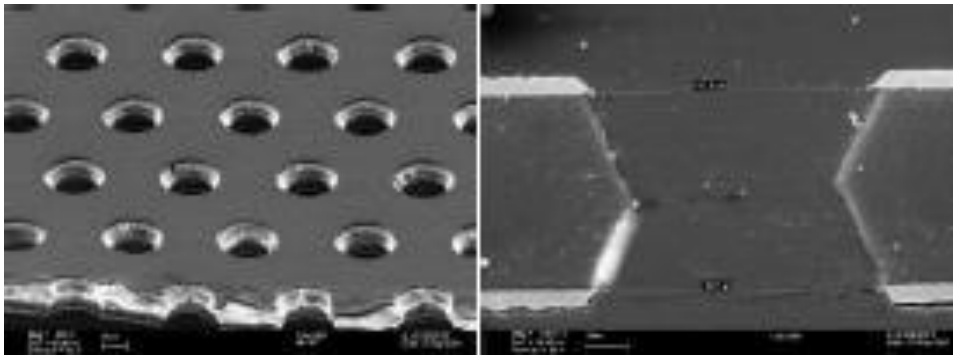

Figure 1-2: Microscopic view of the standard Gas Electron Multiplier [10]

By applying a suitable ΔV (200 V to 500 V) between the two copper faces (called GEM electrodes) a high dipole field develops in the holes, as shown in Figure 1-3. This field forces the ionization electrons to drift in the holes, multiply and transfer to a collection region.

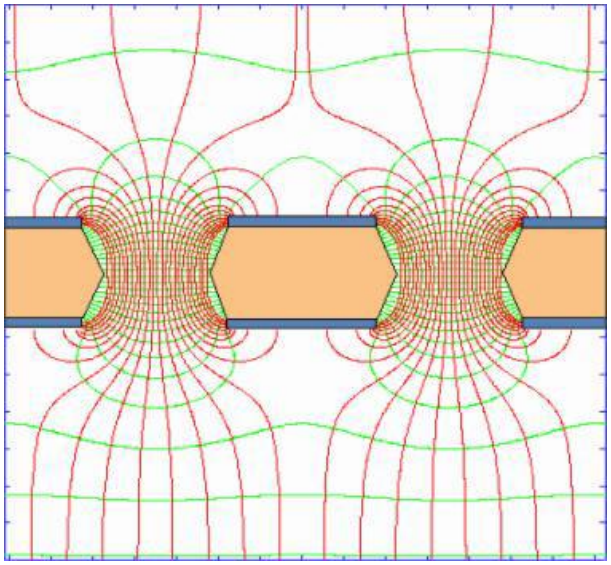

Figure 1-3: Drift field lines (red) and equipotential lines (green) in the holes of a GEM foil. [10]

The simplest GEM-based detector is called *single GEM detector* and it is composed of a cathode, a GEM foil and an anode (Figure 1-4).

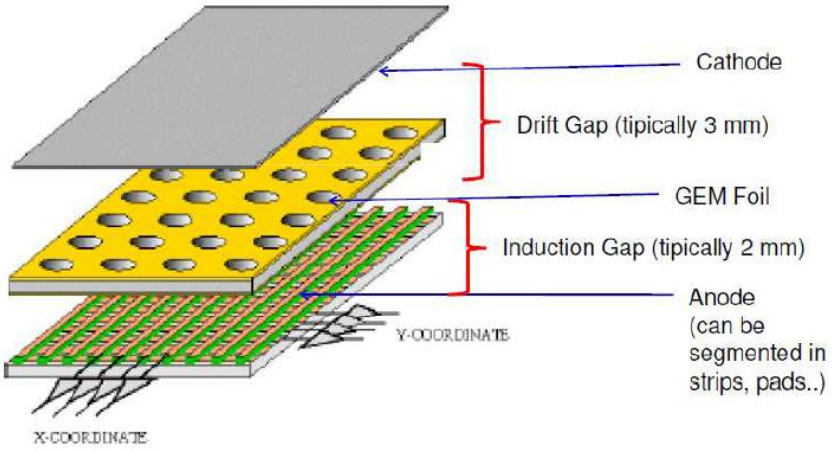

Figure 1-4: Sketch of a single GEM detector

The separation gap between the cathode and the first electrode of the GEM foil (called GEM Top) is called *drift gap* while the gap between the second GEM foil electrode (called GEM Bottom) and the anode is called *induction gap*. The drift gap is the region where the primary ionization charge is created. This region represents the sensitive volume of the detector and the length of the gap must be chosen taking into account the range of the ionizing particles. The holes of the GEM foil act as multiplication stage (each hole works as an individual proportional amplifier), and its gain is a function of the applied voltage between the GEM electrodes [7]. After the multiplication stage, the electrons reach the induction gap, where their motion induces a detectable signal on the anode [8][9]. The signal of a GEM detector is then completely due to the motion of the electrons. On the contrary, the positive ions are directed from the drift region to the cathode and the signal induced by the movement of the positive charges is completely shielded by the GEM foil. This means that the motion of the ions does not modify the induction field and thus the gain of the GEM. The consequence of this property is that GEM detectors can sustain very high rate compared to wire based detectors like the ^{3}He tubes, where the space charge of positive ions makes the shaping time of signals longer. The high rate capability is a key property of the detectors developed and described in this thesis, given that in both the application on which they could be installed, a high counting rate is expected.

A strict definition of the gain in a GEM-based detector is the ratio between the numbers of the electrons detected on the readout anode and the numbers of primary electrons created in the drift gap. In fact, due to the loss of a part of the total charge in the bottom GEM electrode, the number of multiplied electrons (Real Gain of the detector) is generally greater than the number of detected electrons on the read-out anode (Effective Gain of the detector) [10]. Also the drift and the induction field play a key role in the GEM-based detector operation. The drift field intensity (E_{drift}) is the main responsible of the primary charge collection. For low values of $E_{drift,}$ the primary charges can be lost due to recombination. If E_{drift} is too high, part of the field lines will end to the GEM Top surface, with a consequent loss of primary electrons. Between these extreme cases, there is a plateau region, where the whole primary charge is collected in the GEM holes. Typically, this condition is reached for E_{drift} of about 1.5 kV/cm. The induction field intensity (E_{ind}) instead plays a role in determining the size and shape of the signal. In order to obtain faster and narrower signal (avoiding pile-up in high rate application) high induction field must be used. Moreover, E_{ind} has a role in the definition of the gain: the higher E_{ind} value, the lower is the charge loss in the GEM Bottom electrode. On the other hand, if E_{ind} is increased above a threshold (about 8 kV/cm for Ar/CO_2 gas mixtures) parallel plate multiplication will occur in the induction region, with a consequent fast increase of the gain. This mode of operation is unsafe because it may cause a discharge into the detector ; for this reason, the value of E_{ind} is usually limited to 5 kV/cm.

The detector is continuously flushed with a controlled gas mixture ($Ar(70\%)/CO_2(30\%)$ in all the detectors described in this thesis) with a flux in excess of 5 l/h. Argon is ionized by the charged particles, and CO_2 is used as quenching gas, i.e . to absorb photons emitted by the de-excitation of argon molecules.

Multiple GEM foils can be “cascaded” (i. e. series connected) in order to achieve higher gain while keeping a lower voltage on each GEM, decreasing the discharge probability. All the detectors developed in this thesis use a *Triple GEM* detector. A triple GEM is characterised by two induction regions (between the foils) across which the electrons drift before they are multiplied. In these transfer regions (called T1 and T2) an electric field with a typical value of 1 kV/cm must be present, in order to allow the motion of the electrons. Figure 1-5 shows the avalanche development in a triple GEM.

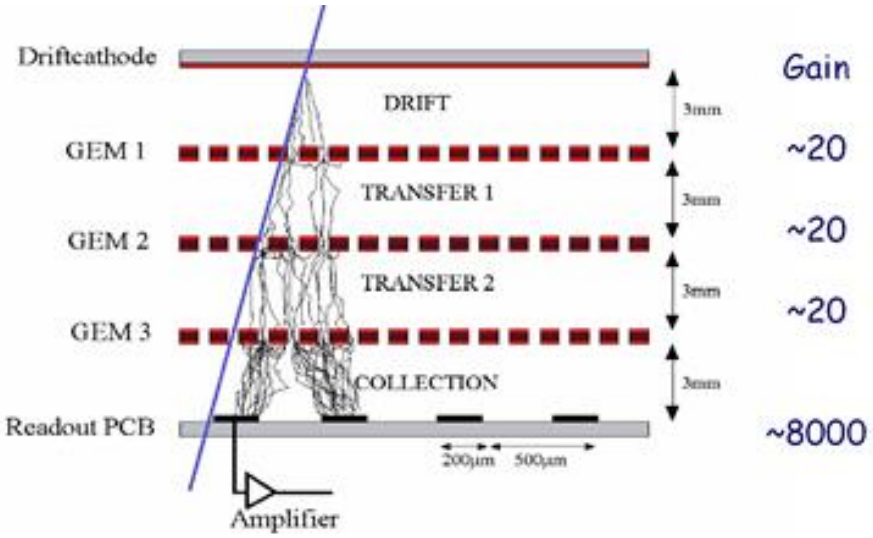

Figure 1-5: Avalanche development in a triple GEM detector

The pros of the GEM detector can be summarized as follows:

- Possibility to cover large areas (m^2) with relatively low cost compared with other technologies (solid state detectors or scintillators);
- It can operate in a harsh radiation environment with a very high γ-background, such as research reactors or spallation neutron sources;
- Good spatial resolution (from 80 µm up to few mm);
- High count rate capability (1 MHz/mm^2 for X-Rays; 10-30MHz/cm^2 for neutrons);
- The multiplication region is physically separated from the readout (possible discharges do not affect the readout electronics);
- The used gas mixture is safe and cheap.

The GEM technology has many applications, both in high energy physics [11] and in plasma diagnostics [12] where a very high rate capability is needed.

1.3 GEM-Based detectors for neutrons

GEMs can detect charged particles or photons. Photons can directly ionize the gas, producing the primary electrons that will be multiplied by the GEM foil. In this case, the gas also acts as a converter. In common with photons, neutrons have no charge, so they cannot interact with matter through the Coulomb force. The interaction of neutrons with matter is mainly with nuclei by means of the Strong force [1]. But while

for photons the interaction probability increases with the atomic number of the material, the neutron cross section can vary erratically between elements of similar atomic number and even between isotopes of the same element. For this reason, in order to use a GEM as neutron detector, it must be coupled with a suitable converter material. This thesis is focused on the development of these converters, which will be installed in the drift region of the triple GEM.

In most cases, when neutrons interact with matter, they produce heavy charged particles (protons or heavier particles). These particles may be produced as a result of a neutron-induced nuclear reaction (neutron absorption or induced fission) or may be the nuclei of the converter material itself that are accelerated by the collision with neutrons (recoil). The probabilities of the different neutron interactions change significantly with neutron energy, thus neutrons may be divided into two main categories: fast (En>0.5 eV) and slow (En<0.5 eV). The value of 0.5 eV is a conventional boundary corresponding to the cadmium cut-off energy. In the next paragraphs, the types of interaction for fast and slow neutrons are described.

1.3.1 Slow neutron interactions

Slow neutrons can only transfer low energy amounts to the nuclei of the converter material in elastic scattering processes. This means that elastic scattering cannot be used as a detection technique for slow neutrons. The neutron-induced reactions which produce secondary radiation with sufficient energy (positive Q-value [1]) to be detected are the only useful for slow neutron detection. Since gamma-neutron discrimination represents an issue for neutron detector, the use of material like cadmium or gadolinium is discouraged because the neutron absorption is via (n, γ) reactions. The reactions of interest for the application of this thesis must, therefore, have a positive Q-value and produce directly detectable charged particles. Typical reactions used to convert thermal neutrons into charged particles are:

- ^{10}B(n,α)^{7}Li reaction.

$$^{10}\mathrm{B}+\mathrm{n}\rightarrow\begin{cases} {}^{7}Li(1.015\ MeV)+\alpha(1.777\ MeV) \quad Q=2.792MeV\ (6\%) \\ {}^{7}Li(0.840\ MeV)+\alpha(1.47\ MeV)+\gamma(0.48\ MeV) \quad Q=2.310MeV\ (94\%) \end{cases}$$

Since the neutron momentum is several orders of magnitude smaller than the momentum of the byproducts, they are emitted back-to-back. In the excited state (94% branching ratio) their energy values are:

$$E_{Li}=0.84 \text{ MeV and } E_{\alpha}=1.47 \text{ MeV}$$

- $^{6}Li(n,\alpha)^{3}H$ reaction.

  $^{6}Li+n \rightarrow {}^{3}H+\alpha \qquad Q=4.78 \text{ MeV}$

The energies of the products (also emitted back-to-back) are:

$$E_{T}=2.73 \text{ MeV and } E_{\alpha}=2.05 \text{ MeV}$$

- $^{3}He(n,p)^{3}H$ reaction.

  $^{3}He+n \rightarrow {}^{3}H+p \qquad Q=0.764 \text{ MeV}$

The energies of the products (also emitted back-to-back) are:

$$E_{T}=0.191 \text{ MeV and } E_{p}=0.573 \text{ MeV}$$

The neutron cross sections of the different reactions of interest are reported in Figure 1-6 as a function of the neutron energy.

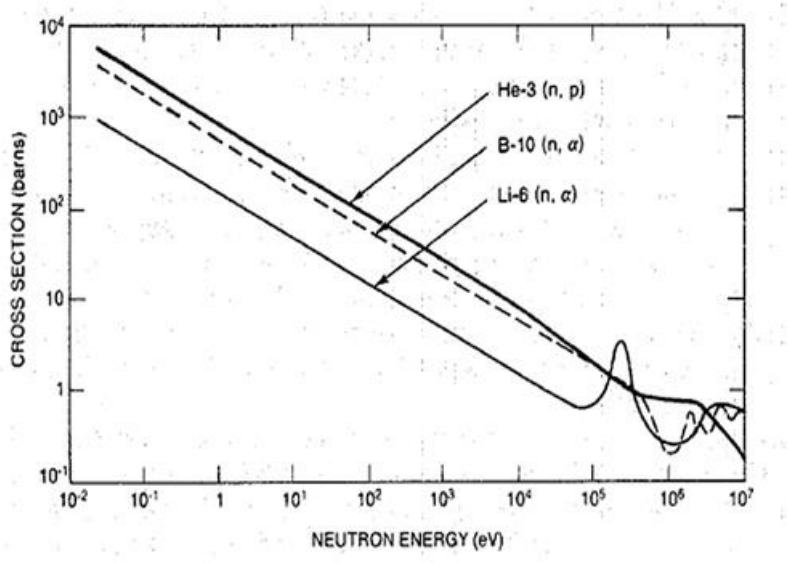

Figure 1-6: Cross section of the reactions of interesting [1]

For thermal neutrons (E_n=25 meV) the cross-section values are:

- 5330 barns for the $^{3}He(n,p)^{3}H$ reaction
- 3840 barns for the $^{10}B(n,\alpha)^{7}Li$ reaction
- 940 barns $^{6}Li(n,\alpha)^{3}H$ reaction

The $^{6}Li(n,\alpha)^{3}H$ reaction has the highest Q-value, but the lowest cross section. Thus, the use of ^{10}B or ^{3}He is preferable for high-efficiency detectors. The choice between ^{10}B and ^{3}He is nowadays oriented towards ^{10}B because of its availability.

The ^{3}He isotope is instead very rare, as reported in [13] and [14].

1.3.2 Fast neutron interactions

As shown in Figure 1-7 for ^{10}B as an example, the cross sections of neutron-induced reactions of most materials drop off rapidly with increasing neutron energy.

Figure 1-7: Comparison between neutron-induced reaction cross section (blue) with neutron scattering cross section (red). [3]

However, the importance of the elastic scattering grows with energy, given that the neutrons can transfer an appreciable amount of energy to the target nuclei in one collision. The elastic scattering of neutrons produces recoil nuclei, which energy E_R is equal to [1]:

$$E_R = \frac{4A}{(1+A)^2}(\cos^2\theta)E_n \qquad \text{Eq. 1-3}$$

Where A is the ratio between the mass of the target nucleus and the mass of the neutron; θ is the scattering angle of the recoil nucleus in the lab coordinate system (see Figure 1-8), E_n is the kinetic energy of the incoming neutron and E_R is the kinetic energy of the recoil nucleus.

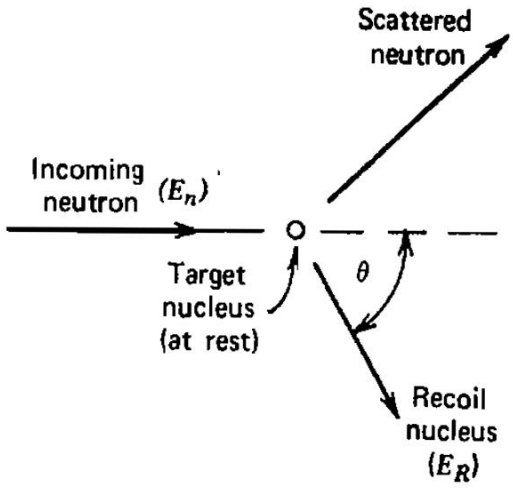

Figure 1-8: The laboratory coordinate system

From this equation, it's clear that the energy of the recoiling nucleus is uniquely determined by the scattering angle. E_R is minimum when θ=90° (grazing angle collision), while it reaches the maximum for θ=0° (head-on collision):

$$E_{RMax} = \frac{4A}{(1+A)^2} E_n \qquad \text{Eq. 1-4}$$

As a function of A, E_{RMax} is maximum (neutron lose all its initial energy in one collision) for A=1 (collision of neutrons with hydrogen nuclei) and decreases rapidly with increasing target nuclei mass.

The fast neutron GEM-based detector presented in this thesis (see chapter 3) uses a hydrogenated cathode to detect the 2.5 MeV neutrons produced by the D-D fusion reaction.

2 Chapter 2: GEM based detector for thermal neutrons

This chapter describes the development of the BAND-GEM detector and a possible design to use it in a Small Angle Neutron Scattering (SANS) instrument. This detector is designed for thermal neutron detection and it is based on the $^{10}B(n,\alpha)^{7}Li$ reaction.

2.1 Introduction to Small Angle Neutron Scattering (SANS)

Neutron scattering is one of the most powerful and versatile experimental methods to study the structure and dynamics of materials at the nanometer scale [15]. In fact, thermal neutrons have wavelengths similar to the spacing between atoms (≈1 Å) so they are well suited to study the structure of matter at the atomic scale. Moreover, the typical energy of atom vibrations of materials is of the order of meV. This allows studying the dynamics of the atoms with thermal neutrons of similar energies.

Neutrons have no charge and this allows them to penetrate deeply into materials and perform non-destructive measurements in the bulk. Neutron scattering provides information that is highly complementary to that from photon or electron scattering techniques. X-ray atomic scattering factor increases with the atomic number while the neutron cross section can vary greatly between elements of similar atomic number and even between isotopes of the same element. Neutrons scattering techniques are in general slowest and more expensive than the X-Ray scattering, but a sample containing hydrogen (like organic samples) is almost invisible to X-rays while its neutron scattering cross section is high: therefore the presence and motion of hydrogen atoms can be easily studied in a neutron scattering experiment. For this reason, neutron scattering is used in several fields, like Biology, Earth Sciences, Planetary Science, Engineering, Nanoscience, and Cultural Heritage. Neutron scattering experiments can be done using several different techniques like Neutron Diffraction [[16]] (that provide information on the material structure), Neutron Reflectometry [17] (for the characterization of thin films) or Small Angle Neutron Scattering (SANS) [18] for microstructure investigations in various materials in a scale of about 1 - 100 nm. Of particular interest for this thesis is the SANS technique. In a typical SANS experiment, a collimated neutron beam with a wavelength in the range of 1-15 Å, is directed on a sample, illuminating a small volume

(typically less than 0.5 cm^3). A fraction of the neutrons is absorbed by the material, a fraction passes through the sample without any collision (attenuated transmitted beam) and another fraction is scattered by the sample (Scattered beam). The aim of the SANS experiments is the 2D detection of the scattered beam. Figure 2-1 shows a schematic of a SANS experiment setup.

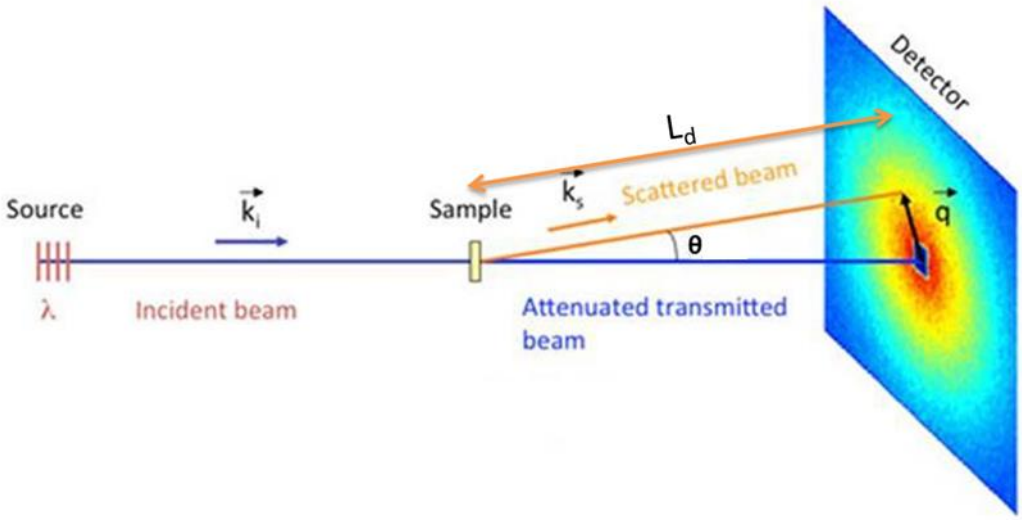

Figure 2-1: Schematic of a SANS experiment setup

In a typical SANS experiment, a detector bank is composed of a series of detector elements with dimensions *dx* x *dy.* Each detector element is positioned at a certain distance L_d and scattering angle θ from the sample. Each detector element records the part of the scattered beam contained in the solid angle element $\Delta\Omega = (dx\ dy)/L_d^2$. By indicating with I_0 the incident neutron flux, with V the illuminating sample volume, with η the detector efficiency, with *T* the sample transmission, with Q the module of the scattering vector $\vec{q} = \overrightarrow{k_s} - \overrightarrow{k_i}$,and with *(dσ/dΩ)(Q) the microscopic differential cross-section*, it is possible to obtain the flux at the detector element I(λ,θ) as following [19]:

$$I(\lambda,\theta) = I_0(\lambda) \cdot \Delta\Omega \cdot \eta(\lambda) \cdot T \cdot V \cdot \frac{\partial\sigma}{\partial\Omega}(Q) \qquad \text{Eq. 2-1}$$

The microscopic differential cross-section can be defined as:

$$\frac{d\sigma}{d\Omega} = \frac{number\ of\ scattered\ neutrons\ inside\ a\ solid\ angle\ d\Omega\ with\ scattering\ angle\ \theta\ per\ nucleous\ per\ second}{number\ of\ incident\ neutrons\ per\ cm^2\ per\ second}$$

The microscopic cross-section contains all the information on the shape, size, and interactions of the scattering bodies (assemblies of scattering centres) in the sample. We can then affirm that the aim of a SANS experiment is the determination of the differential cross section.

The scattering vector Q is defined as the module of the difference between the incident (**ki)**, and scattered (**ks)** wavevectors (shown in Figure 2-1). Q is then given by:

$$Q = |\vec{q}| = \left|\overrightarrow{\mathbf{ks}} - \overrightarrow{\mathbf{kı}}\right| = \frac{4\pi n}{\lambda}\sin(\frac{\theta}{2}) \qquad \text{Eq. 2-2}$$

Q has dimension length^{-1} and it is expressed in Å^{-1}.

By substituting the Q value found in the Bragg's law:

$$2dsin(\theta/2) = n\lambda \qquad \text{Eq. 2-3}$$

One can find a direct relationship between the scattering vector Q and the characteristic length of the observed structure of the sample (d):

$$d = \frac{2\pi}{Q} \qquad \text{Eq. 2-4}$$

The BAND-GEM detector is one of the possible detector options to be installed in the LoKI instrument [20], a broad-band instrument at the European Spallation Source (ESS) [21]. The ESS is a long-pulse spallation neutron source (with a pulse length of 2.86 ms and a repetition rate of 14 Hz) presently under construction at Lund, Sweden designed to reach a neutron brightness of the order of 7x10^{14}n/s/cm^2/sr/Å), i.e several times the neutron brightness of the source actually in operation in the world (as shown in Figure 2-2). ESS will host several neutron scattering instruments that will use the Time-of-Flight (TOF) technique [22] to perform scattering experiments. In most of the ESS instruments, a new generation of neutron detector must be installed. This is mainly

necessary for two reasons: the first one is related to the ^{3}He crisis [13], that has led to a significant increase in the price of ^{3}He. The second one is related to the expected neutron flux at the detector position in most of the ESS instruments. The high neutron brightness of the source implies a high neutron flux at the detector position in all the ESS instruments. For example, in LoKI a neutron flux peak of about $5x10^{5}$ n/cm^{2}s is expected at the detector position: this rate is not sustainable by the ^{3}He tubes that feature a maximum counting rate of about 20 kHz per tube [1].

In par 2.2 a numerical method for a principal design of an innovative detector system for LoKI is described.

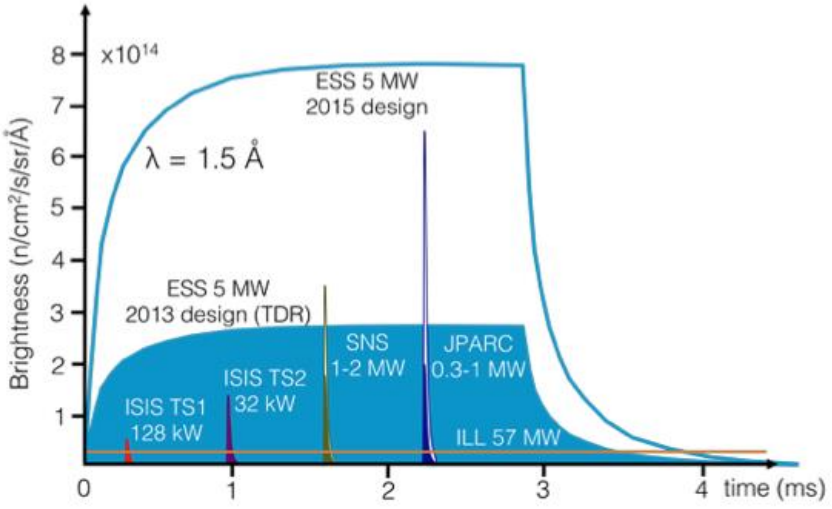

Figure 2-2: ESS pulses compared to the pulses of present-day spallation sources or reactors.[21]

2.2 Optimization of the experimental resolution for the LoKI instrument

2.2.1 Overview of the LoKI instrument

The LoKI instrument is designed primarily for users interested in biophysics, soft matter and materials science. In general, a series of studies on the bulk proprieties of the materials will be carried out, in particular for structural inhomogeneity in polymers and solutions. The samples that will be studied in LoKI will have high complexity and spatial and timing heterogeneity and, as said, they will have a small volume. Spatial

heterogeneity manifests with the different structures at different scales and requires a wide Q range and small neutrons beams. Moreover, these systems need to be studied with sufficient time resolution that can be provided by a high neutron flux and a wide simultaneous Q range. Based on the characteristics of the experiments that will be performed, the LoKI requirements are the following:

- Simultaneous Q-range of $1x10^{-3}Å^{-1} < Q < 3Å^{-1}$
- High neutron flux (about 10^9 n/cm^2s at the sample position)
- Q resolution (dQ/Q)<10% in the whole Q range

A schematic layout of the instrument can be found in Figure 2-3. Starting from the moderator, the overall length of the LoKi system will be about 35 m. The instrument is composed by two benders, three chopper systems, a series of neutron guides, the sample holder and the detector system. A detailed description of each part can be found in [23]. The sample is positioned at about 20 m from the source, while it is foreseen the installation of multiple detector banks positioned in the range of 1-10 m from the sample position.

LoKI has two modes of operation, offering different wavelength bands and hence different Q ranges. In Mode 1 operation, the choppers are running at 14 Hz. This mode allows to access the wavelength range from 2 to 12 Å. Mode 2 has the choppers running at 7 Hz. This allows accessing the wavelength band from 2 to 19 Å.

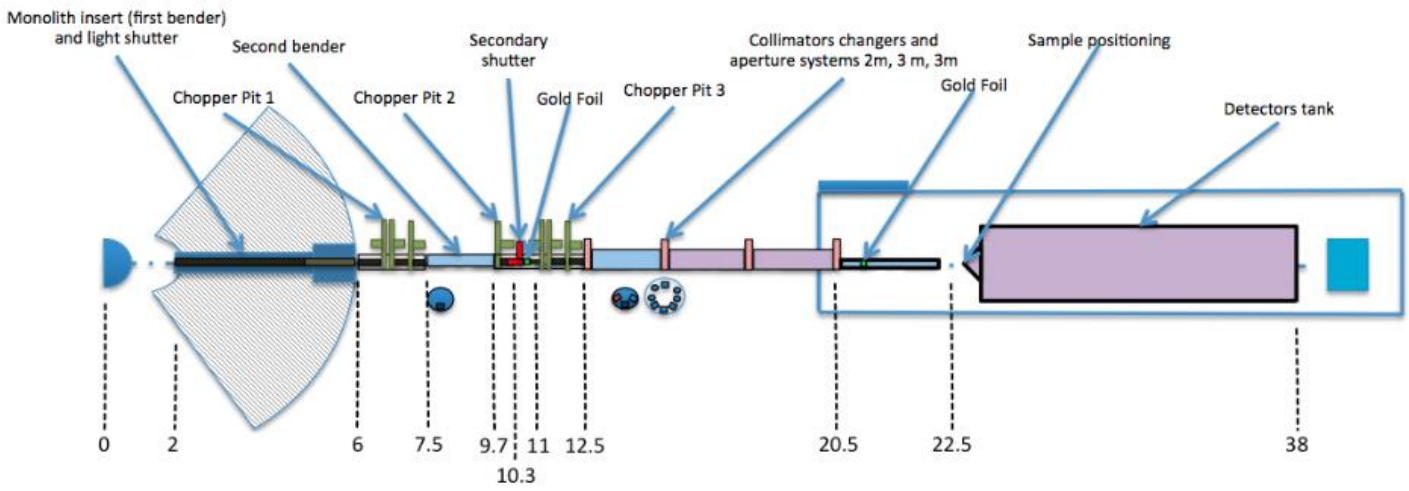

Figure 2-3: Layout of the LoKI instrument

While the design of the instrument from the moderator up to the sample holder is almost complete, the design of the detector tank, together with the design of the detector banks is still under discussion. However, also for the detector banks, a principle design already exists and it foresees the installation of three detector banks. The first detector bank will measure the high Q band, and it will be installed at about 2 meters from the sample; the middle bank, installed at about 5 meters from the sample will focus on the intermediate Q,; finally the rear bank, installed at about 10 m from the sample, will take care of low Q and direct beam measurements. In the following, a possible solution aiming at maximizing the LOKI performance while keeping the cost as low as possible will be discussed.

2.2.2 Method for the resolution optimization in LoKI

The detector system for the LoKI instrument must be designed in order to meet the requirement imposed by [24]. The summary of such requirements is:

- Efficiency > 30% over the entire wavelength band of LoKI (2-12 Å for 14 Hz;2-19 Å for 7Hz)
- Angular resolution $d\theta/\theta < 5\%$ (FWHM)
- Time-of-flight resolution < 0.1 ms
- Polar angle coverage of +/- 45 degrees from the beam axis (scattering angle, θ)
- Azimuthal angular coverage of +/- 180 degrees around the beam axis (azimuthal angle, ϕ)

- Possibility to distinguish events at overall rates of up to $5x10^8$ n/s
- Capability to measure direct beam shape (intensity distribution in direct beam)
- Fast neutrons sensitivity as low as possible
- Intrinsic noise (beam off noise) < 0.001 counts/s/cm^2
- Minimization of secondary scattering (detector should not scatter incoming neutrons)

If the detector system meets the above described requirements than LOKI will have the following performances:

- The instrument will allow data to be collected to a Q_{min} of 0.001 Å^{-1}.
- The instrument will allow data to be collected to a Q_{max} of 3 Å^{-1}.
- The instrument will allow the Q resolution (dQ/Q) to be optimised for the specific experiment.
- The instrument will be capable of providing a Q resolution < 10% dQ/Q between 0.001 Å^{-1} and 2 Å^{-1}.
- The instrument will allow data collection from samples < 8 mm^3 volume
- The instrument will maximize the signal-to-background (S/B) ratio of the small angle scattering.

In this paragraph, the discussion will be focused on the Q resolution of the whole instrument system by adopting different detector system design.
The resolution of a SANS instrument is due to contributions from the geometry of the collimation system (beam divergence), the solid angle subtended by the detection element (pixel size), and the wavelength resolution. The detector system should be designed so that its contribution is approximately matched to the other two for the most critical parts of the science case. We can assume that the resolution function of the whole system is well described by a Gaussian function, so we can calculate the resolution as the ratio between the variance $\sigma_{\mathbf{Q}}^2$ and the Q vector itself. To perform the resolution calculation the equations reported in [25] are used for rectangular apertures. In this case the standard deviation for vector **Q**, $\sigma_{\mathbf{Q}}$, is given by:

$$\left(\sigma_{\boldsymbol{Q}}\right)^2 = \frac{k^2}{12}\left[\frac{x_1^2 + y_1^2}{L_1^2} + \frac{x_2^2 + y_2^2}{L'^2} + \frac{x_3^2 + y_3^2}{L_2^2} + \frac{R^2}{L_2^2}\left(\frac{\Delta\lambda}{\lambda}\right)^2\right] \quad \text{Eq. 2-5}$$

where

- x_1 and y_1 are the dimensions of the source aperture
- x_2 and y_2 are the dimensions of the sample aperture
- x_3 and y_3 are the dimensions of the detection element
- Δλ is the FWHM of the wavelength distribution
- L_1 is the distance between source and sample apertures
- L_2 is the distance between the sample aperture and the detector
- R is the radial distance of a given detector element from the direct beam path
- $1/L' = 1/L_1 + 1/L_2$

For a detector system equipped with a padded anode (like the BAND-GEM), we can assume that the Point Spread Function (PSF) of the detector is adequately represented by a rectangular distribution. In this case, starting from the standard deviation of the point spread function of the detector σ, it is possible to obtain the equivalent pad size, that is:

$$Eq.PADSize = \frac{FWHM * \sqrt{12}}{\sqrt{8 \cdot \ln 2}} \qquad \text{Eq. 2-6}$$

For example, a padded detector with a 5.5 mm FWHM Gaussian is equivalent to a pixel with edge equal to 8.1mm.

Eq. 2-5 is strictly valid for "small angles", i.e. up to about 10 degrees. At higher angles, the sample will appear smaller and its thickness becomes important, so the result of Eq. 2-5 should be an overestimation.

In order to perform the resolution optimization, Eq. 2-5 was implemented in an IDL [26] code in the equivalent form:

$$\frac{\sigma_Q(L2,R)}{Q} = \frac{\sqrt{\frac{k^2}{12}(A+B+C+D)}}{Q} \qquad \text{Eq. 2-7}$$

With:

$$k = \frac{2\pi}{\lambda} \; and \; Q = k \cdot \frac{R}{\sqrt{{L_2}^2 + R^2}}$$

And:

$$A = \frac{x_1^2 + y_1^2}{L_1^2}, B = \frac{x_2^2 + y_2^2}{L'^2}, C = \frac{x_3^2 + y_3^2}{L_2^2}, D = \frac{R^2}{L_2^2}\left(\frac{\Delta\lambda}{\lambda}\right)^2$$

In the following an analysis of the parameters A, B, C, and D will be carried out, taking into account that the worst case for the calculation of the detector contribution to the overall resolution is the case on which the contribution of all the other parameters is minimum. This approach is based on the fact that if the detector system contribution to the resolution is approximately matched to the beam divergence and wavelength contributions for the minimum value of these last two parameters, the detector contribution will be negligible for all the other science cases.

The meaning of the parameters is the following:

- Parameter *A* is related to the geometry of the source aperture. L_1 is fixed and equal to 8 m, x_1 and y_1 are fixed at the beginning of the calculation. The worst case is represented by the smallest source aperture, which is 2.5x2.5 mm^2.
- Parameter *B* is related to the geometry of the sample aperture. L' is a function of L_2, while x_2 and y_2 are fixed at the beginning of the calculation. The worst case is the smallest sample aperture, which is 5x5 mm^2.
- Parameter *C* is related to the solid angle subtended by the detection element (pixel size). x_3 and y_3 are the dimensions of the detection element and these are the parameter that must be optimized.
- Parameter *D* is related to the wavelength spread. It is due to the long pulse nature of the ESS source (Figure 2-2). The source pulse duration at ESS is about 2.86 ms (FWHM). This means that the t_0 used as a reference for the derivation of the neutron wavelength [22] has an error that depends on the wavelength of the neutrons (slowest neutrons take a longest time to reach the detector position, so the pulse duration becomes negligible) and on detector position (detectors closer to the source mean less time for the neutrons to reach them). The

wavelength contribution for different neutron wavelengths and for different detector positions is shown in Figure 2-4 [24].

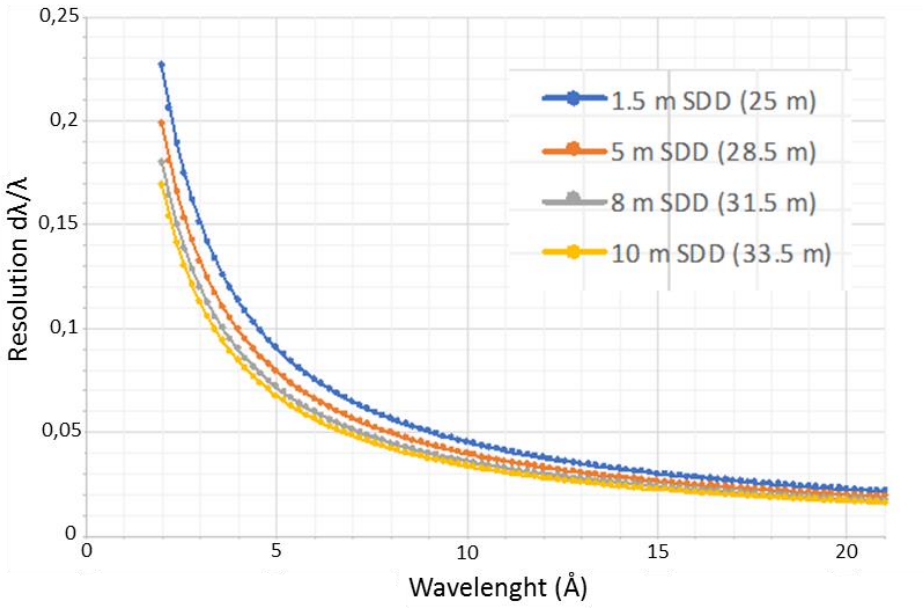

Figure 2-4: Wavelength (TOF) resolution as a function of wavelength for various sample-to-detector distances (SDD).

Eq. 2-7 in the code is solved for $0 < L_2 < 11$ m and $0 < R < 1.5$ m (in steps of 1 cm). The coordinate (0,0) corresponds to the sample position, neutrons come from negative L_2 coordinates. The maximum values for L_2 and R are the maximum allowable space for the detector tank. For each parameters set, the output of the code is an image, the colours corresponding to the calculated σ_Q/Q at a given position inside the detector tank.

Eq. 2-7 was than solved for the following reference case:

- σ_Q/Q calculation for L_1 = 8 m; x_1=y_1=2.5 mm ; x_2=y_2= 5mm, λ=12 Å.

This is taken as reference because it is the worst case for mode 1 operation (the standard operation mode for LoKI). In fact in the reference case the values of x1,y1 and x2,y2 are the smallest as possible and for long neutron wavelength, the Parameter D contribution is minimal.

In Figure 2-5 the overall σ_Q/Q for x_3=y_3=16mm for the reference case is shown.

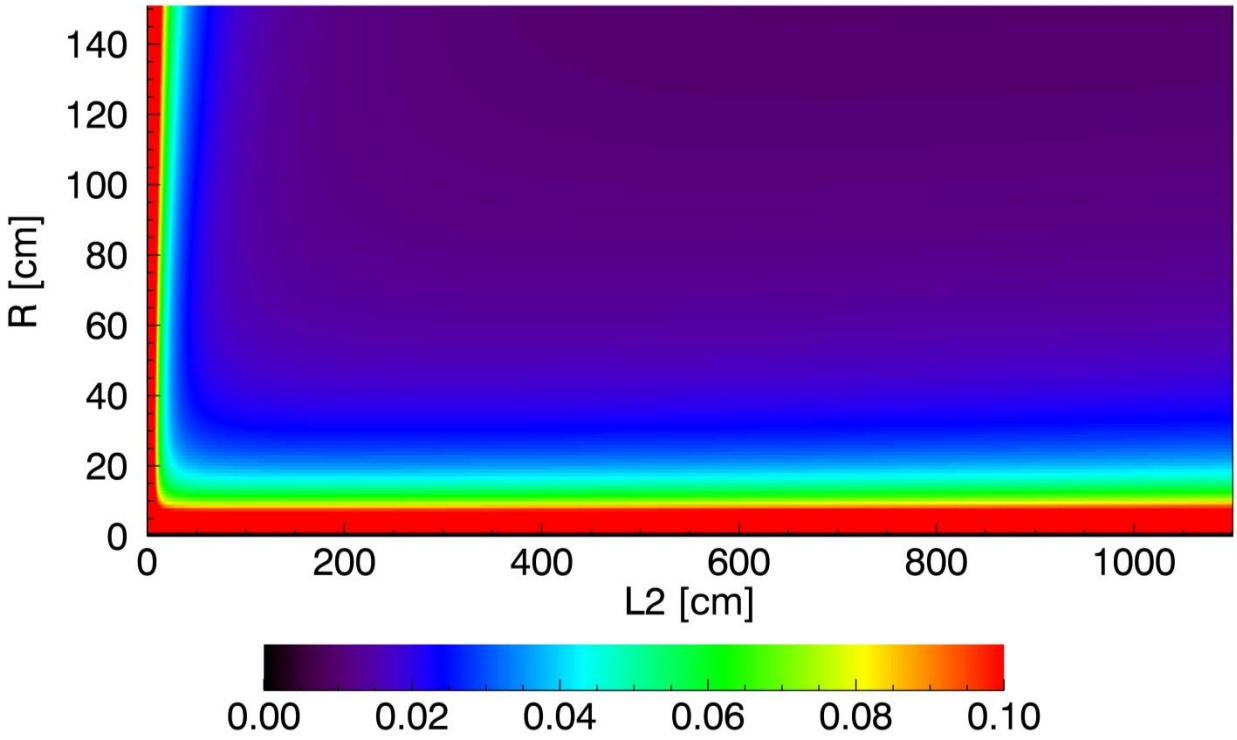

Figure 2-5: σQ/Q value calculated for L1=8m; $x_1=y_1$=2.5 mm ; $x_2=y_2$= 5mm, λ=12 Å,x3=y3=16mm. Red pixels represent the positions on which the σQ/Q exceeds 10%.

From the code it is now possible to extract the contribution of each parameters of Eq 2.6 in order to understand the detector contribution. The contribution of each parameter reported in the following is normalized to the calculates σ_Q/Q value, so that the sum of all the contributions on each point of the space is equal to one.

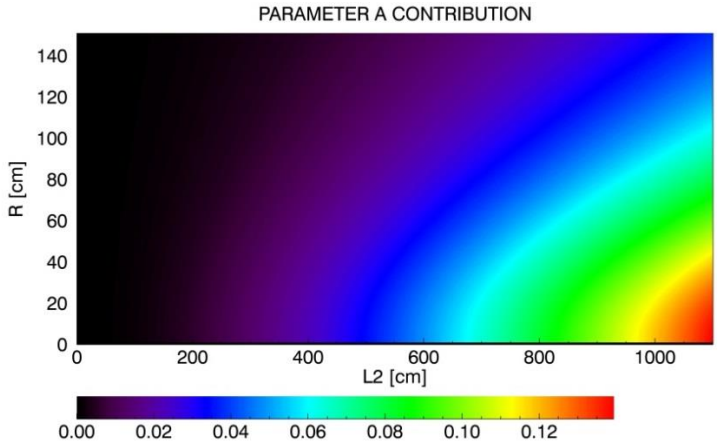

Figure 2-6: relative contribution of parameter A to the σQ/Q value calculated for L1=8m; $x_1=y_1$=2.5 mm ; $x_2=y_2$= 5mm, λ=12 Å,x3=y3=16mm.

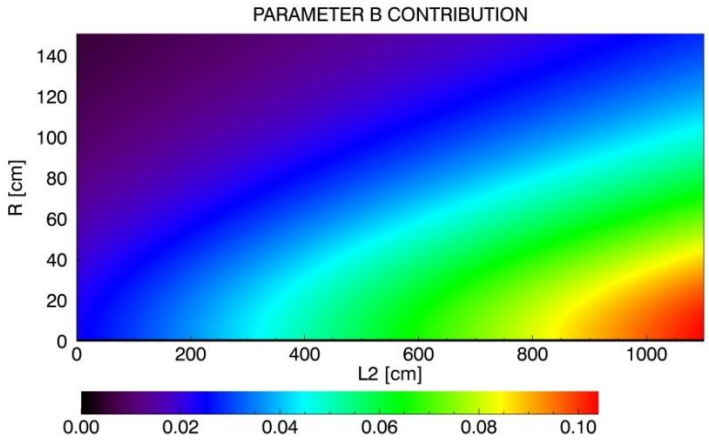

Figure 2-7: relative contribution of parameter B to the σQ/Q value calculated for L1=8m; $x_1=y_1$=2.5 mm ; $x_2=y_2$= 5mm, λ=12 Å,x3=y3=16mm.

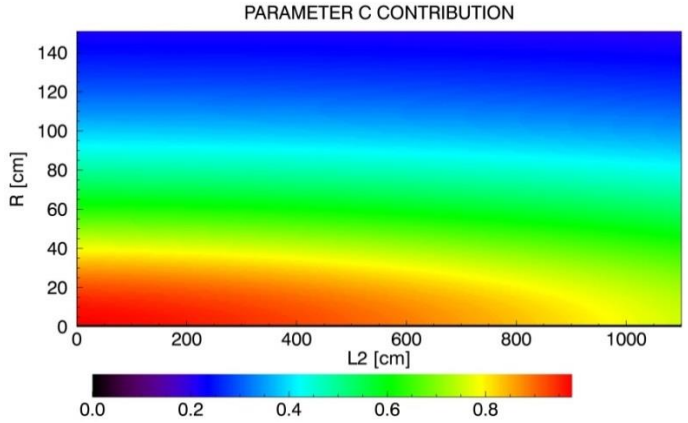

Figure 2-8: relative contribution of parameter C to the σQ/Q value calculated for L1=8m; x1=y1=2.5 mm ; x2=y2= 5mm, λ=12 Å,x3=y3=16mm.

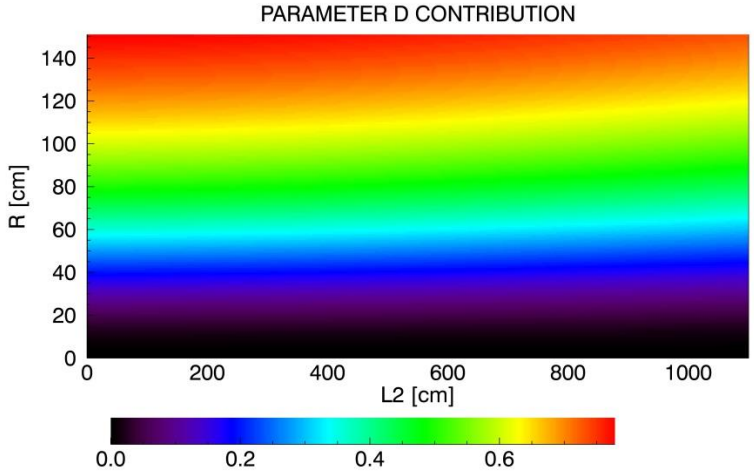

Figure 2-9: relative contribution of parameter D to the σQ/Q value calculated for L1=8m; x1=y1=2.5 mm ; x2=y2= 5mm, λ=12 Å,x3=y3=16mm.

Figure 2-6 to Figure 2-9 show the contribution to σQ/Q of the A, B, C and D parameters respectively. The contributions of parameters A and B become important only for small Q values (low scattering angle). Parameter D becomes very important for high values of R, while its contribution is negligible for low R. With this pixel size, however, the main contribution comes from parameter C. The chosen pixel size can be used only for high scattering angles and the 16x16 mm^2 pad size can be seen as an upper limit for the pads dimension.

Another approach that can be used for the minimization of the detector channels is the calculation of the maximum allowed pad dimension in each point of the LoKI detector tank. We can affirm that the maximum allowed pad dimension at a given point (L2,R) is found when the contribution of the pad dimension matches the contribution of all the other parameters. In other words, when the relative contribution of the parameter C is less than 0.5 (its contribution is a half of the overall σ_Q/Q). A strict approach should be used for the rear detector, given that at its envisaged position the contribution of parameters A and B become important (as shown in Figure 2-6 and Figure 2-7). In this area (L2>6m) we can say that the maximum pad dimension is found when the relative contribution of the parameter C is less than 0.3.

This approach is implemented in the IDL code as follows:

- For each coordinate (L2,R) the initial value of the pad dimension is set to the upper limit (16x16 mm^2)
- The values of σ_Q/Q and the relative contributions of all the parameters are calculated for the given point (L2,R)
- If the relative contribution of parameter C is less than 0.5 (0.3 for L2>6m), than the maximum allowed pad dimension is found; else the pad dimension is reduced by 1 mm in both directions and the calculation is repeated.
- Once the maximum allowed pad dimension is found the same method is applied to the next set of (L2,R) coordinates.

Using this method, one can obtain the map of the maximum allowed pad dimension and the relative map of the σ_Q/Q with the calculated maximum pad dimension. The results of these calculations are shown in Figure 2-10 (maximum pad dimension) and Figure 2-11 (σ_Q/Q).

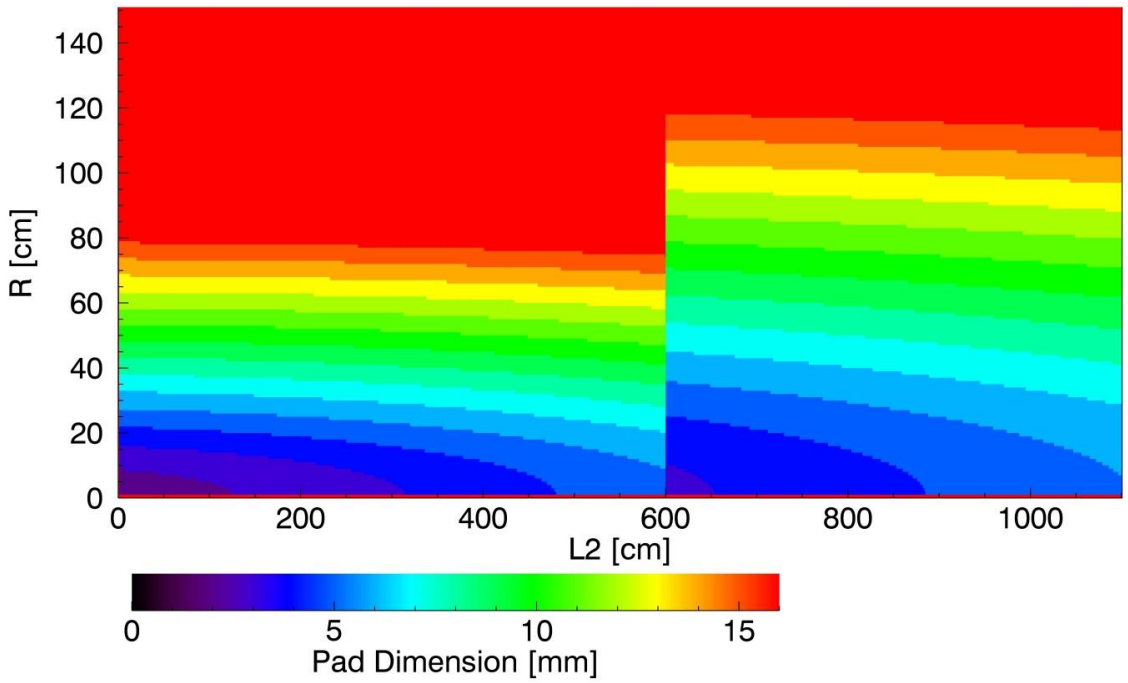

Figure 2-10: Maximum allowed PAD dimension to contain the relative contribution to the calculated σQ/Q of Parameter C within the limit of 0.5 (0.3 for L2>6 m). Colors represent pad size in mm.

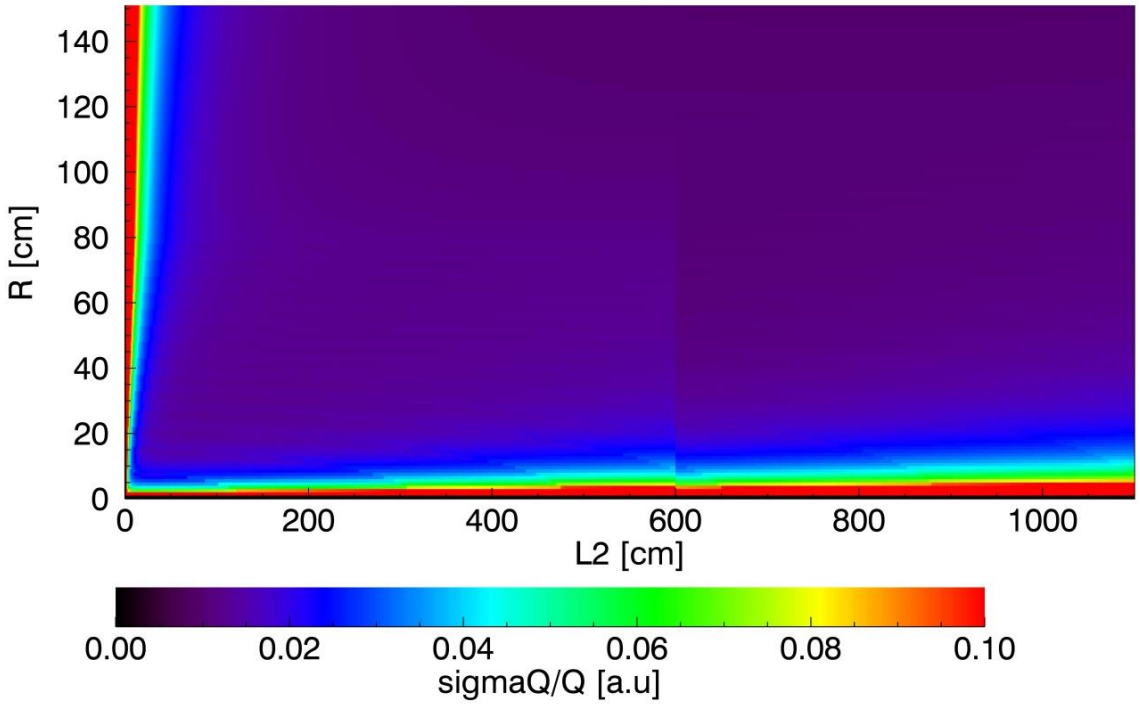

Figure 2-11: Calculated σ_Q/Q with the PAD dimensions reported in Figure 2-10

These results show the minimum required PAD size for a general padded detector. In order to perform the cost minimization, the specific detector that one want to use must be specified.

In the case of the BAND-GEM detector (as described in par 2.3), the detector works if it is tilted by few degrees with respect to the incoming neutron beam. The design of the detector system with BAND-GEM detectors, must be driven by the following technical criteria:

- Each BAND-GEM module should cover a maximum θ range of 5°, in order to reduce the degradation of the detector spatial resolution in θ.
- The maximum size of the converter grid (see par 2.3) is equal to 250x100 mm^2.
- The converter cathode should not be exposed to the direct beam component in order to minimize secondary scattering

The proposed detector system design foresaw 3 detector banks:

- Front bank detector: covers scattering angles from 5.7° to 45°. Based on BAND-GEM modules placed on a spherical surface of radius 1.6 m from the sample. Azimuthal angle coverage is equal to $\frac{5}{4}\pi$. Pad size goes from 16 mm x16 mm for the largest angles down to 4 mm x 4 mm for the smallest angles.
- Middle bank Detector: L_2 = 5 m (based on the BAND-GEM full module described in par 2.3.6): covers scattering angles from 1° to 5.7°. Azimuthal angle coverage is equal to π. Pad sizes ranges from 4 mm x 4 mm (at small scattering angles) to 8 mm x 8 mm at large angles.
- Rear bank detector: L_2 = 10 m, covers scattering angle from 0 ° to 1°. This serves both as transmission beam monitor and at the same time as small angle scattered neutron detector and has pads of 4 mm x 4 mm area.

A 2D sketch of the detector system, together with the pad dimension for each module is shown in Figure 2-12.

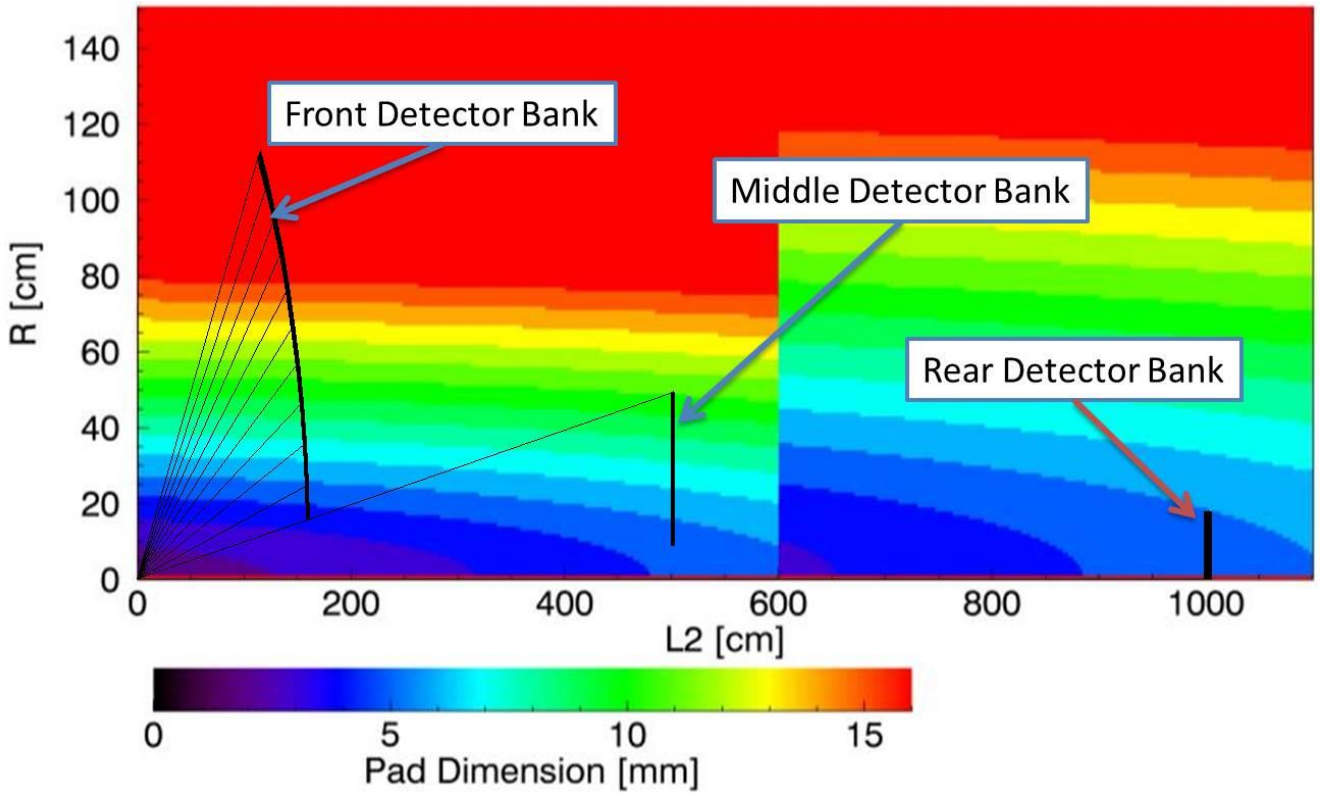

Figure 2-12: 2D sketch of the detector system with the corresponding pad dimensions

The front and middle banks will be BAND-GEM detectors, while in the rear bank the BAND-GEM should be avoided. In fact, the rear bank will be exposed to the direct beam component (neutron flux of about 10^9 n/cm^{2}s). In order to minimize the secondary scattering, the total amount of material intercepted by the direct component has to be minimized. In the proposed design the rear bank is a triple-GEM equipped with a single boron based converter layer (b-GEM[27]). The b-GEM converter is much less massive then the BAND-GEM one, and it can sustain very high rate (up to 50 MHz/cm^2[28]) and has an efficiency of about 5% at 2 Å.

A first design of the first detector bank is reported in Figure 2-13: each BAND-GEM module is represented with a different color. A total of 125 BAND-GEM modules is foreseen for the first detector bank.

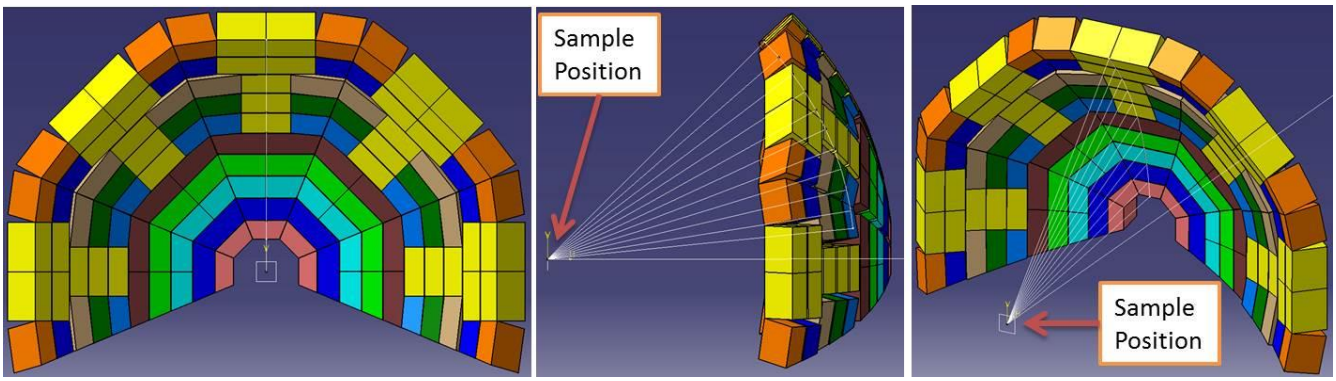

Figure 2-13: Principle design of the first detector bank. Front view (left), lateral view (center), Isometric view (right). The envelope of each different BAND-GEM module is represented with different color.

The second detector bank, it's based on the BAND-GEM full-module described in par 2.3.6. Figure 2-14 shows the foreseen design for the middle bank detector.

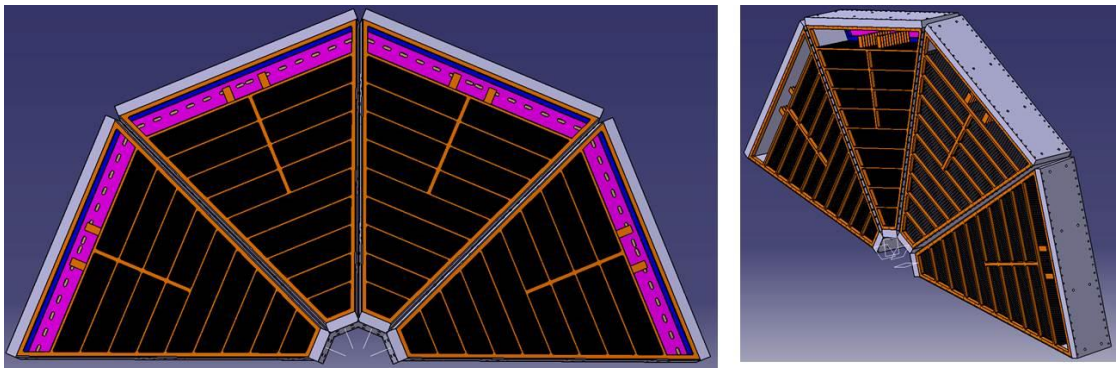

Figure 2-14: Design of the middle bank detector. Front view (left) and isometric view (right).

2.3 The BAND-GEM neutron detector

The BAND-GEM detector is a high-efficiency thermal neutron detector developed during my PhD period. It is based on a triple-GEM equipped with a three-dimensional converter cathode (3D-C). The BAND-GEM is based on the $^{10}B(n,\alpha)^{7}Li$ reaction. During this PhD, three BAND-GEM prototypes were developed and tested. In this paragraph the design of these prototypes, the simulation methods developed for the optimization of the 3D geometry, the construction technique used and the tests made on the prototypes are presented. Finally, it is shown the design of the full-module detector presently under construction, which can be part of the detector banks for LoKI.

2.3.1 BAND-GEM detector: principle of operation

The BAND-GEM idea comes from the need to improve the performance of the bGEM in terms of efficiency. In fact, the tests carried out with the bGEM detector [27],[Paper 4] have highlighted that the use of the GEM technology in thermal neutron detection can offer several advantages: high rate performance, good timing and spatial resolution, low-cost, and possibility to cover large area. The main limit shown by the bGEM is the low efficiency value (<5% at 2 Å). Detector efficiency is the result of two competing processes: the neutron capture efficiency in boron and the escape probability of the α and ^{7}Li byproducts from $^{10}B(n,\alpha)^{7}Li$ reaction. Therefore, to enhance the efficiency of a boron-based GEM neutron detector, the quantity of ^{10}B crossed by neutrons must be increased (to enhance the neutron absorption probability) keeping at the same time the boron layer thin enough to allow the reaction byproducts to reach and ionize the gas.

The three-dimensional cathode of the BAND-GEM detector is composed of a series of lamellas coated with a thin layer of $^{10}B_4C$ and stacked together in order to produce the so-called "3D Lamella System". The three-dimensional cathode is then coupled with a triple-GEM detector. The converter lamellas and the GEM foils are then sealed in a gas box where a constant flow of Ar/CO2 (70% -30%) at room temperature and atmospheric pressure is forced to flow.

The BAND-GEM principle of operation is shown in Figure 2-15. The BAND-GEM works with the whole detector structure tilted by few degrees with respect to the incoming neutron beam (θ angle). In this way, the thickness of each B_4C layer crossed by the neutrons is increased by a factor 1/sin(θ). Therefore, the neutron absorption probability is increased, while the thickness of B_4C layer seen by the α and ^{7}Li particles doesn't change, leaving their probability to reach the gas unchanged. The α and ^{7}Li ions are emitted back-to-back. This means that only one of the two products can reach the gas. In order to get a signal, the primary electrons created either by α or ^{7}Li ions must be able to move inside the lamella system and reach the Triple GEM structure where they are multiplied. To do this, each lamella is segmented into strips, each kept at a different voltage: this allows the generation of a drift field in the system that should be as uniform as possible.

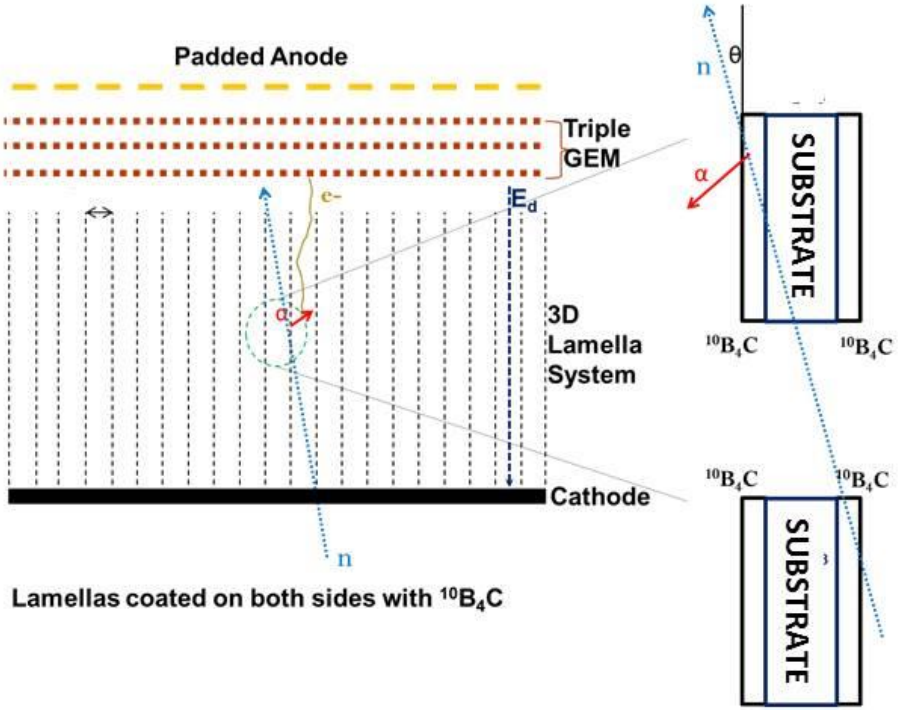

Figure 2-15: BAND-GEM schematics and principle of operation

2.3.2 First BAND-GEM detector prototype

2.3.2.1 Design and construction of the first BAND-GEM prototype

An isometric view of the 3D-C of the first BAND-GEM prototype is shown in Figure 2-16. It is composed by 48 Al_2O_3 lamellas (each 250 µm thick) composed of 15 strips (2mm wide) coated on each side with 1 µm of $^{10}B_4C$ (see Figure 2-17). The lamellas are stacked orthogonally to the triple-GEM, one next to the other, with a 2mm gap. The $^{10}B_4C$ coating is slightly conductive, so only the strips of the lamella (and not the entire lamella) should be coated if we want to apply an electric fled to the lamellas system to extract the primary electrons. To do this, before the coating procedure (performed at the Linkoping University [29]) each lamella was inserted in an especially designed aluminium support covering the surface of the lamella not to be coated. For the final 3D-C assembly, each coated lamella was inserted between 4 Printed Circuit Board (PCB) as the one shown in Figure 2-18. The assembly procedure can be seen in Figure 2-19: a small amount of conductive glue is placed on each copper plate of the 4 PCB boards; the lamella is then sandwiched between the 4 PCBs. The conductive glue keeps the assembly together and ensures the electric contact between the lamella strips and the

copper plates of the PCBs. This procedure is repeated for all 48 lamellas. Finally, the 48 lamellas with their PCBs are stacked and strengthened by using four M4 threaded insulating rods (shown in yellow in Figure 2-16).

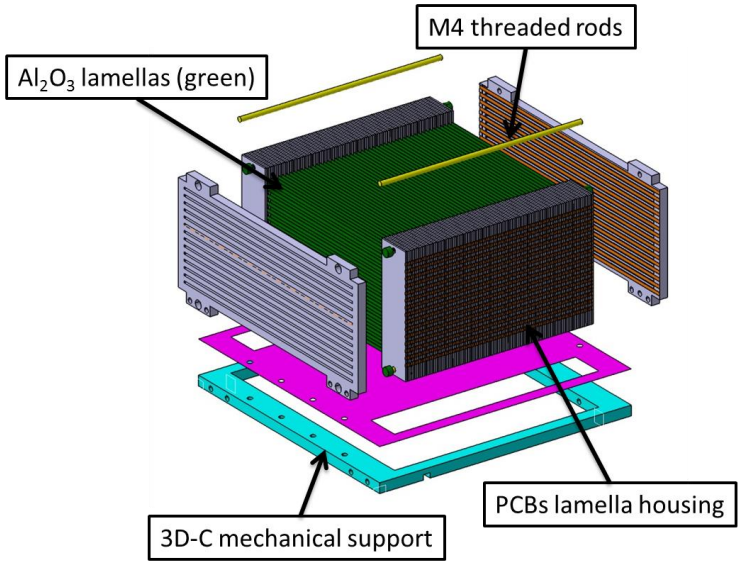

Figure 2-16: Isometric view of the three dimensional cathode o the first BAND-GEM prototype

Figure 2-17:Al_2O_3 lamella coated with 1 µm of $^{10}B_4C$ along he strips.

Each strip of the lamellas should now be connected to the external resistor chain. This is done by putting in contact each strips plane of the lamellas (first strip of lamella 1 with first strip of lamella 2, lamella 3 etc.) and finally by connecting the 15 planes to the resistor chain (Figure 2-20). The lamella system can thus be considered as a *field cage* (similarly to what is done in [31]) and the potential to each strip is given through an external voltage divider that has the two ends connected to the planar cathode and the top electrode of the first GEM foil (GEM 1 Top).

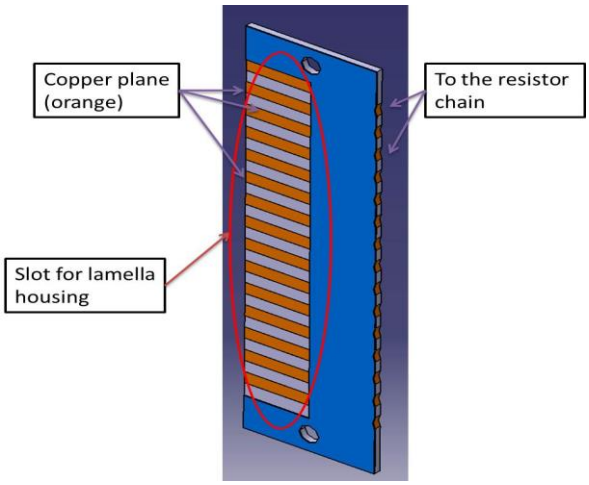

Figure 2-18: PCB board used to house the lamella and to connect each strip of the lamella to the resistor chain.

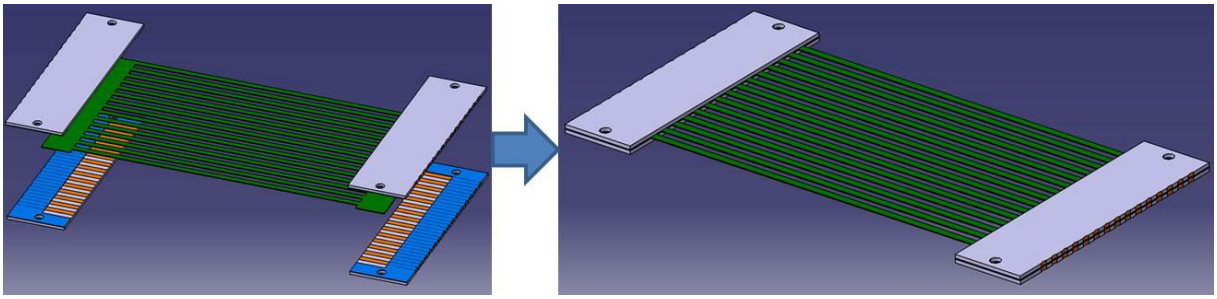

Figure 2-19: Procedure for single lamella assembly.

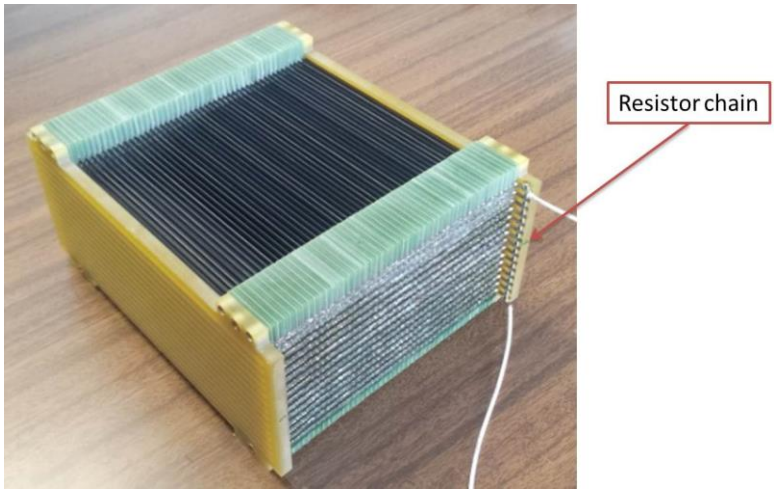

Figure 2-20:Final assembly of the three dimensional cathode. The resistor chain is highlighted.

The 3D-C is then inserted into its containing box (called lamellas box). In the lid of this box is installed the triple-GEM (Figure 2-21) thus completing the BAND-GEM. This BAND-GEM detector is equipped with a padded anode (see Figure 2-22) composed of 128 pads each with dimensions of 12 x 6 mm^2. The signal of each pad is routed to a

different channel of one CARIOCA [32] chip whose connector is located on the back of the read-out anode board. The LVDS (Low Voltage Differential Signal) signals of each CARIOCA channel are then managed by a FPGA Motherboard [33] that is located away from the detector and elaborates the signals in real-time, thus giving the possibility to on-line monitor the neutron beam. The high voltage is given to the three GEM foils and to the lamella system by means of a custom designed NIM Module (HVGEM) realized at the *Laboratori Nazionali di Frascati-INFN* [33]. Figure 2-23 shows the final assembly of the BAND-GEM detector.

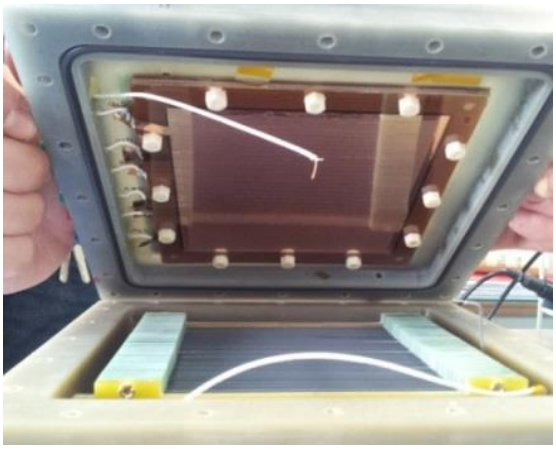

Figure 2-21: Coupling of the lamellas box with the triple-GEM box.

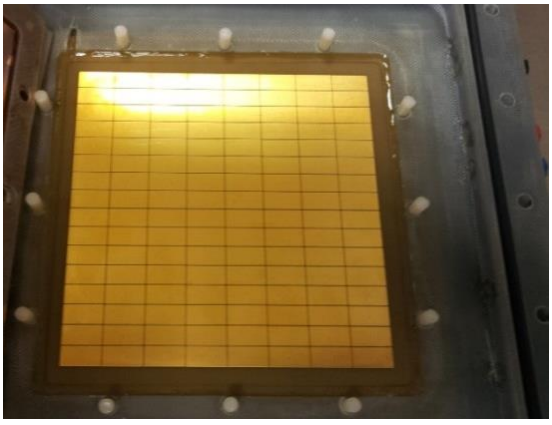

Figure 2-22: Triple-GEM padded anode.

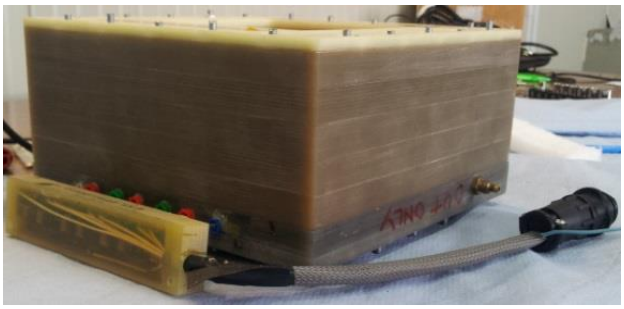

Figure 2-23: The BAND-GEM detector

2.3.2.2 Characterization of the $^{10}B_4C$ coating

In order to characterize the $^{10}B_4C$ coating of the lamellas, its thickness, uniformity and atomic composition were measured. This was done on a limited number of lamellas using some destructive techniques (Scanning Electron Microscopy (SEM), Energy Dispersive X-ray Spectroscopy (EDX), the Elastic Recoil Detection Analysis (ERDA) and the X-ray photoelectron spectroscopy (XPS). These measurements were performed at IENI-CNR in Milan [30]. The combination of these techniques gives a complete characterization of the samples, but at the price of sectioning and sampling the lamella elements, thus making them unsuitable for the installation on the 3D-C. As a consequence, to characterize all the lamellas the non-destructive method of the neutron radiography (or neutrography), combined with the information found in the limited number of lamellas characterized with the destructive methods, was used.

Preliminary characterization techniques

For the preliminary study of the coating thickness, the Scanning Electron Microscopy (SEM), was used. This analysis gives a measurement of the coating thickness and, by repeating the measurement all along the strips length, one can obtain an estimation of the thickness uniformity. Figure 2-24 shows a 0.9 µm B_4C thick coating on the alumina substrate. The same measurement was repeated in different locations along the strips and it was noticed that the film thickness is not perfectly uniform**.** The values found lie between 0.85 µm (near the strips edges) and 0.95 µm (at the center of the lamellas). For the data analysis of the neutron radiography, a reference value of 0.9 µm was taken.

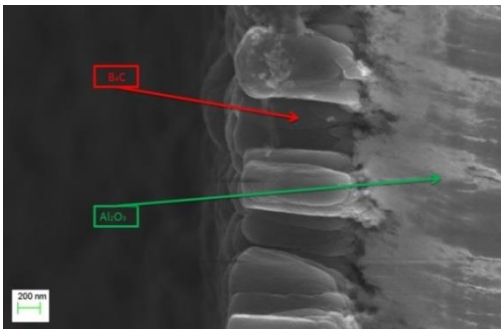

Figure 2-24: Result of the SEM analysis

The atomic composition of the coating was instead studied with the EDX, ERDA and XPS techniques. EDX and ERDA analyses were performed in order to obtain an estimation of the impurities in the coating, while XPS analysis to measure the variation of the coating atomic composition all along its thickness. These techniques are intrinsically point-like, and this causes small discrepancies between local values. However, the obtained results with the different analyses are compatible with the typical errors associated with these estimations, which are in the order of a few percent. The XPS has shown that the atomic composition of the coating is constant all along its thickness. The found values with the different techniques are reported in table 1.

Isotopes	B	C	Fe	Cr	Ni	Cu	O	Mg	Al
EDX	73	20	4	1	1	1	/	/	/
TOF-ERDA	77	16	/	/	/	/	1	2	0.4

Table 1: Average atomic composition found using the different analysis techniques. Values are in percentage.

As one can see, not only B and C are found in the coating, but also O, Mg, Al and some heavier elements (Fe, Cr, Ni and Cu). The elemental composition found in these analyses is taken into account in the neutron radiography data analysis.

Neutron Radiography

In order to characterize the boron carbide film deposited on all the lamellas, the neutron radiography technique was used. This is a non-invasive, non-destructive technique to obtain images of the inner parts of an object using a neutron beam to illuminate it. Neutrons transmitted through the sample are described by the following exponential law:

$$I(E) = I_0(E)e^{-\Sigma(\mathrm{E})z} \qquad \text{Eq. 2-8}$$

where $I_0(E)$ is the incoming neutron flux onto the sample, I(E) is the attenuated flux after crossing the sample, z is the thickness and Σ is the total macroscopic cross section that is defined as a function of the atomic density ρ and the total neutron cross section σ of the elements which compose the sample of molecular weight PM:

$$\Sigma = \sigma(\mathrm{E})\frac{n}{V} = \sigma(\mathrm{E})\frac{\rho N_A}{PM} \qquad \text{Eq. 2-9}$$

where N_a is the Avogadro constant. For the characterization of the lamellas we were interested in the total amount of neutrons absorbed from the boron contained into the $^{10}B_4C$ coating. In the analysis all the materials that compose the sample are taken into account, but the main contribution to the neutron absorption comes from the ^{10}B, which presents the largest cross section (about 3 order of magnitude), as shown in Figure 2-25.

The characterization of the film uniformity is done by comparing the expected transmission $\left(\frac{\tilde{I}}{\tilde{I}_0}\right)^{expected}$ with the measured one $\left(\frac{\tilde{I}}{\tilde{I}_0}\right)^{measured}$.

The value of the transmitted radiation is calculated by introducing the equivalent thickness *t* of the B_4C film:

$$t = \frac{\rho_{B_4C} z_{B_4C}}{PM_{B_4C}} \qquad \text{Eq. 2-10}$$

so that the expected transmission can be written as:

$$\left(\frac{\tilde{I}}{\tilde{I}_0}\right)^{expected} = \frac{\int_{E_{min}}^{E_{max}} I_0(E) e^{-\sigma(E) N_{Av} t^{expected}} dE}{\int_{E_{min}}^{E_{max}} I_0(E) dE} \qquad \text{Eq. 2-11}$$

with the expected equivalent thickness ($t^{expected}$) calculated using $\rho_{B_4C} = 2{,}242\,\frac{\mathrm{g}}{\mathrm{cm}^3}$ [29] and the value of z_{B4C} = 0.9 µm obtained from the SEM analysis. The measured transmitted radiation can be written as:

$$\left(\frac{\tilde{I}}{\tilde{I_0}}\right)^{measured} = \frac{\int_{E_{min}}^{E_{max}} I_0(E) e^{-\sigma(E) N_{Av} t^{measured}} dE}{\int_{E_{min}}^{E_{max}} I_0(E) dE}$$ Eq. 2-12

Where t^{measured} is calculated by using the mass density value obtained from the residuals evaluation after estimating the average of the neutrons absorbed by the lamella's strips ($\text{neutron}_{\text{abs}}$), and the values of z and of the impurities concentration obtained in the SEM and in the EDX, ERDA and XPS analyses.

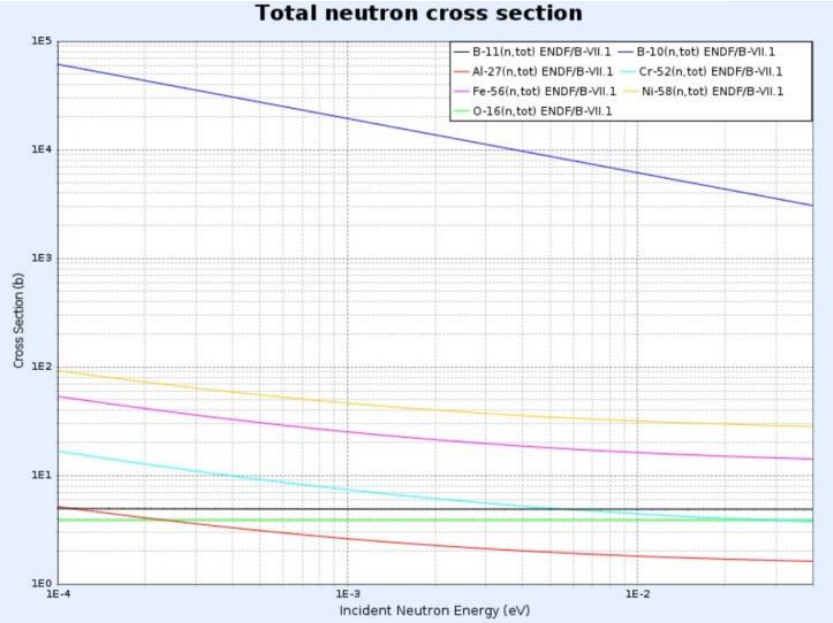

Figure 2-25: Total neutron cross section of the elements in the coating.[3]

The neutron radiography measurements have been performed at the *ROTAX* beamline [34] at ISIS [36], using the radiography-tomography system for the *IMAT* [37] beamline. Figure 2-26 shows a schematic of the used experimental setup. Neutrons transmitted through the sample strike a scintillator screen which converts the incoming neutrons into photons, the latter being detected, through a focusing mirror, by a digital camera (CCD). The lamellas were positioned on a rotating sample holder, which permits to select the angle between the incoming neutron beam and the lamellas. Moreover, the neutron beam in the ROTAX beamline has dimensions of about 40x35 mm^2, therefore the rotating sample holder has been mounted on an x-y positioner, which allows to enlighten all the lamella.

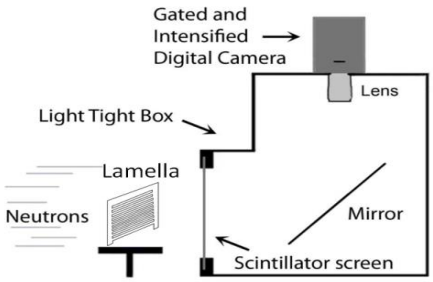

Figure 2-26: schematic of the experimental setup

The neutron flux used for the irradiation has an energy spectrum "cleaned" of fast neutrons and gamma components thanks to an upstream t-zero chopper. The details of the operation of the chopper on the ROTAX beamline can be found in [38]. The resulting spectrum is shown in Figure 2-27. The use of a gamma suppressing chopper is a common procedure at ISIS when transmission (i. e*. in the beam*) diagnostics are used, as in this case. In the present case, the scintillator coupled to the radiography system has a residual sensitivity to gamma rays: while this sensitivity is low (in the order of 10^{-6}) enough to make negligible the background due to activation inside the block-house and from the sample itself, it may not be the case when a large flux of gammas is expected, as the one coming from the spallation target.

These measurements give as output an image of 512x512 16-bit pixels. An example of neutron radiography can be found in Figure 2-28. All the lamellas for the 3D-C production (48 lamellas + 20 spares +10 coated with 1.1 µm of B_4C for data validation) were irradiated with neutrons, producing a total of 546 images (in order to characterize all the lamellas surface, 7 measurements for each lamella had to be taken, given that the ROTAX beam dimension is 40x35 mm^2). This big amount of data was analysed using a custom-made IDL code. This code implements an automatic method for the strip "detection" into the image. For each measurement the code extrapolates a set of measured values (one value for each strip in the enlightened area), which is then used for the evaluation of the $^{10}B_4C$ coating uniformity. A lamella is considered suitable to compose the 3D-C if the coating has a value of non-uniformity less than 10% with respect to the average of all the $t^{measured}$ values found on the whole lamella surface, and if the average of the $t_{measured}$ values obtained differs at maximum from the 10% with respect to the $t_{expected}=7.1x10^{10} mol/\mu m^2$.

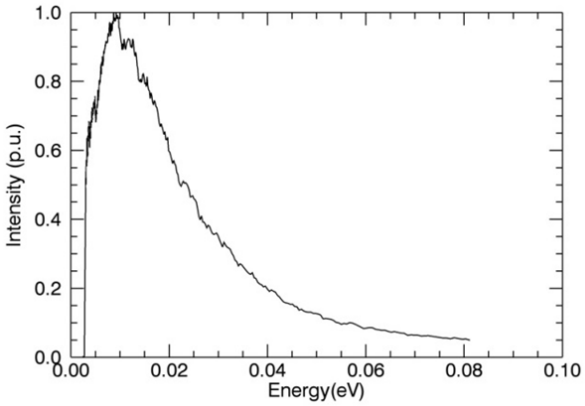

Figure 2-27: Neutron spectrum in the ROTAX beam line

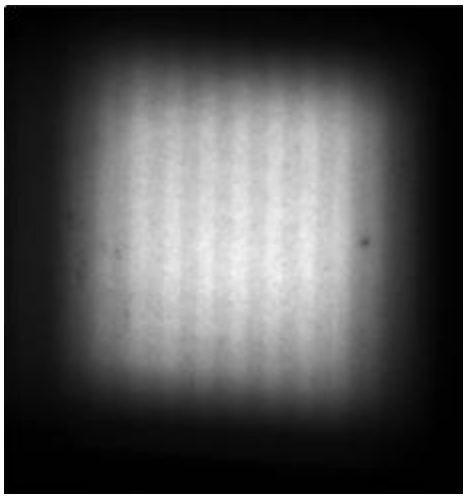

Figure 2-28: Output of a neutron radiography on one lamella. The darker parts of the image are the strips.

A detailed description of the methods implemented in this code can be found in [paper 1].To validate the method, the neutron radiography technique was also applied to a set of 10 lamellas with a higher thickness (credited to be 1.1 µm) of B_4C in order check if it was possible to distinguish coatings that have a 10% difference in thickness. Figure 2-29 shows that using this technique two different values of *t* are obtained for the lamellas with 1.1 and 1 um of B_4C, respectively. As expected, the two groups of lamellas are well separated beyond the estimated error bars. For clarity, only a small fraction of the samples is shown in Figure 2-29.

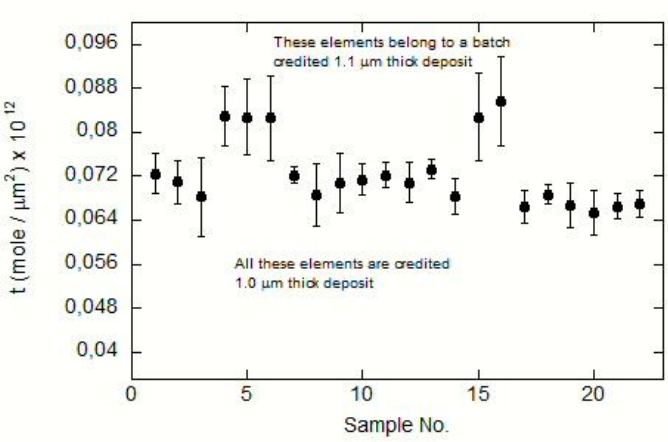

Figure 2-29: comparison between the t measured for lamellas with 1 and 1.1 µm B4C coatings. Some of the samples are shown

More than the 90% of the enlightened samples satisfy the acceptance criterion. Moreover, these measurements have shown that the deposition process is reasonably reproducible: therefore only a small number of samples will be checked in the future, (one or two samples for deposition run) in order to highlight possible major failures in a particular deposition run.

2.3.2.3 Test of the detector with neutrons

After the assembly procedure, the detector was tested under neutron irradiation in the R2D2 beam line, situated at channel 6 of the JEEP II reactor in Kjeller, Norway.

Experimental setup

In R2D2 beam line the neutron flux is about 10^5 n/cm^{2}s. Neutrons produced in the reactor pass through a Soller-type collimator (multiple parallel plates collimator) made of Cd layers with a divergence angle of 36'. The beam is then monochromated by a composite Ge wafer monochromator, and exits the shielding at 90 degrees through a second Gadolinium Soller-type collimator with a divergence of 30' inserted in a borated-polyethylene tube. By rotating the monochromator, it is possible to obtain a highly monochromatic neutron beam with wavelengths ranging from 0.8 to 2.0 Å. At the collimator exit, there are two motor-controlled slits (IB-C80 Air by JJ X-Ray, Denmark), each with four borated aluminium blades, that allow obtaining highly collimated neutron beams (up to 0.5 x 0.5 mm^2). The beam line is provided with two

^{3}He tubes that are used as flux monitors. The first one, located before the two collimating slits, has an efficiency of about 0.01% at 1.54 Å. The other one has an efficiency of about 87% at 1.54 Å and was used as reference detector during the efficiency measurements. The sample stage, positioned just after the collimation system, consists of a fully motor-controlled assembly (two perpendicular translation stages and two rotation tables) that allows the positioning of the specimen at different angles (precision better than 0.01 degree), heights and focus with respect to the incident monochromatic beam. The BAND-GEM detector was positioned in this sample stage, allowing to measure the efficiency as a function of the angle with respect to the incoming neutrons and to scan the full detector active area. Figure 2-30 shows a schematic of the experimental setup, while Figure 2-31 shows a picture of the BAND-GEM detector positioned on the sample stage.

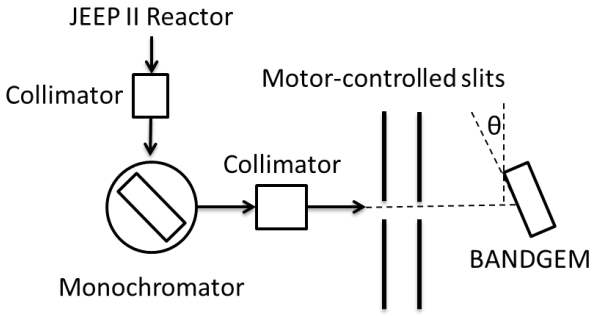

Figure 2-30: Schematic of the experimental setup of the first BAND-GEM at R2D2 beam line

The lamella system resistor chain was biased by connecting one of its terminals to the Cathode and the other to the GEM 1 Top (the electrode of the first GEM foil facing the lamellas) using the HVGEM module. Following this configuration, the maximum achievable ΔV on the 3D-C is about 1.5 kV. The gas flow used during all the measurement was Ar/Co2 70%/30% with a flow of about 10 l/h.

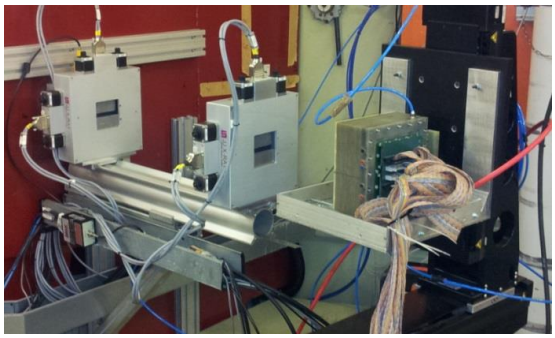

Figure 2-31: Experimental setup used on the RD2D beam line. The BAND-GEM is located behind the two slits on the sample stage.

Working point gas gain determination

The first test carried out was the working point gas gain determination. In a triple-GEM detector, the gas gain exponentially depends on the sum of the potential differences applied to the three GEM foils ($\Delta V_{GEM1} + \Delta V_{GEM2} + \Delta V_{GEM3} = V_{GEM}$) [10]. A thermal neutron detector must be highly insensitive to gamma-rays, so the gain of the GEM must be high enough to be able to detect the α and ^{7}Li ions coming from the $^{10}B(n,\alpha)^{7}Li$ reaction, but not too high in order to reduce the gamma-ray sensitivity of the detector. A first test was then carried out using a ^{137}Cs source emitting 662 keV photons (activity of about 100 kBq) positioned in front of the BAND-GEM detector, in order to determine the voltage value where the gamma ray contribution becomes relevant. Figure 2-32 shows the counting rate recorded on the whole detector area as a function of the applied voltage on the triple-GEM, with the maximum allowable voltage difference applied to the 3D-C system (V_{LAM}=1500 V), transfers field (the electric field applied between the GEM foils) $E_{T1}=E_{T2}$=3 kV/cm, and induction field (the electric field between the last GEM foil and the anode) E_i=5kV/cm. As you can see, the detector becomes sensitive to gamma rays for V_{GEM} > 1000V.

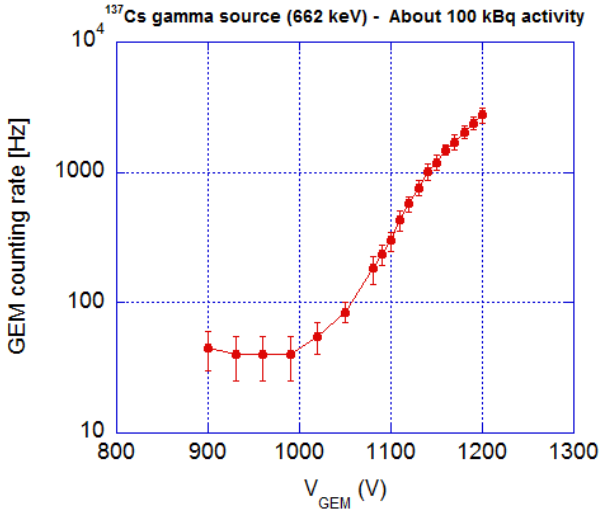

Figure 2-32: Gamma ray (662 keV) counting rate as a function of V_{GEM}.

A similar test was carried out under neutron irradiation with the detector tilted by 7° with respect to the beam direction. During the measurements, the neutron beam was set to a wavelength λ=1.54 Å (corresponding to 34.5 meV) and dimensions of 5 mm x 5 mm. Figure 2-33 shows the counting rate recorded on the whole detector as a function of the detector gain, with the same electrical parameters used for the gamma ray

measurement described above. As one can see, the counting rate is an increasing function of $V_{GEM.}$ The detector starts to detect neutrons for V_{GEM}=810 V (corresponding to a gain of about 50). A slightly change of the slope of the curve can be noticed for V_{GEM}=920 V, and the curve changes slope again at V_{GEM}=1000 V, where the detector becomes highly sensitive to gamma-ray as shown in Figure 2-32.

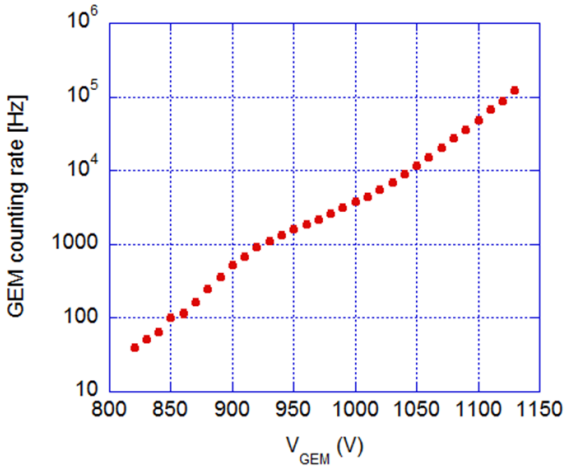

Figure 2-33: BAND-GEM counting rate as a function of the applied voltage

The slope of the curve found in this measurement is different from the one obtained here [paper 4] or here [paper 3]. In fact, previous measurements showed in general a plateau in counting rate between V_{GEM}=870 V and V_{GEM}=1000 V. The counting rate is an increasing function of V_{GEM} for values less than 870 V and higher than 1000 V, the latter effect being due to γ rays sensitivity. The absence of a plateau region in this measurement is due to the limited voltage difference applicable to the 3D-C system and to the geometry of the 3D-C as explained in details in par 2.3.3.

The working point chosen for the following measurements was V_{GEM} = 980 V, corresponding to the higher voltage on which the detector is quite insensitive to gamma-rays.

Counting rate measurement as a function of tilting angle

With the electrical parameters found in par 0 (V_{GEM}=980V, E_{T1}=E_{T2}=3 kV/cm, E_i=5kV/cm and V_{LAM}=1500 V) the counting rate of the detector was measured as a function of the tilting angle (i. e. the angle between the beam direction and the lamella system) in order to verify the principle of operation of the device itself (see Figure 2-15). Figure

2-34 shows the result of these measurements. The BAND-GEM counting rate oscillates with different amplitudes up to 10°, where it stabilizes on a plateau. The reasons for these oscillations are linked to the geometrical parameters of the 3D-C and can be partially reproduced by the simulations of par 2.3.3. In order to confirm this, the same measurement was repeated by putting an ^{3}He tube (Reuter Stokes ^{3}He proportional counter) as reference behind the BAND-GEM. The BAND-GEM was kept off and its signal cables and electronics were removed. Figure 2-35 shows the ^{3}He counting rate as a function of the GEM rotation angle. It is possible to appreciate that the ^{3}He counting rate is complementary to what has been measured using the BAND-GEM: if the BAND-GEM shows a deep, the ^{3}He shows a peak for the same tilting angle. This confirms that the oscillations observed on the BAND-GEM efficiency are due to geometrical parameters of the 3D-C, which absorbs a different fraction of neutrons when the incidence angle is varied. The same ^{3}He tube in front of the BAND-GEM was used as reference for an estimation of the detector efficiency for 1.54 Å neutrons. To do this, the so-called cluster size (CL_{GEM}) measurement was also performed. This is the average number of pads highlighted by a single event (a single neutron), i.e. a measurement of the charged products range effect inside the lamella system. To measure it, the neutron flux must be reduced to the minimum and the acquiring window on the DAQ must be as shorter as possible, so that each neutron event can be clearly distinguished.

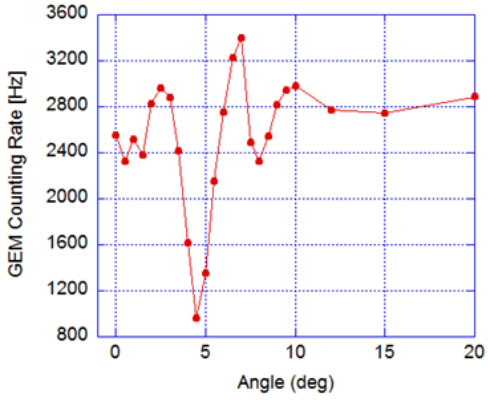

Figure 2-34: BAND-GEM counting rate versus the tilt angle θ.

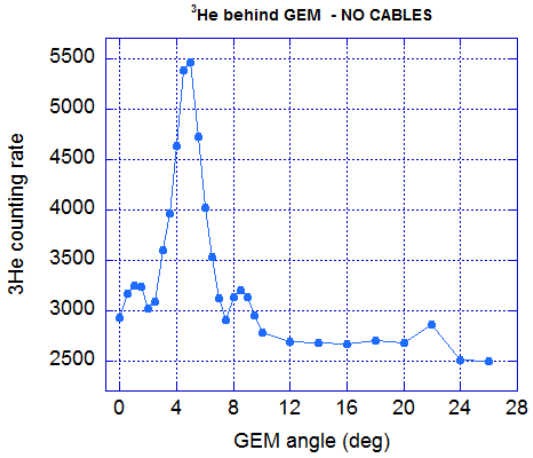

Figure 2-35: ^{3}He counting rate as a function of the GEM rotation angle

The neutron flux was thus reduced by further collimating the beam up to 0.5 mm x 0.5 mm and the acquiring window was set equal to 10 µs. The result of the measurement is CL_{GEM} = 1.15, meaning that in average each detected neutron highlights 1.15 pads.

The efficiency of the detector at 7° and with V_{GEM} = 980 V can be thus calculated using the following formula:

$$\varepsilon_{GEM} = \frac{C_{GEM}}{C_{3_{He}}} \times \frac{\varepsilon_{3_{He}}}{CL_{GEM}} \qquad \text{Eq. 2-13}$$

Where C_{GEM} is the recorded counting rate with the BAND-GEM detector and CL_{GEM} represents the cluster size; C_{3He} is the counting rate recorded with the ^{3}He tube, and ε_{3He} is the efficiency of the ^{3}He tube at 1.54 Å (87%). The resulting BAND-GEM efficiency is about 16% at 1.54 Å.

2.3.3 Numerical simulation for the optimization of the BAND-GEM geometry

The tests carried out on the first BAND-GEM prototype have shown encouraging progress in terms of neutron detection efficiency respect to the results obtained with the bGEM. However the performance of the detector can be further improved, so it was decided to develop a series of numerical simulations for the optimization of the geometrical parameters of the 3D-C.

The calculation of the neutron detection efficiency of the BAND-GEM must consider three important aspects:

- The neutron conversion efficiency in the boron layer, that is the number of charged particles (α particles or Li ions) created inside the converter
- The capability of these particles to escape the conversion layer and to deposit their energy in the gas between the lamellas
- The capability of the primary electrons (created by neutron products) to be extracted from the lamella system and to reach the tripleGEM amplifying structure.

2.3.3.1 Optimization of the neutron conversion efficiency

The optimization of the neutron conversion efficiency was done by using a custom made IDL code [26]. This optimization is done to increase the detector efficiency and to avoid strong dependence of the efficiency from the detector tilt angle, as the one shown in Figure 2-34. In particular, the parameters of the 3D-C that must be optimized by the code are:

- The distance between the lamellas ("lamellas gap")
- The length of the B_4C coating
- The distance between the strips
- The lamella thickness
- The total number of strips for each lamella.

In the code the lamellas system and the incoming beam are represented using two matrixes of integer values, called "beam matrix" and "lamellas matrix". In the beam matrix all neutrons tracks are perfectly parallel and all the neutrons are monochromatic. Figure 2-36 shows an example of beam matrix. As one can see, the matrix is composed of zero values everywhere (black area), apart in the area where the neutron beam is simulated (grey area). In the picture, neutrons enter into the detector from the bottom (y coordinate=0) while the GEM is located on the top (y coordinate=y_{MAX}). For each angle a different beam matrix (with different inclination of the neutron tracks) is produced. In the lamellas matrix only the B_4C coating is represented, given that only neutron absorption is considered in this code. This means that the lamellas matrix is equal to zero everywhere, apart in the areas on which the

coating is present. The change of the lamellas matrix parameters, allows the simulation of different 3D-C geometries. The granularity of both the matrixes is equal to 1 μm. A total of 4 gaps (5 lamellas) are simulated.

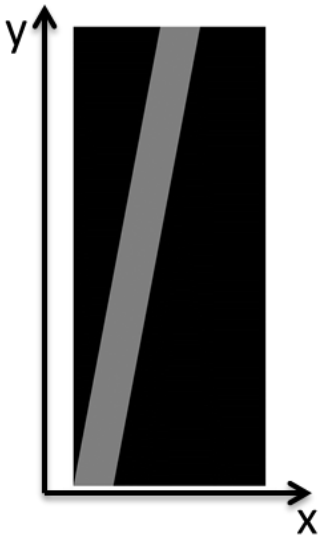

Figure 2-36: Example of beam matrix (angle=7.1°). Grey area represents the beam.

The calculation of the neutron conversion efficiency for each different beam angle and for each lamella matrix is performed by multiplying element by element the lamella matrix with the beam matrix. The resulting matrix gives the positions where the neutrons have an interaction with the B_4C coating. For each interaction position, the number of absorbed neutrons is calculated as:

$$neutron_{absorbed} = I_0^i(E) - I_0^i(E)e^{-\Sigma(E)(\frac{z}{\sin(\vartheta)})} \quad \text{Eq. 2-14}$$

where $I_0^i(E)$ is the incoming neutron flux for a given position, z is the thickness of the B_4C coating, ϑ is the neutron beam tilting angle, E is the neutron energy, and Σ is the total macroscopic cross section.

After the calculation of the neutrons absorbed at a given position, the value of $I_0(E)$ is updated for the successive interactions, and its value will be equal to:

$$I_0^{i+1}(E) = I_0^i(E) - neutron_{absorbed} \quad \text{Eq. 2-15}$$

The output of this calculation provides a map of the neutron interaction points: the numbers of charged particles as well as the coordinates of the charged particle production position were recorded as output. This information is saved in a three-dimensional matrix that is used in the simulations described in the next paragraph.

Figure 2-37 shows the total number of absorbed neutrons for the case of the first BAND-GEM prototype (par 2.3.2). The lamella matrix was set using a 2 mm gap between the lamellas, a strip length of 2mm, an empty space between the strips equal to 2mm and a total number of strips equal to 15.

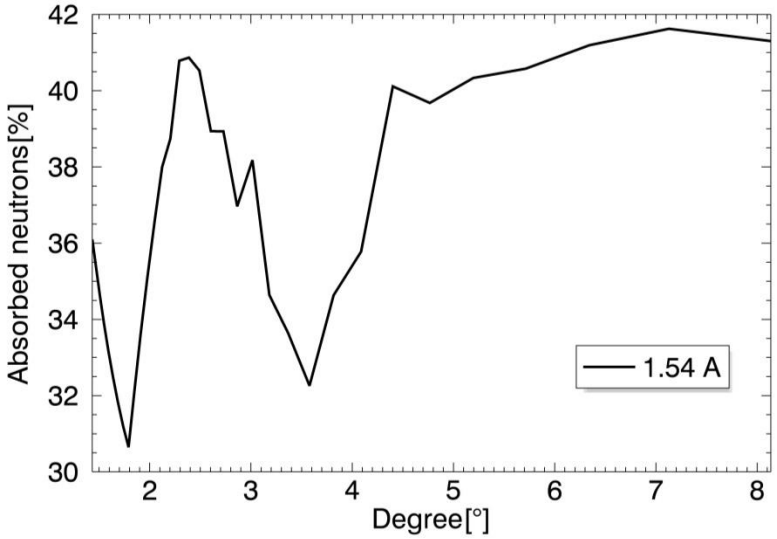

Figure 2-37: Calculated number of absorbed neutron with the geometrical configuration used for the first BAND-GEM prototype

As one can see, the calculation of Figure 2-37 has the same trend as the data shown in Figure 2-34. The discrepancies will be explained in the next paragraphs when the electron extraction efficiency from the field cage will be taken into account. However, one of the aims of this numerical simulation is to find a geometrical configuration of the 3D-C that avoids the strong angular dependence of the detector efficiency. To do this, several numerical simulations as the one of Figure 2-37 were performed. The geometrical parameters used in these simulations were set taking into account that the gap between the lamellas should allow the energy deposition of α an Li, and that the B_4C/empty ratio of the single lamellas should allow a good electrons extraction from the field cage. The result of the simulation with the best configuration found is shown in Figure 2-38. The parameters used in this simulation are:

- Gap between the lamellas=4mm;
- length of the B_4C coating=3mm;
- gap between the strips=1mm;
- total number of strips=24

As one can see, with this configuration the angular dependence of the detector efficiency is weaker, and the efficiency is higher than for the geometrical parameters of the first BAND-GEM prototype.

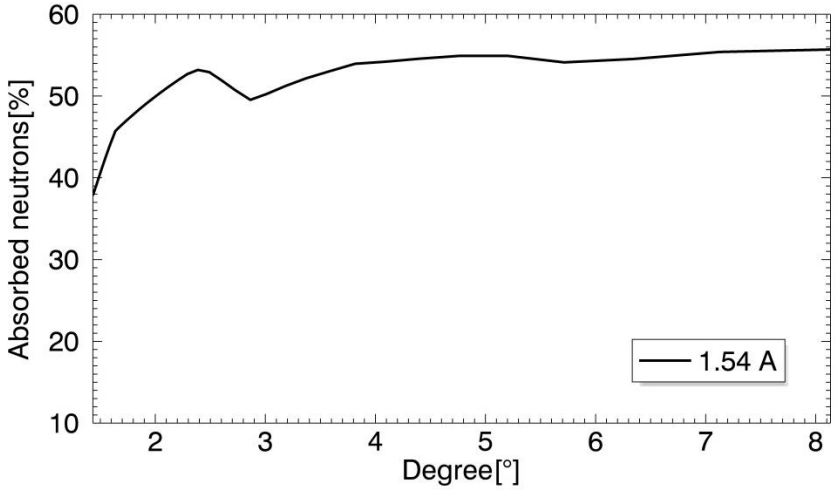

Figure 2-38: Calculated number of absorbed neutron with the best geometrical parameters found for the 3D-C. Parameters are: Gap between the lamellas=4mm; length of the B_4C coating=3mm; gap between the strips=1mm; total number of strips=24

2.3.3.2 Optimization of the electrons extraction efficiency from the field cage

The optimization of the electrons extraction efficiency is performed by a C++ code that coupled SRIM [56], Ansys [39] and Garfield++ [40] simulations. The input of this code is the matrix seen in par 2.3.3.1. The matrix produced by IDL gives as output the positions of the B_4C layer were neutrons interact. Since the layer is very thin (about 1 μm), the neutron probability of interaction inside the layer is considered uniform. The n(^{10}B,^{7}Li)α reaction leaves the Li ion in an excited state. As a consequence the starting energy of α and Li are respectively E_{Li} = 0.84 MeV and E_{α} = 1.47 MeV and they are emitted almost back-to-back: only one of the two particles will move towards the gas. Since the emission of the two charged particles is almost isotropic, there is an equal probability

that this is an α or a Li. The SRIM tables of energy deposition of these two particles inside a B_4C layer with 2.242 g/cm^3 density [29] were calculated.

Following these prescriptions the simulation program:

1) Randomizes the charged particles production point (that is coincident with the neutron capture point) inside the B_4C layer with a precision of 1 nm
2) Decides whether an α or a Li ion was moving towards the gas gap and assigns the correct starting energy. The particle moving towards the strip is discarded.
3) Randomizes the direction of the motion of the charged particle inside the B_4C layer.
4) By knowing the starting point and the inclination inside the B_4C of the particle trajectory, the code calculates the full path inside the layer and, by exploiting the SRIM tables, the energy loss in this layer.
5) If the particle reaches the boundary between the B_4C layer and the gas with energy higher than 10 keV, than the simulation continues; otherwise the particle is stopped in the boron layer. This contribution is kept into account in the determination of the detector efficiency.

The result is the ratio of the particles able to escape the conversion layer and to deposit their energy in the gas between the lamellas. This number resulted to be about 70% for 1 μm thick B_4C, as expected by analytical calculations if a uniform conversion probability is considered.

If the charged particle reaches the gas mixture with energy higher than 10 keV, the code takes into account the generation of primary electrons inside the lamella gaps and moves the primary electrons in the system (using the Garfield++ library and the electric field map obtained using ANSYS). The primary electron generation is performed via the SRIM tables calculated for the Ar/CO_2 70%/30% gas mixture. Charged particles release energy in the gas by creating clusters of primary electrons with a Bragg curve distribution [1].

Figure 2-39 shows a simulated distribution of the primary electrons for the geometrical configuration of the first BAND-GEM prototype (Gap between the

lamellas=2mm;length of the B_4C coating=2mm; gap between the strips=2mm; total number of strips=15). This is converted into keV equivalent by knowing the first ionization energy for the specific gas mixture (27 eV). The conversion from primary electrons to keV equivalent is simply done as:

$$E_{prim}(keV\ equivalent) = N_{prim} \cdot W(Ar/CO_2) \quad \text{Eq. 2-16}$$

where N_{Prim} is the number of primary electrons liberated by gas ionization and $W(Ar/CO_2$ 70/30) is the first ionization energy for the used gas mixture. As it can be seen in Figure 2-39, the released energy distribution has a peak at around 450 keV.

This named distribution is influenced by several aspects:

- The charged particles reach the gas with almost a uniform energy distribution that ranges from 10 to 800 keV for ^{7}Li and from 10 to 1400 keV for alphas.
- The range of the particles in the gas varies as a function of their energy
- The presence of the lamellas generates the so called “wall effect” [1], so a particle movement is limited also by the presence of the lamella walls. This point is particularly important since it severely limits the generation of primary electrons. The distance between the lamellas is thus a very critical point that must be optimized.

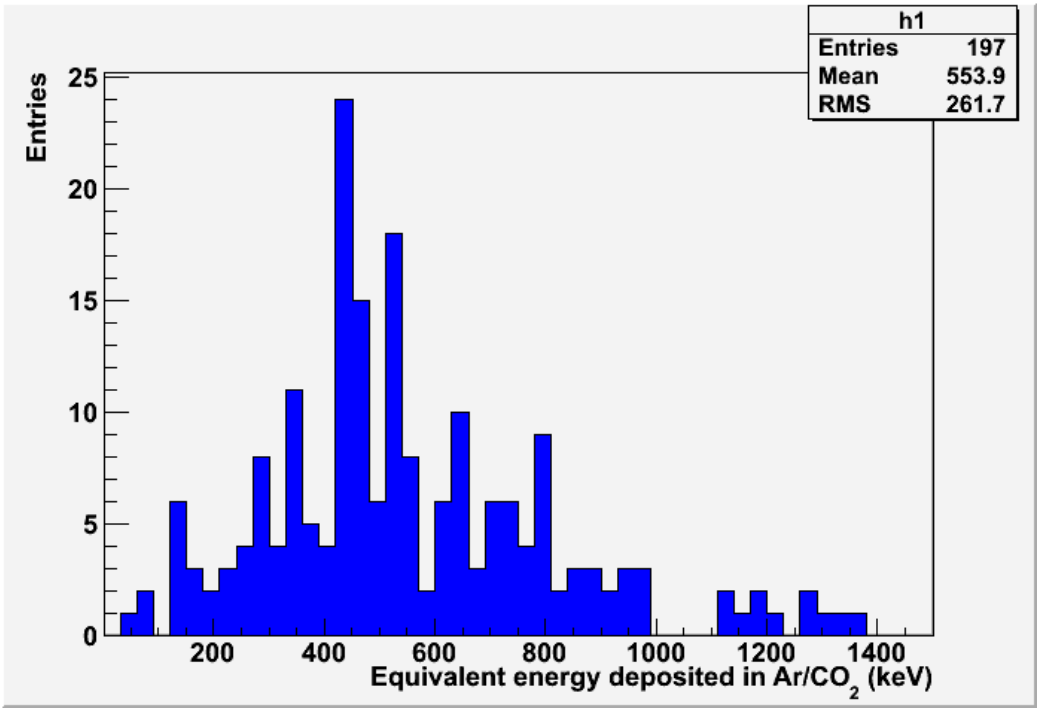

Figure 2-39: Histogram of generated primary electrons per charged product (in terms of keV equivalent) due to the ionization of alpha or lithium ion in gas gaps between lamellas with the following geometrical parameters: Gap between the lamellas=2mm;length of the B4C coating=2mm; gap between the strips=2mm; total number of strips=15

The final part of the simulation concerns the capability of the primary electrons to move inside the lamella system, in order to understand how many of them reach the amplification zone. The electrical configuration of the lamella system was generated using the Ansys finite element method package [39]. A Total of 5 lamellas loaded with the appropriate potentials were included in the simulation; the program solves the electrostatic equation and determines the electric field map present in the gap between the lamellas. The specific potentials were applied to all the lamella strips and to a plane resembling the top electrode of the first GEM foil (GEM1 Top). The electric field map calculated by Ansys is an input for the calculation of primary electron extraction efficiency performed by GARFIELD++. Figure 2-40 shows the calculation of the electron drift lines (without diffusion) and of the equipotential lines performed by GARFIELD++. The primary electrons generated inside each cluster (whose x and y coordinates are known) are left free to move inside the gaps and the number of electrons per cluster that is able to reach the GEM plane is counted.

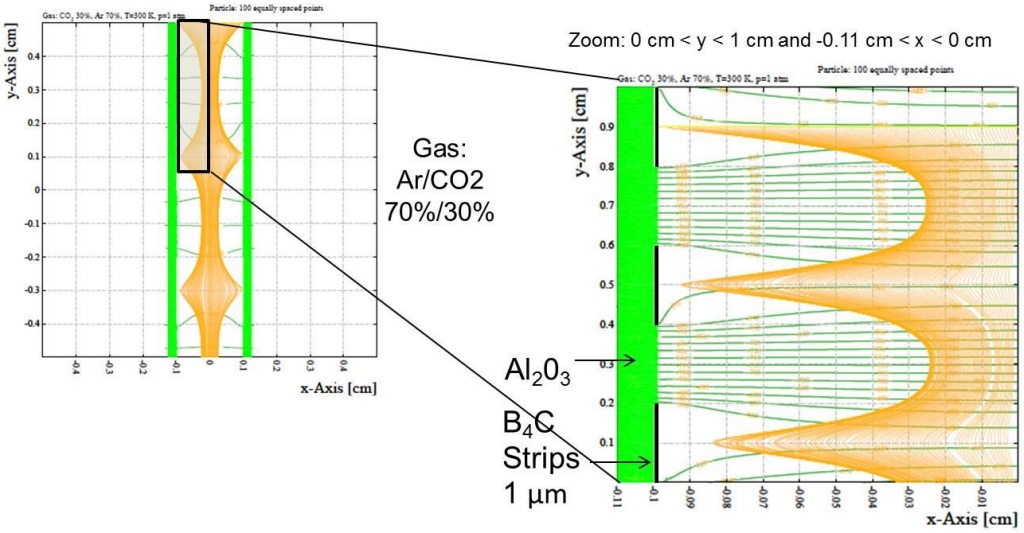

Figure 2-40: Equipotential lines and electron drift lines calculated using Ansys and Garfield with the following geometrical parameters: Gap between the lamellas=2mm;length of the B4C coating=2mm; gap between the strips=2mm; total number of strips=15

This gives the total number and distribution per keV equivalent of primary electrons that will give a signal per charged particle (Figure 2-41). The distribution shrinks towards lower energy since part of the primary electrons are lost inside the lamella system.

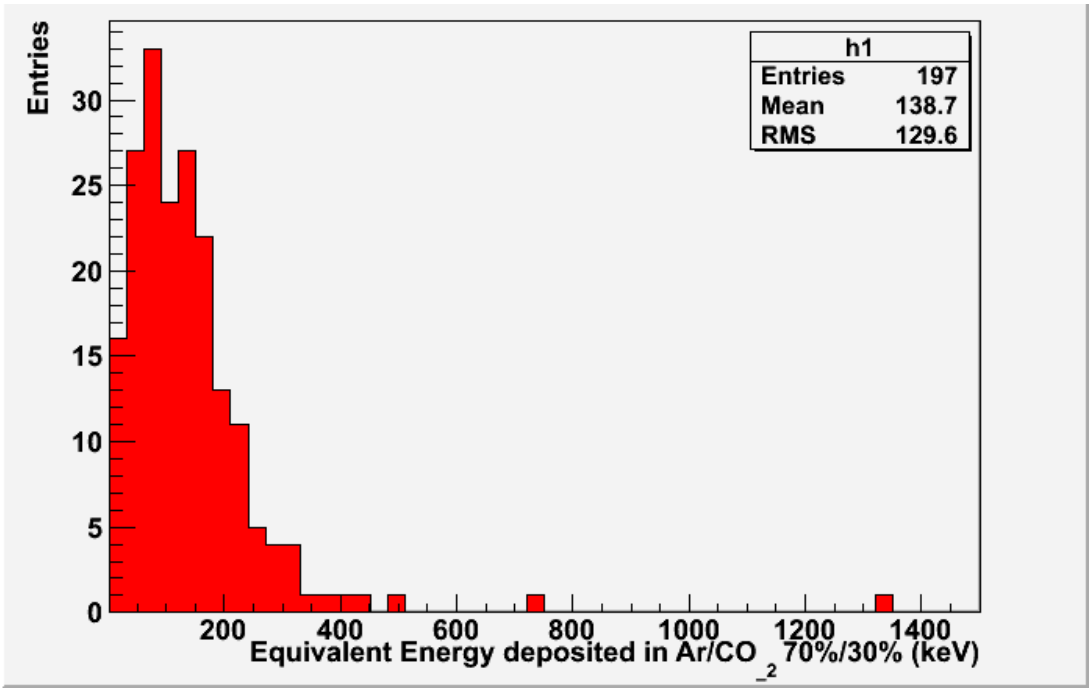

Figure 2-41: Histogram of the number of primary electrons per charged product (in terms of keV equivalent) that are able to exit from the lamella system and reach the GEM amplification region with the following geometrical parameters: Gap between the lamellas=2mm;length of the B4C coating=2mm; gap between the strips=2mm; total number of strips=15.

From these simulations, it is possible to extract some parameters that define an expected detection efficiency using the following equation:

$$\varepsilon(\lambda, thr) = abs(\lambda) \cdot f_{esc} \cdot N(thr) \quad \text{Eq. 2-17}$$

where ε(λ,thr) is the expected efficiency as a function of neutron wavelength and with a certain energy threshold, abs(λ) is the neutron absorption probability in the lamella system, f_{esc} is the fraction of the charged products able to escape from the B_4C layer, and N(thr) is the percentages of events (given to gas ionization by either an alpha or a lithium ion) that, after passing through the lamella system, still own a sufficient number of primary electrons over a certain threshold in terms of equivalent keV energy. By considering a threshold of about 80 equivalent keV the N(thr) is 60%. Since the conversion efficiency is about 40% in the plateau region (Figure 2-37) and f_{esc} is constant around 70%, the expected efficiency for neutrons of wavelength λ = 1.54 Å (E = 34.5 meV) is about ε(1.54 Å, 80 keV)=16.8±2 %, in accordance with the measured efficiency of par 2.3.2.3.

The same approach was used for the best geometrical parameters of the 3D-C found in par 2.3.3.1; the associated neutron absorption curve is shown in Figure 2-38. Figure 2-42 shows the histogram of the primary electrons generated inside the lamella gaps with the following geometrical parameters:

- Gap between the lamellas=4mm;
- length of the B_4C coating=3mm;
- gap between the strips=1mm;
- total number of strips=24

As one can see, the deposited energy peak moves from about 450 keV to about 900 keV. This is due to the fact that α and Li ions can travel for a longer distance and therefore ionize more gas.

The electric field inside the lamellas system with the new geometrical parameters was than calculated using ANSYS, and the resulting field lines are shown in Figure 2-43.

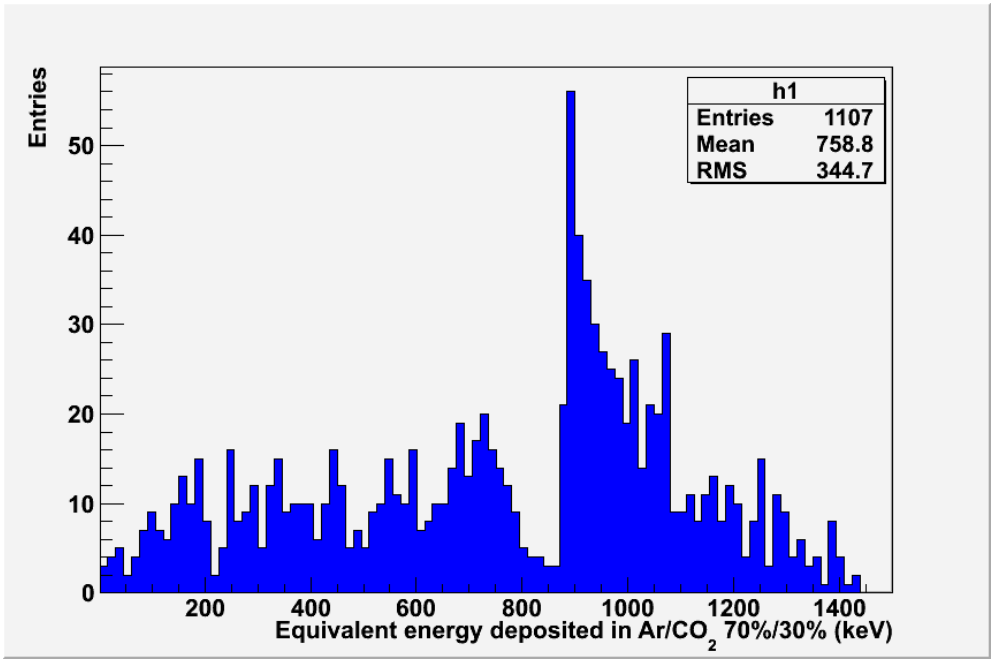

Figure 2-42: Histogram of generated primary electrons per charged product (in terms of keV equivalent) due to the ionization of alpha or lithium ion in gas gaps between lamellas with the following geometrical parameters: Gap between the lamellas=4mm;length of the B4C coating=3mm; gap between the strips=1mm; total number of strips=24.

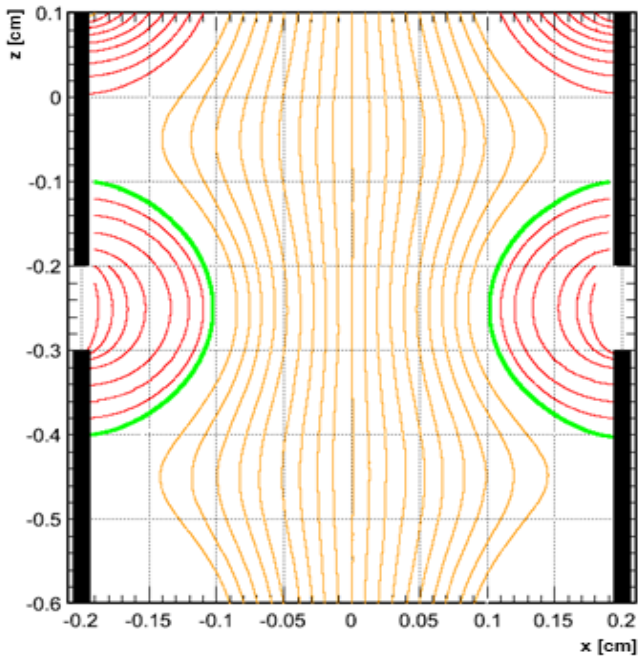

Figure 2-43: Electron drift lines calculated using Ansys and Garfield with the following geometrical parameters: Gap between the lamellas=4mm; length of the B4C coating=3mm; gap between the strips=1mm; total number of strips=24. In the plot, the orange lines represent the drift lines of the electrons able to escape from the grids system; red lines represent the drift lines of the electrons that are not able to escape from the grids system; the green lines represent the border between the area on which the created primary electrons are able to escape from the 3D-C and the area on which the primaries are lost in the 3D-C.

This electric field map was then used to simulate the motion of the electrons in the lamellas system. Figure 2-44 shows the primary electrons (in terms of keV equivalent) that were able to exit from the lamella system. As in the previous case, the distribution shrinks towards lower energy, but the mean energy of the events is now about 3 times higher than in Figure 2-41 and the event over threshold N(thr), considering a threshold of 80 equivalent keV, is now the 75% of the generated primaries instead of the 60% of Figure 2-41.

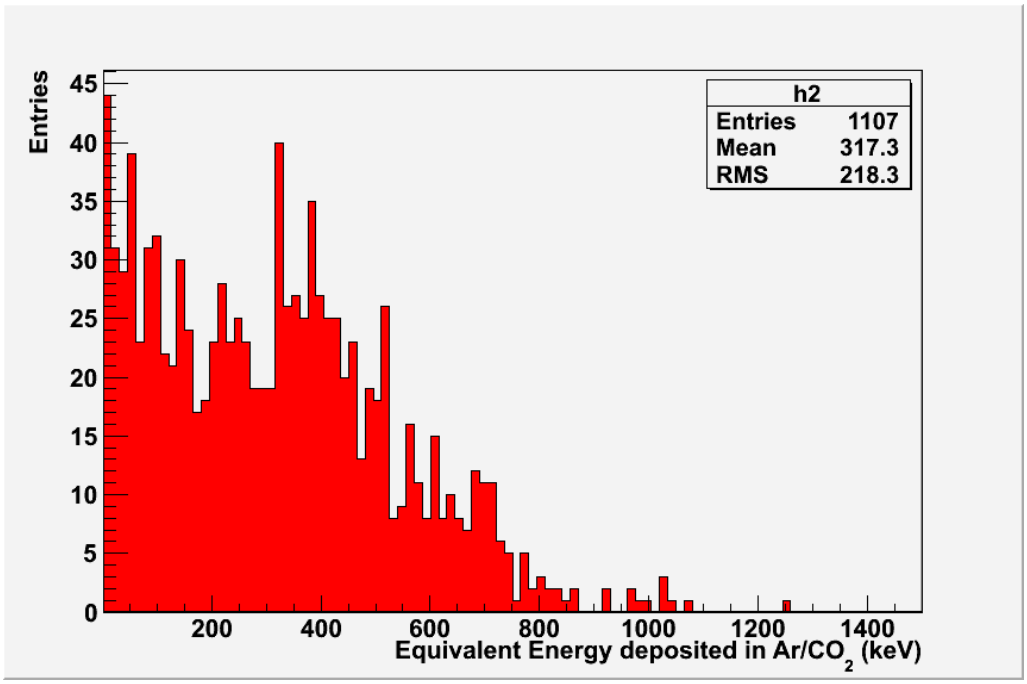

Figure 2-44: Histogram of the number of primary electrons per charged product (in terms of keV equivalent) that are able to exit from the lamella system and reach the GEM amplification region with the following geometrical parameters: Gap between the lamellas=4mm;length of the B4C coating=3mm; gap between the strips=1mm; total number of strips=24.

Taking into account that the conversion efficiency is about 50% in the plateau region (Figure 2-38) and f_{esc} is constant around 70%, the expected efficiency for neutrons of wavelength λ = 1.54 Å (E = 34.5 meV) is about ε(1.54 Å, 80 keV)=26.3%.

These simulations allowed the optimization of the lamellas system geometrical parameters, optimizing the fraction of absorbed neutrons (abs(λ)) and the electrons extraction efficiency from the field cage (N(thr)). It remains now to optimize the escape fraction of the charged products from the B_4C layer f_{esc} by studying the effect of the B_4C layer thickness.

2.3.3.3 Optimization of the charged products extraction from the B_4C layer

The optimization of the charged products extraction from the B_4C layer was done by using a slightly modified version of the IDL code described in 2.3.3.1. The neutron incidence angle was fixed to 5° (in the plateau region of Figure 2-38) and the fraction of absorbed neutrons (abs(λ)) was calculated for different B_4C layer thickness (ranging from 0.05 µm up to 1.5 µm) and for different neutron wavelengths (from 1Å up to 12 Å).

Another code that implements the SRIM tables was used for the calculation of the charged particles fraction that can leave the B_4C layer for different layer thicknesses. A set of f_{esc} (one for each layer thickness) was than obtained after this simulation.

The set of the abs(λ) and f_{esc} values were than used to calculate the expected neutron efficiency, using N(thr)=75% (par 2.3.3.2). The results of this calculation is shown in Figure 2-45, where the fraction of detected neutrons with and without taking into account the f_{esc} values are represented by dashed and full lines respectively.

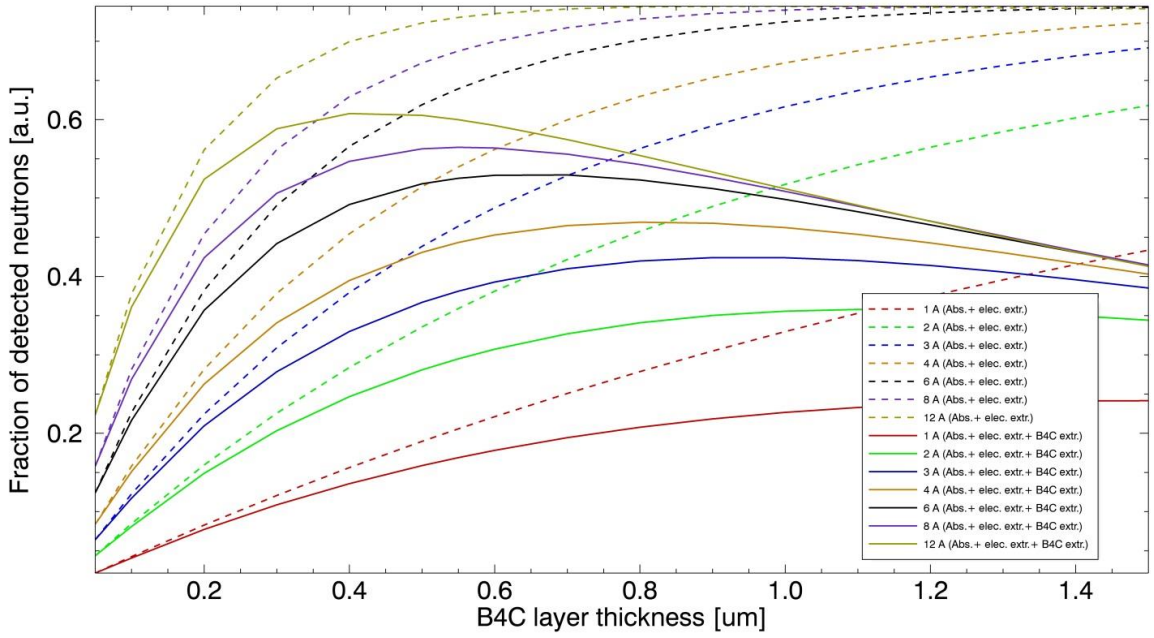

Figure 2-45: Calculated neutron detection efficiency for different B_4C layer thickness and for different neutron wavelength. Dashed line represents the calculation without f_{esc}; continuous lines represent the calculation with f_{esc}

As one can see, each neutron wavelength has an optimal B_4C layer thickness that ranges from 0.4 μm (for 12 Å neutrons), up to 1.5 μm (for 1 Å neutrons). The choice of the B_4C layer thickness depends on the application of the BAND-GEM detector. For the LoKI case (neutron wavelength ranging from 2 to 12 Å) it was decided to coat the lamellas with 0.75 μm of B_4C: with this value of thickness the expected neutron detection efficiency is higher than 30% for all the neutron wavelengths under consideration.

2.3.4 Second BAND-GEM detector prototype

The numerical simulations described in par 2.3.3 have suggested a geometrical configuration of the 3D-C that can increase considerably the performances of the BAND-GEM with respect to the first BAND-GEM prototype. The optimization of par 2.3.3 has then lead to the development of a second BAND-GEM prototype with an optimized 3D-C.

2.3.4.1 Design and construction of the second BAND-GEM prototype

In addition to the limited efficiency, the first BAND-GEM prototype of par 2.3.2 has shown a series of limits in the technology used for its construction. In fact, the alumina lamellas are very fragile and the technique used for the realization of the electrical contacts on each strip takes a long time. This approach can be useful for the production of a single prototype, but cannot be used for the production of the big amount of modules requires by the LoKI instrument (about 130). For this reason the second BAND-GEM prototype was built using an industrialized process that is easily replicable.

The 3D-C of the second BAND-GEM prototype is composed by a planar aluminium cathode and 24 aluminium grids coated with 0.75 μm of ^{10}B4C. Each grid is 3 mm high, has an overall area of 12 x 7 cm^2 (active area of 5x10 cm^2) and is composed by eleven strips 10 cm long, 3 mm high and 200 μm thick. The pitch between the strips is 4 mm. Figure 2-46 shows one of the grids used for the production of the 3D-C.

Figure 2-46: One of the 3 mm thick grids used for the production of the 3D-C after $^{10}B_4C$ coating. The thin walls are 200 µm thick

During the boron deposition process, high temperature is required (about 400°C) and this causes the deformation of the aluminium grids and a tensioning is required to bring the strips straight again. The tensioning is made through screws hosted in the side holes of the grids frame. Further details of the grids production is reported in par 2.3.6.

The 3D-C is built by sandwiching the 24 coated grids separated by 24 fiberglass frames with 1 mm thickness. In this way each grid is insulated from the others and is kept a different potential, allowing the generation of the electric field and the extraction of the electrons. In this way the geometrical parameters of the 3D-C are the one found during the optimization process of par 2.3.3.

The potential to each grid is given through an external voltage divider that has the two ends connected between the planar cathode and the grid closest to the Triple GEM. The grid system is powered with a CAEN A1540N module that is able to deliver up to 15 kV. The 3D-C structure is followed by a standard tripleGEM equipped with a padded anode with pads of different dimensions (shown in Figure 2-47). The high voltage is given to the three GEM foils by means of the HVGEM module [34].

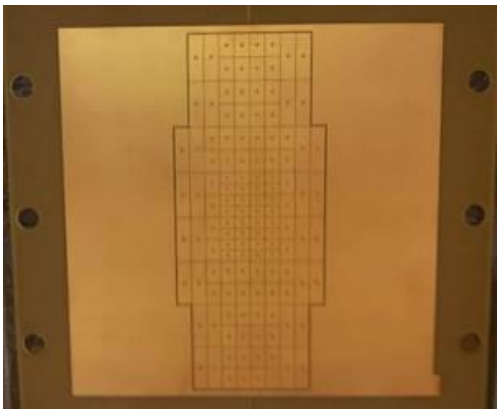

Figure 2-47: The padded anode used in the second BAND-GEM prototype. The pad have three different dimensions: 4x3 mm^2 the smallest, 4x6 mm^2 the intermediate and 4x12 mm^2 the bigger.

A schematic of the detector can be found in Figure 2-48.

The gas mixture used in the detector is again Ar/CO_2 70%/30%.

After its realization, the 3D-C was inserted in a gas tight box made of fiberglass, and finally the box was closed with its lid, on which it is installed the tripleGEM with its padded anode. Figure 2-49 shows some pictures of the assembly procedure together with the CAD model used for the realization of each part of the detector.

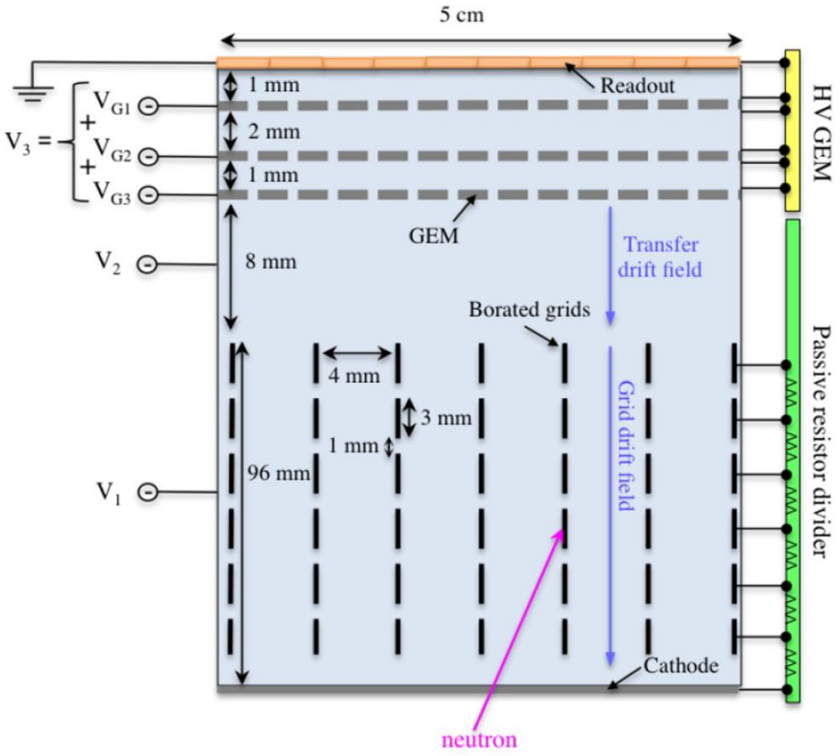

Figure 2-48: Schematic of the second BAND-GEM prototype. V_1 is the voltage difference applied to the 3D-C; V_2 is the voltage difference applied between the last grid and the first GEM foil; V_3 is the total voltage difference applied to the tripleGEM;

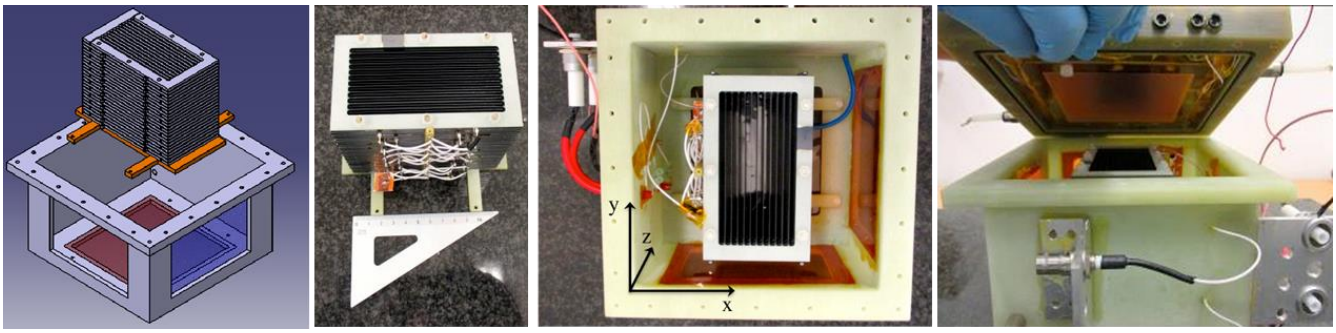

Figure 2-49:CAD model (on the left) and assembly procedure of the second BAND-GEM prototype

2.3.4.2 Test of the second BAND-GEM prototype with X-Rays

The first test carried out with the second BAND-GEM prototype was with the detector under X-Rays irradiation. This test was carried out to study the electrons extraction from the 3D-C with the new geometrical parameters.

Experimental Setup

The X-Rays used during this test were generated by an Amptek mini X-Rays tube [41] set with an acceleration voltage equal to 10 kV, a beam current equal to 100 µA and a

copper filter (thickness 1 mm) installed at the exit of the X-Rays tube. With this setup, the expected X-Rays spectrum is a continuous decreasing exponential function from low energy photons up to the maximum expected energy (10 KeV, corresponding to the maximum acceleration voltage) with a characteristic peak centred at 8.04 keV corresponding to the copper K-α emission line. The X-Rays beam was irradiating the detector from a diagnostic window on the side of the box, as shown in Figure 2-50. The X-Rays beam has a diameter of about 2.5 mm, so with this setup is possible to study the charge extraction from each grid by moving the x-ray tube. Only one of the 128 pads of the detector was read-out by using a standard setup composed by a preamplifier (Ortec 142 IH [42]), an amplifier (Ortec 579[43]) and an ADC-MCA analyzer (Maestro MCA [44]) so to obtain a pulse height spectrum (PHS). The sum of the voltages applied to the tripleGEM (V_3 in Figure 2-48) was set to 1050 V, corresponding to a gain of about 10^4. This was set taking into account that the number of primary electrons created by a 10 keV X-Ray is about 270. The primary electrons created by a 900 keV α are about 25000. Given that with a good electrons extraction we expect to use a gain of about 100 for neutron detection (the same gain used in the bGEM), the gain that should be used to detect X-Rays is about 100 times higher.

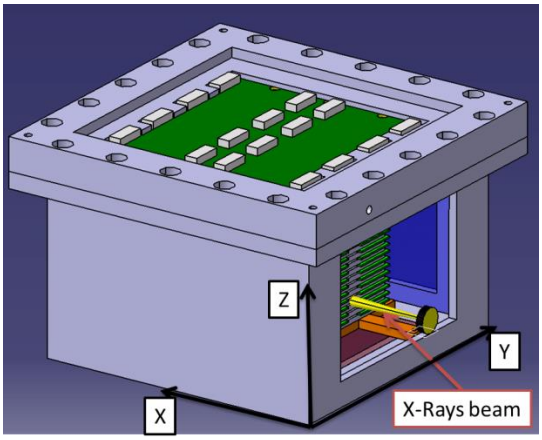

Figure 2-50: CAD model describing the experimental setup during the X-Rays test. X-Rays beam enter from the side window.

During the test, several PHS were obtained by irradiating the detector in different positions for a fixed time (120 seconds for each position): using the coordinate system in Figure 2-50, the x and the y position of the x-ray tube were fixed, while the z position was varied between z=0 mm (irradiating the grid farthest from the tripleGEM) and z=68 mm (irradiating the 18th grid of the stack) with a step of 4mm, corresponding to the distance between the centres of the grids. The irradiation of the grids closer to the

tripleGEM (from the 19th grid to the 24th), was not possible because of the detector box (Figure 2-51) was shadowing them.

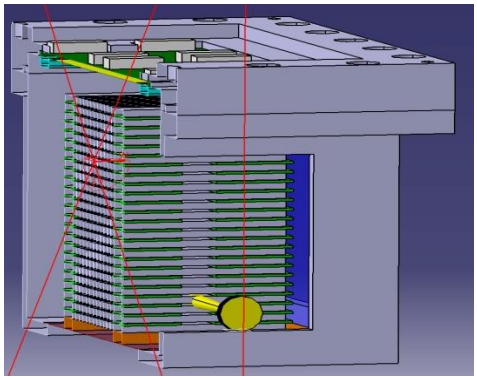

Figure 2-51: Section view of the CAD model of the experimental setup. The grids closer to the tripleGEM are shadowed by the detector box

Moreover, the ΔV applied to the 3D-C (V_1 in Figure 2-48) was varied during the test in order to study its effect on the charge extraction. V_1 was varied between 4700 V and 10700V in step of 1000V. Therefore, a total of 126 PHS were recorded and compared during this test (18 x-ray position x 7 different applied voltages on the 3D-C).

Test results

Figure 2-52 shows the recorded PHS for 3 different positions with V_1=10700 V. The threshold was set just above the electronic noise (ADC channel n° 100) and the energy spectrum was not calibrated. As one can see the effect of the electrons extraction from the 3D-C is clearly visible. When the detector is irradiated near the tripleGEM (black curve in Figure 2-52), the ADC records events up to the channel n° 2500 and the k-α peak of the copper, together with the Ar escape peak [45], are clearly visible around channel n°1500 and channel n°600, respectively. On the other hand, when the detector is irradiated far away from the tripleGEM (red curve in Figure 2-52) the ADC records events up to the channel n° 1000 only, the characteristic peaks are not visible and the low-energy component (< channel n°500) of the PHS is about twice the low energy component of the black curve. By integrating the recorded spectra in all the irradiated positions, the graph shown in Figure 2-53 is obtained. By increasing the x-ray tube z coordinate, the total number of over threshold counts increases. This means that part of the electrons is lost during their motion from the bottom to the top of the 3D-C. This is confirmed by the difference in the low-energy component of the recorded PHS.

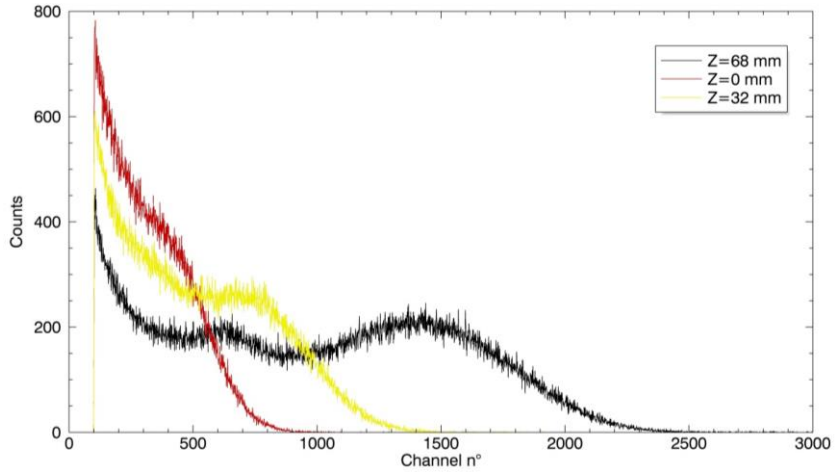

Figure 2-52: Recorded PHSs in three different position with V_1=10700V.Red curve: z=0 mm (farthest from the GEM);Yellow curve: z=32 mm (intermediate position); Black curve z=68 mm (near the GEM).

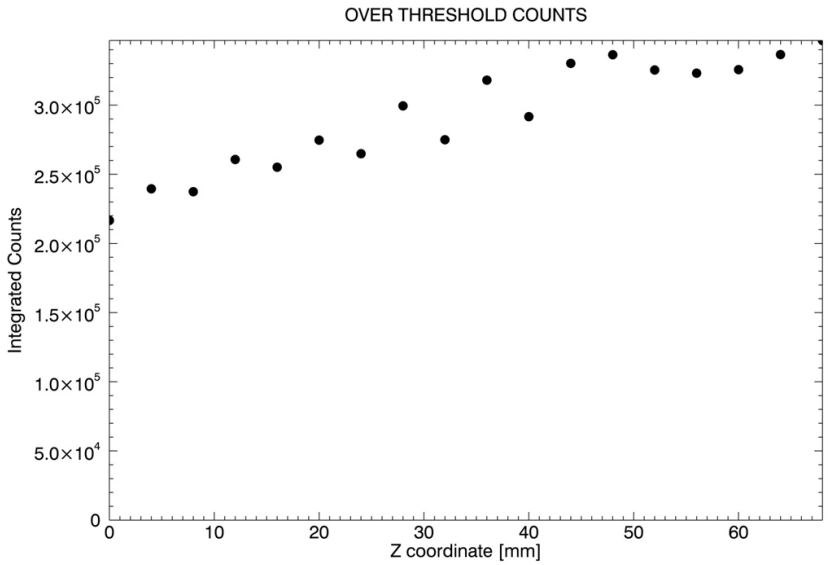

Figure 2-53: Over threshold counts obtained by irradiating the detector in different position with V_1=10700V

The same test was repeated for different V_1 values, as shown in Figure 2-54.

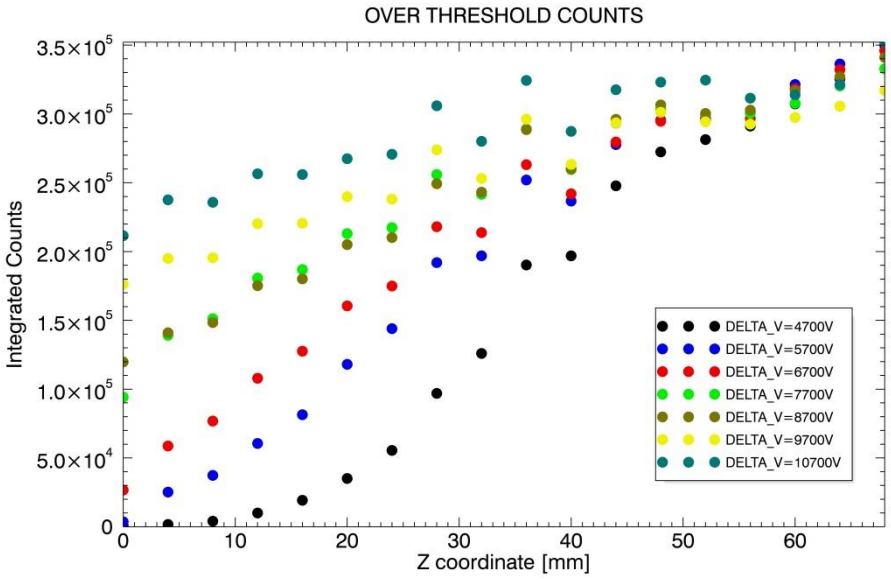

Figure 2-54: Over threshold counts obtained by irradiating the detector in different position with different applied voltage to the 3D-C. Black dots V_1=4700 V; blue dots V_1=5700 V; red dots V_1=6700 V; green dots V_1=7700 V; brown dots V_1=8700 V; yellow dots V_1=9700 V; navy dots V_1=10700 V

For low z coordinate the effect of V_1 on the electrons extraction is dramatic: after 120 seconds of x-rays irradiation, the over threshold counts recorded at z=0 mm with V_1=4700V are about 100, while they are $2.1 \cdot 10^5$ with V_1=10700V. On the other hand, the recorded over threshold counts are the same for all the applied potentials when the detector is irradiated near the triple GEM. This can be explained taking into account the electrons transverse diffusion coefficient for the used gas mixture, shown in Figure 2-55 [46].

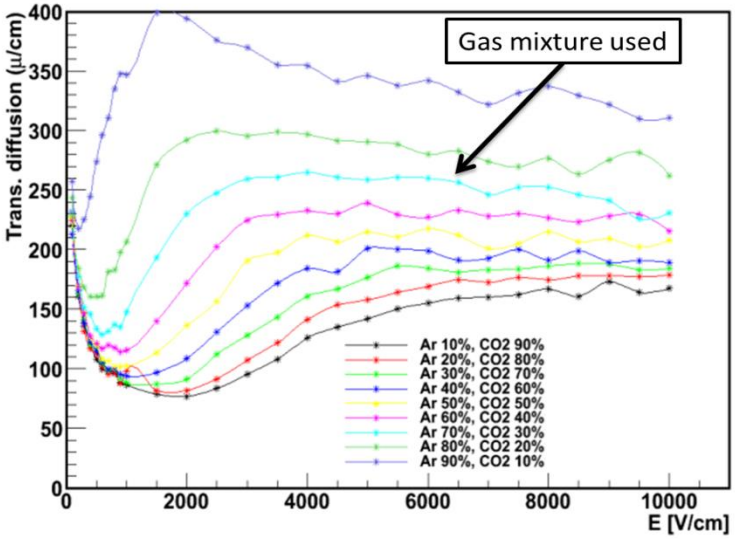

Figure 2-55: Transverse diffusion for different Ar mixture. The mixture used during the test is Ar/CO_2 70/30 %.

The transverse diffusion coefficient is high for very low applied electric field, it drops down rapidly showing a minimum around E=1000 V/cm, and finally it increases again for E>1500 V/cm. We can now use the ANSYS script described in 2.3.3.2 to obtain the map of the electric field module inside the 3D-C for the two extreme cases of applied voltage, V_1=10700V (Figure 2-56) and V_1=4700V (Figure 2-57).

With V_1=10700V in more than the 70% of the total area, the module of E ranges between 40 and 120 V/mm, that is the range of E in which the transversal diffusion coefficient of the used gas mixture is minimum (Figure 2-55). With V_1=4700V (Figure 2-57) the E module is lower than 40 V/mm in 50% of the total area. When the X-rays interact in the area corresponding to the first grid (z=0 mm), the liberated primary electrons should travel along the entire grid stack (i.e about 100 mm for the shortest path) before reaching the triple-GEM. If the diffusion coefficient is high (σ>200 μm/cm as in the case of V_1=4700V) , the electrons lateral displacements will also be high, leading to an higher probability for the electrons to be lost in collisions with the strips of the 3D-C. On the other hand, with low transverse diffusion coefficient, the electrons lateral displacements will be small, leading to a limited probability of electrons collision with the 3D-C strips. This means that part of the electrons are lost along the path, but the total charge reaching the triple-GEM is still enough to give an over threshold signal. When the detector is irradiated near the tripleGEM the electrons path will be shorter and this makes the effect of the transversal diffusion negligible, leading to the saturation value shown in Figure 2-54 for high z.

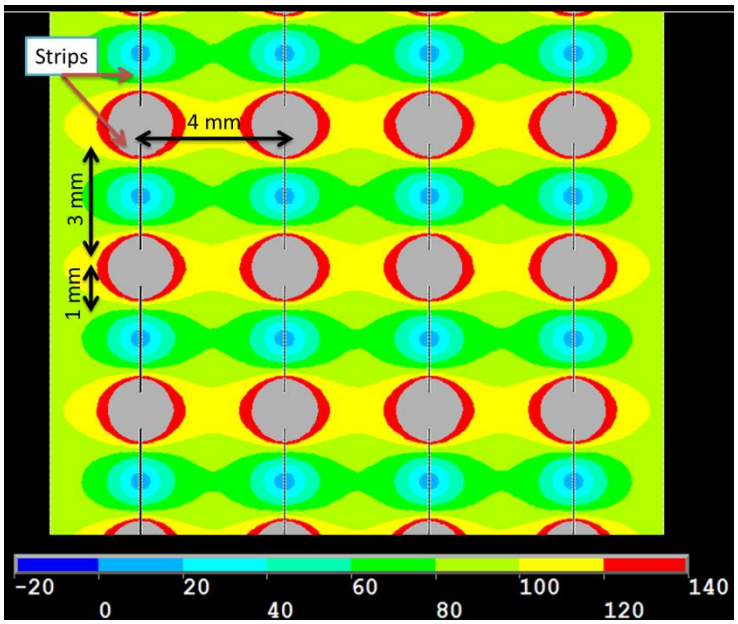

Figure 2-56: Contour plot of the calculated electric field module inside the 3D-C with V_1=10700V. Legend is in V/mm. In gray areas the electric field is greater than 140 V/mm

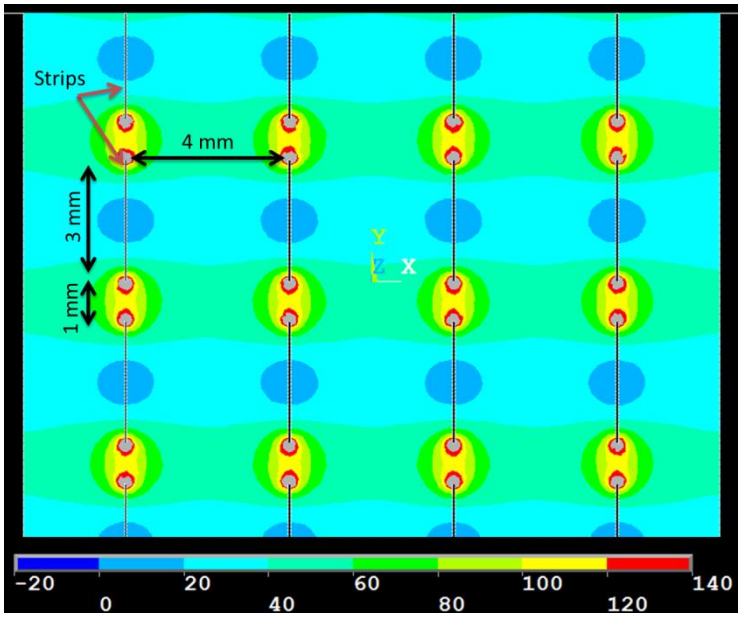

Figure 2-57: Contour plot of the calculated electric field module inside the 3D-C with V_1=4700V. Legend is in V/mm. In gray areas the electric field is greater than 140 V/mm

2.3.4.3 Test of the second BAND-GEM prototype with neutrons

After the characterization performed with the X-Rays, the second BAND-GEM prototype was tested under neutron irradiation at the EMMA beamline at ISIS [36].

Experimental Setup

The aim of the experiment was to conduct a characterization of the detector and measure the efficiency of the detector with respect to the tilt angle and the neutron wavelength. EMMA is a new instrument at ISIS and it is located in the same place of the previous HET instrument [48]. The EMMA beam has maximum dimensions of 45 x 45 mm^2 but motorized jaws can define smaller beam sizes. The sample position is 16 m away from the moderator and it is provided with a rotating and movable support. The range of available neutron wavelengths is about $\lambda = 1 - 4$ Å corresponding to the energy range $E_n = 5 - 81$ meV. The EMMA beam monitor, positioned immediately after the jaws, is a commercial GS-20 Lithium Glass Scintillator (glass thickness equal to 1mm) with an efficiency $\varepsilon_{BeamMonitor}$ ($\lambda = 1$ Å) = 0.60% ± 0.06%. The beam monitor efficiency scales linearly with λ in the range of interest of the instrument. A scheme of the EMMA instrument is shown in Figure 2-58. The Θ angle is defined as the BAND-GEM tilting angle with respect to the incoming neutron beam. Θ is set using a turn-table with a precision better than 0.1°.

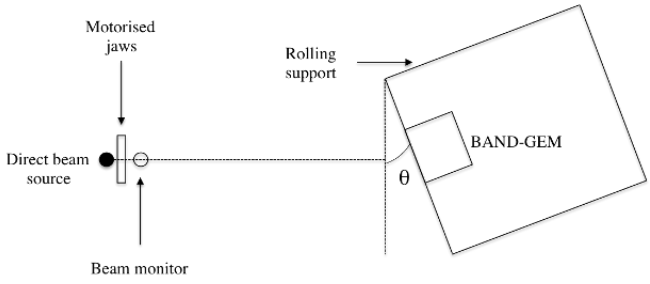

Figure 2-58: Scheme of the experimental setup on EMMA

Different setups were used for the various measurements performed, as summarized in Table 2-1.

Experimental Setup Used	Performed measurement
Θ=0°	V_1, V_2, V_3 scans
Θ=90°	Z scan (extraction efficiency η_C)
0°< Θ < 6°	Efficiency ε
0°< Θ < 5°	Position Resolution (FWHM – mm)
Θ=5°, 1 Å < λ < 4 Å	Efficiency ε

Table 2-1: List of the performed measurements at the EMMA beamline. The definition of the x, y and z axis is shown in Figure 2-59 (rightmost panel) Θ is the tilt angle of the movable support. The potential difference V_1, V_2 and V_3 are defined in Figure 2-48

The BAND-GEM detector was positioned in the beam immediately after the beam monitor and it was mounted on the x/y/z/Θ positioner. In Figure 2-59 the setups for Θ=0°, with the cathode facing the beam source and Θ=90°where the beam hits the side of the 3D converter passing through a diagnostic window are shown.

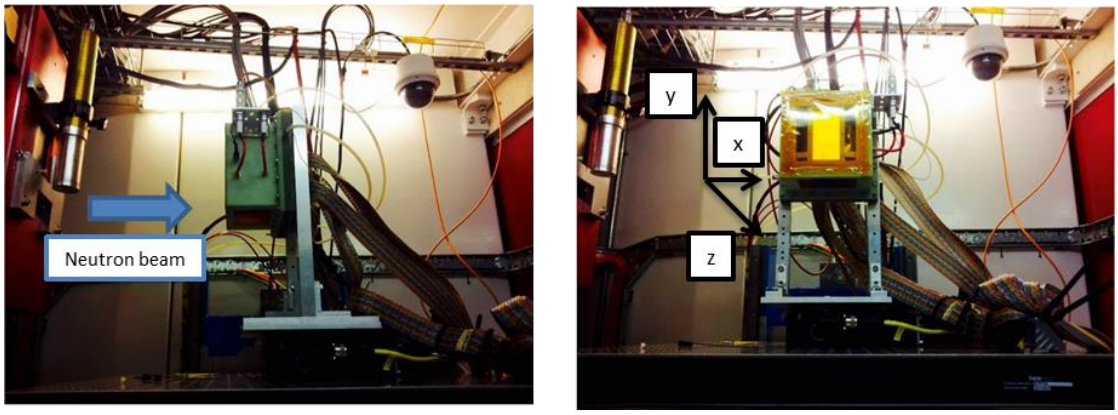

Figure 2-59: BAND-GEM setup on EMMA for Θ=0° (left) and Θ=90° (right) with the coordinate system used.

The high voltage system used in EMMA is the same used for the measurements with the X-Rays: the grid system resistor chain was biased using two channels of the CAEN A1540N 15 kV high voltage module, while the triple-GEM was biased using the custom made HVGEM module. The gas flow used during all the measurement is Ar/CO_2 70%/30% with a flow of about 15 l/h. This gas flow assures a gain stability better than 10%.

Due to the pulsed structure of the ISIS spallation source, energy-resolved measurements can be performed using the Time of Fight technique (ToF). This feature represents a crucial point in order to characterize the response of the BAND-GEM at different neutron wavelength λ. The LVDS signals generated by the CARIOCAs were routed to a user-designed FPGA board that formed the interface between the front-end electronics and the standard ISIS Data Acquisition Electronics (DAE), known as DAE2. Data from the CARIOCAs were first buffered inside the FPGA, using an individual buffer per GEM pad, so that the interface electronics didn't introduce any additional dead time. When the FPGA found data in one of the buffers, the position of the corresponding GEM pad that generated the signal was sent to the DAE for histogramming. The DAE performed the time stamping of these events and incremented the corresponding bin in the ToF histogram associated with this GEM pad, thereby creating a ToF spectrum Si(t) for each BAND-GEM pad. The signal from the

reference EMMA beam monitor was also routed to the DAE2 and a time of flight spectrum M(t) was created also for this detector. The results are shown in Figure 2-60.

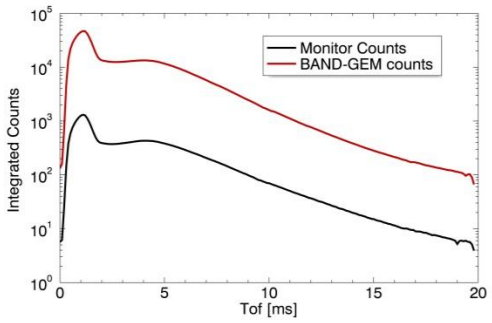

Figure 2-60: ToF Spectra recorded for the BAND-GEM (red line) and for the EMMA GS20 beam monitor (black line).

The analysis for different neutron wavelength is performed by slicing the ToF spectrum. The relation between ToF and neutron wavelength for EMMA are shown in Table 2-2.

λ(Å)	TOF (μs)
1	4000
2	8060
3	12560
4	17060

Table 2-2: ToF and λ relationship on EMMA

The counting rate for a certain λ interval is thus calculated for the i-th pad of the BAND-GEM and for the beam monitor respectively as:

$$C_i(t=\lambda) = \int_{t1}^{t2} S_i(t)dt \quad C_M(t=\lambda) = \int_{t1}^{t1} M(t)dt \qquad \text{Eq. 2-18}$$

Where t_1 and t_2 represents the ToF interval used for the calculation and $S_i(t)$ & $M(t)$ are the ToF spectra. If more than one BAND-GEM pad is hit by the beam, the quantity I_{GEM}

$$I_{GEM} = \sum_{i=1}^{n} C_i \qquad \text{Eq. 2-19}$$

represents the integrated counting rate for that specific λ interval over all the *n* active pads.

The DAE2 system, can separates events on which a single pad is highlighted by the detected neutron (single hit count), from the events on which multiple pads are highlighted by a single neutron (double hit, triple hit, …). This means that, we can re-write Eq. 2-19 as follows:

$$I_{GEM} = \sum_{i=1}^{n} Csh_i + \frac{\sum_{i=1}^{n} Cdh_i}{2} + \frac{\sum_{i=1}^{n} Cth_i}{3} + \cdots + \frac{\sum_{i=1}^{n} Cxh_i}{x} \qquad \text{Eq. 2-20}$$

Where Csh_i is the number of single hits; Cdh_i is the number of double hits; Cth_i is the number of triple hits and so on.

Working point determination

In order to establish the working points, three different potential difference scans have been performed for the three main voltage values (V_1, V_2 and V_3) reported in Figure 2-48.

All the measurement done for the working point determination have been performed at Θ=5° and using a neutron beam with dimensions of 4 mm x 4 mm. The beam-footprint reconstructed using this setting is shown in Figure 2-61.

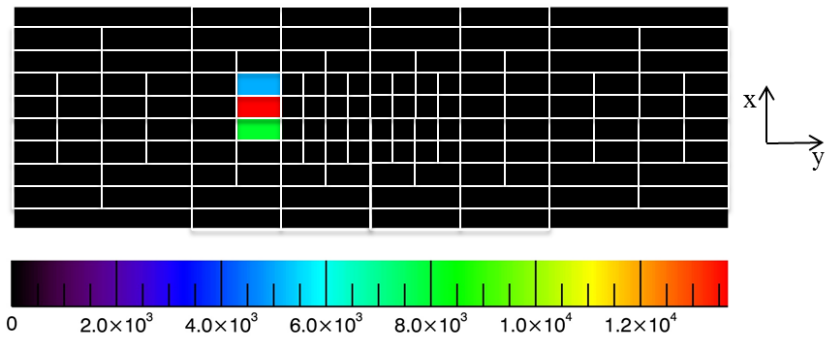

Figure 2-61: Beam footprint reconstructed using a beam dimension of 4 mm x 4 mm and a tilting angle Θ=5°. The colour scale represents $C_{BAND\text{-}GEM,PAD\ i}$ normalized to the pad area calculated for 1 Å < λ < 4 Å.

V_1 Scan

The first scan carried out was the V_1 scan with V_2=1.5 kV and V_3=0.9 kV. During the test V_1 was varied between 0 and 11.1 kV, keeping constant values of V_2 and V_3. The results of the scan are shown in Figure 2-62. The integrated counting rate I_{GEM} is an increasing function of V_1 that reaches a plateau for values higher than V_1= 8 kV. As shown in Figure

2-54, V_1 has a strong effect on the charge extraction efficiency from the 3D-C. The occurrence of a plateau indicates that the charge extraction is practically saturated. However, as shown in Figure 2-54, with V_1 higher than 8 kV, the charge extraction from the first grids of the stack is further improved (see par 2.3.4.2), so the highest available value of V_1 (V_1 = 11.1 kV) was chosen as working point.

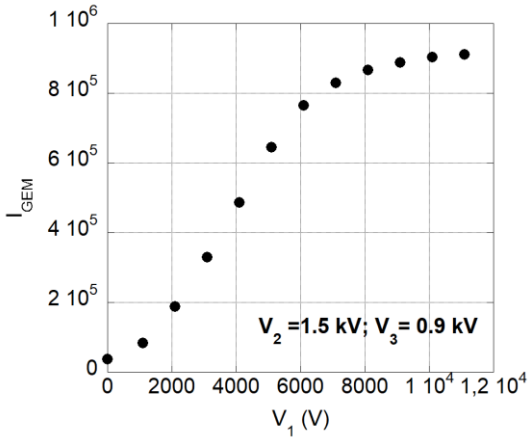

Figure 2-62: V_1 scan. I_{GEM} is calculated for 1 Å < λ < 4 Å.

V_2 Scan

The second scan carried out was the V_2 scan with V_1=11.1 kV and V_3=0.9 kV. During the test V_2 was varied between 600 and 1500 V, keeping constant values of V_2 and V_3. The results of the scan are shown in Figure 2-63. As you can see, V_2 has a threshold value of 600 V (for lower values the electrons may recombine), reaching a plateau for V_2 > 1.2 kV. A value of V_2 = 1.5 kV was chosen as working point.

V_3 Scan

The last performed scan was the V_3 scan with V_1=11.1 kV and V_2=1500 V. During the test V_3 was varied between 800 and 1020 V, keeping constant values of V_1 and V_2. The results of the scan are shown in Figure 2-64. The two curves shown in Figure 2-64 represent an open/free beam measurement (black dots) and a measurement with a sheet of 1 mm of Cd interposed between the EMMA jaws and the BAND-GEM (blue square). The second setup has been used to measure the gamma sensitivity of the detector, since the Cd foil stops all the thermal neutrons with energies lower than 0.5 eV (i.e λ > 0.4 Å) and through neutron capture generates gamma rays with energy ranging between 0.6 and 4 MeV. The counting rate is a slightly increasing function of

V_{GEM} and, as expected, the detector starts to detect thermal neutrons at a voltage V_{GEM} = 810 V (i. e. gain of about 50). In order to increase the counting rate, the voltage was pushed up to 1020 V and a slight variation of the curve slope is observed at V_{GEM} = 920 V. The gain corresponding to this voltage (i.e. 300) was interpreted as the gain where the detector starts to be sensitive to gamma rays. This statement is confirmed by the Cd measurement where I_{GEM} changes slope for V_{GEM} > 900 V, (effective gain > 200). A value of V_3 = 900V was chosen as working point.

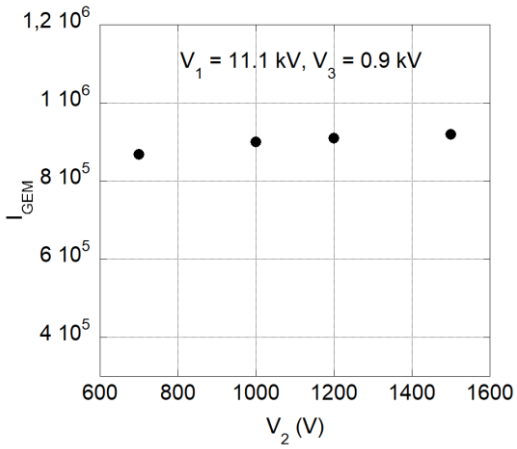

Figure 2-63: V_2 scan. I_{GEM} is calculated for 1 Å < λ < 4 Å.

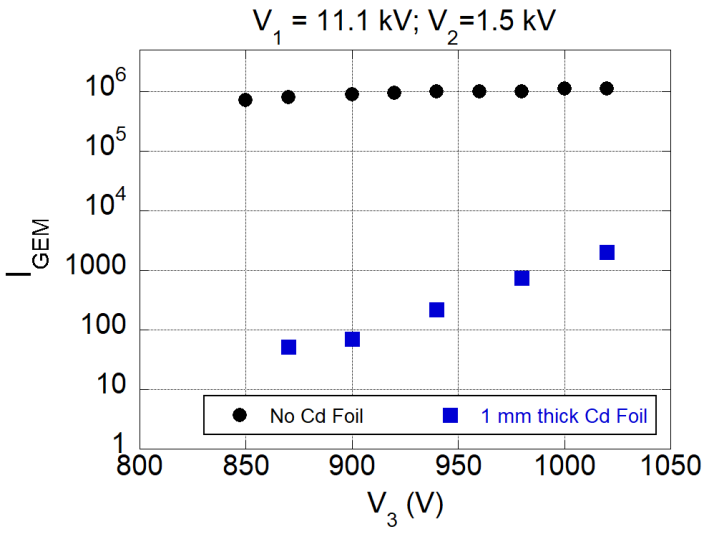

Figure 2-64: V_3 scan. I_{GEM} is calculated for 1 Å < λ < 4 Å.

Measurement of the electrons extraction efficiency with neutrons

The characterization made in par 2.3.4.2 with x-rays, was repeated during this measurements campaign using neutrons. In order to perform these measurements the neutron beam area was set to 4 mm x 4 mm and Θ was set to 90° so that the beam enters the grid system from the side through the diagnostic window that has a dimension of 75 mm (z) * 100 (x) mm (see Figure 2-58 and Figure 2-59). The beam position was moved along the z axis (starting from the farthest grid from the GEM (z=0mm) up to the last grid (z=96mm)) and the measurement was repeated for different values of V_1 ranging from 3.3 kV to 11.1 kV. The beam footprint for one of the measurement is shown in Figure 2-65.

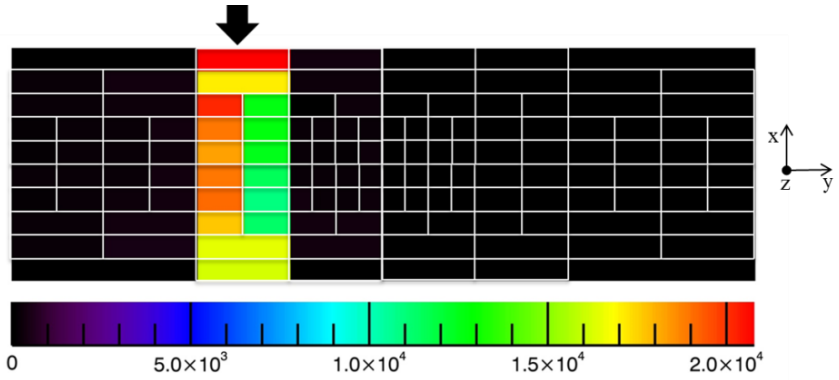

Figure 2-65: Beam footprint reconstructed using a beam dimension of 4 mm x 4 mm and a tilting angle Θ=90°. The color scale represents $C_{BAND\text{-}GEM,PAD\ i}$ normalized to the pad area calculated for 1 Å < λ < 4 Å. The arrow indicates the neutron direction

In Figure 2-66 the plots of the z scan for six different values of V_1 are shown. Since the width of the lateral diagnostic window is about 75 mm, the neutrons that hit the detector at lowest and highest z are blocked by the frame. However the values of I_{GEM} for such extremes z can be extrapolated from the measured ones (see Figure 2-66 where the extrapolation is shown in blue). The relative charge extraction efficiency η_C could be defined as:

$$\eta_C(V_1) = \frac{I_{GEM}\ (Z = 0)}{I_{GEM}(Z = 96)} \qquad \text{Eq. 2-21}$$

and the values for different applied V1 are shown in the different panels of Figure 2-66 (z=0 mm is the cathode position and z = 96 mm is the final position of the grid system).

Ideally one would like that η_C would be as close as possible to unity, that means that the charge extraction efficiency is uniform along the whole 3D converter. With V_1=11.1 kV, the maximum η_C=67% is found. This justify the choice of V_1=11.1 kV as working point.

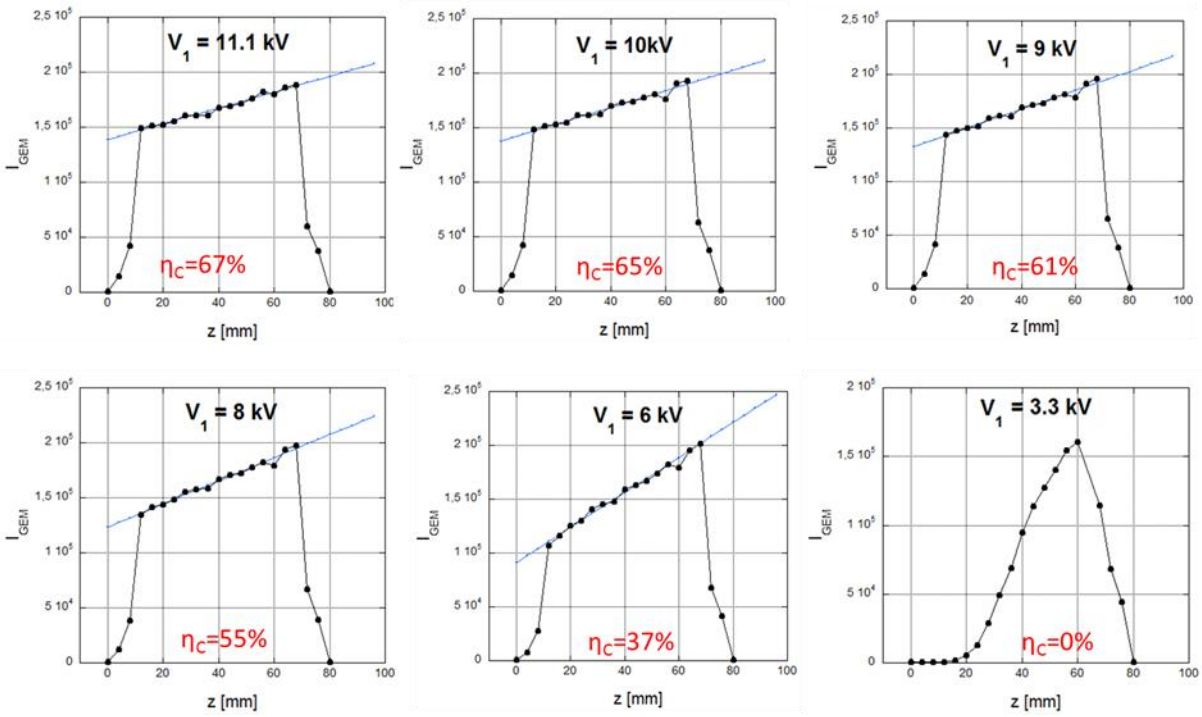

Figure 2-66: Measurement of the charge extraction efficiency for different V_1. The extraction efficiency η_c increases for increasing V_1 values.

Measurement of the neutrons detection efficiency

The neutron detection efficiency was measured using a beam dimension of 4 mm x 4 mm and for Θ values ranging from 0° to 6°. In this configuration the beam footprint is similar to the one shown in Figure 2-61. The efficiency ε_{GEM} of the BAND-GEM detector has been obtained as:

$$\varepsilon_{GEM}(\lambda) = \frac{I_{GEM}(t=\lambda)}{C_{Mon}(t=\lambda)} \cdot (\varepsilon_1 \cdot \lambda) \qquad \text{Eq. 2-22}$$

Where $\varepsilon_1 = \varepsilon_{BeamMonitor}$ (λ = 1 Å) = 0.60 ± 0.06%. The efficiency of the beam monitor has previously measured using a well calibrated ^{3}He tube. In Eq. 2-22, the cluster size parameter is not present because, by calculating $I_{GEM}(t=\lambda)$ as shown in Eq. 2-20, the cluster size parameter is already taken into account. The efficiency as a function of Θ was measured only for the two wavelengths with the higher neutron flux (λ=1 and 2 Å) by considering the corresponding ToF periods. The working points V_1, V_2, V_3 obtained in the previous paragraphs have been used in the following measurements. Figure 2-67 shows that for Θ > 2° the detector reaches an efficiency plateau of about 17% and 30% respectively for λ = 1 and 2 Å. The measurement has been compared with the numerical simulation described in par 2.3.3 that has been superimposed. Figure 2-67 shows that measurements and simulations results are compatible.

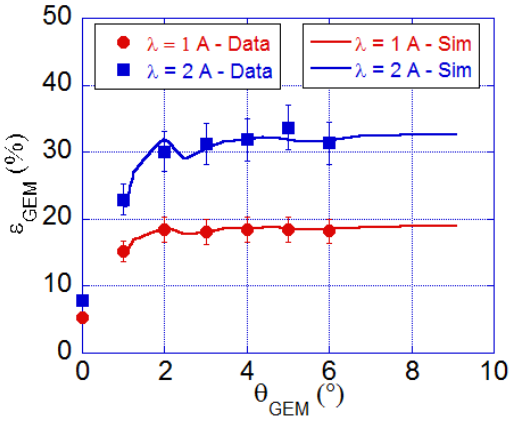

Figure 2-67: BAND-GEM efficiency as a function of the tilting angle Θ for two different neutron wavelengths. Data are compared with simulations.

The efficiency of the detector for neutron wavelengths higher than 2 Å (up to 4 Å) was measured in a dedicated 4 hours long run on which the detector was titled of Θ=5°. The obtained results are shown in Figure 2-68.

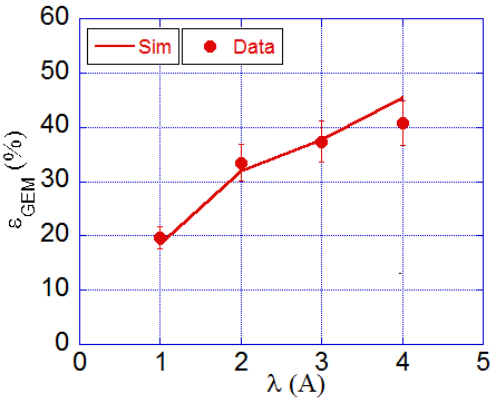

Figure 2-68: BAND-GEM efficiency as a function of neutron wavelength and its comparison with IDL+Ansys+Garfield simulation.

A value of efficiency higher than 40% obtained at λ = 4 Å was measured. This feature makes this technology competitive with other detectors for small angle neutron scattering (SANS) applications.

Position resolution determination

Given that the BAND-GEM detector must be tilted with respect to the incoming neutron beam in order to increase the detection efficiency, one neutron trajectory could give signals in N adjacent gaps and so more than one pad per event can collect charge. This is due to the probability *p* of a neutron to be absorbed in a single strip (each made of two boron layers). If p is the absorption probability every time a neutron crosses a thin wall of a borated grid (*p* only depends on the boron capture cross section and the angle at which the strip is crossed), then a probability density function can be constructed following the description in Figure 2-69.

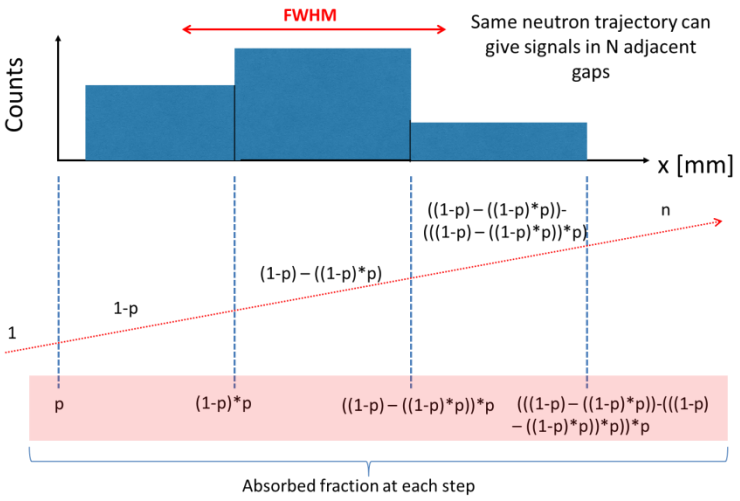

Figure 2-69: BAND-GEM position resolution in terms of FWHM of a probability density function describing the detector absorption probability

The spatial resolution could so be defined as the FWHM of the distribution of the joint probability P of a neutron to be absorbed in either one of the two strips adjacent to a specific gap and to release by-products into this specific gap. The centroid (μ) and the FWHM of the distribution shown in Figure 2-69 can be calculated as:

$$FWHM = 2.35 \cdot \sqrt{\sigma} \qquad \text{Eq. 2-23}$$

With:

$$\sigma^2 = \frac{\int (x-\mu)^2 \cdot p(x)dx}{\int p(x)dx}$$

And:

$$\mu = \frac{\int x \cdot p(x)dx}{\int p(x)dx}$$

These calculations were performed for different tilting angle using the simulation tools described in paragraph 2.3.3.

The measurement of the detector spatial resolution was done by varying the detector tilting angle from θ=0° up to θ=5°. The beam dimension was set to 1mm (along the strips length) x 4 mm (corresponding to the gap between the strips). The beam was accurately centred in order to exactly match the strip gap and the spatial resolution was measured. The beam footprint of these measurements is similar to the one reported in Figure 2-61. The results of these measurements are shown in Figure 2-70, together with the FWHM calculation made with the simulation tools of par 2.3.3. The simulations are compatible with the measured data.

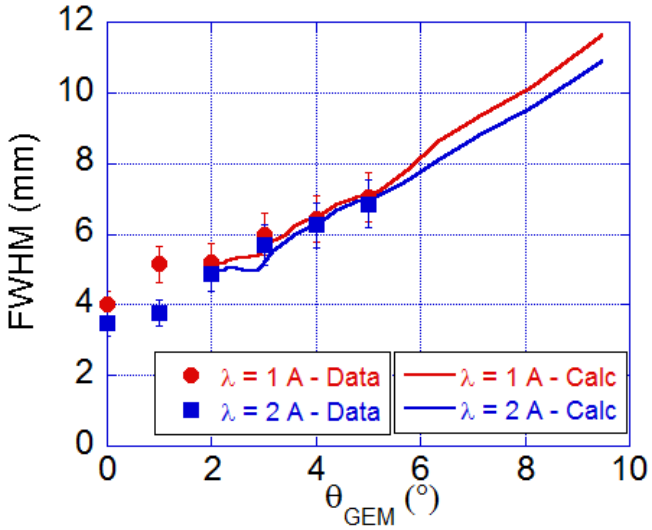

Figure 2-70: Measured BAND-GEM spatial resolution versus the tilt angle and comparison with calculation

As expected, the spatial FWHM of the detector is an increasing function of the tilting angle. To meet the detector requirements for LoKI described in par 2.2, neutrons must intercept the detector with $2°<\theta<6°$ in order to have good detection efficiency and to get a spatial resolution of about 5-7 mm.

High rate Measurements

The high rate capability of the BAND-GEM detector was tested at the G3-2 irradiation station of the 14MW ORPHEE reactor in Saclay (France) [49]. The G3-2 irradiation station is located at about 20m from the ORPHEE reactor core; it provides a white neutron beam of peak energy of about 3.5 meV with a $25x50mm^2$ spot and 0.4° divergence. The expected thermal neutron flux at the measurement position is $\phi = 7.88x10^8$ n/cm^2s [50], and it thus constitutes a very valuable test bed for counting rate capability, radiation hardness and other detector properties requiring a high neutron flux. The data acquisition system used in this experiment was the same described in par 2.3.2.3.

The maximum counting rate capability as well as the linearity of the BAND-GEM were obtained by comparing the data recorded by the BAND-GEM with a fission chamber (FC) detector (a well-proven neutron flux monitor) constituted of a 4mm diameter gas proportional counter with a 2 cm section internally coated with a ^{235}U deposit. The FC was positioned in front of the BAND-GEM and simultaneous measurements were taken. A series of 1.8mm thick polyethylene slabs were placed in the neutron beam in order to attenuate, via multiple scattering, the flux impinging on both detectors. As a rule of thumb, such polyethylene slabs are credited to reduce the G3-2 neutron flux of about a factor 2 for every mm of thickness.

Due to the behaviour of the electronic system, our detector setup can be modelled using a *non-paralizable* model. We consider the FC as the reference detector so that its measured interaction rate is strictly linked to the real interaction rate. The non-paralizable model leads to the following relation between BAND-GEM and the real counting rates:

$$N_{real}-N_{GEM}=\tau N_{real}N_{GEM} \qquad \textbf{Eq. 2-24}$$

where N_{Real} and N_{GEM} are the true and BAND-GEM detector count rates and τ is the saturation time. Since the FC is taken as reference detector we can say that $N_{Real} = aN_{FC}$

and we rewrite the saturation time τ as τ=b/a, where b and a are parameters that can be determined through a fitting procedure. By applying the described changes to Eq. 2-24 we can obtain the saturation formula that links the GEM counting rate to the FC counting rate:

$$N_{GEM}=a\ N_{FC}/(1+bN_{FC}) \qquad \textbf{Eq. 2-25}$$

where N_{FC} and N_{GEM} are the reference detector and BAND-GEM detector count rates. Assuming the reference detector is perfectly linear in its whole dynamic range, the b/a ratio assumes as expected the physical meaning of the saturation time of the (non-paralizable) system constituted by the BAND-GEM detector and its front-end electronics. Fitting of the data in Figure 2-71 with Eq. 2-25 gives an estimated saturation time τ of about 23 ns/pad. The BAND-GEM is linear until 4 MHz/cm^2 (with a deviation from linearity less than 5%). The deviation from linearity for 1.8 mm plastic (half flux) is about 24%, and for the full beam is about 55%.

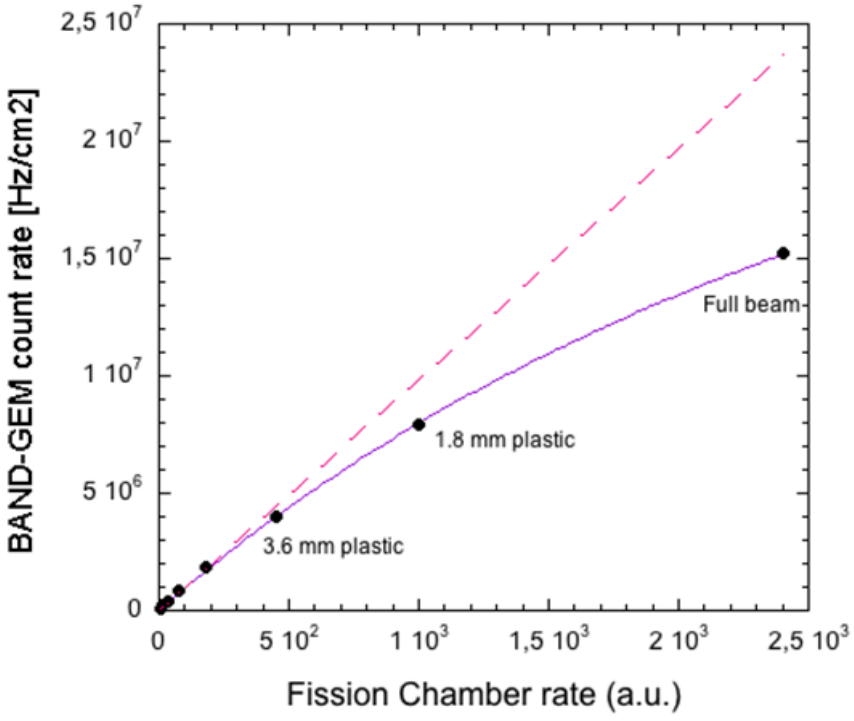

Figure 2-71: BAND-GEM counting rate per pad vs Fission chamber counting rate for different thickness of plastic absorbers interposed in the beam before both detectors.

2.3.5 Third BAND-GEM detector prototype

The third BAND-GEM prototype is an improved version on the second one: the technology used for its construction is the same used for the second one (it is based on the grids technology). The main improvement is the insertion of a GEM foil in the middle of the grids stack that allows a further improvement of the charge extraction from the 3D-C structure.

2.3.5.1 Design and construction of the third BAND-GEM prototype

The optimization of the 3D-C geometrical parameters carried out after the tests on the first BAND-GEM prototype, has significantly improved the electrons extraction efficiency from the grids system (par 2.3.3.2). However, even if this represents an optimized solution, part of the primary charges produced in the region of the 3D-C far away from the triple-GEM are still lost.

The most important improvement of the third BAND-GEM detector is represented by the insertion of a GEM foil in the middle of the grids stack (called “middle GEM”). The middle GEM is set to have a gas gain of about 1.5, in order to restore part of the primary charge lost due to the geometrical configuration of the field and therefore to further improve the electron extraction efficiency and the neutron detection efficiency.

The steps for the realization of the 3D-C of the third BAND-GEM prototype are shown in Figure 2-72.

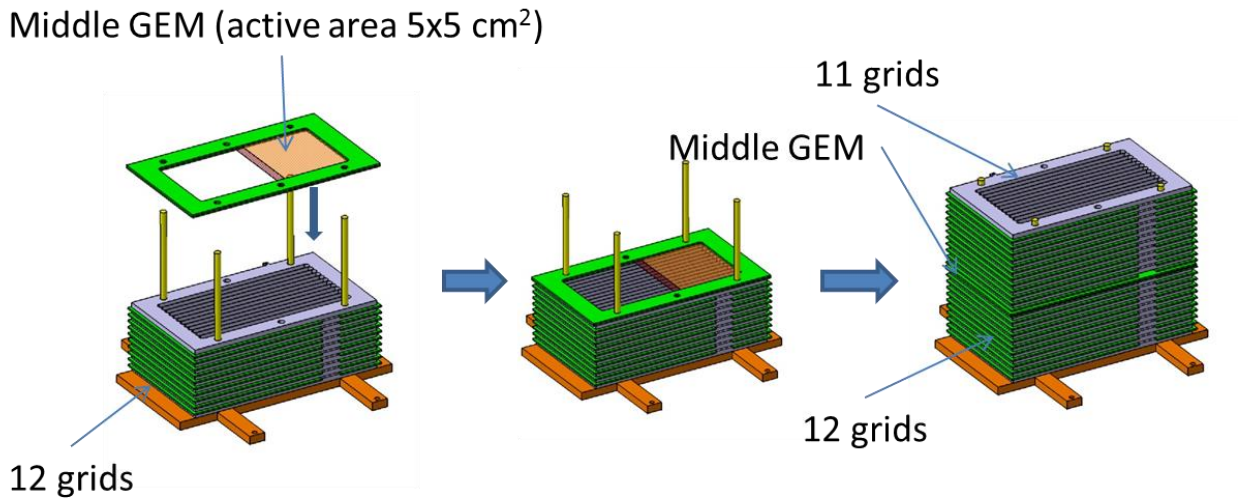

Figure 2-72: CAD model representing the procedures for the realization of the grids system for the third BAND-GEM prototype.

The shape of the grids is exactly the same of the grids used for the realization of the second BAND-GEM prototype (active area of 5x10 cm^2). The thickness of the $^{10}B_4C$ coating is 0.85 µm in order to slightly increase the efficiency to the short neutron wavelength (see Figure 2-45). The 3D-C is built following three steps: first the first 12 grids separated by their fiberglass frames are inserted; than the middle GEM is positioned and then the last 11 grids are used to close the 3D-C. Due to the presence of the middle-GEM one grid was removed with respect to the second prototype. The potential to each grid is now given through two external dividers: the first one has the two ends connected between the first grid of the stack and the bottom of the middle GEM (the bottom is the side of the middle GEM that is not facing to the triple-GEM). The second one has the two ends connected between the top of the middle GEM and the last grid of the stack. The two voltage dividers are powered with 4 channels of a CAEN A1540N module. The 3D-C structure is followed by a standard triple-GEM equipped with a padded anode with 128 pads with dimensions of 4x3 mm^2 (shown in Figure 2-73). The area covered by the pads (active area of the detector) is equal to 4.5x5 cm^2 (area of the middle GEM used).

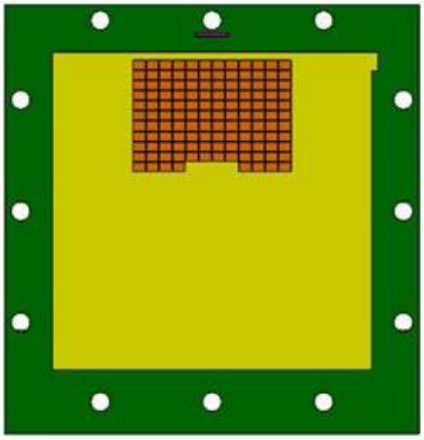

Figure 2-73: CAD model of the padded anode for the third BAND-GEM prototype.

The high voltage is given to the three GEM foils by means of a custom designed NIM Module (HVGEM) [33]. Once realized, the 3D-C is inserted in a detector box (the same used for the second BAND-GEM prototype) and the box is closed by using the lid on which the triple-GEM and the padded anode are installed (Figure 2-74).

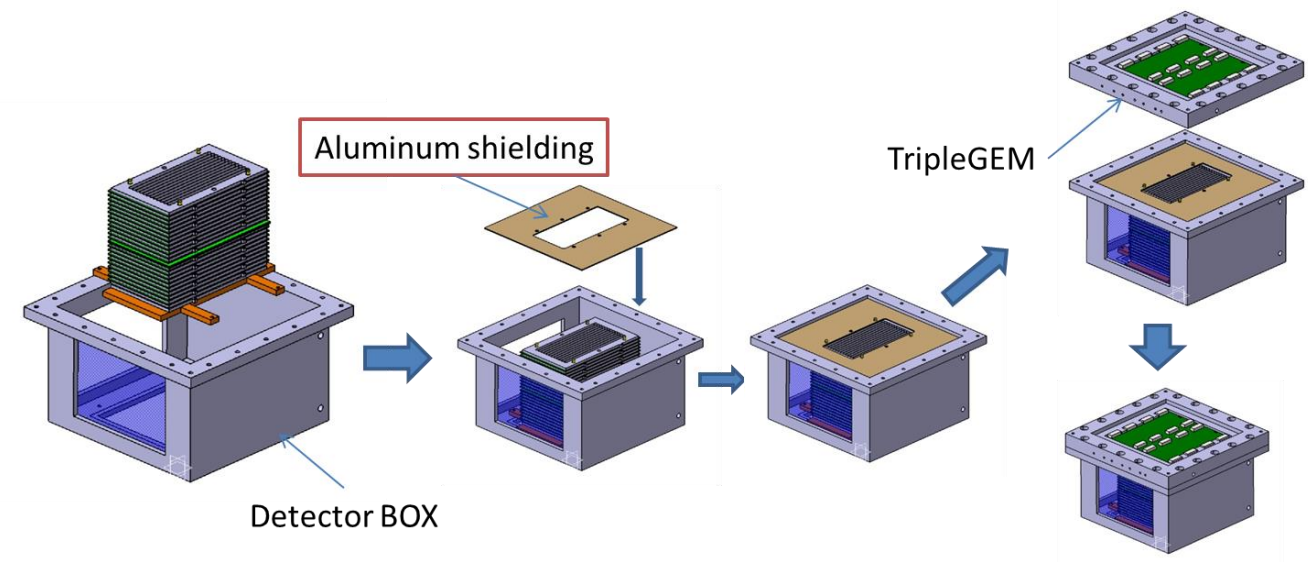

Figure 2-74: CAD model representing the procedures for the assembly of the third BAND-GEM prototype.

A further aluminium plate on the top of the grids stack kept at the same electric potential of the last grid of the stack has been added in order to shield the triple-GEM from the high voltage contacts that bring the potentials to the grids stack. Figure 2-75 shows some pictures of the detector assembly.

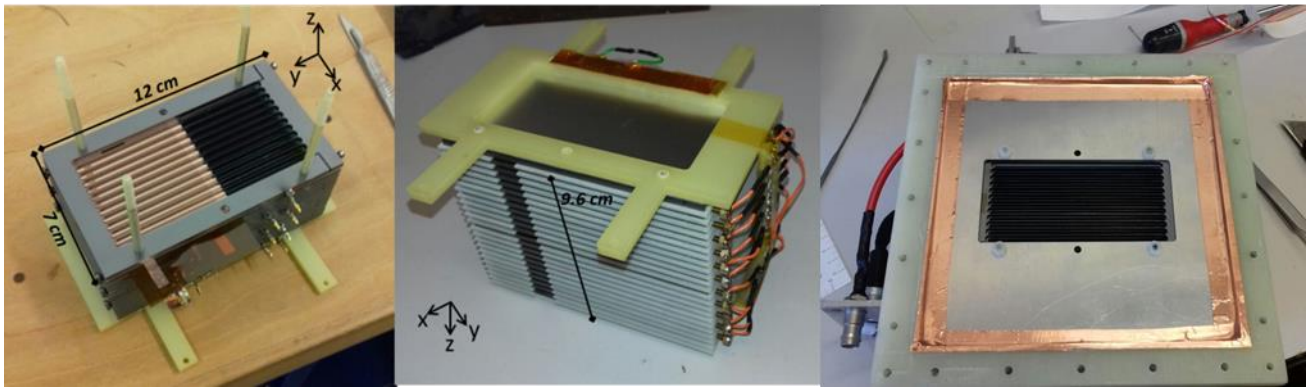

Figure 2-75: Assembly of the 3D-C for the third BAND-GEM prototype

2.3.5.2 Test of the third BAND-GEM prototype with neutrons

The third BAND-GEM prototype was tested under neutron irradiation in two different beam lines. The first test was carried out in the TREFF beam line [61] at the FRMII reactor in Munich, while the second test was carried out on the EMMA beam line at ISIS in order to obtain a direct comparison with the performance of the second BAND-GEM prototype.

Figure 2-76 and Figure 2-77 show a picture of the experimental setup at the TREFF beam line together with a schematic of the setup. The TREFF beam line provides a mono-chromatic beam with a neutron wavelength of 4.73 Å.

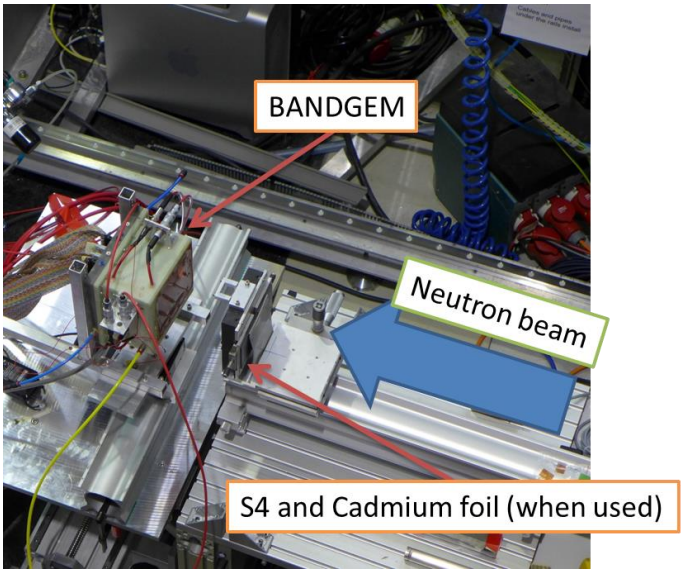

Figure 2-76: BAND-GEM setup at TREFF

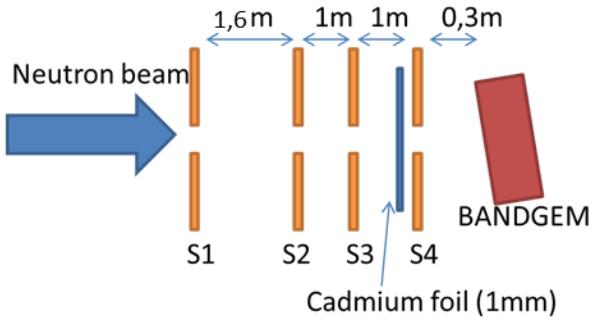

Figure 2-77: Schematic of the BAND-GEM setup at TREFF

The BAND-GEM detector was installed on a rotational stage, which was mounted on x-y positioner. A total of four jaws are installed along the beam path (called S1, S2, S3, and S4 see Figure 2-77). S1 and S2 are motorized jaws, while S3 and S4 are operated manually. By using the jaws, it is possible to obtain highly collimated neutron beams (up to 0.2x0.2 mm^2). The data acquisition system was composed by 8 Carioca cards (16 Carioca chips) [32] readout by a custom made FPGA [33]. The gas flow used during all the measurement is Ar/CO_2 70%/30% with a flow of about 15 l/h.

Initially the triple-GEM working point was determined. For this test the beam dimensions was set equal to 20x20 mm^2. The BAND-GEM was tilted by 5° with respect to the incoming beam and the counting rate of the detector as a function of the applied voltage V_{GEM} ($=\Delta V_{GEM1} + \Delta V_{GEM2} + \Delta V_{GEM3}$) was recorded. The potential difference applied to the grids stack was equal to 10400 V, while a potential difference of 230 V was applied to the middle-GEM (this is the reference case, corresponding to a gain of about 1.5). Subsequently the same measurement was repeated with a cadmium foil in front of the detector, in order to obtain an estimation of the detector gamma sensitivity. The results of the scans are shown in Figure 2-78. As usual, the detector becomes sensitive to gamma rays for V_{GEM}>900 V. A value of VGEM=900 V was used for all the tests carried out at TREFF.

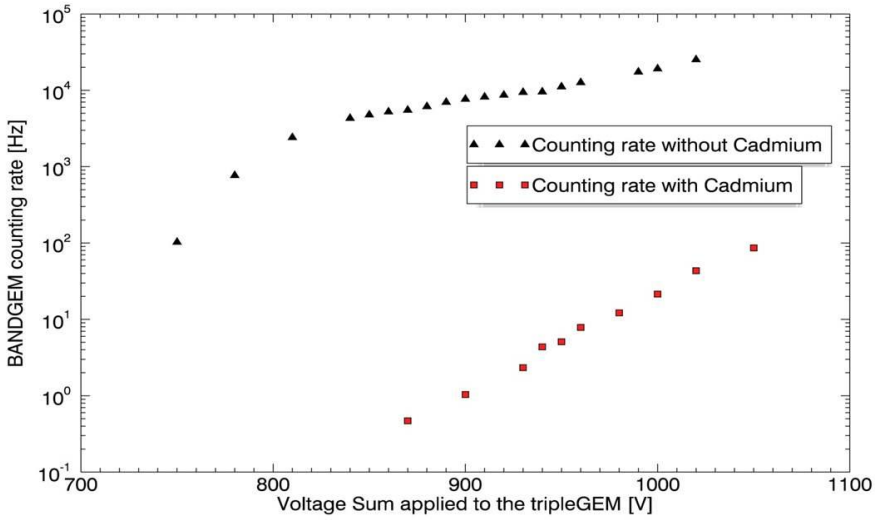

Figure 2-78: Counting rate recorded as a function of the voltage sum applied to the triple-GEM with the detector under neutron irradiation (black triangles) and under gamma rays irradiation (red squares)

Since the presence of the middle-GEM represents a novelty, the corresponding working point was determined. For this test the beam dimensions was set equal to 2x2 mm^2. The voltage applied to the triple-GEM was V_{GEM}=900V and the potential difference applied to the grids stack was equal to 10400 V. The test was performed by recording the counting rate of the BAND-GEM detector as a function of the potential difference applied to the middle GEM. Figure 2-79 shows the results of the scan. The counting rate recorded by the detector is an increasing function of the voltage difference applied to the middle GEM, showing a slope change for an applied voltage greater than 230 V. The chosen working point for the middle GEM is than 230V.

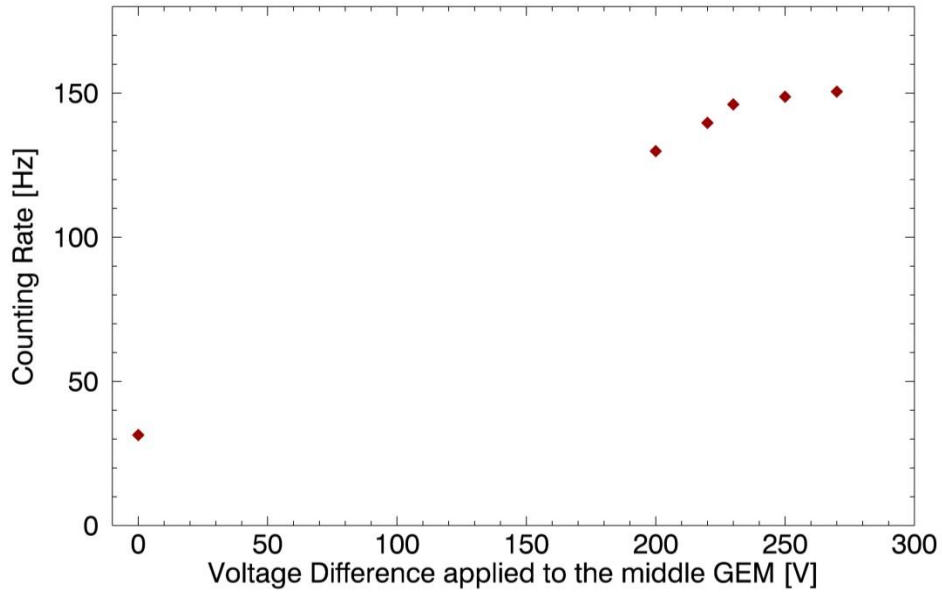

Figure 2-79: Measured counting rate on the BAND-GEM detector as a function of the potential difference applied to middle GEM. The beam is composed by monochromatic neutrons with λ=4.73 Å

Using V_{GEM} and $V_{middleGEM}$ working points, the BAND-GEM efficiency as a function of the tilting angle was measured. For this test the beam dimension was set equal to 2x2 mm^2 and the potential difference applied to the grids stack was equal to 10400. The efficiency value was obtained by comparing the counting rate recorded by the BAND-GEM with the counting rate recorded by a ^{3}He tube. The ^{3}He tube has an efficiency of 96% at 4.73 Å. The ^{3}He tube was then installed in front of the BAND-GEM detector, measuring a counting rate of 473 Hz. This value was used as a reference for the BAND-GEM efficiency estimation. The ^{3}He tube was then removed from the beam and the counting rate of the BAND-GEM was recorded for different tilting angle. The results are shown in Figure 2-80.

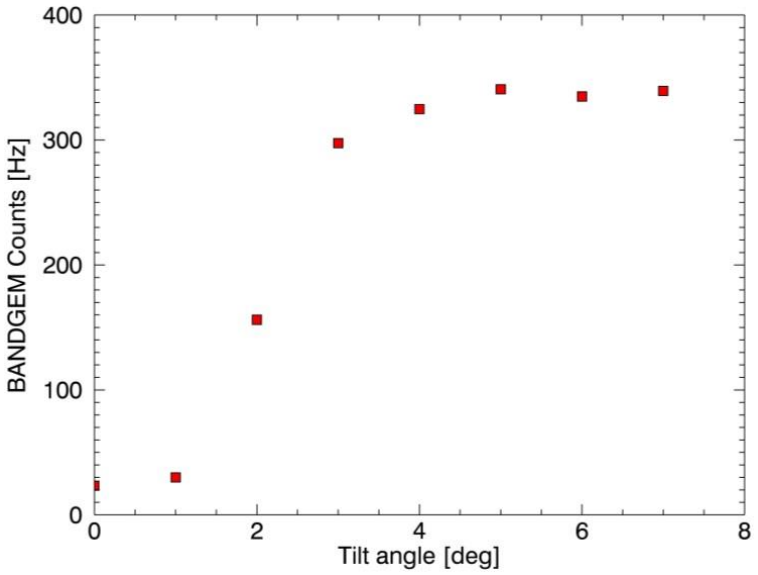

Figure 2-80: BAND-GEM counting rate as a function of the tilting angle

In order to obtain the efficiency estimation, the so called "cluster size" measurement must be performed. This is a measurement of the average number of pads highlighted by a single event (a single neutron). In fact, taking into account that the range of the $^{10}B(n,\alpha)^{7}Li$ reaction by-products can exceed the pad dimensions, a single neutron can highlights more than one pad. The cluster size parameter was obtained by setting the detector acquisition window to the minimum allowable value (10 μs in our case). As measured by the calibrated ^{3}He tube, the neutron flux impinging on the detector is in the order of 500 Hz (1 neutron every 2.0 ms). Such a low neutron flux gives a very low probability that two neutrons give a signal in the same acquisition window. The measurement of this parameter was thus performed by acquiring a total of 10000 events and by using the following formula

$$ClusterSize = \frac{\sum number\ of\ highlighted\ pads\ \ per\ event}{number\ of\ \ acquired\ events}$$

The obtained cluster size is equal to 1.45, meaning that on average with this pad dimension each neutron highlights 1.45 pads. The efficiency value can now be calculated as following:

$$BANDGEM\ Efficiency = \frac{\text{BAND-GEM counting rate}}{^{3}He\ tube\ counting\ rate}\ x\ \frac{^{3}He\ tube\ efficiency}{Cluster\ Size}$$

Figure 2-81 shows the result of the measurement.

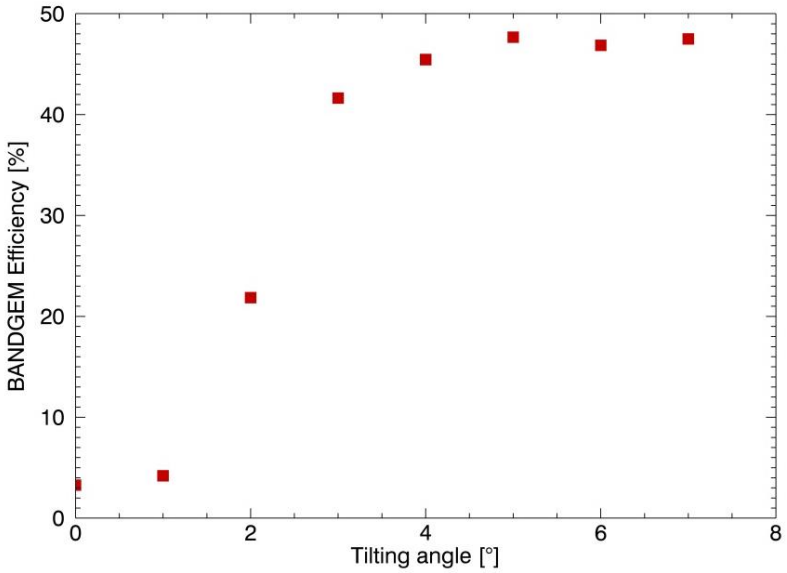

Figure 2-81: BAND-GEM efficiency as a function of the tilting angle

The spatial resolution (in terms of full with at half maximum of the counts distribution in the directions orthogonal and parallel to the strips) was also studied as a function of the tilting angle. Figure 2-82 shows the results in terms of FWHM along the direction orthogonal to the strips (x axis in Figure 2-75). The results are very similar to the one obtained with the second prototype (see Figure 2-70), showing that the presence of the middle GEM does not modify the spatial resolution of the detector.

Figure 2-83 shows that the measured FWHM along the direction parallel to the strips (y axis in Figure 2-75) stays constant at a value of about 5 mm.

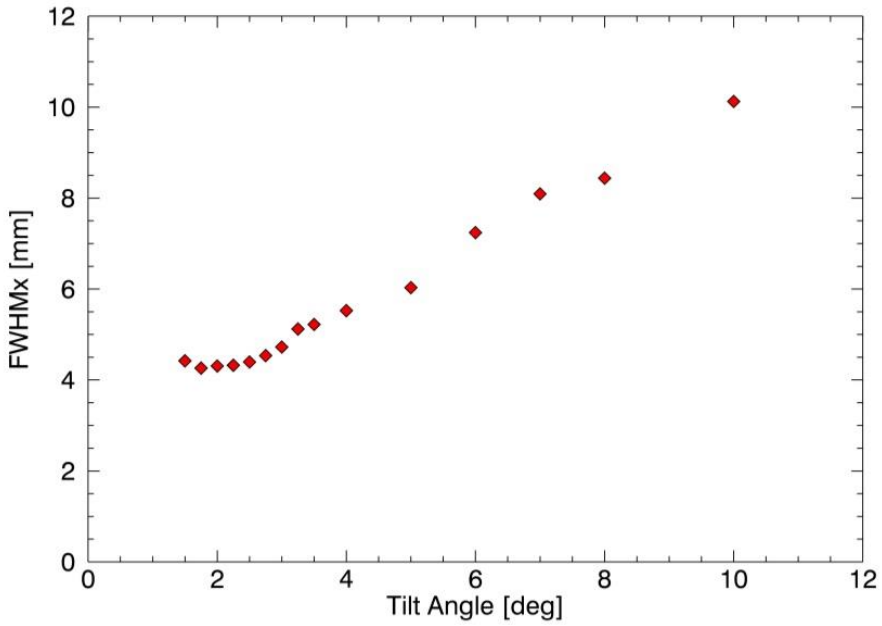

Figure 2-82: Measured BAND-GEM spatial resolution along the direction orthogonal to the strips versus the tilt angle

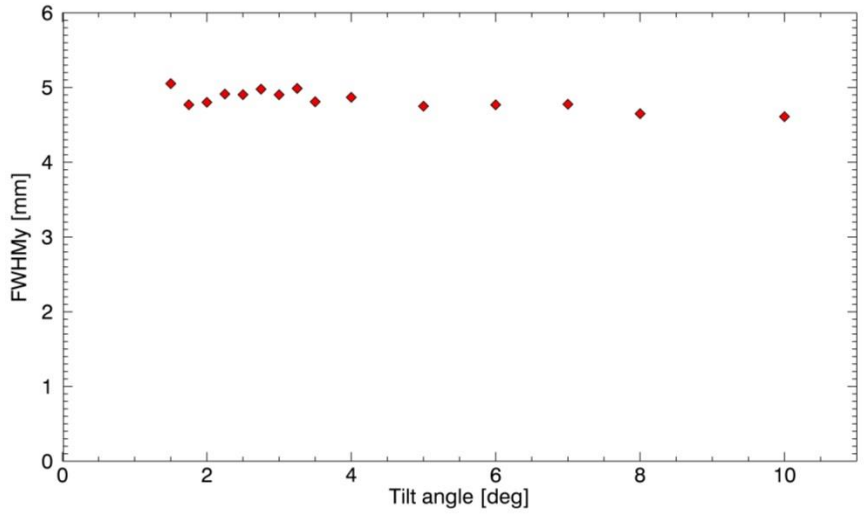

Figure 2-83: Measured BAND-GEM spatial resolution along the direction parallel to the strips versus the tilt angle

The measurement of the electrons extraction efficiency from the grids system was repeated for this detector in order to estimate which is the gain with respect to the second prototype. The detector was tilted by ϑ=90° as described in par 2.3.4.3. In this configuration the beam (whose profile was set to 2x2 mm^2) enters the grid system from the side (parallel to the x-axis in Figure 2-75) through the diagnostic window that has a dimension of 75 mm (z) * 100 (x) mm. The beam was then moved along the z axis (see Figure 2-75) in steps of 4 mm. In this case z=0 mm represents the position of the

grid closest to the cathode, z=48 mm represents the position of the middle GEM while z=96 represents the position of the grid of the stack closest to the tripleGEM. The results of this scan are shown in Figure 2-84, while Figure 2-85 reports the beam footprint recorded for one measurement. The effect of the middle GEM is clearly visible: its presence divides the grids system in two regions that show approximately the same charge extraction probability, meaning that the amplifying foil is able to restore part of the primary charge lost during the drift in the field cage. If the GEM in the middle is removed, the dependence would become strictly linear, as shown in Figure 2-66 .

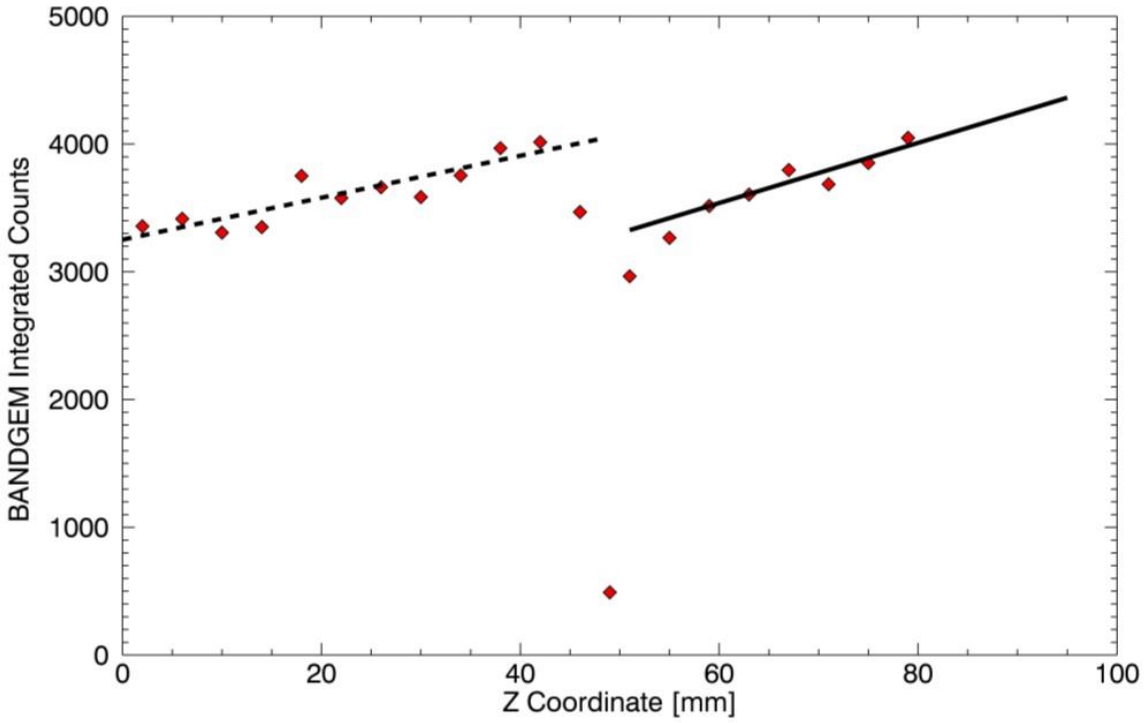

Figure 2-84: Measurement of the charge extraction efficiency. The first grid of the stack is at z=0mm, the middle GEM is at z=48mm, and the tripleGEM is at z=93mm

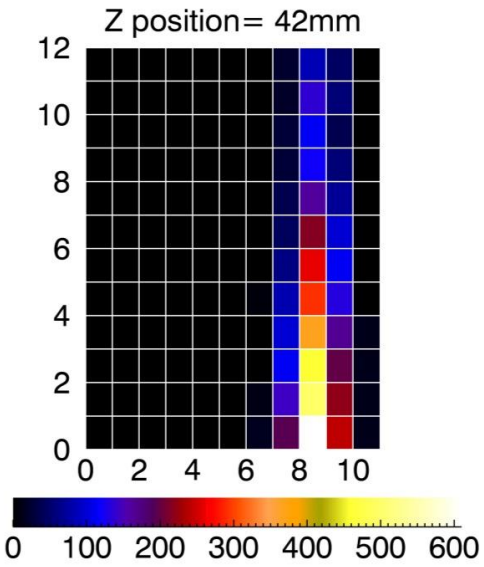

Figure 2-85: Example of beam footprint recorded during the charge extraction efficiency measurement

The response of the detector was studied also as a function of the neutron wavelength by performing the measurements at the ISIS spallation source [36] on the EMMA beam line. These measurements can be directly compared with the measurements carried out with the second BAND-GEM prototype described in par 2.3.4.3. The experimental setup during these tests was exactly the one described in par 0, except for the beam monitor used as reference that in this case was a GS-20 Lithium Glass Scintillator (glass thickness equal to 3mm) with an efficiency at $\lambda = 1$ Å, $\varepsilon_{BeamMonitor}(\lambda = 1 \text{ Å}) = 1.80 \pm 0.1\%$. Even in this case, the beam monitor efficiency scales linearly with λ in the range of interest of the instrument (1-4 Å).

The first test carried out at EMMA was the scan of voltage difference applied to the middle GEM. The detector was tilted by 5° with respect to the incoming beam (beam dimensions equal to 4x4 mm^2). The potential difference applied to the grids stack was equal to 10400 V, while the potential difference applied to the middle GEM was varied between 0 and 290 V. The scan of the middle GEM was repeated for two different V_{GEM} values: during the first scan the sum of the voltage differences applied to the triple-GEM (V_{GEM}) was equal to 870 V (corresponding to a gain of about 100), while during the second scan V_{GEM} was set equal to 900V (corresponding to a gain of about 200). The results of the scans are given in terms of detection efficiency for different neutron wavelengths calculated as shown in Eq. 2-18 and Eq. 2-20.

Figure 2-86 and Figure 2-87 show the result of the scans respectively for V_{GEM}=870 V and for V_{GEM}=900 V.

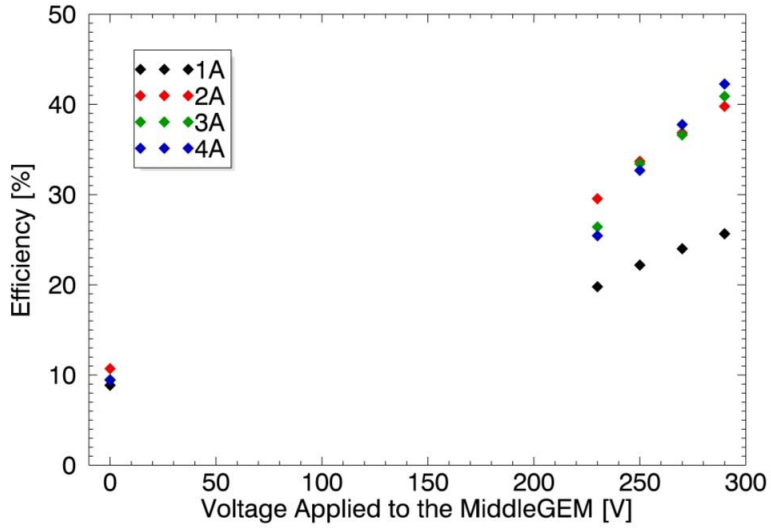

Figure 2-86: Measured detection efficiency for different neutron wavelengths as a function of the potential difference applied to the middle GEM. The sum of the voltage differences applied to the triple-GEM was equal to V_{GEM}=870 V.

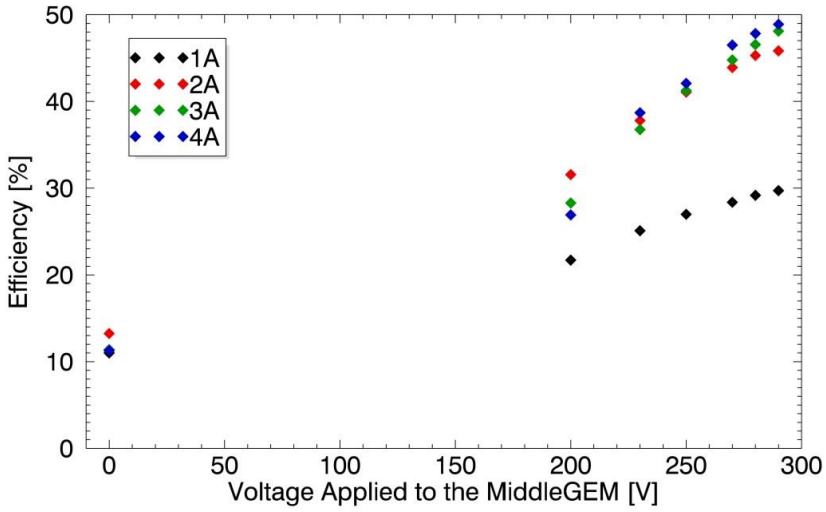

Figure 2-87: Measured detection efficiency for different neutron wavelength as a function of the potential difference applied to the middle GEM. The sum of the voltage differences applied to the triple-GEM was equal to V_{GEM}=900 V.

As you can see, the efficiency is an increasing function of the voltage applied to the middle GEM: by increasing the gain of the middle GEM, the fraction of extracted electrons from the converter region located close to the cathode increases and therefore the detection efficiency.

The two scans were repeated with a cadmium foil positioned in front of the detector. In this way it is possible to obtain an estimation of the impact of the middle GEM gain on the gamma sensitivity. Figure 2-88 shows the results of this scan, together with the counting rate recorded with the detector under neutron irradiation. The counting rate with the detector under gamma irradiation is an increasing function of the middle GEM gain. However, since the ratio between the values recorded with and without Cadmium is quite constant (Figure 2-89), we can consider negligible the impact of the middle GEM gain on the gamma ray sensitivity.

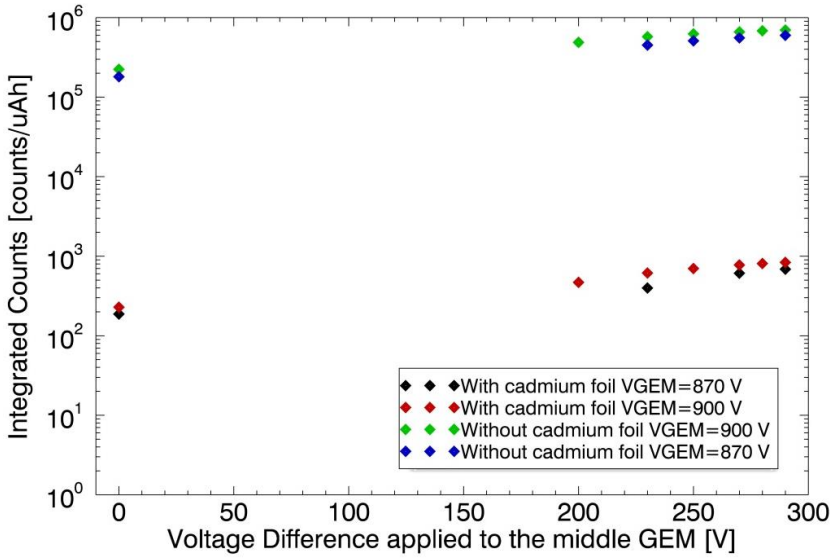

Figure 2-88: Counting rate recorded with the detector under neutron irradiation (blue squares and green squares for V_{GEM}=870V and V_{GEM}=900V respectively), and under Cd-induced gamma radiation (black squares and red squares for V_{GEM}=870V and V_{GEM}=900V respectively)

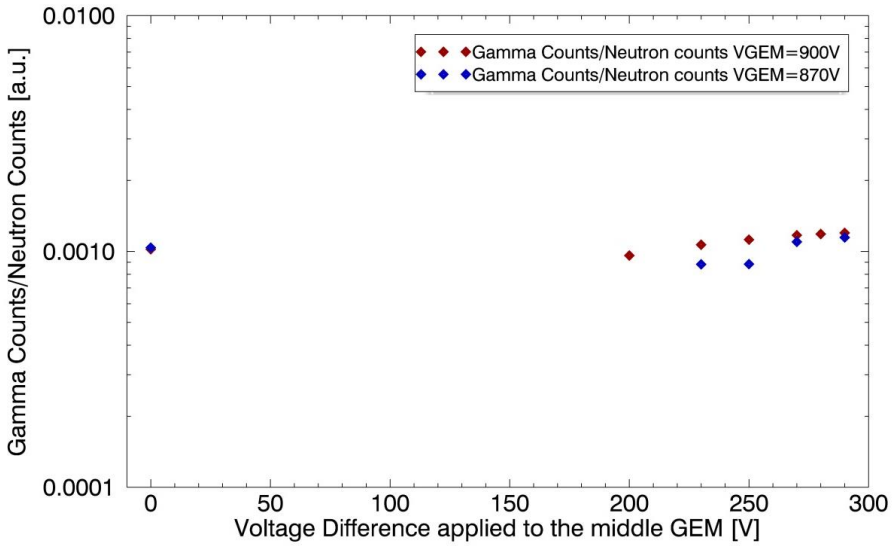

Figure 2-89: Ratio between the counting rates recorded with the detector under gamma and neutron irradiation for VGEM=870 (blue squares) and for VGEM=900V (red squares).

Using the same data, it is also possible to obtain an estimation of the cluster size value as a function of the middle GEM gain. In fact, the acquisition system used can separate events on which a single pad is highlighted by the detected neutron (single hit count), from the events on which multiple pads are highlighted (double hit, triple hit, …). The value of the cluster size is then calculated as:

$$ClusterSize = \frac{\sum number\ of\ highlighted\ pads\ \ per\ event}{number\ of\ acquired\ events} = \\ = \frac{\sum SingleHit + (\sum DoubleHit) \cdot 2 + \sum (TripleHit) \cdot 3 + \cdots}{\sum SingleHit + (\sum DoubleHit)/2 + \sum (TripleHit)/3 + \cdots}$$

The values of cluster size found during the scan are shown in Figure 2-90 for V_{GEM}=870 V and in Figure 2-91 for V_{GEM}=900 V.

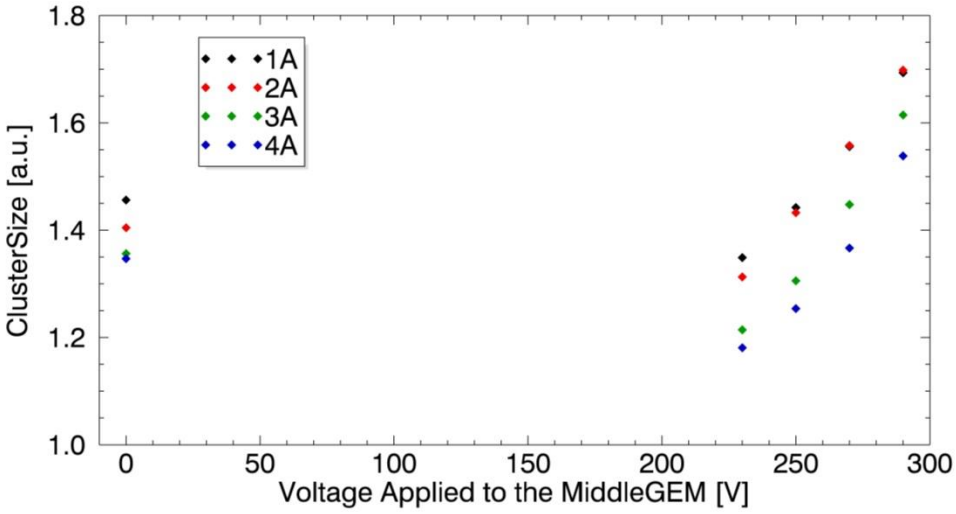

Figure 2-90: Measured cluster size as a function of the voltage difference applied to the middle GEM. The sum of the voltage differences applied to the triple-GEM was equal to V_{GEM}=870 V.

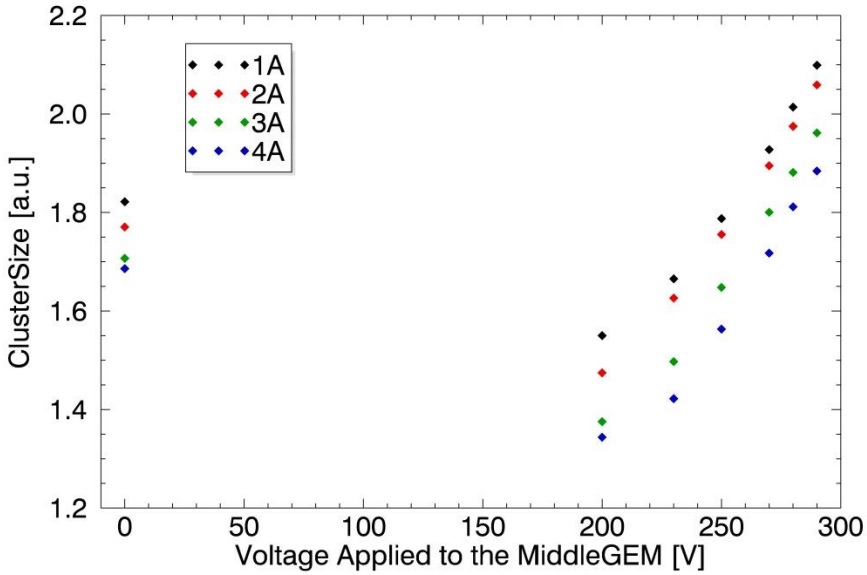

Figure 2-91: Measured cluster size as a function of the voltage difference applied to the middle GEM. The sum of the voltage differences applied to the triple-GEM was equal to V_{GEM}=900 V.

In both scans, it should be noticed that the values of cluster size found is a decreasing function of the neutron wavelength. Moreover, for $V_{MiddleGEM}$=0 V (half of the detector is inactive), the values of cluster size found are higher than the values found for $V_{MiddleGEM}$=230 V. This means that events due to neutrons capture close to the cathode imply a lower number of highlighted pads per event respect to events due to neutrons capture near the triple-GEM.

Finally the efficiency of the detector as a function of neutron wavelengths was performed and the results are shown in Figure 2-92. The detector was then tilted of 5° and the middle GEM was set equal to 270 V. The efficiency values found for different neutron wavelengths are compared to the efficiency values found for the second BAND-GEM prototype (already reported in Figure 2-68). The improvement in terms of detection efficiency obtained with the third BAND-GEM prototype is clearly visible, showing the benefits due to the presence of the middle GEM.

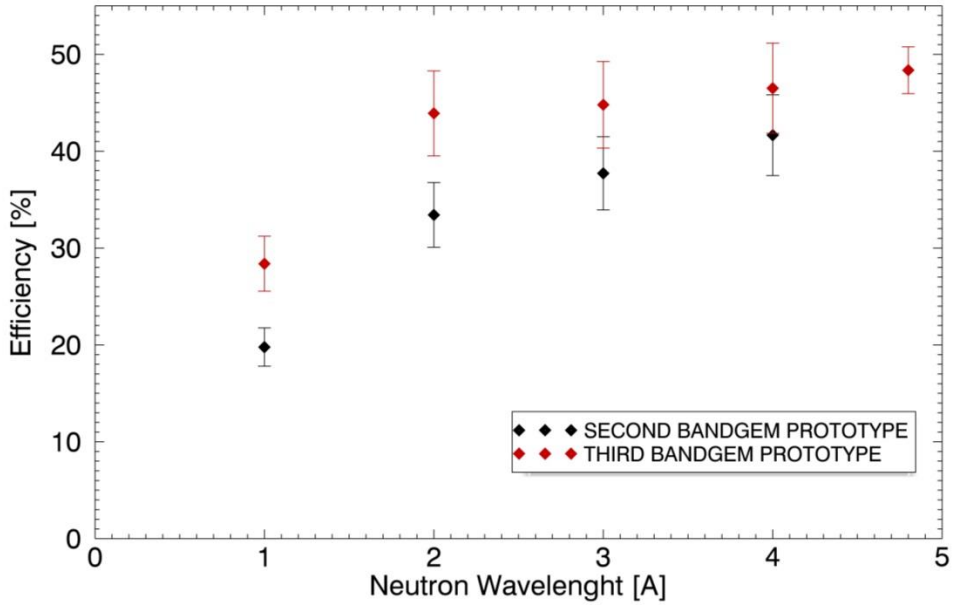

Figure 2-92: Neutron detection efficiency as a function of neutron wavelength (red squares) and its comparison with the efficiencies obtained with the second BAND-GEM prototype (black squares).

2.3.6 Design of the full-module detector for the LoKI middle bank

The small detector prototypes described in par 2.3.4 and in par 2.3.5 have shown the possibility to meet the LoKI detector requirements. This makes this technology a possible candidate to be used in the LOKI detector system. The next step needed to make this technology enough mature to be installed in LoKI concerns the production of a full scale detector (full-module). During my thesis, the CAD design of the final full-module was developed together with the engineering analysis performed for its optimization and validation. In addition possible industrial methods to be used for its production are presented.

2.3.6.1 Engineering of the BAND-GEM full-module detector

Design of the BAND-GEM full-module

Mechanical design

The design and the production of the BAND-GEM full module is driven by the LoKI requirements described in par 2.2. Figure 2-94 shows an isometric view of the detector with its external dimensions. This detector, installed 5m away from the sample position in LoKI, can cover scattering angles ranging from 1° to 5.7°; 4 of these modules assure an azimuthal angular coverage of π. The design of the 3D-C is constrained by the maximum grid dimensions that must be smaller than 10x25 cm^2. This constrain is due to the method used for the grids boronization. As shown in Figure 2-93, uniformity better than 10% is guaranteed for samples shorter than 25 cm.

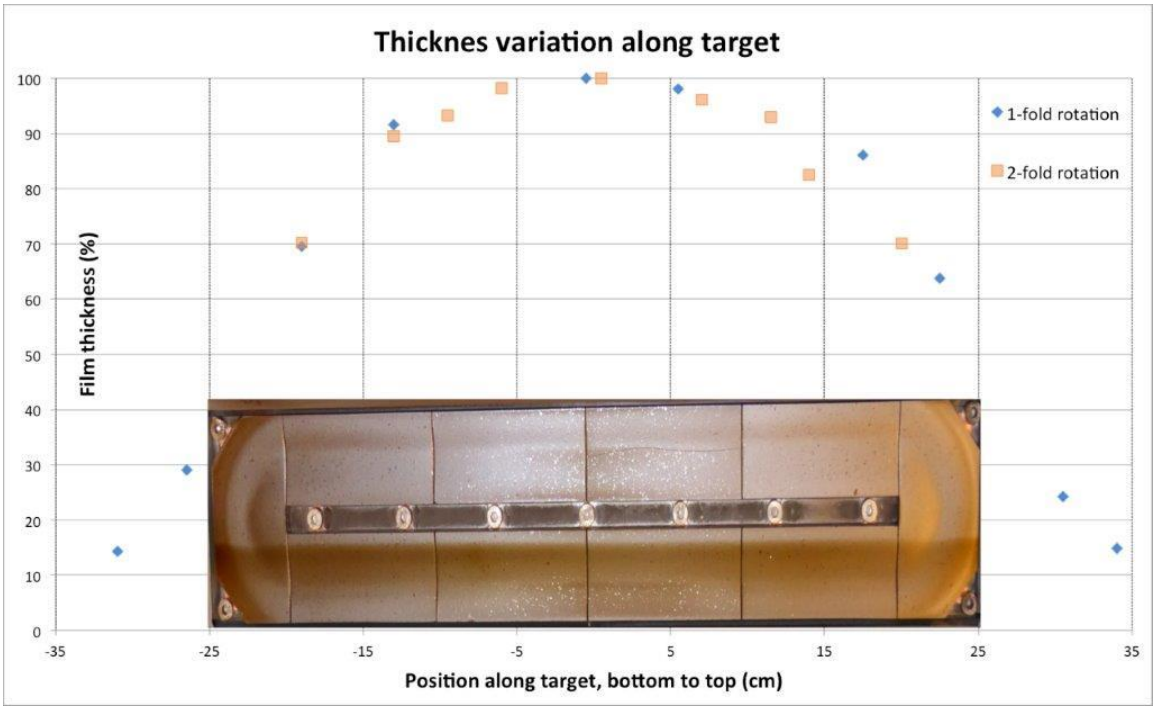

Figure 2-93: Uniformity of $^{10}B_4C$ film thickness as function of the sample length. The uniformity of the film thickness is ensures up to a sample length equal to 20 cm, while it drop off rapidly for longer sample.

Since the external dimension of the full module is 428 mm x 526 mm, a grid plane is composed of multiple grids with smaller dimensions. Figure 2-95 shows a grid plane assembly (left panel) and an exploded view of each grid separately (right panel). The design of each grid is the result of a series of mechanical simulations described later. The thickness of each grid is equal to 3 mm. The thickness of the strips is equal to 200 µm and distance between the strips is equal to 4mm (the same geometrical parameters of the second and third small area BAND-GEM prototype). In order to limit the dead-space area of the detector, the external frames of each grid were reduced to 2 mm (the grids of the small prototypes have an external frame of 12 mm). Therefore in order to maintain the straightness of the thin strips, another frame was added in the grids (see Figure 2-96). Each grid plane is separated from the neighbouring by using a fiberglass frame (thickness 0.95 mm) covered on one side by a thin layer of copper (thickness 0.05 mm). The copper layer is used to guarantee the electrical contact to all the grids of one plane.

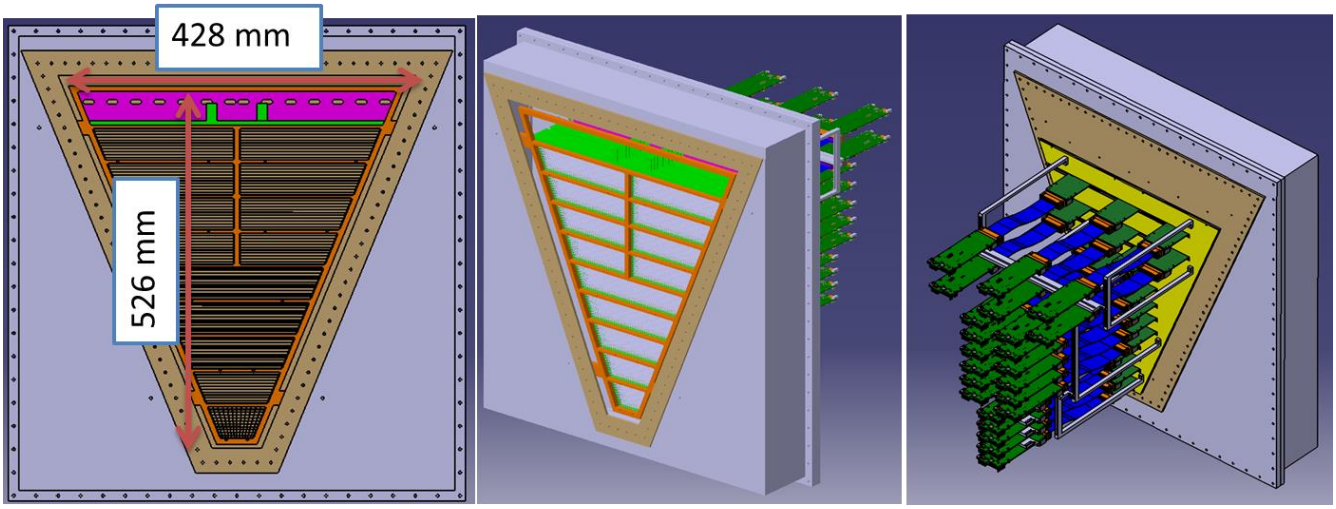

Figure 2-94: CAD model of the full module detector: Front side view (left panel) and isometric view showing the front side (central panel) and the rear side of the detector with the readout electronics (right panel). Neutrons enter from the front side of the detector.

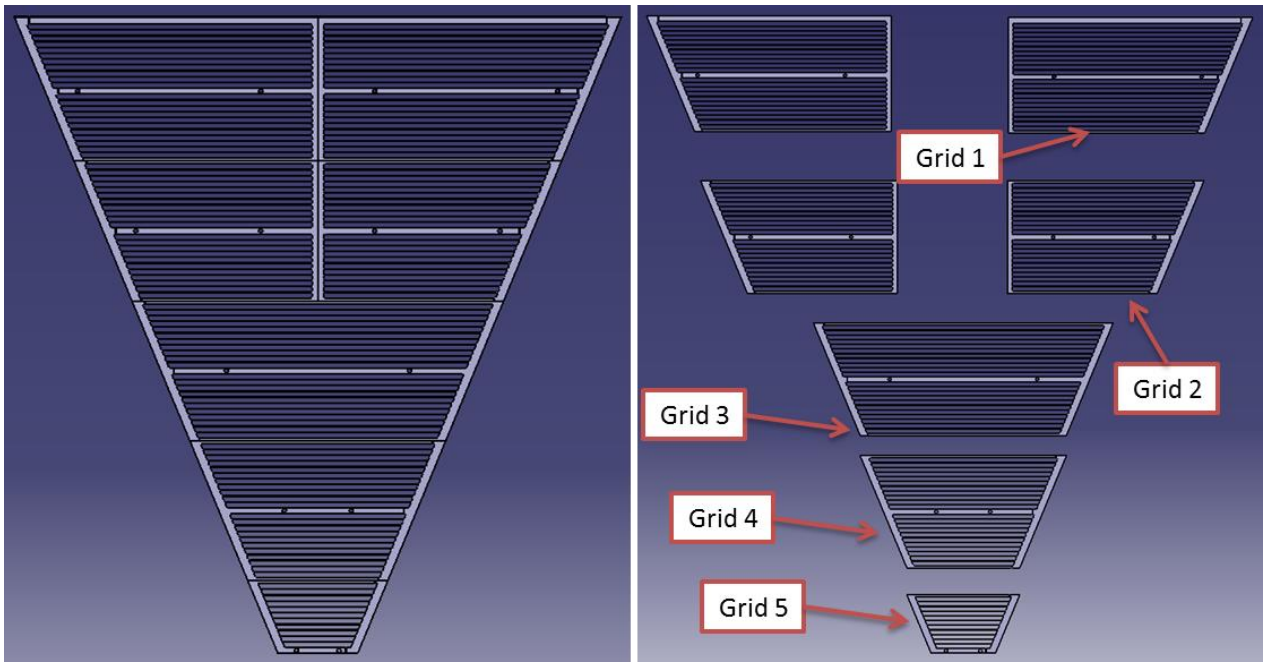

Figure 2-95:Assembly of the grid plane (left) and exploded view of the plane (right).

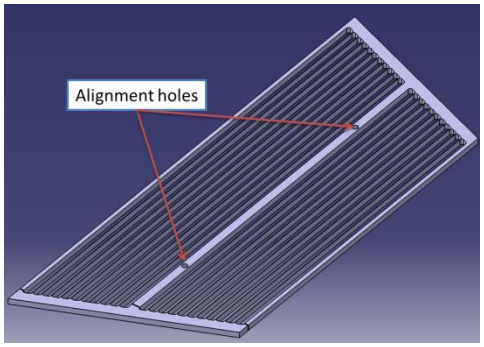

Figure 2-96: Isometric view of the central grid. The alignment holes are highlighted.

The assembly procedures of the 3D-C are shown in Figure 2-97: it is assembled by sandwiching the first 12 grid planes separated by 12 fiberglass frames. Once half of the stack is realized, the middle GEM with its fiberglass frame is inserted. Finally the other 11 grid planes are sandwiched and the 3D-C is ready.

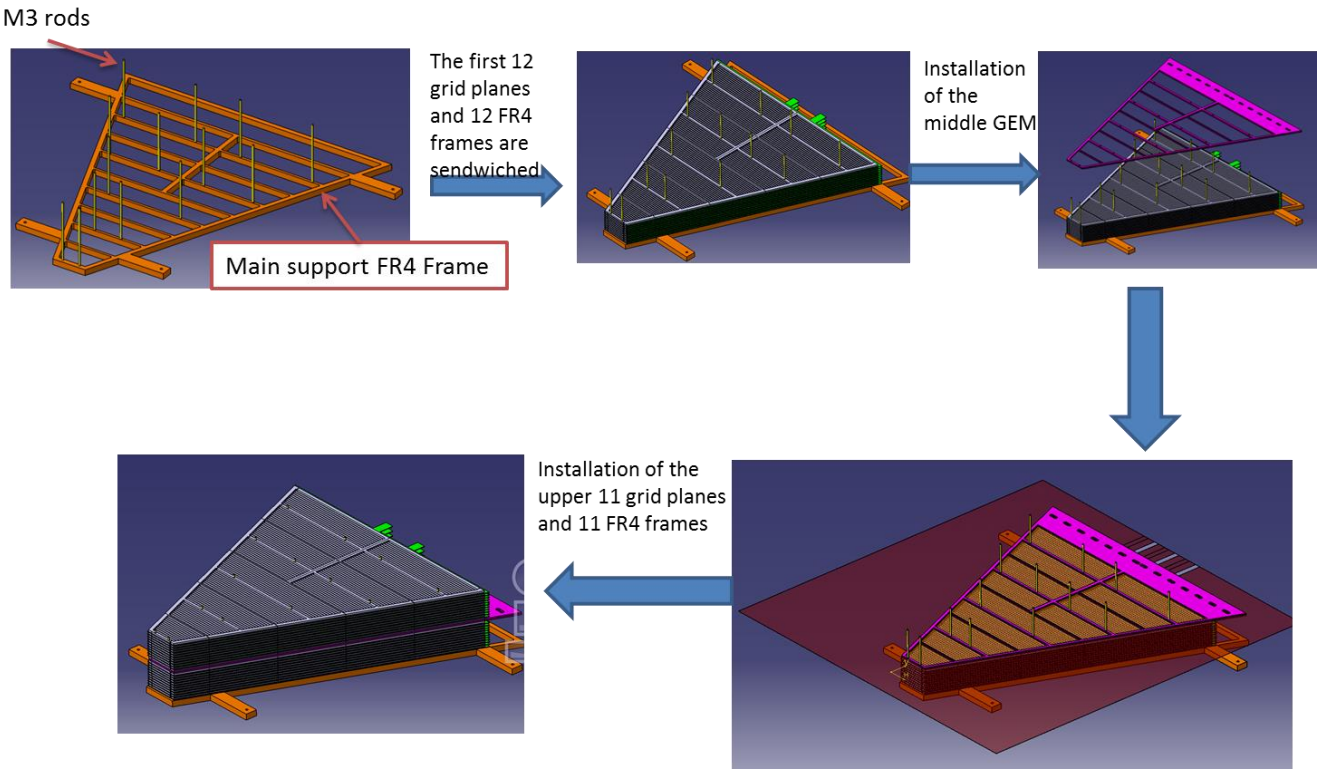

Figure 2-97: Procedure for the 3D-C assembly. The M3 threated rods are inserted in the main support frame. The grids plane and the fiberglass frame are stacked using the M3 threated rods.

The 3D-C is followed by a tripleGEM. The GEM design is shown in Figure 2-98: the GEM foil is sectorized on the top electrode in order to reduce the possible damage caused by a spark: in this case we created 13 sectors on the top electrode. Each sector covers an area smaller than 100 cm^2.

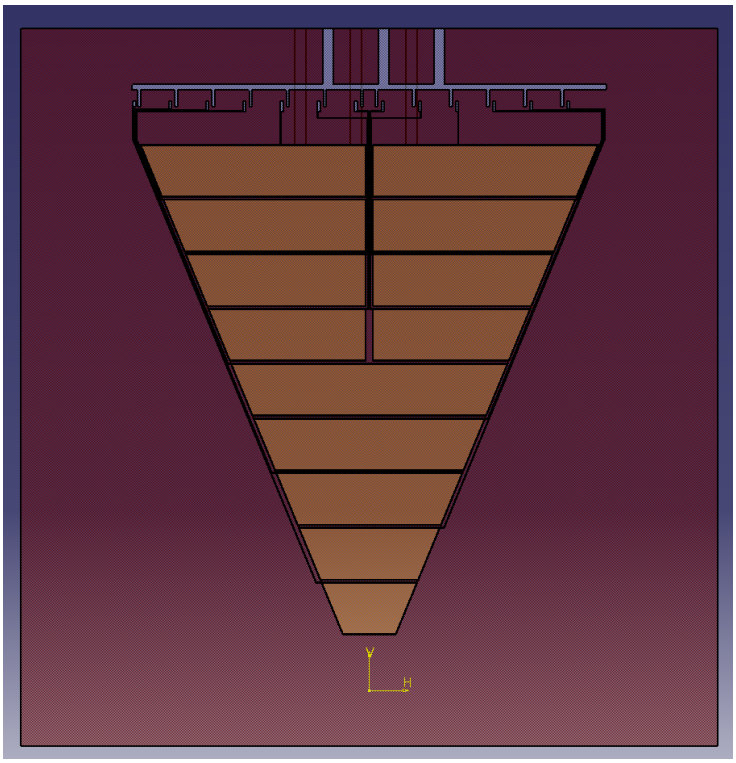

Figure 2-98: Top electrode of the GEM foil. A total of 13 sectors it's foreseen,

Each GEM foil is separated from the other by a 2mm thick fiberglass frame. In this way the geometrical parameters of the tripleGEM is 2/2/2mm (transfer1/ transfer2/ induction gap). The 3D-C is coupled to the tripleGEM by using the same method used for the assembly of the small prototypes: the 3D-C is installed inside detector box (Figure 2-101), while the tripleGEM is installed in the detector box lid (Figure 2-102). The readout anode is closes the lid. By connecting the lid to the detector box (Figure 2-103), the 3D-C is coupled to the tripleGEM and to the readout anode and the full-module is ready.

Electronics and Data Acquisition

The design of the readout anodic pads is driven by the results obtained with the calculations described in par 2.2.2. Figure 2-99 shows a front view of the padded anode. The read out electronics is composed by 23 boards (called GEMINI board) connected to 23 FPGA using a flexible PCB. In the GEMINI board 4 GEMINI chips are wire-bonded. These chips are the front-end electronics that read the signals coming from 64 pads (each GEMINI chip read 16 pads). The LVDS signals produced by the GEMINI board are analysed by the corresponding custom made FPGA that produces for

each signal a 64 bit word containing the number of the channel on which the event was recorded and the arrival time of the event (tof). The produced data are then sent to the PC using an optical fibre. The GEMINI chips are designed using rad-hard technology. Further studies of the GEMINI radiation hardness are foreseen in the future. The FPGA board mount instead commercial components whose radiation hardness is not specified. For this reason the FPGA boards must be shielded from incoming neutron beam. This is done by using an aluminium plate (that acts also as support for the readout electronics) painted with high concentration gadolinium paint. Figure 2-100 shows the CAD model of the shielding plate sustaining the readout electronics. Since this shielding features some buttonholes leaving room to the GEMINI board connectors, neutrons can still penetrate. A misalignment of the FPGA from the GEMINI board (Figure 2-100 right panel) solves this issue.

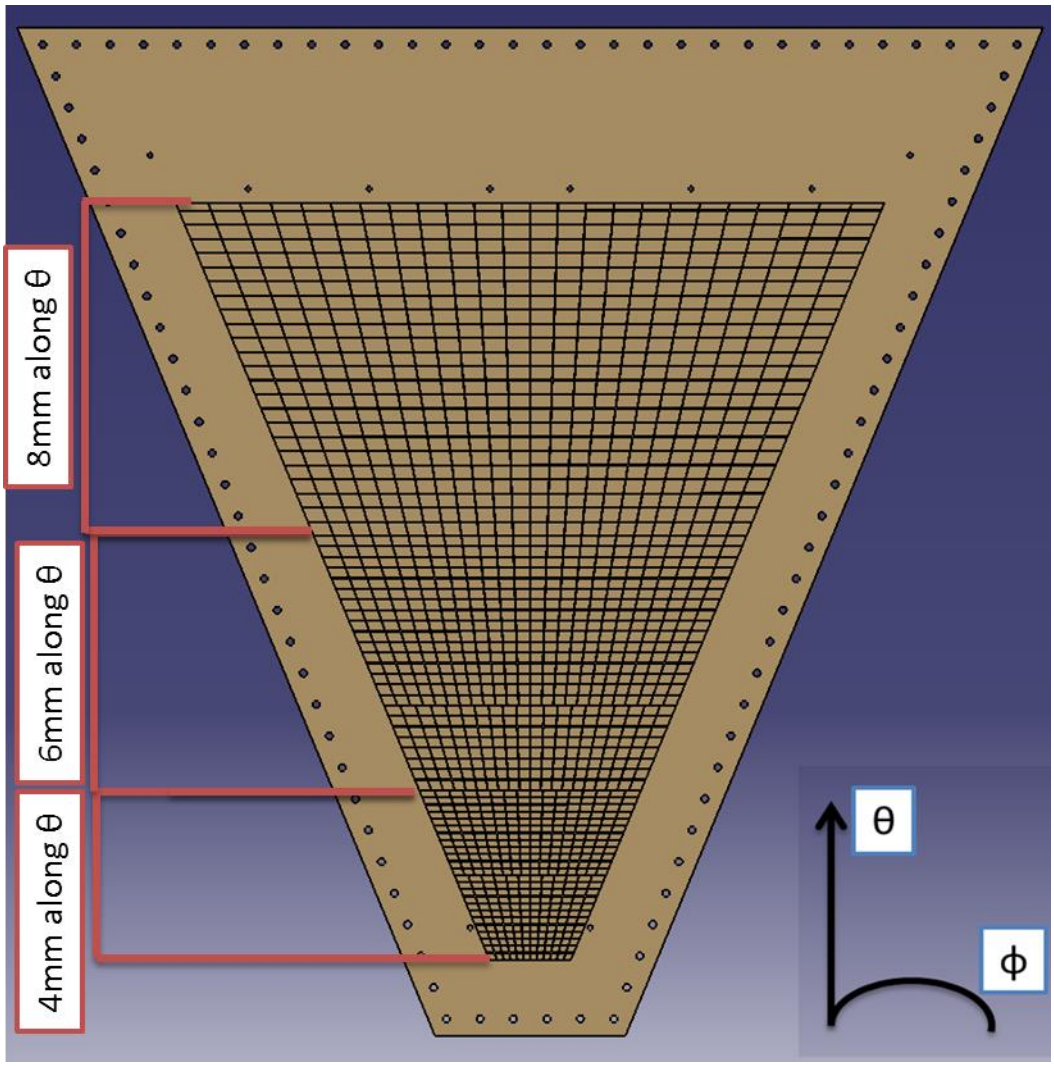

Figure 2-99: Front view of the padded anode

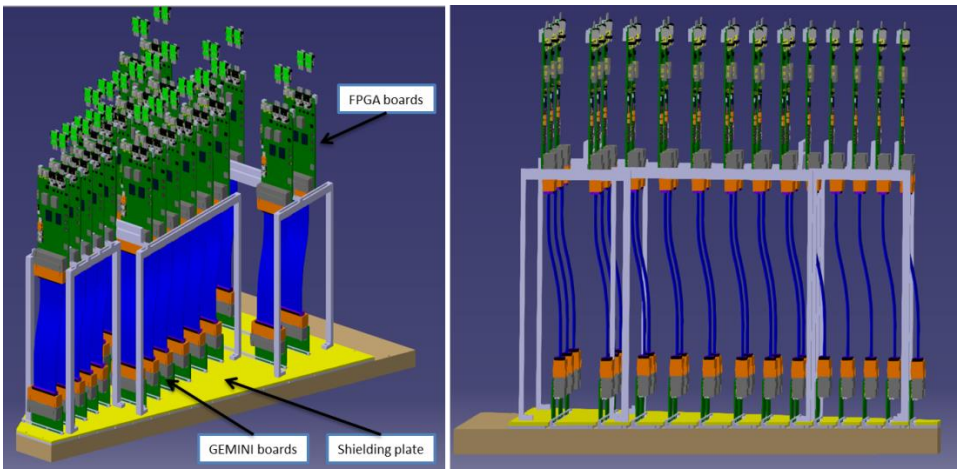

Figure 2-100: Isometric view of the readout electronics connected to the readout anode (left panel). The FPGA board are slightly misaligned from the GEMINI board in order to reduce the neutron irradiation due to the neutron streaming through the GEMINI board.

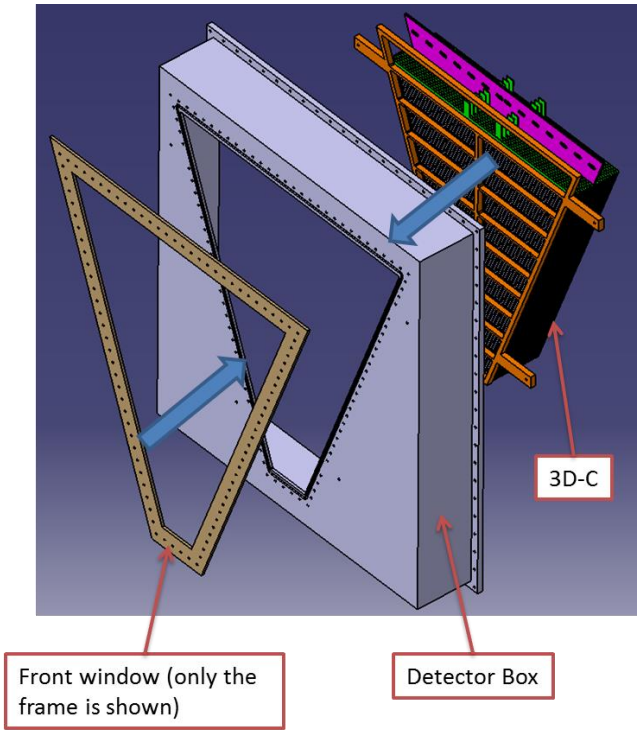

Figure 2-101: CAD model representing the installation of the full-module 3D-C inside the detector box. The front window is bolted to the detector box.

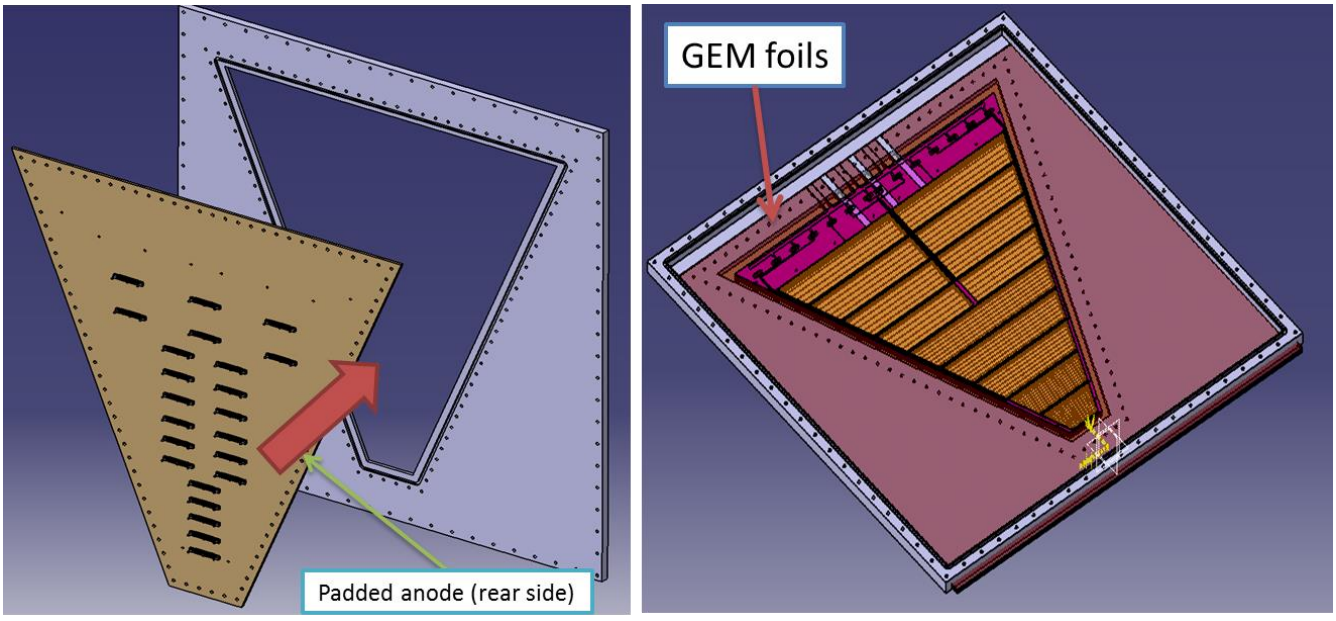

Figure 2-102:CAD model representing the assembly procedures of the tripleGEM. The padded anode is bolted to the detector box lid, and the 3 GEM foils are stacked on the padded anode using some alignment holes.

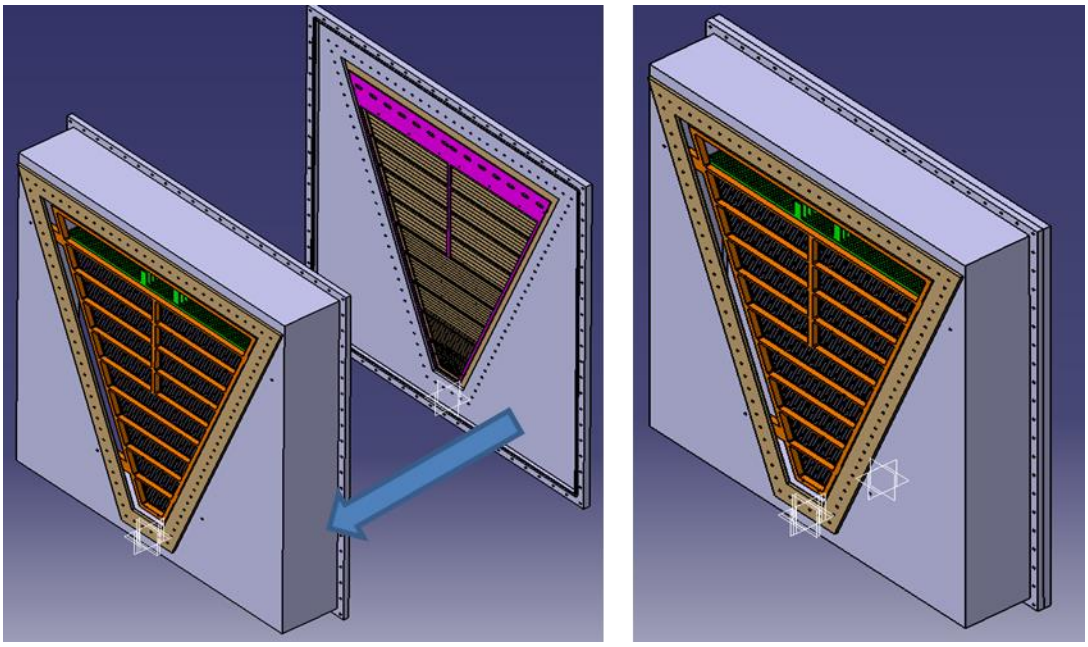

Figure 2-103: CAD model representing the coupling of the 3D-C with the tripleGEM.

Production of the BAND-GEM full module

The most critical components for the production of the full module are the grids that will compose the 3D-C. Each strip of the grids must be absolutely straight and parallel to the adjacent strips. Moreover the alignment of the strips between different planes of grids must be guaranteed with a maximum tolerance of 50 µm. Several simulations of possible misalignments between the strips were carried out using the simulation tools of par 2.3.3. The results of these simulations show that each imperfection on the grids produces a perturbation of the electric field inside the 3D-C leading to the loss of a fraction of the primary electrons. This loss becomes non-negligible for misalignments higher than 50 µm. In order to have the possibility to build a so particular and geometrically arduous component, it is essential to use a technology characterized by total absence of heat exchange with the target material to avoid thermal modifications and distortions on the thin walls. This requirement automatically excludes technologies like conventional laser, EDM and plasma. In addition, the selected technology must have the possibility to cut with very high precision and high quality on the entire kerf (low value of roughness and waviness) a thickness of 3 mm of aluminium. This requirement automatically excludes a technology like femtoseconds laser, which is a very good cutting process up to a maximum thickness of 1 mm. Finally the selected technology must be characterized by very low values of mechanical forces exchanged

with the target material. If this property is not respected, it wouldn't be possible to generate 0.2 mm width aluminium walls without destroying them during the cutting process. This requirement automatically excludes a technology like micro-milling. The technology that has been identified for the grids production is the Micro Abrasive Waterjet. In Micro Abrasive Waterjet processes, the cutting power is obtained by transforming hydrostatic energy in kinetic energy (carried by a jet) that is used to disintegrate the material. The water is pressurized up to very high pressures (up to 600 MPa) by a pump and forced to pass through a very small primary orifice (0.05-0.5 mm): in this way the water beam acquires very high velocity (up to 1000 m/s).. The typical cutting head of an abrasive water jet machine is shown in Figure 2-104: it is composed by a mixing chamber, a focusing tube and an abrasive feeding line. As the thin stream of water leaves the primary orifice, abrasive is added from the feeding line to the mixing chamber. The abrasive particles are accelerated through the focusing tube to the target material. In this way, the cutting power is increased at high level and the abrasive stream can cut through almost all kinds of materials such as stone, glass, metal and composites.

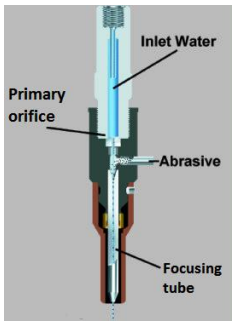

Figure 2-104: Section view of the cutting head of an abrasive water jet machine

Figure 2-105 shows how a grid appears immediately after it has been machined using the micro-waterjet process: also if the lateral forces given by the water jet are small in magnitude, they are not zero and therefore sufficient to slightly bend the thin strips. This effect is most pronounced when using soft materials (like Al) with respect to hard material (like Ti) and if thinner strips are produced. In addition, the elastic deformation of the strips becomes more evident when increasing the length of the walls.

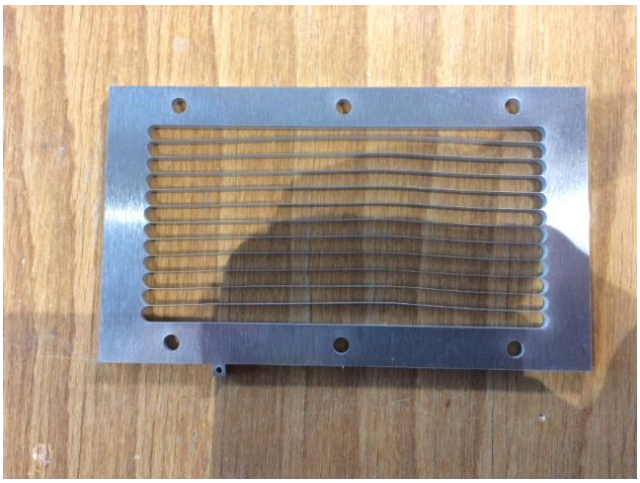

Figure 2-105: A rectangular grid with external frame thicknesses of 10 mm and thin internal walls of 0.2 mm immediately after the water jet cut.

In order to have the possibility to recover the straightness of the walls after all the processes, the grid design has been slightly modified by exploiting the results of F.E.M (Finite Element Method) analysis described later. The modified design of the grids includes a separation of the lateral external frames parallel to the thin walls. In this way the obtained rim is orthogonal to the thin strips. The creation of two threated holes orthogonal to this rim allows the insertion of two M2 screws. (Figure 2-106).

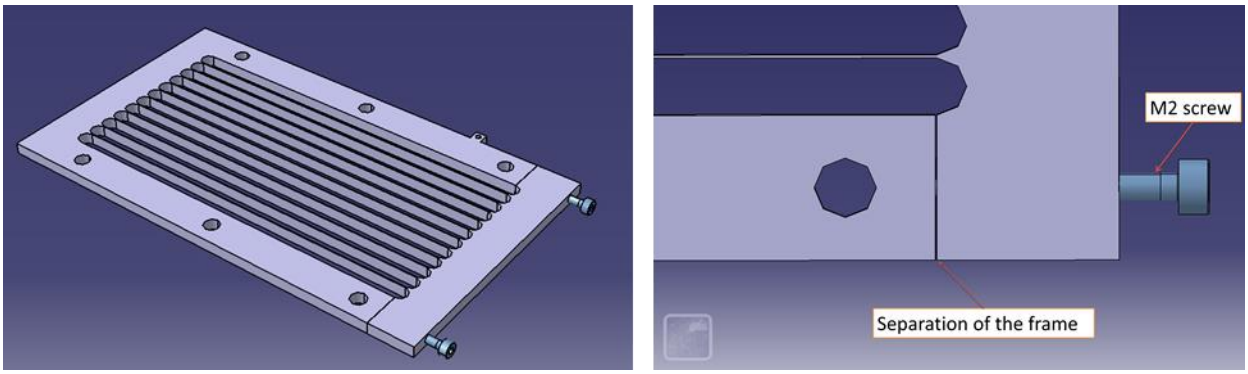

Figure 2-106: CAD model of the grid with the M2 screws used to stretch the thin strips

By acting on these two screws it is possible to restore the straightness of the thin walls.

Figure 2-107 shows an example of grid stretching: as you can see, after the cutting (and the boronization) processes the strips are very bended, while after the re-tensioning using the screws the straightness of the strips is restored.

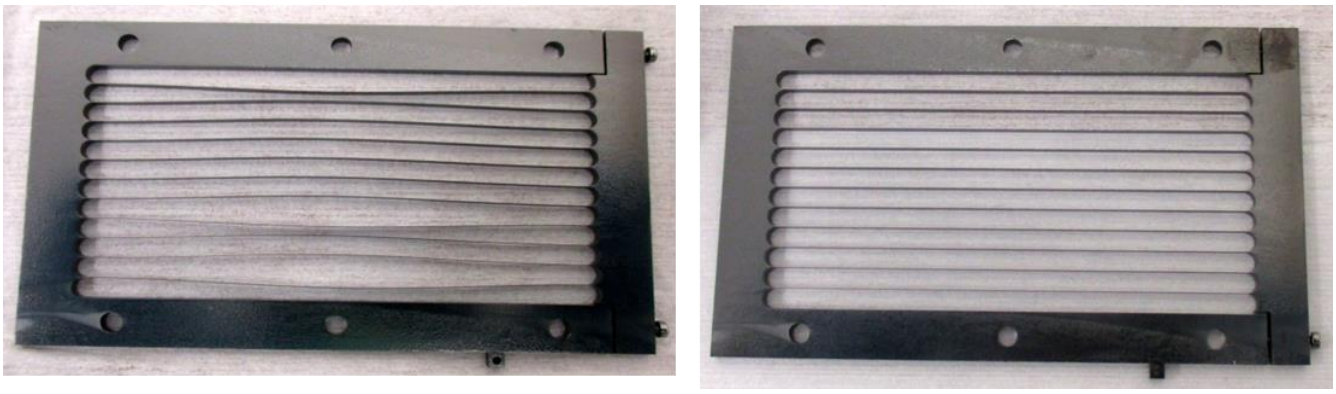

Figure 2-107: One grids of the second BAND-GEM prototype after the boronization process (left panel) and after the re-tensioning with the screws.

The success of this method depends on several geometrical parameters such as the length and the thickness of the thin walls, the thickness of the external frames and the thickness of the raw material. The BAND-GEM prototype described in par 2.3.4 was realized in order to demonstrate the principle of operation described in par 2.3.1. The design of the grids that compose the 3D-C was then focused on the straightness of the thin walls. For this reason it was preferred a robust design of the external frame (width equal to 12 mm) at the expense of the ratio between the active area of the detector and the total area of the grid (the so called “dead space”). This approach cannot be used for in the full module, where several grids will compose a plane of the 3D-C. In order to minimize the dead space of the full module detector a series of mechanical simulation were carried out for the optimization of the grids design. The goal is to reach a grid design that allows a good straightness of the strips while keeping the dead space below 10 %. The software used for this simulation is ANSYS. Figure 2-108 shows an example of the model used in the static structural simulation, together with the applied loads. The loads are constituted by two forces of 150 N on both internal surfaces of the separations of the grid. The geometry is directly imported from the CAD model. The FEM program was set-up in order to solve equations involving non-linear mechanical properties of the materials.

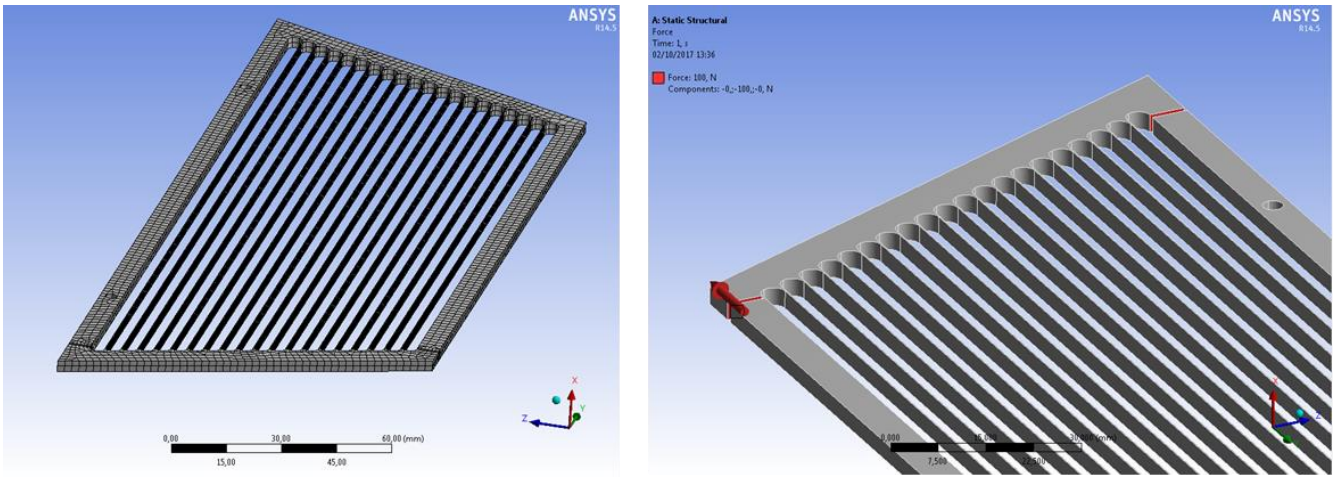

Figure 2-108: Meshed model of a trapezoidal grid of the full module (left) and loads applied to the model (right)

The trapezoidal grids were initially designed following the same method used for the realization of the rectangular grids of the small BAND-GEM prototype. The aim of the simulation was to determine the minimum thickness of the external frame that still guarantees strip straightness. The geometry of the grid is considered suitable for the installation on the 3D-C of the full module when the deformation of the strips due to the grid stretching is less than 50 µm. Figure 2-109 shows the result of the simulation for a trapezoidal grid with an external frame width equal to 10 mm. The deformation is less than 30 µm everywhere, so this geometrical configuration can be accepted. However, this design would imply a dead space of 20%. Figure 2-110 shows the result of the simulation with 6 mm of external frame width. In this case also if the dead space is about 10%, the deformation of the strips is higher than 500 µm. The design of the grid was thus further optimized by inserting a supporting column in the middle of the grid and by adding an additional M2 screw acting on this supporting column.

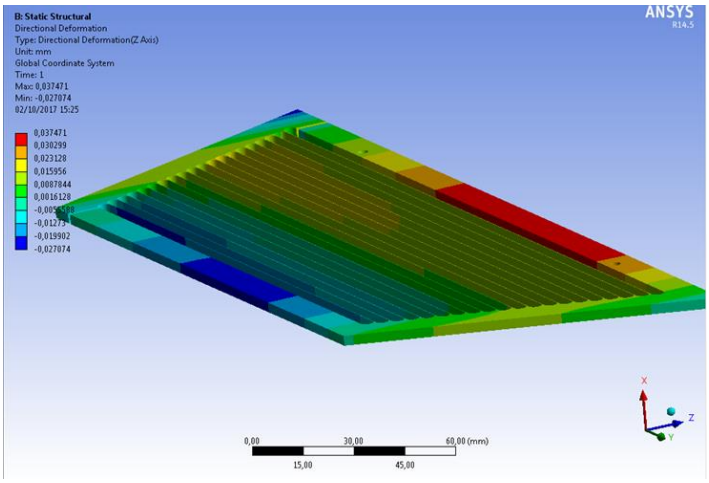

Figure 2-109: Deformation of the strips due to the grid stretching of a trapezoidal grid with an external frame width equal to 10 mm

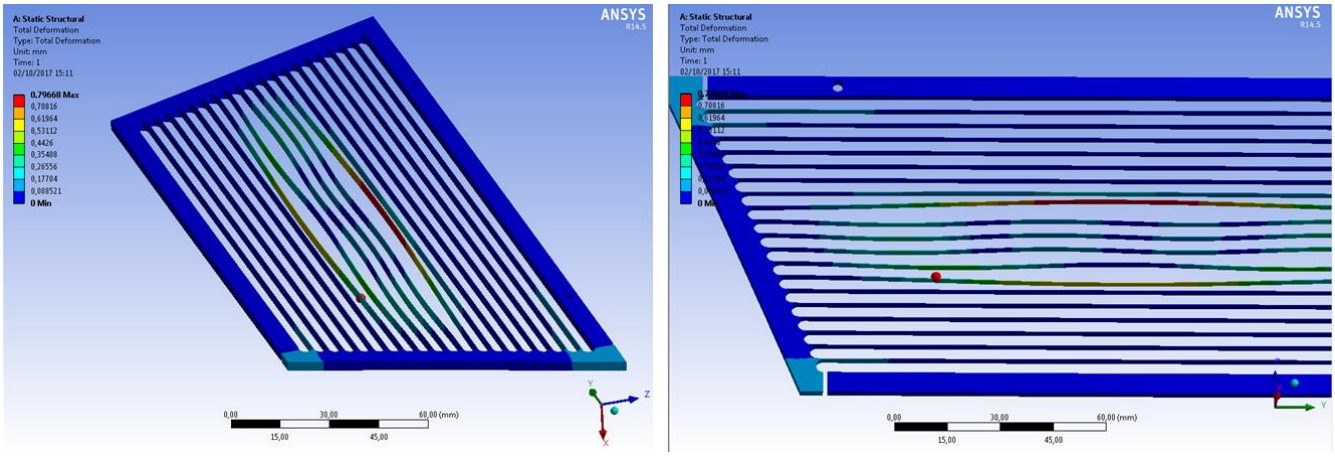

Figure 2-110: Deformation of the strips due to the grid stretching of a trapezoidal grid with an external frame width equal to 6 mm

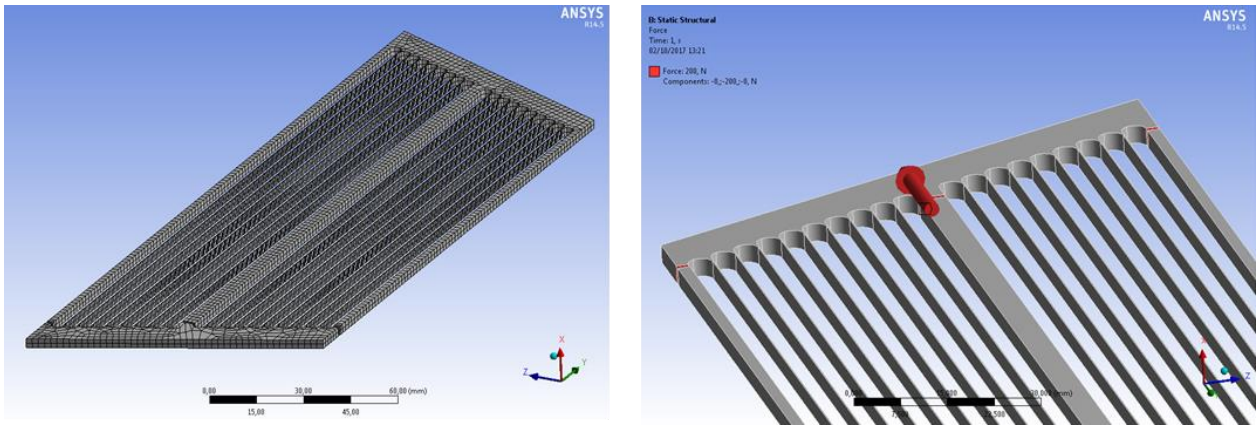

Figure 2-111: Geometry of the grid with the insertion of the supporting column in the middle of the grid. The width of the frame is 2mm for the external part and 4mm for the middle column

The result of the simulation of the new geometry (Figure 2-111) in terms of deformation is shown in Figure 2-112. As you can see, the addition of the column in the

middle of the grid allows keeping the deformation of the strips within the imposed limit of 50 µm. Since the width of the external frame and of the internal columns is respectively 2mm and 4 mm, the dead space results to be 8% of the total grid active area: this value is acceptable for the full module detector.

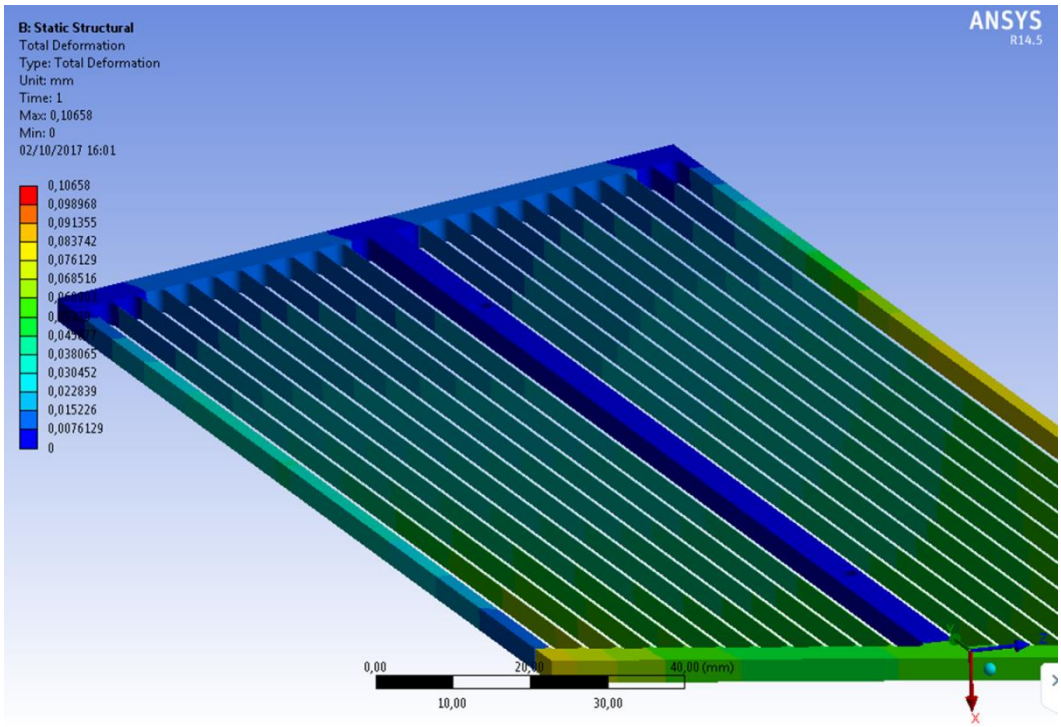

Figure 2-112: Deformation of the strips due to the grid stretching of a trapezoidal grid with an external frame width equal to 2 mm and an internal column width equal to 4 mm

The same simulation was carried out for each grid that composes the grid plane of the full module, leading to the design shown in Figure 2-95. In order to validate the simulations, two types of grid were realized: the final grid of Figure 2-111 and the grid that has an unacceptable bending of the strips of Figure 2-110. Figure 2-115 shows the grid realized with the design simulated in Figure 2-110, while Figure 2-113 shows the grid realized with the design simulated in Figure 2-114. As predicted by the simulations, the grid simulated in Figure 2-110 presents an unacceptable bending of the strips, while with the new design the strips are well straight.

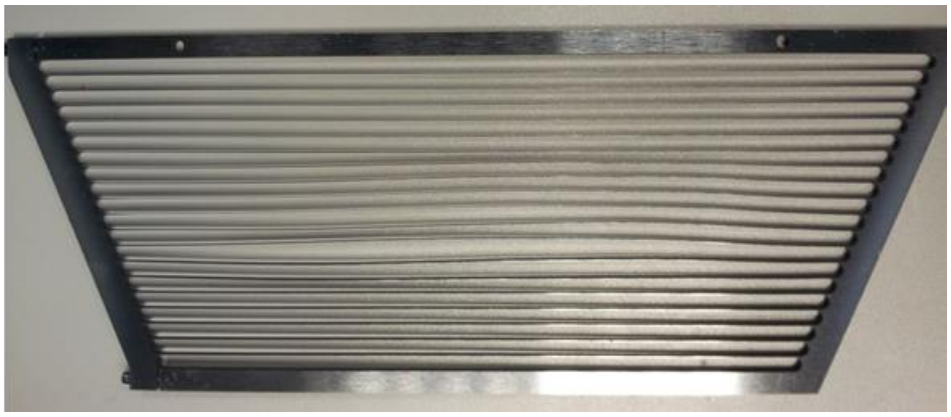

Figure 2-115: Grid realized with the design of the simulation reported in Figure 2-110. The bending of the strips is not acceptable.

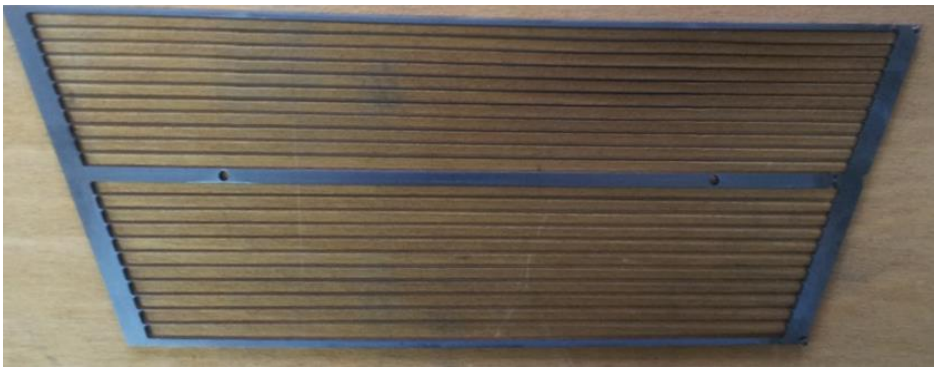

Figure 2-116: Grid realized with the design of the simulation reported in Figure 2-110. The strips are now well stretched.

The validation of the simulations represents the kick-off for the production of all the grids composing the full module. Presently all the components of the full-module detector are in production. The assembly of the detector will start in 2018.

3 Chapter 3: GEM-based detector for fast neutrons

This chapter describes the development of the nGEM detector for the CNESM diagnostic system and its installation inside the vacuum vessel of the SPIDER experiment. The detector is designed for the detection of fast neutrons, in particular for the detection of the 2.45 MeV neutrons produced by the D(d,n)^{3}He fusion reaction.

3.1 Introduction to the SPIDER experiment

The SPIDER experiment (Source for Production of Ion of Deuterium Extracted from Rf plasma) represents the first step towards the realization of MITICA (Megavolt ITer Injector Concept Advanced), the full-size Neutral Beam Injector for the International Thermonuclear Experimental Reactor (ITER) [48]. ITER is a large international project aimed at demonstrating the production of energy from the controlled thermonuclear fusion of deuterium and tritium for a period of about 30 minutes. To provide the plasma with the energy required to make a sufficient number of nuclear reactions and enter an operational regime suitable for a reactor, it is necessary to inject energy either by high frequency and high power electromagnetic waves or by neutral beams. The main requirement of the HNB (Heating Neutral Beam Injector) system is the capability to provide the ITER plasma with a total power of 33 MW for up to one hour in a stationary condition by means of two injectors. Each injector is required to accelerate to 1 MeV a beam of negative deuterons carrying a 40 A current at the end of the acceleration. These requirements have never been experimentally verified simultaneously and therefore there is a strong experimental activity with the aim of optimizing the crucial components and systems that must be installed in ITER. The two main experimental devices are SPIDER and MITICA, actually under construction at Consorzio RFX [52] in Padova, Italy. The goal of SPIDER is the development of the know-how on negative ion sources and the optimization, in terms of production and uniformity, of the beam. The optimised SPIDER source will be duplicated for MITICA, the full-scale injector for ITER. This chapter describes a neutron system that will be used on SPIDER in order to diagnose the SPIDER deuterium beam using neutron emission.

Figure 3-1 shows the CAD model of the SPIDER experiment. The main components of SPIDER are [53]:

- The vacuum vessel cylindrical with 4 meters diameter, and a total length of 5.5 m.
- The negative ion source, on which 8 inductive RF generators (operated at 1 MHz) produce the negative deuterium ions. The ions are extracted by using a grid with a surface having 1280 holes of 12 mm diameter, with pitch distance equal to 20 mm and 22 mm in the horizontal and vertical directions, respectively.
- The acceleration stage, which is composed of a series of grids that have to accelerate the deuterium ions up to 100 keV.
- The stopping system, composed of two separated devices. The first one is a diagnostic calorimeter (called "STRIKE"), installed close to the source and able to operate for short periods (up to 10 s), realized in CFC (Carbon-Fibre-Composite). The second one is called "beam-dump" and is a water-cooled system made of a CuCrZr-alloy (with an elemental composition of about 99% Cu) aimed at stopping the beam and absorb the thermal load (about 7 MW at the maximum performance conditions). The beam dump is placed at a distance of 2.28 to 2.72 meters from the accelerator exit, and the deuterium beam impinges onto it with an incident angle of 60° (Figure 3-2).

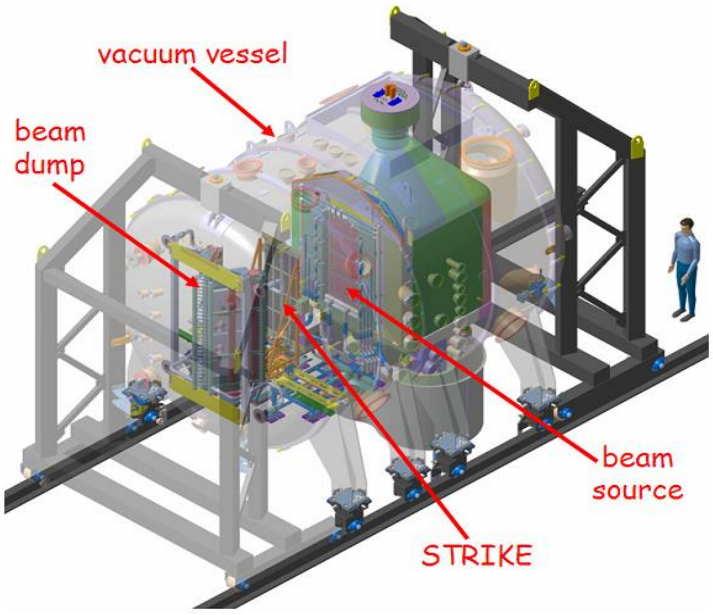

Figure 3-1: Isometric view of the SPIDER experiment with some of the most important components highlighted

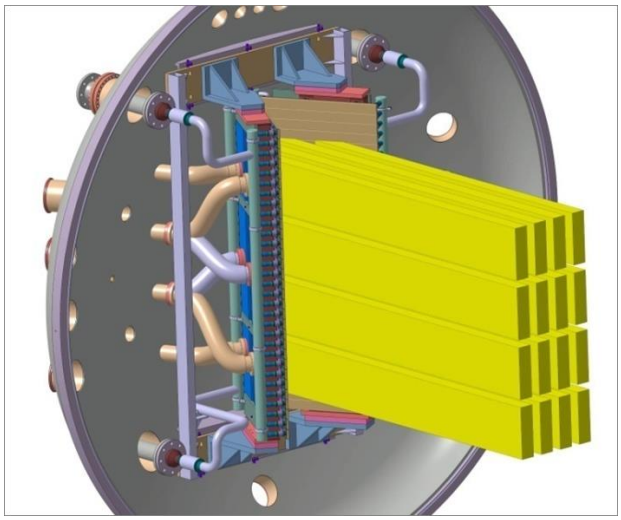

Figure 3-2: The SPIDER beam dump area: the beam (in yellow) impinges on the beam dump surface with an incident angle of 60°

The SPIDER beam is composed of 1280 beamlets (corresponding to the holes present in the grids of the extraction and acceleration stages) arranged in 16 groups, each made of 80 beamlets in a matrix arrangement of 5 (horizontal) × 16 (vertical). The circular beamlet footprint on the beam dump surface becomes an ellipse whose major (horizontal) and minor (vertical) axis are 40 mm and 22 mm respectively. The power of each beamlet has its maximum at the centre and decays from this point according to a Gaussian distribution. The power density (in MW/m^2) contour plot is shown in Figure 3-3. The beamlet centres start at coordinate (0,0) and are spaced by 40 mm and 22 mm in the horizontal and vertical directions, respectively. The power density profile is maximum at the beamlet centres and minimum halfway between them.

In the beam dump a large amount of neutrons will be produced via fusion reaction between the incoming deuterium beam and the deuterium already implanted in the beam dump ($D(d,n)^3He$ reaction). During this thesis period I took part in the development of a neutron diagnostic system called Close-contact Neutron Emission Surface Mapping (CNESM) that will be installed behind the SPIDER beam dump and will provide the map of neutron emission from the beam dump with a spatial resolution approaching the size of an individual beamlet footprint.

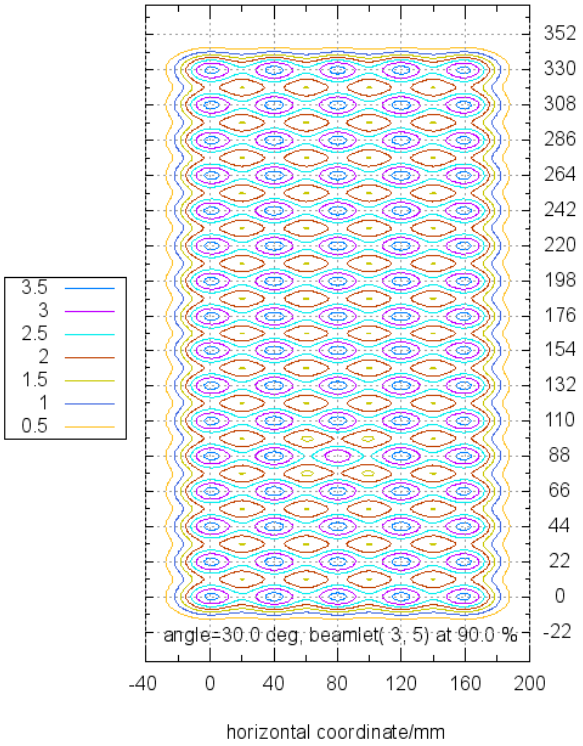

Figure 3-3: Contour plot of the power density profile of a 5X16 beamlets matrix hitting the beam dump. The power density levels are in MW/m^2.

3.2 Neutron production and transport in the SPIDER beam dump

During deuterium operation in SPIDER, the beam current of 40 A is spread out over a surface of about 1 m^2 for a reference average current density of 40 A/m^2 and deuterium flux of 2.5 · 10^{20}D/m^2·s. The expected neutron production for 100 keV deuterons on saturated copper alloy is about 3 · 10^{10}n/As [55]. This gives a total neutron production per SPIDER pulse (lasting 3600 s) of about 4 · 10^{15} neutrons. The aim of CNESM diagnostic system is the reconstruction of the deuterium beam profile from the detection of the neutron beam profile produced in the beam dump via the D(d,n)^{3}He fusion reaction between the incoming deuterium beam and the deuterium adsorbed in the beam dump.

The fundamental relation that describes the neutron production on the SPIDER beam dump can be written as:

$$y(x,y,z) = \phi(x,y,z) \cdot \sigma \cdot n_d \qquad \text{Eq 3.1}$$

Where $y(x,y,z)$ is the neutron yield at a given (x,y,z) position, $\phi(x,y,z)$ is the deuterium flux impinging on the beam dump surface, σ is the D(d,n)^{3}He fusion cross section and n_d is the concentration of the deuterons implanted on the beam dump. From this relation it's clear that, in order to obtain the deuterium flux profile $\phi(x,y,z)$ from $y(x,y,z)$, one must know the profile of the cross section σ and of the deuterium density n_d. These profiles were evaluated through a series of simulations described in [54].

The deuterium implantation profile in the beam dump was evaluated by using the TRIM (Transport of Ions in Matter) [56] code. When the energetic ions hit the beam dump, they can loss their energy mainly in two ways:

- Inelastic collisions with the electrons, where energy is lost but the direction of motion is not changed (ionization loss). This is the main channel of energy loss for the incident ions.
- Elastic collisions with solid nuclei, where both energy and direction of motion are changed. In this case the energetic deuteron transfers part of its energy to the nuclei of the target material (the beam dump). If the target atom retains enough energy it will leave the lattice site and will continue to loose energy as the incident ions (creation of Frenkel pair). If the imparted energy is less than the displacement energy, the target atoms return to the original site by losing their energy by lattice vibrations (energy loss by phonons).

About the 97% of the ions energy is lost by collisions with electrons, 2.9% is lost through phonon energy loss and about 0.1% is lost by elastic collisions from ions or displaced target atoms.
Figure 3-4 shows the ionization energy loss of the incident ions and of the recoiling atoms as a function of the target depth. As one can see, all the deuterons are stopped in the first 0.8 μm of the beam dump surface.

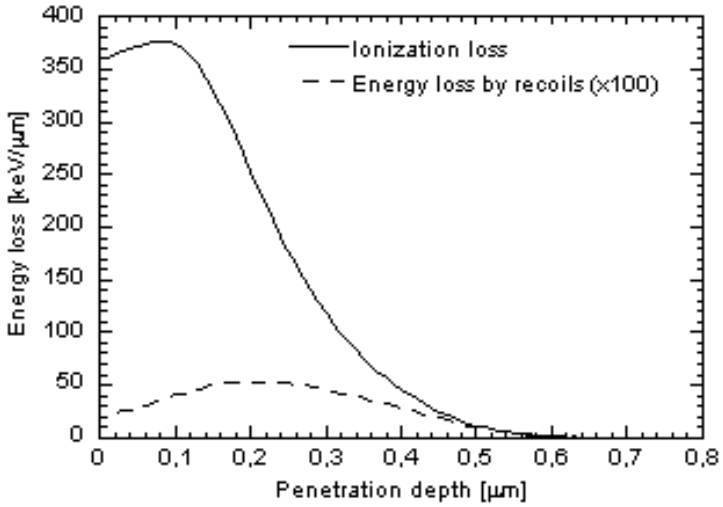

Figure 3-4: Ionization energy loss of deuterium ions vs penetration depth. Also shown is the energy loss due to recoiling target atoms (x100)

Even if the energy loss by recoiling nuclei plays a marginal role in the energy deposition process, it is the main contributor to the deuterium concentration n_d. In fact, during the slowing down of the incident ion, each nuclear collision will transfer energy to the target atoms. At sufficiently high energy transfer, the primary knock-on atom may create a collision cascade and further material defects. This leads to the production of Frenkel-Pairs, i.e. vacancies and interstitials that do not recombine. A vacancy in the target material lattice represents a "trap" for the incoming deuterium ion. In this situation the diffusivity of the implanted deuterium is small, and this leads to a deuterium concentration on the beam dump surface that grows with increasing the deuterium fluence. Clearly the material cannot accommodate an arbitrarily high concentration of implants. There is experimental evidence of release of the implanted gas over a certain value of fluence [57] that leads to a maximum deuterium concentration on the beam dump surface equal to 20% (atomic fraction, i.e. number of deposited deuterium atoms per solid atom). The deuterium concentration as a function of the penetration depth for different irradiation time is shown in Figure 3-5: after 200 seconds of irradiation, the profile is fully saturated up to a penetration depth of 0.7 µm.

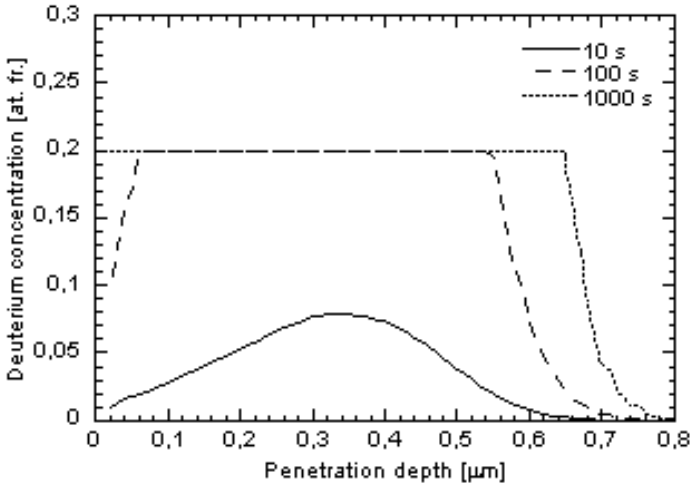

Figure 3-5: Deuterium concentration profile for different irradiation times.

Figure 3-6 shows the fusion cross section σ as a function of deuterium energy.

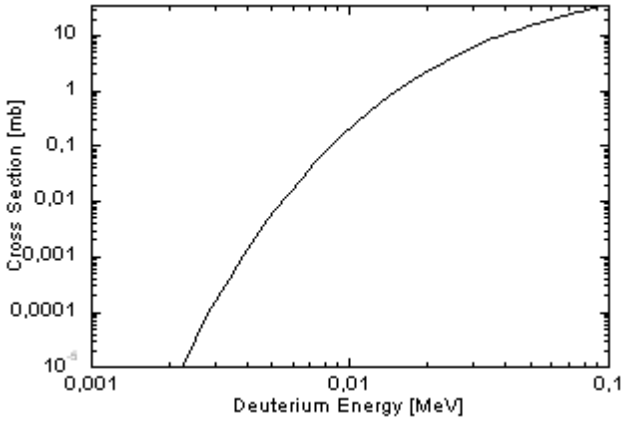

Figure 3-6: Cross Section for the $D(d,n)^3He$ reaction as function of deuterium energy

The neutron emissivity can now be calculated as a function of the penetration depth using Eq 3.1. Figure 3-7 shows the neutron emissivity as a function of the penetration depth for different irradiation times. For low irradiation times (< 30 s) the saturation is not reached and there is no saturation point in the neutron emission profile. For longer irradiation times the neutron emission saturation occurs when the deuterium concentration profile reaches the value of 20% at. fr. Considering an irradiation time greater than 200 s, the deuterium concentration is saturated up to 0.7 µm and the

neutron emissivity is fully saturated over most of the profile. This means that after this irradiation time the neutron emissivity is only dependent on the deuterium beam intensity.

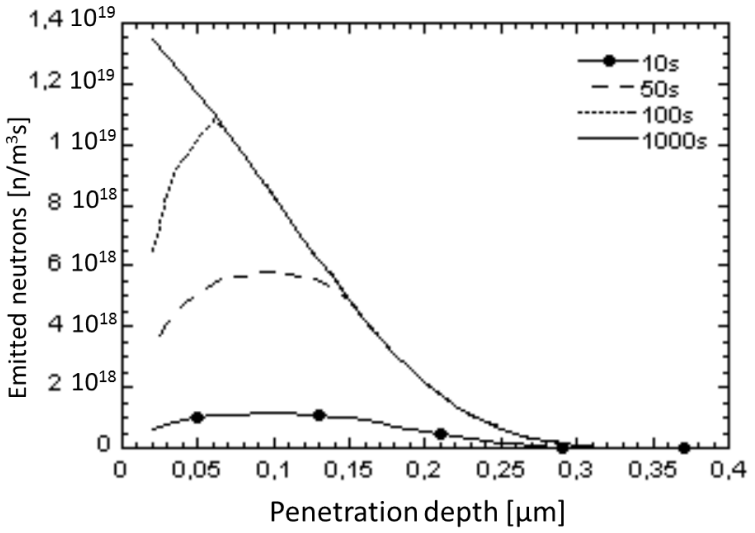

Figure 3-7: Neutron emission profile as a function of penetration depth (z) after different irradiation times.

Eq. 3.1 can be integrated along the penetration depth to give the neutron brightness of the source:

$$b = \phi \int \sigma * nd\, dz \qquad \text{Eq. 3-1}$$

The neutron brightness b (in units of n/m^2s) as a function of the irradiation time is shown in Figure 3-8. It features a linear growth lasting for about 50 s followed by an asymptotic approach to a saturation value of $1.4 \cdot 10^{12}$ n/m^2s. At times longer than 200 seconds, the brightness is fully saturated. The neutron brightness reported in Figure 3-8 is representative of the peak value reached at the centre of the deuterium beamlet footprint (the point with the highest deuterium flux). The brightness will rise more slowly at the footprint boundary, reaching a lower saturation value in proportion to the local deuteron flux. This means that when the saturation value is reached, the neutron brightness map is also a map of the beam intensity, so by measuring the neutron intensity map is possible to obtain the deuterium intensity map.

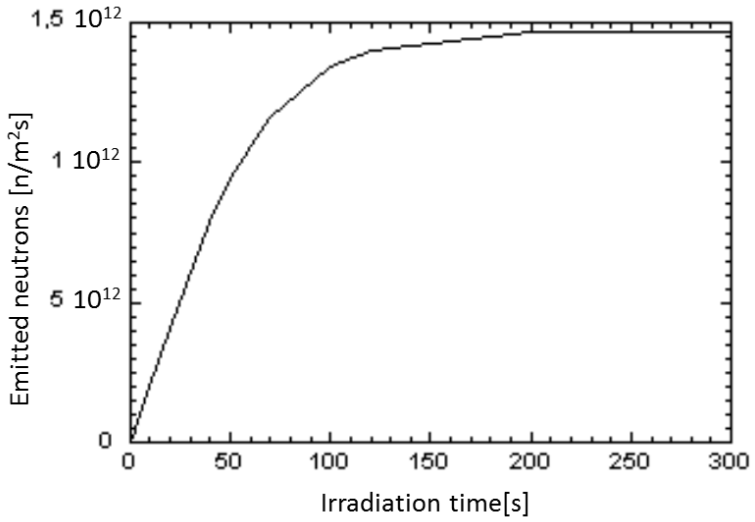

Figure 3-8: Neutron emission rate as a function of the irradiation time.

The results of the simulations carried out have shown a clear relationship between the produced neutrons and the impinging deuterium flux on the beam dump. However, as shown in Figure 3-7, neutrons are produced on the beam dump surface, while the detection position is on the rear side of the beam dump, which has a thickness of about 20 mm. This means that the emitted neutrons must cross the dump in order to be detected on the back side, and in this process a fraction of the neutrons are scattered. Moreover, neutrons are emitted isotropically (there is a small anisotropy due to the deuterium ions energy that can be here considered negligible). Thus, the neutron emission due to a single beamlet on the beam dump surface produces an intensity distribution on the detector surface (placed at 35 mm from the emission plane) as the one shown in Figure 3-9: the intensity profiles along the x and z directions are shown in Figure 3-10 and Figure 3-11 respectively. As one can see, the intensity distribution has a FWHM (Full Width Half Maximum) of about 60 mm along the z direction, and of about 80 mm along the x direction. This means that the fraction of neutrons scattered by the beam dump structure and the isotropic emission of the neutrons on the beam dump surface lead to the degradation of the space resolution of the detector. This degradation increases with the distance of the detection point from the emission point and, as a consequence, the detector must be installed as close as possible to the emission surface.

We can now simulate the intensity recorded at the detector position due to the neutron emission of a group of 80 beamlets (the array of beamlets shown in Figure 3-3). The result of this simulation is shown in Figure 3-12.

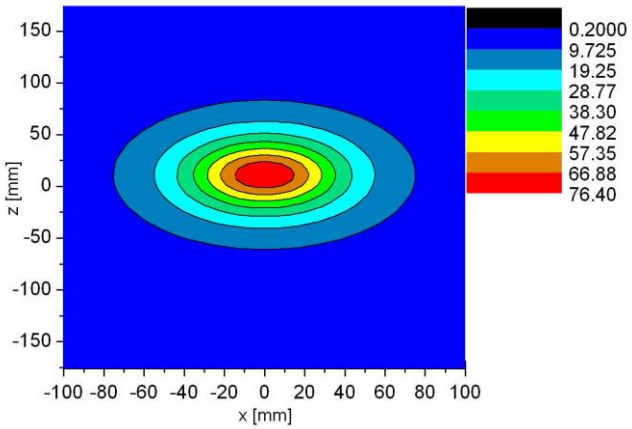

Figure 3-9: Contour plot of the neutron intensity on the detector surface due to a single beamlet centred at the coordinate origin. The intensity is in m^{-2}.

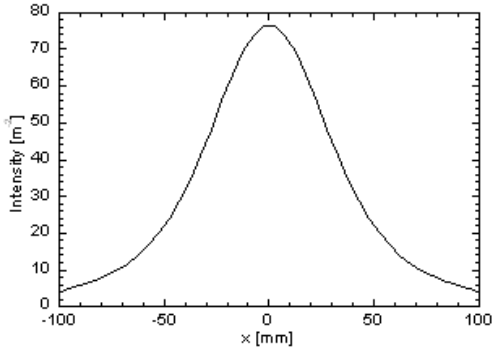

Figure 3-10: Neutron intensity profile along the x direction for z=0. Data from Figure 3-9.

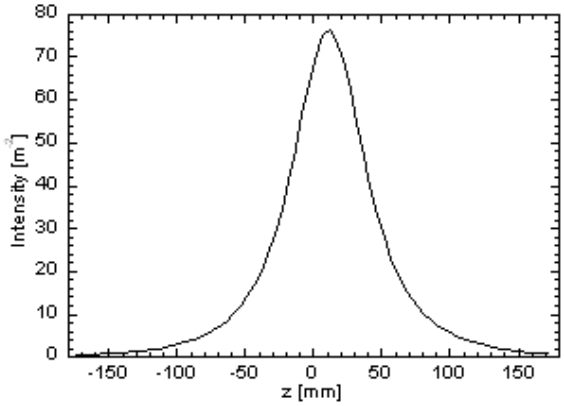

Figure 3-11: Neutron intensity profile along the z direction for x=0. Data from Figure 3-9.

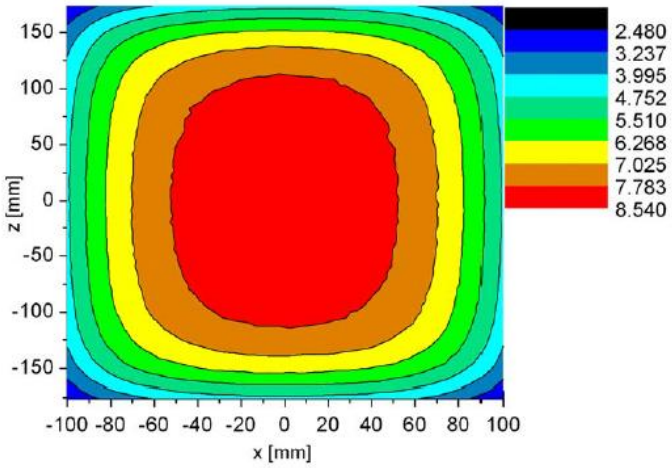

Figure 3-12: Contour plot of the neutron intensity on the detector surface due to a group of 5 x 16 beamlets. The intensity is in m^{-2}.

If we now compare the normalized intensities (considering the area of the respective sources) of the intensities profiles along the x detection for z=0 of Figure 3-12 and of Figure 3-9, we obtain the plot shown in Figure 3-13.

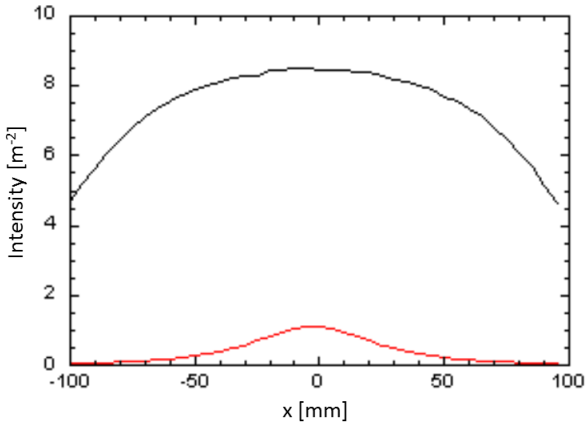

Figure 3-13: Neutron intensity on the detector surface due to a single beamlet (red line) and to a group of 5x16 beamlets (black line). The intensity is in m^{-2}.

The graph of Figure 3-13 tells us that about the 10% of the intensity is due to the beamlet facing the detection point. The remaining 90% is due to the integrated intensity from the other 79 beamlets.

Of course in this situation it is not possible to distinguish between the neutron emission of the different beamlets, so the detector must be able to discriminate neutrons respect to their incidence angle in order to improve the spatial resolution and to give information about the single beamlet of a group.

3.3 The nGEM detector of the CNESM diagnostic system

In the last paragraph it has been shown that the detector component of the CNESM diagnostic system must present the following proprieties:

- Minimization of the distance between the detection point and the neutron emission point.
- Directionality discrimination in order to improve the space resolution of the detector.

These proprieties can be achieved by using a tripleGEM equipped with a plastic converter foil, where neutrons coming from the beam dump are converted into protons by elastic recoil, coupled with an Al plate that acts also as cathode for the detector. As said in par 1.3.2, the energy of the recoiled proton after the n-p reaction is equal to:

$$E_p = E_n \cos^2 \vartheta_{n-p} \qquad \text{Eq. 3-2}$$

Where E_p is the energy of the recoiled proton, E_n is the energy of the neutron and ϑ_{n-p} is the recoiling angle. In order to obtain a neutron emission map representative of the deuterium beam uniformity, the signal read on a nGEM pad must be due to neutrons emitted from the corresponding 40×22 mm^2 beamlet footprint on the dump front surface and this can be obtained only if we can select neutrons impinging the cathode surface with an incident angle smaller than 45°.

Figure 3-14 shows how this can be achieved by adding an Al foil of suitable thickness between the n-p converter (in the schematic a CH_2 layer) and the tripleGEM drift gap region. The recoiled protons produced by elastic scattering of 2.5 MeV neutrons have an energy ranging from 1.77 MeV (for ϑ_{n-p}=45°, p_b and p_d in Figure 3-14) up to 2.5 MeV (for ϑ_{n-p}=0°, p_a and p_c in Figure 3-14). The range of a 2.5 MeV proton in aluminium is equal to 60 µm, so for the reference case of Figure 3-14 and an Al layer thickness of 50 µm, only the proton p_a can cross the Al layer retaining enough energy for the ionization of the gas in the drift region. The proton emitted at 45° (p_b) has an initial energy lower than p_a and its path in the Al layer is increased by a factor $\sqrt{2}$ with respect to the path of p_a. This means that the proton p_b lose all its energy in the Al layer and will not be detected by the tripleGEM. If the neutron impinges the detector surface with an angle of 45° (n_b in Figure 3-14) the proton emitted at ϑ_{n-p}=0° (p_c) has an initial

energy of 2.5 MeV, but it has to travel for a long path inside the Al layer and therefore it is stopped. If the proton is emitted at ϑ_{n-p}=45° (p_d), the path in the Al layer is shorter but its initial energy is lower and the proton is not able to reach the gas region.

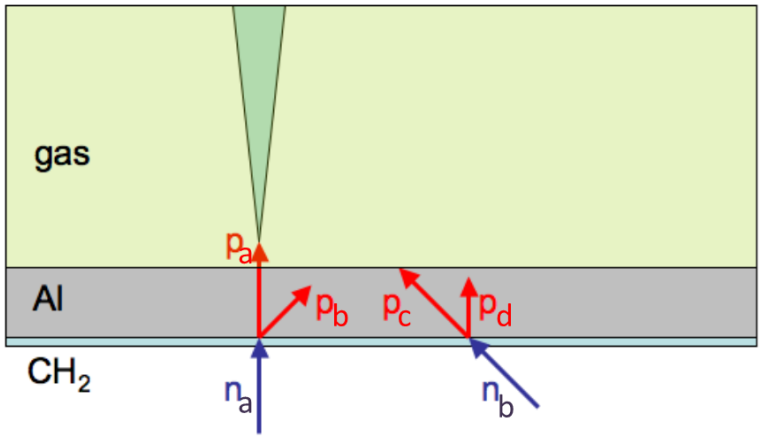

Figure 3-14: Schematic of the detection principle: al Al layer (grey) is used to suppress detection of neutrons with oblique incidence. Only one of the four protons in the figure can cross the Al layer ionize the gas in the tripleGEM drift region.

This simple analysis shows that the detection of neutrons hitting the nGEM with a large incidence angle can be suppressed using an opportune Al-foil thickness. This analysis is confirmed by the graph of Figure 3-15, on which it is reported the energy deposited in the gas region as function of different neutron incident angles ϑ_n: as one can see, only neutrons hitting the detector with an incidence angle lower than 40° can be detected by the tripleGEM, while neutrons with an incidence angle higher than 40° cannot be detected.

Simulation of Figure 3-9 was then repeated in order to check the effective improvement of the detector spatial resolution. Figure 3-16 shows the normalized neutron intensity profile along the x direction for the case without the Al foil (plot of Figure 3-10, dashed line in Figure 3-16) and with the Al foil (continuous line in Figure 3-16). As you can see the FWHM of the detector response for the neutron emission of a single SPIDER beamlet is about 30 mm with the Al foil, showing a clear improvement in terms of detector spatial resolution that is now approaching the SPIDER beamlet size.

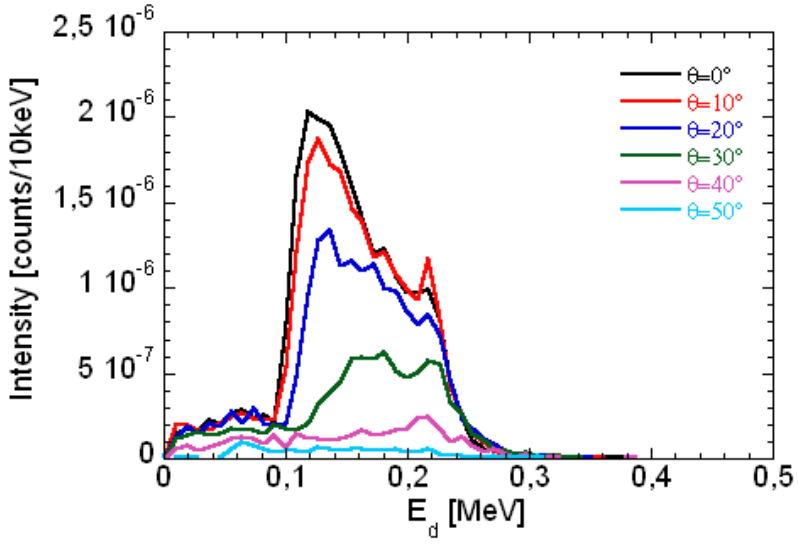

Figure 3-15: Simulated distribution of proton energy deposition inside the nGEM gas for different neutron incident angles ϑn. The thickness of the Al foil was t=50 µm.

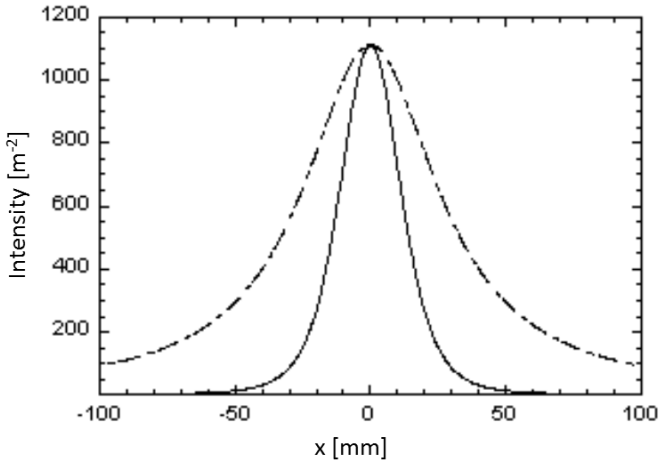

Figure 3-16: Neutron intensity profile along the x direction calculated when a single beamlet is impinging on the beam dump surface (detector surface at 30 mm from the emission plane) without the Al layer (dashed line) and with the Al layer (continuous line).

3.4 Construction of the nGEM detector for the CNESM diagnostic system

The nGEM detector for the CNESM diagnostic system was produced following the criteria found in par 3.3. The detector has an active area of 32.5 x 20 cm^2: this area is needed to detect neutrons coming from one of the 5x16 beamlets group of the SPIDER deuterium beam. The converter cathode is composed of a polypropylene (CH_3) foil

(2mm thick) followed by an aluminium layer 50 µm thick. The detector is composed of the converter cathode, a drift region 4mm thick, the first GEM foil, a transfer region 2 mm thick, the second GEM foil, the second transfer region (2 mm thick), the third GEM foil, the induction region (2 mm thick) and finally the padded readout anode. The readout anode (shown in Figure 3-17) is composed of 256 channels that are connected to the front end electronics. The size of each pad is 22x13 mm^2. The front-end chip used to readout all the pads are the CARIOCA-GEM digital chips. All CARIOCAs are connected to a custom-made FPGA Mother Board [33] that analyses the LVDS signal coming from the chips. The high voltage configuration was generated using the HVGEM NIM module [34] and the potentials were applied to each electrode by means of passive resistive-capacitive filters properly designed for a TripleGEM detector.

Figure 3-17: The padded readout anode of the nGEM detector

The detector is assembled as following:

- Stretching of all the GEM foil by using the custom made device (Figure 3-18)
- Gluing of the GEM frame while keeping the GEM foil in tension (Figure 3-19)
- Assembly of the detector by stacking all the component (Figure 3-20)
- The detector is finished when the padded anode is glued to the frame of the last GEM foil (Figure 3-21)

The last phases of the detector construction consisted in the soldering of the GEM foils HV terminals to the HV pads where there are connectors used to deliver the voltages produced by the HV-GEM NIM module; finally, the gas inlet and outlet connectors and pipes were glued to the assembled detector. Figure 3-22 shows the nGEM for the

CNESM diagnostic system fully assembled together with the HV connectors and the gas pipes.

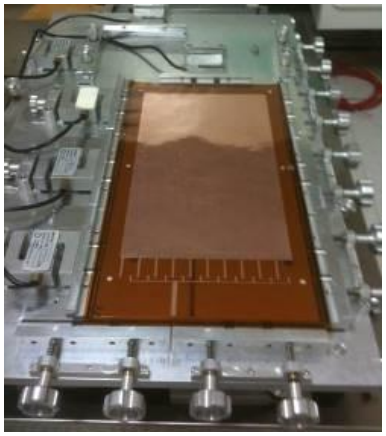

Figure 3-18: Stretching operation of the GEM foil

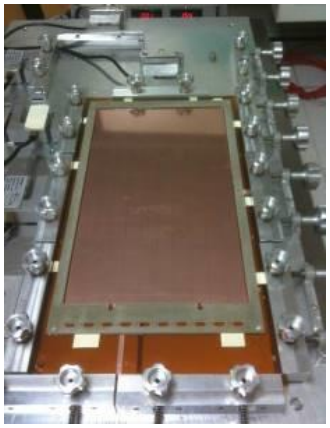

Figure 3-19: Gluing of the frames to the foils while keeping the tension

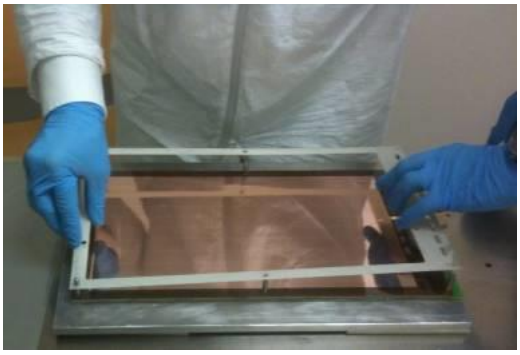

Figure 3-20: Assembly of the detector: the components are stacked together.

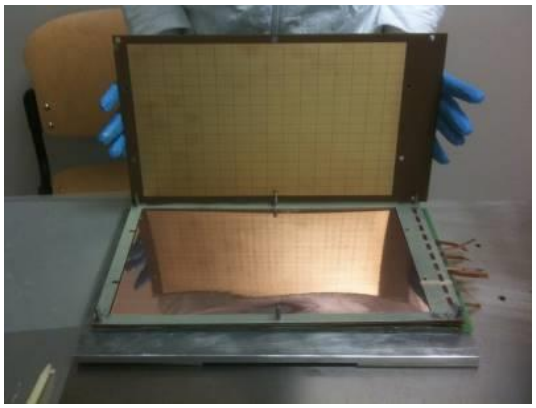

Figure 3-21: The last phase of the assembly, when the padded anode is glued to the full detector structure.

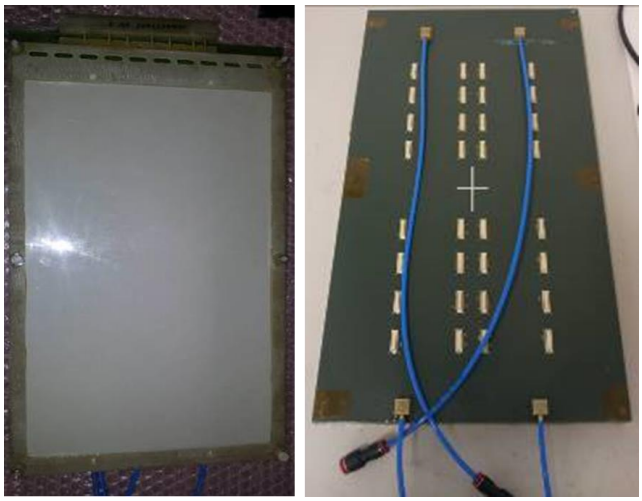

Figure 3-22: Front view (left panel) and rear view (right panel) of the nGEM detector for the CNESM diagnostic system

3.5 Test of the nGEM detector with neutrons

After the assembly, the detector was tested with neutrons at the ROTAX [58] beam line (at ISIS) in order to test the uniformity of the detector response, the stability and the gamma sensitivity. A second test was performed at the Frascati Neutron Generator (FNG) [59] in order to test the directionality response of the detector with a 2.5 MeV neutron beam.

3.5.1 Test of the nGEM detector at the ROTAX beam line

Figure 3-23 shows a picture of the nGEM installed inside the ROTAX beam-line. The ROTAX beam profile widths $FWHM_x$ and $FWHM_y$ are in a range between approximately 30 mm and 40 mm respectively. The nGEM was placed in the direct beam, exiting a methane moderator at 95 K, at a distance of 15.5 m from it. The neutron energy (E_n)

spectrum is known to feature a peak at about 10 meV and a $1/E_n$ tail in the epithermal/fast-neutron region, as shown in Figure 3-24 . The fraction of neutrons with energy between 2 and 3 MeV is about 1.6% of the total amount of neutrons.

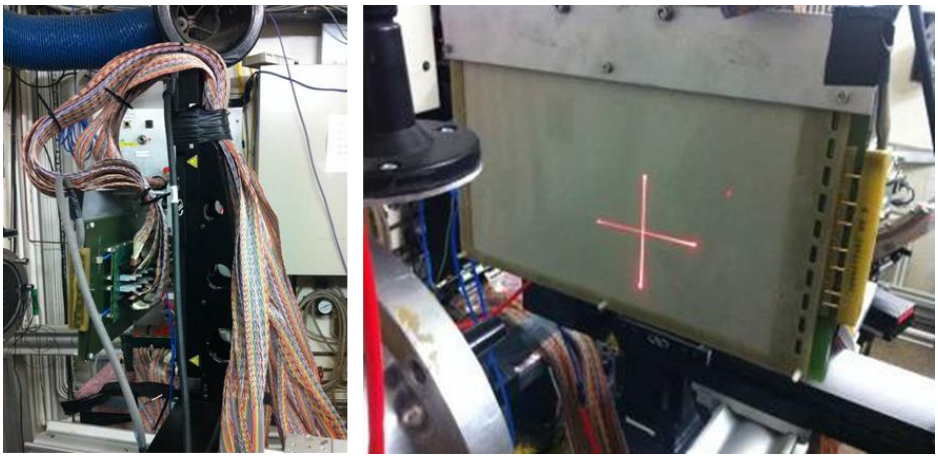

Figure 3-23: Pictures of the nGEM installed inside the ROTAX beam-line. Right picture shows the beam alignment procedure.

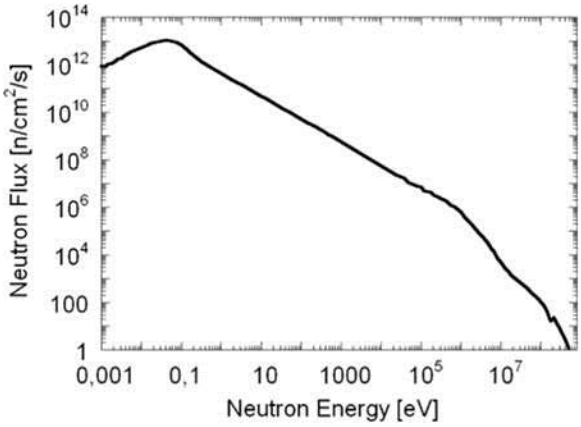

Figure 3-24: The ROTAX neutron spectrum

A total of 16 Carioca cards (32 Carioca chips) have been used to read-out the full detector. Two FPGA motherboards located out of the beam were used contemporarily to acquire the data from all the chips. The detector was mounted on a X-Y positioner, orthogonal to the beam direction, in order to move the beam in different positions on the active area. The gas mixture used for all the measurement is Ar/CO_2 70%/30 with a flow of 5 l/h.

3.5.1.1 Working point determination

The nGEM counting rate was measured as a function of the effective gain by varying the sum of voltage drops across the three GEM foils ($\Sigma\Delta V_{GEM}=V_{GEM}$). Two different

measurements were performed, scanning the high voltage V_{GEM} when the neutron beam was on and off. The former is a measurement of the neutron counting rate while the latter provides the counting rate for photons coming from surrounding activated materials. The results of these measurements are shown in Figure 3-25. As expected, the detector is insensitive to gamma rays at V_{GEM} less than 900 V: for V_{GEM}=900 V the gamma rays counting rate on the whole detector is about 0.1 Hz while the neutron counting rate in excess of 100 Hz). The γ rays are detected only for V_{GEM} >900 V; a V_{GEM} value of 870 V was thus chosen as the working point for all the subsequent measurements. The values of the external fields used for all the subsequent measurements were E_d (electric field in the drift gap)=0.75 kV/cm, E_{T1} (electric field in the transfer 1 gap)=1.5 kV/cm, E_{T2} (electric field in the transfer 2 gap)=3 kV/cm and E_I (electric field in the induction gap)=4 kV/cm.

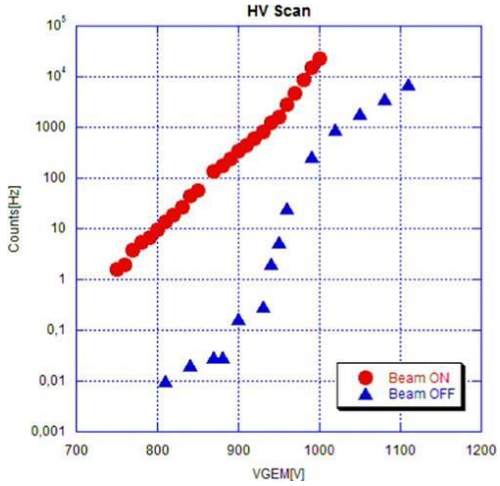

Figure 3-25: nGEM counting rate as a function of VGEM (applied voltage) when the beam was on (neutrons – red squares) and off (gamma rays – blue triangles).

3.5.1.2 Beam profile reconstruction and counting rate uniformity

Using the detector electrical settings determined in the previous paragraph, a high-statistics beam profile measurement was performed (Figure 3-26). The measured $FWHM_x$=41.1 mm and $FWHM_y$=34.1 mm are compatible with the technical specifications of the beam.

The measurement of the detector response uniformity was performed by scanning the beam over the entire detector active area apart from two rows of pads at top and

bottom, because the used X–Y positioner 30 cm maximum excursion does not cover the full detector height. A total of 192 neutron beam profiles (the number of PADs that we can irradiate with this positioner) were acquired for each x–y position and the scan was performed with steps along the x direction (Stepx)=22 mm (the x-dimension of the pad) and with steps along the y direction (Stepy)=13 mm (the y-dimension of the pad). In this way the detector response was checked pad by pad. The 192 profiles were all summed together giving a matrix of 192 elements. The average counting rate of the nGEM was determined by averaging the 192 counting rates per pad. The level of non-uniformity (per pad) was calculated by dividing the actual counting rate of each pad by the average counting rate. The resulting uniformity map is shown in Figure 3-27. In order to evaluate the uniformity of the detector (in terms of deviation from the average), an histogram of the uniformity was calculated. This histogram (shown in Figure 3-28) has a bin size of 0.05 and can be fitted by a Gaussian function. The HWHM (Half Width Half Maximum)= 0.12 is a measurement of the non-uniformity of the detector with respect to the average. This means that more than 70% of the pads have a non-uniformity lower than 12% with respect to the average.

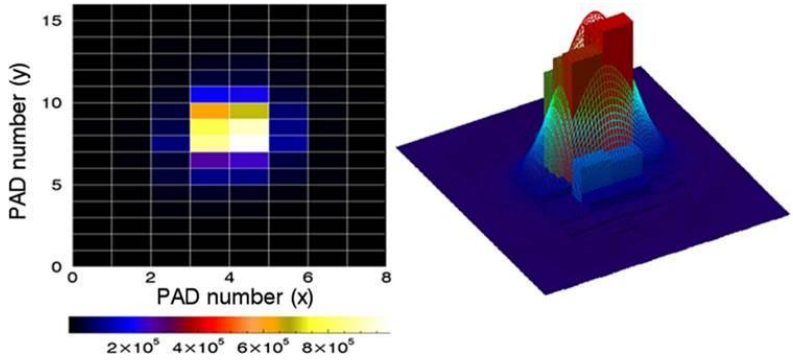

Figure 3-26: Neutron beam profile reconstruction

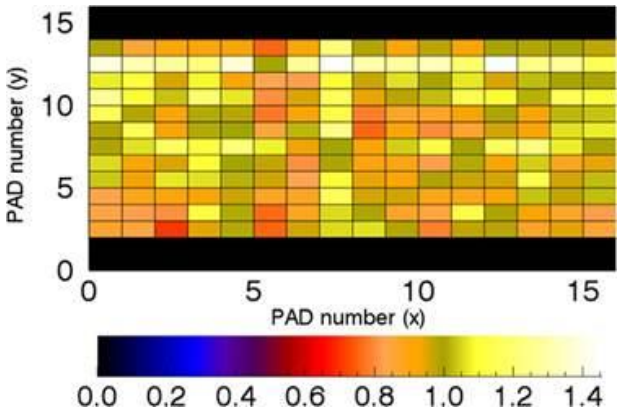

Figure 3-27: the nGEM uniformity map.

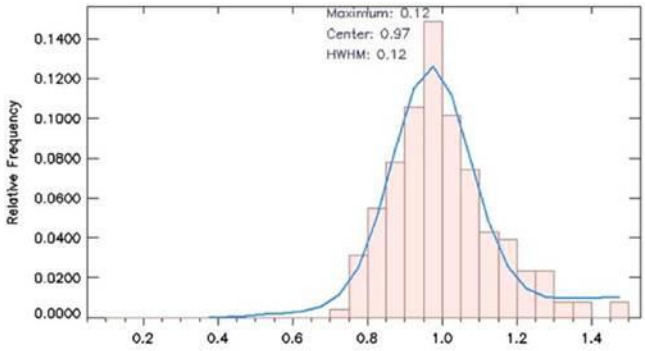

Figure 3-28: Histogram of nGEM uniformity

3.5.1.3 Stability of the detector

An important feature that the beam profile monitor for the CNESM system must possess is the stability in time. Many factors including charge accumulation or the variation of atmospheric parameters can influence the behaviour of the detector. In order to study the stability, the detector was irradiated in a single position for several hours and the counting rate was recorded. The counting rate was also compared to the beam current in order to prove that there is a correlation between the nGEM counting rate and the ISIS beam current. Since the FPGAs were located outside the neutron beam, they were able to run for several hours without experiencing any error due to radiation. Figure 3-29 shows the nGEM counting rate as well as the ISIS proton beam current during the irradiation.

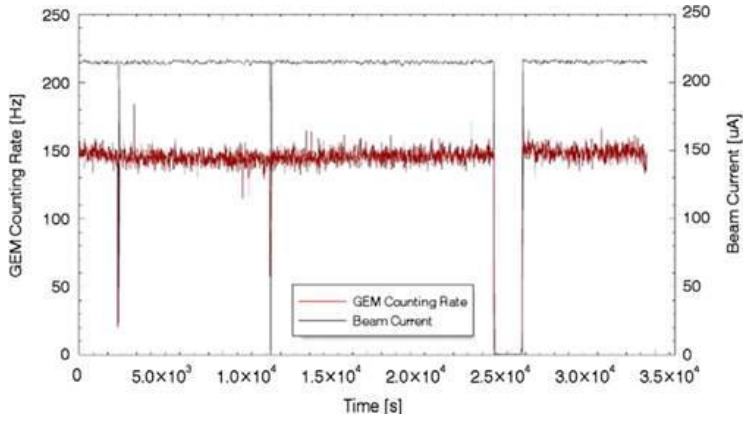

Figure 3-29: nGEM counting rate as a function of time (stability in time) compared to the ISIS beam current.

Figure 3-30 shows the histogram of the recorded counting rate, with a bin size equal to 1 s: the sigma of the fitted Gaussian divided by the most probable counting rate gives a measurement of the nGEM detector stability in time. A value of about 8% has been measured. This value is adequate for the operation of the CNESM diagnostic system (where it is required that the detector must present a non-stability factor lower than 10%), but it can be further improved by introducing an active control of the detector gain as a function of the gas temperature, humidity and pressure. This control is foreseen during the SPIDER operation.

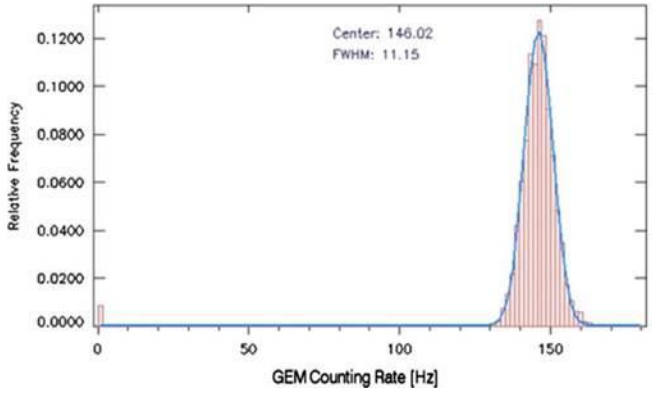

Figure 3-30: Histogram of nGEM counting rate

3.5.1.4 SPIDER-like analysis

During the tests, a series of measurements were taken in order to “reproduce” the SPIDER neutron emission from the beam dump surface. The SPIDER-like neutron emission was obtained by taking a series of 2(x) x 3(y) beam images spaced by 40 mm (x) and 22 mm (y) (the beamlets spacing expected in SPIDER) by moving the beam. The six beam images were than summed in order to obtain a resulting image similar to the

one expected in SPIDER for the neutron emission due to 6 adjacent beamlets impinging on the beam dump. The six images of the beam in different positions are reported in Figure 3-31, while the resulting SPIDER-like image is reported in Figure 3-32.

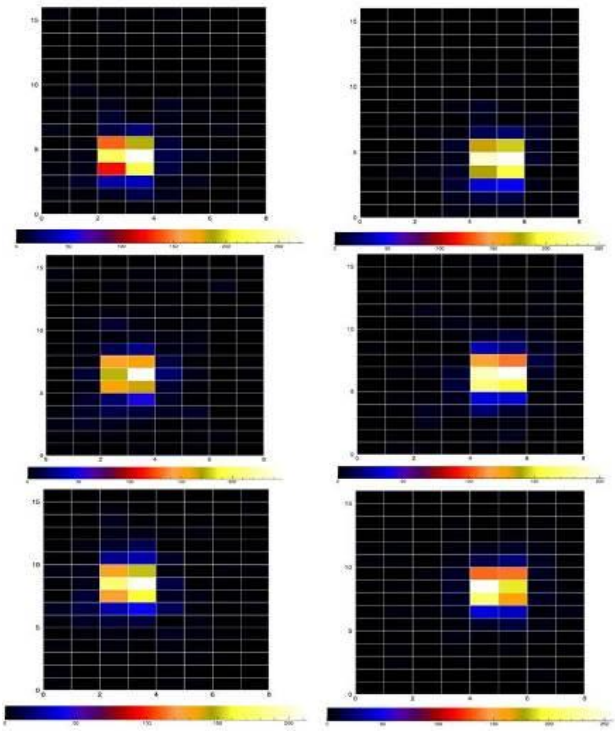

Figure 3-31: The six beam images. The distance between the beams is 22 mm (y) and 40 mm (x). Beam enumeration: (top left: beam 0); (top right: beam 1); (mid left beam 4); (mid right beam 5); (bottom left beam 2); (bottom right beam 3)

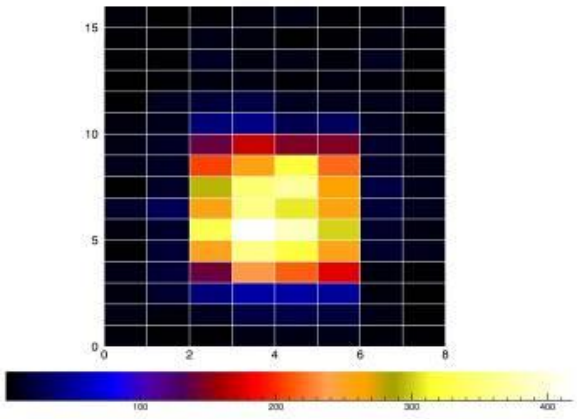

Figure 3-32: The resulting SPIDER-like image.

In this analysis we have a worse situation than in SPIDER, given that the FWHM of the single “beamlet” in the ROTAX beam line is bigger than the beamlet of SPIDER. In

ROTAX the beam has a FWHMx = 47.6 mm and a FWHMy = 37,7 mm a while in SPIDER the expected detected signal due to a single beamlet has a FWHMx of about 30 mm and FWHMy of about 20 mm.

The analysis is made by using an appropriate IDL code that reconstructs the beam profiles by fitting to the data the sum of six bi-gaussian functions using a method that employs the Levenberg-Marquardt technique to solve the least-squares problem:

$$f(x,y) = \sum_{i=0}^{5} a_{0i} \cdot exp\left[-\left(\frac{(x-a_{3i})^2}{2a_{1i}{}^2}\right)-\left(\frac{(y-a_{4i})^2}{2a_{2i}{}^2}\right)\right]$$

Where: a_{0i} is the maximum of the i-th beam, a_{1i} and a_{2i} are the square root of variances along x and y respectively, a_{3i} and a_{4i} are the position of the center along the x and y directions. In the fit procedure the parameters a_{1i} and a_{2i} are fixed to the values found in par. 3.5.1.2, so that a total of 6x3=18 degree of freedom are used in the fit.

The starting parameter values are obtained through a rough analysis of the data, in which by knowing the position of the beams, a set of six maxima and six center coordinates are found. These initial parameters are then passed to the least-squares routine. In order to avoid a solution corresponding to a local minimum, the six maxima are limited between (a_{0i}-0.3a_{0i}) and (a_{0i}+0.3a_{0i}) and the six centers between (a_{3-4i} - 1[pad]) and (a_{3-4i} + 1[pad]). The resulting profile is shown in Figure 3-33, where the lego histogram represents the real data, while the surface represents the fit.

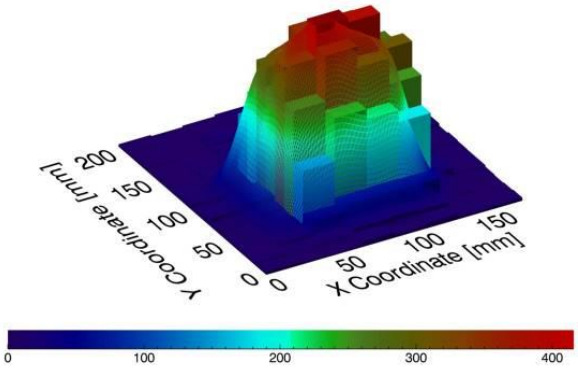

Figure 3-33: Surface plot of the real data (lego) with the fit data (mesh)

Figure 3-34 and Figure 3-35 show the surface plot and the contour plot of the single gaussians reconstructed by the fit.

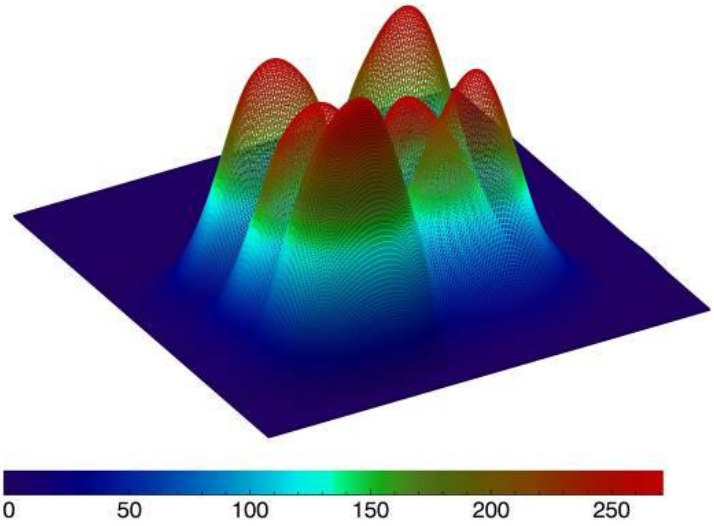

Figure 3-34: Surface plot of the six gaussians resulting from the fit

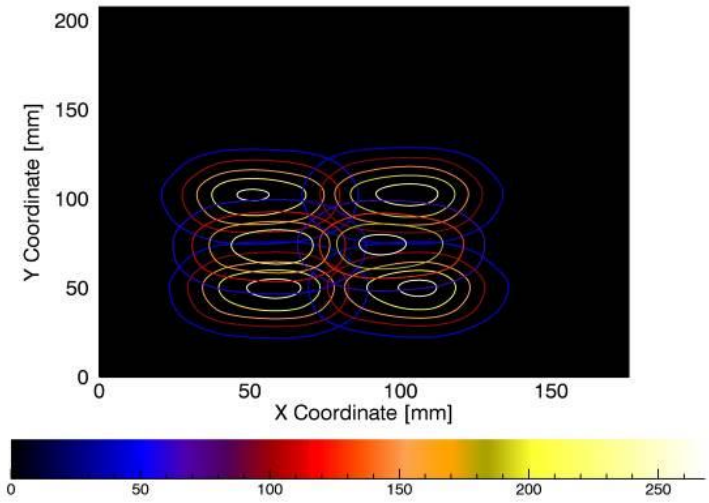

Figure 3-35: Contour plot of the six gaussians resulting from the fit

The detector is able to reconstruct the correct position and the maximum of each beamlet even in a worse condition than the one expected in SPIDER (in ROTAX the "beamlets" are wider than SPIDER): we can conclude that the detector is suitable for reconstructing the SPIDER beam.

3.5.2 Test of the nGEM detector at Frascati Neutron Generator (FNG)

In order to completely qualify the nGEM detector for SPIDER, a directionality measurement has been performed at the Frascati Neutron Generator (FNG).Figure 3-36 shows a picture of the detector installed in the FNG experimental hall in front of the deuterium target, while Figure 3-37 shows a schematic of the experimental setup.

Figure 3-36: Experimental setup at FNG: the second full size prototype was positioned at 18 cm from the target

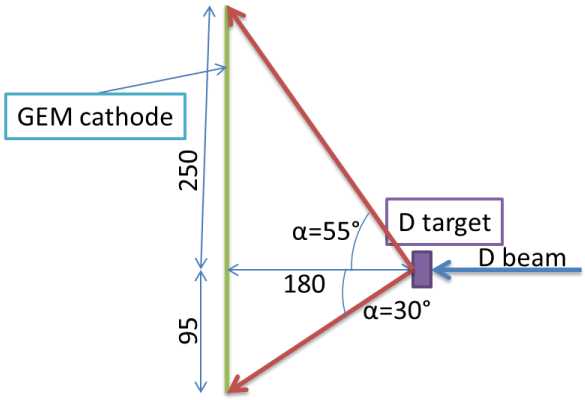

Figure 3-37:Schematic of the Experimental setup at FNG

In order to detect neutrons and to be insensitive to photons, the following electrical configuration was applied to the detector: E_d (Drift Field) = E_{T1} (Transfer 1 Field)= E_{T2} = 3 kV/cm, E_{Ind} (Induction Field) = 5 kV/cm and $\Sigma\Delta V_{GEM}$ = 870 V. This configuration in the Ar/CO_2 70%/30% gas mixture corresponds to an effective gain of about 100. With this gain value γ-rays are completely rejected. Directionality capability of the detector was measured using a 10^7 n/(cm^2· s) flux of 2.5 MeV neutrons. The neutron flux was

continuously monitored by a NE213 scintillator. The detector was aligned with the center of the target of the neutron generator and several PH spectra were acquired in order to measure the detector response for different neutron impinging angle. For PH measurements only one pad (at the center of the detector) out of 256 was read-out using a 142IH Ortec preamplifier, a spectroscopy amplifier and an ADC-MCA.

The detector was then tilted by an angle θ_{GEM} = 10° to 80° (in steps of 10°) with respect to the axis of the neutron generator and a pulse height spectrum was acquired for each detector angle. Each pulse height spectrum was normalized to the total number of neutrons measured by the NE213 monitor (Figure 3-38**)**. Up to a value of θ_{GEM} =20°, no variation in the pulse height shape and area is detectable. On the other hand for values of θ_{GEM} > 30-45°, the counting rate is reduced down to almost zero for θ_{GEM} = 50°. Figure 3-39 shows the comparison for θ_{GEM} = 0° between the MCNPX simulated PH spectra for aluminum thickness of 50 μm and the measured one. The agreement between data and simulation (for a deposited energy higher than 150 keV) is good for the Al thickness considered (50 μm).

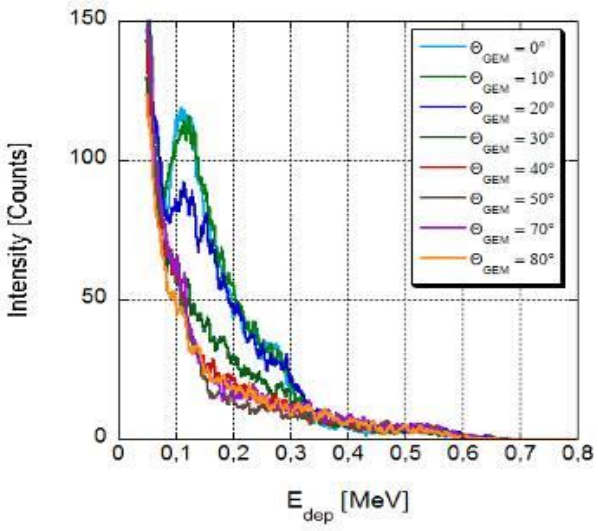

Figure 3-38: Measured PH spectra at different tilt angles with respect to the neutron generator axis.

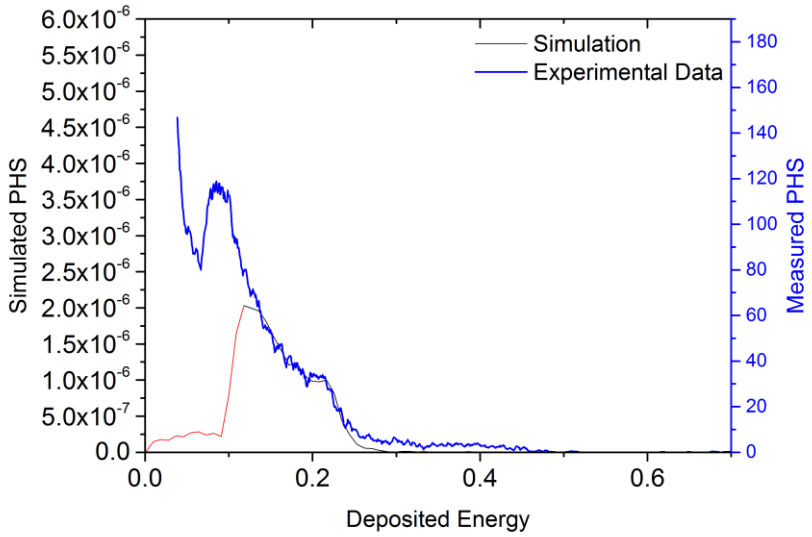

Figure 3-39: Comparison (for Θ_{GEM}=0°) between MCNP simulated energy deposition in the detector with Al thickness = 50 µm and the measured PH spectrum

The PH spectra have been integrated starting from the bin corresponding to a deposited energy of 150 keV. This value has been chosen in order to fully discriminate any possible gamma background component: energy deposition values higher than 150 keV can be due only to fast neutrons since gamma rays (interacting mainly through Compton scattering) usually release less than 100 keV.

Figure 3-40 shows the integrated counts under the PH spectra for the experimental and simulated data.

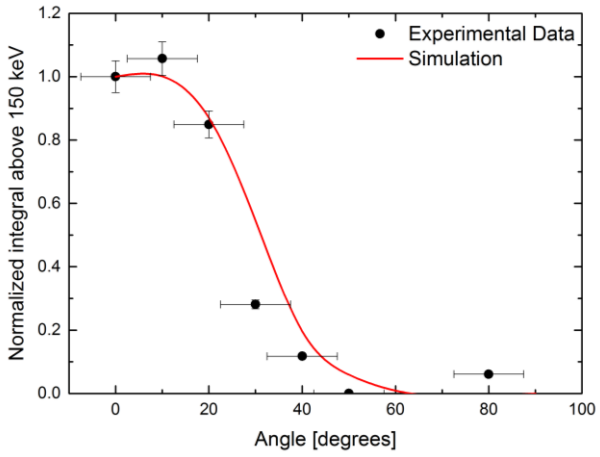

Figure 3-40: Integrated PH area as a function of the tilt angle: comparison between measurements and MCNP simulations (Al thickness = 50 µm)

Data and simulations results have been normalized to 1 at θ_{GEM} = 0°. As predicted by the simulations, the integrated counts start to decrease at tilt angles around 30°.

In addition to the analog measurements, the directionality properties of the detector were tested also with the full digital acquisition system (the one that will be used in SPIDER). Using this setup the full detector (256 channels) was read-out at θ_{GEM} = 0°, while half of the detector (128 channels) was read-out at θ_{GEM} = 40°. Figure 3-41 and Figure 3-42 show the FNG beam profile for these two different measurements. The FNG neutron beam comes from a beam-target interaction and as a consequence it has a 4π solid angle aperture: the nominal neutron intensity on this solid angle is about 10^8 neutrons/s. As one can see from the measurement at θ_{GEM} = 0° the recorded counting rate is maximum for the pads on which the neutron beam is orthogonal to the cathode plane, while it rapidly decreases for the pads on which the incoming neutrons are tilted with respect to the cathode plane. The same situation happens also for θ_{GEM} = 40° where the maximum of the intensity results to be displaced as expected for this tilting angle.

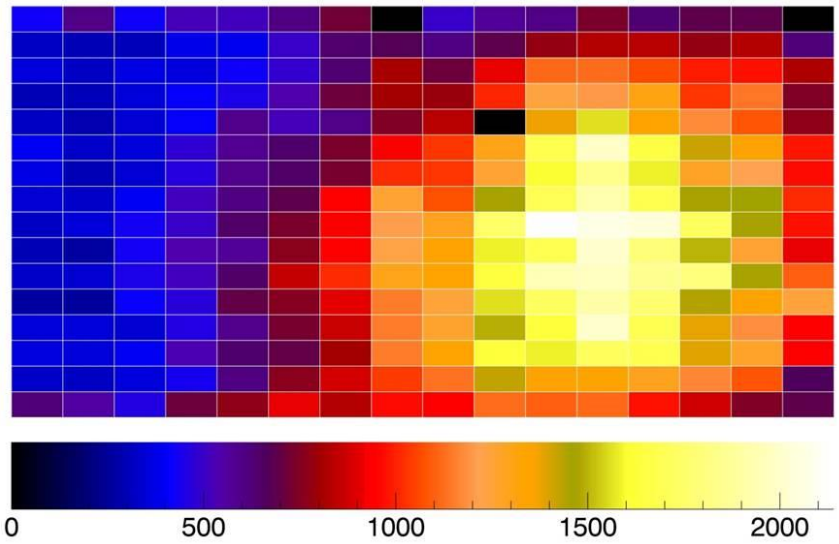

Figure 3-41: Measured FNG beam profile at θ_{GEM} = 0°

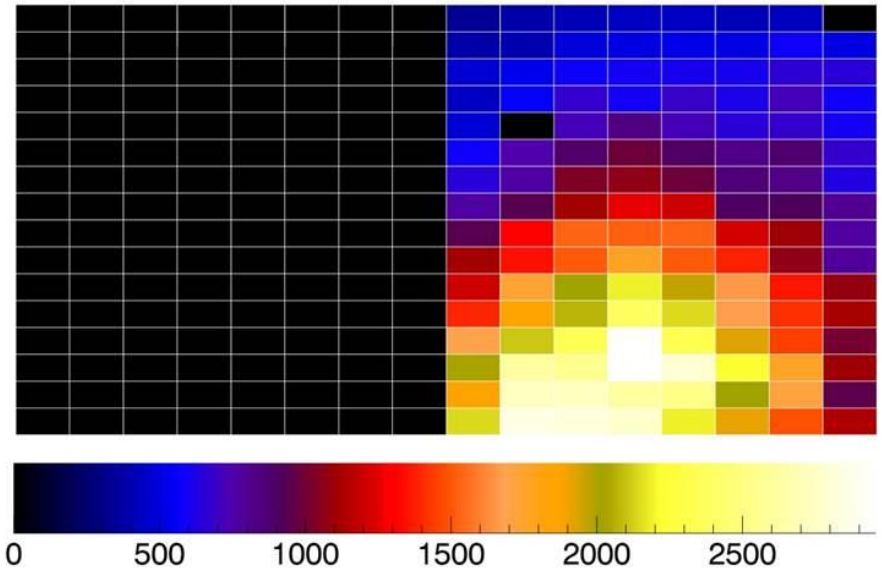

Figure 3-42: Measured FNG beam profile at θ_{GEM} **= 40°**

3.6 Integration of the CNESM diagnostic system with the SPIDER beam dump

As said, the CNESM diagnostic system will be installed on the back side of the SPIDER beam dump, in an ultra-high vacuum environment. Since the nGEM detector operates at room pressure, it will be placed inside a steel containment box (called detector box) connected to the off-vacuum environment outside of the SPIDER vacuum vessel by one flexible pipe (Figure 3-43) used to keep the neutron detector at atmospheric pressure and to provide access for electric cables and for two thin pipelets needed to keep the constant flow of Ar/CO2 gas inside the nGEM detector. The detector box was designed with the possibility to install two nGEM detectors, even if at the beginning of the SPIDER operation only one nGEM will be installed. We have seen in par 3.2 that one of the critical parameters that impact on the spatial resolution of the CNESM diagnostic is the distance between the nGEM detector and the beam dump front surface. The front side of the detector box was then designed in order to minimize this distance, taking into account the steady state load due to the pressure difference between the internal side (1 bar) and the vacuum environment inside the SPIDER vacuum vessel. Mechanical design rules for monotonic type damage have been applied as well as those specified in

the ASME boiler and pressure vessel Code and in the ITER Structural Design Criteria for In-vessel Components [60].

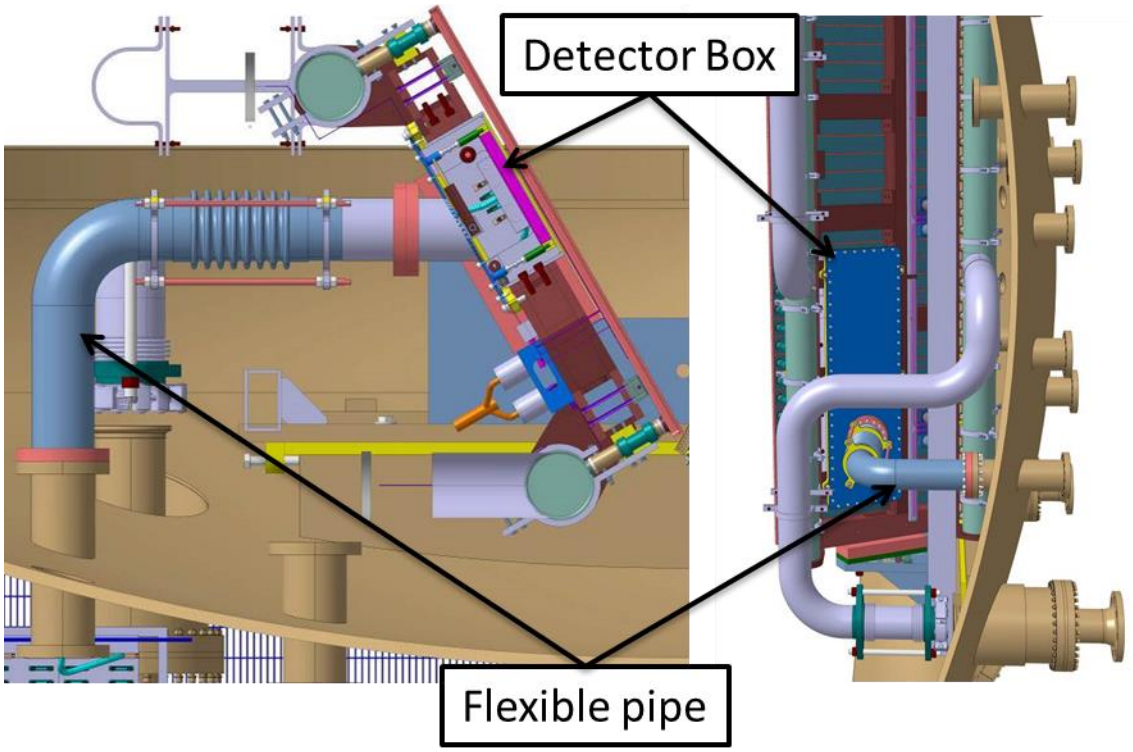

Figure 3-43: Upper view (left panel) and lateral view (right panel) of the detector box installed on the rear side of the SPIDER beam dump

With the geometrical parameters found following the rules reported in [60], a mechanical verification was carried out (using ANSYS) by limiting the local primary stresses to the maximum allowable stress value set at half the AISI 304L material yield stress, which is about 200 MPa [60]. In order to keep the equivalent stress within the set limit, the front side of the detector box was designed with a thickness of 4 mm and with a rib in the middle across the width. The junction between the front side and the lateral walls and between the front side and the rib was designed with a 10 mm radius fillet, in order to improve the stress distribution and to reduce the stress peak present along the rib. The results of the static structural mechanical analysis (reported in Figure 3-44) show that the stress does not exceed the value of 120 MPa, which can be still considered acceptable.

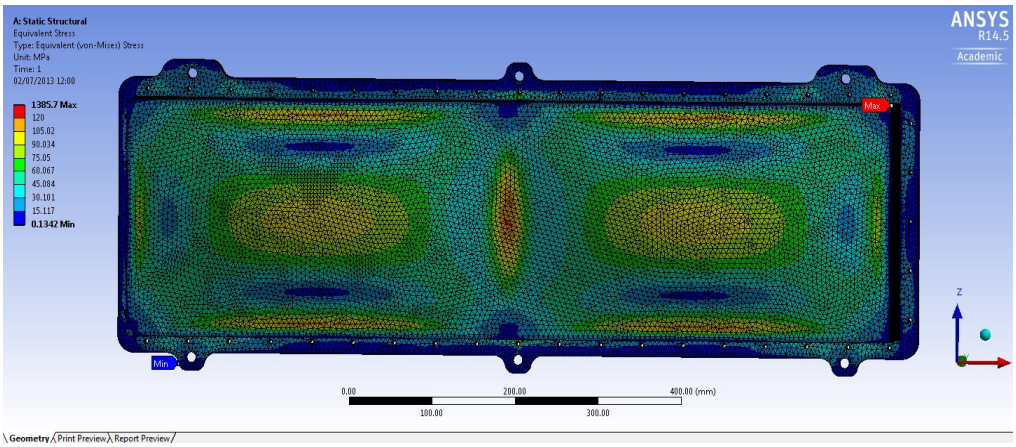

Figure 3-44: Equivalent stress in the front side of the detector box (red=stress exceeds 120 MPa)

The analysis provides also an estimation of the deflection on the front side of the detector box, which must be less than about 2 mm in order to avoid interference with the beam dump back panel face. The maximum deflection on the front side of the detector box was found to be about 1.2 mm (Figure 3-45), a value that can be considered acceptable. Once the design was verified by the static-structural analysis, the detector box was produced. Before the final system installation on the SPIDER beam dump, a series of leak test was carried out in order to verify any possible gas leakage that can afflict the SPIDER operation. The nGEM detector was then installed on the detector box lid (Figure 3-46) and then the lid with the nGEM was closed on the detector box. Subsequently, the entire system was installed inside a large vacuum chamber with the flexible pipe connecting the detector box to the off-vacuum environment.

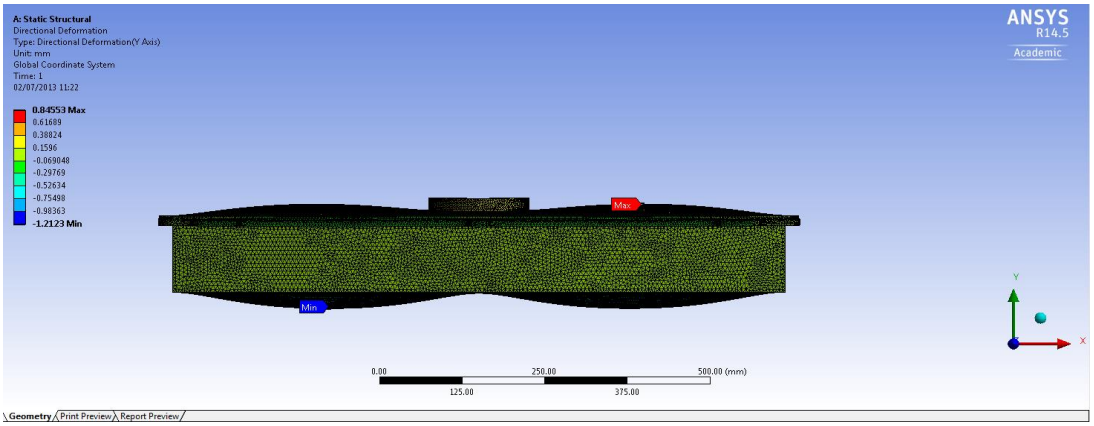

Figure 3-45: Lateral view of the detector box that highlights the box deflection (deflections are in scale 21x)

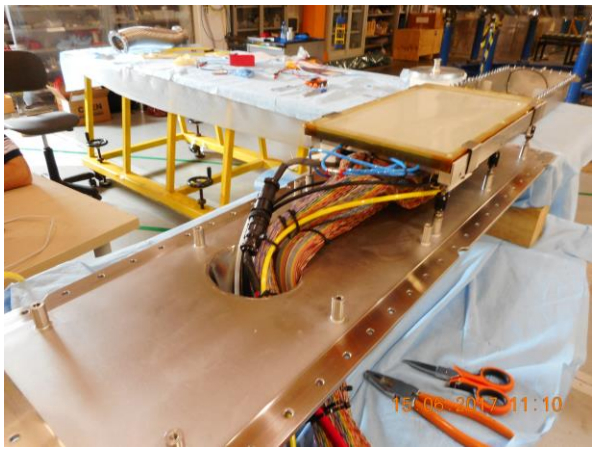

Figure 3-46: The nGEM detector installed on the detector box lid.

In order to test if the detector works in vacuum conditions, *a slightly radioactive camping net for lighting purpose* was installed on the rear side of the detector (Figure 3-48). This is a commercial item (no special permission are needed to buy it) that contains a small fraction of thorium whose decay products emit a series of gamma rays that can be detected by the nGEM detector if a proper gain is used. Figure 3-48-right shows the map of the counts with a potential applied to the GEM equal to 1050 V (corresponding to a gain of about 10^4) and the detector box in the vacuum environment. As you can see, the detector can detect the gammas emitted by the source, proving that the detector is working. It was then decided to maintain the gamma source in position even during the SPIDER operation: its presence does not affect the neutron measurements (the gain used for neutron detection is about 100) while it can test if the detector is working between the SPIDER pulses simply by changing the gain of the detector.

Figure 3-47: The detector box with the nGEM detector inside.

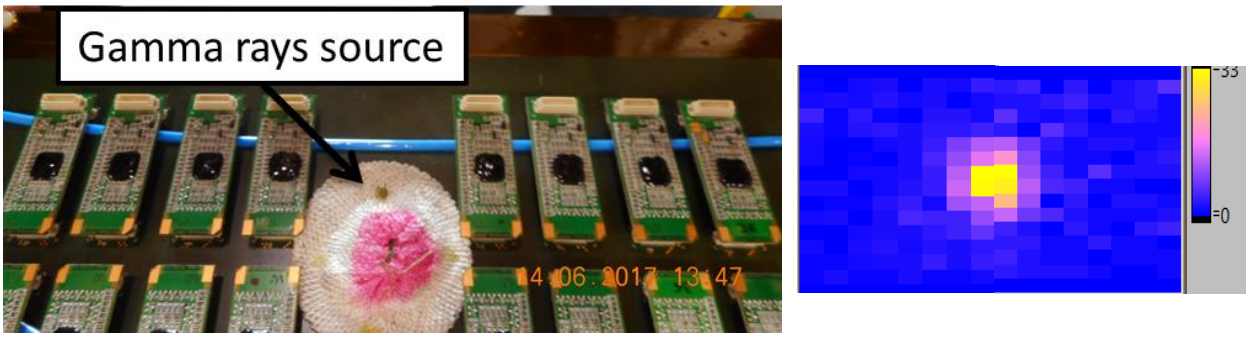

Figure 3-48: Left: Rear side of the detector. The gamma source is highlighted. Right On-line profile of the source

Figure 3-49: Installation of the detector box in the vacuum chamber

After the vacuum tests, the detector box was installed on the back side of the SPIDER beam dump (Figure 3-50). The latter will be installed inside the SPIDER vacuum vessel in the first months of 2018 and the SPIDER operation will start in April 2018.

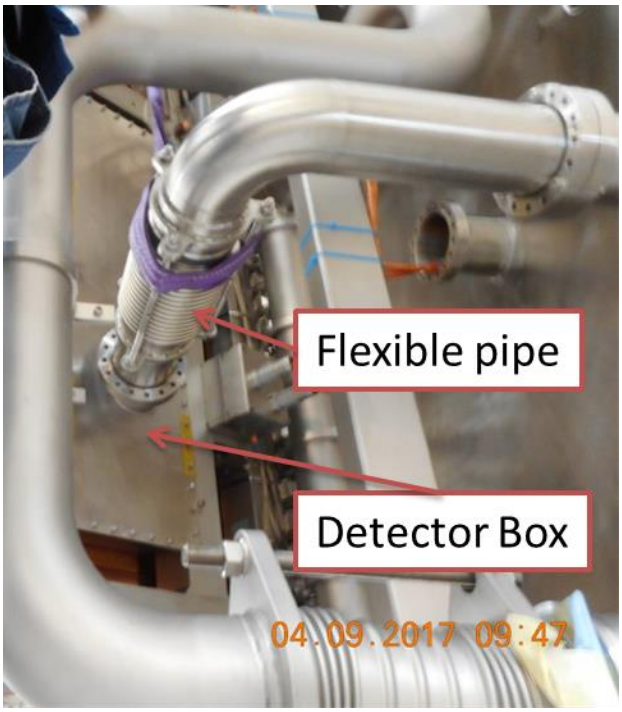

Figure 3-50: The CNESM diagnostic system installed on the SPIDER beam dump.

4 Conclusions

The two main projects described in this PhD thesis are focused on the development of GEM based detectors for neutrons.

Chapter 2 describes the development of the Boron Array Neutron Detector (BAND-GEM). This is a detector for thermal neutrons equipped with a three-dimensional converter (3D-C) made of aluminium grids coated with a thin film (0.5-1 μm) of $^{10}B_4C$. The nuclear reaction $^{10}B(n,\alpha)^7Li$ provides the "conversion" of thermal neutrons into charged particles that can escape the thin film layer and ionise the detector gas, thus producing a detectable signal. The aim of the BAND-GEM is the improvement in terms of detection efficiency of the performance obtained with the bGEM described in [PAPER 4]. A key feature of the BAND-GEM detector is the angular tilting which increases the neutron conversion probability (by a factor 1/sinθ) thus enhancing its efficiency. A first BAND-GEM prototype (par 2.3.1) was developed in order to demonstrate its proof of principle. This prototype was tested under neutron irradiation at the JEEPII reactor in Oslo, showing an improvement in terms of efficiency with respect to the bGEM. A series of numerical simulations (par 2.3.3) was carried out in order to optimize the geometry of the 3D-C, leading to the development of the second BAND-GEM prototype (par 2.3.4). The latter was tested with neutrons at the EMMA beam line, at ISIS. The measured detection efficiency at λ=4Å was about 40%, while the spatial resolution of the detector was about 6 mm with the detector tilted of θ=5°. Even if the obtained performances make the BAND-GEM technology an attractive solution for the detector system of LoKI (a SANS instrument under construction at ESS) the efficiency of the detector can be further increased by improving the charge extraction from the 3D-C. This was done in the third BAND-GEM prototype (par 2.3.5), by inserting a GEM foil in the middle of the 3D-C. The third BAND-GEM prototype was tested with neutrons at the TREFF beam line in the FRMII reactor and in the EMMA beam line. The measurements have shown an increase of the detector efficiency (ε>45% for λ>2 Å) keeping constant the spatial resolution.

Thanks to the results obtained during this thesis period, the BAND-GEM technology became a mature technology and it is now considered as a possible solution for the LoKI instrument. A first design of the LoKI detectors is described in par 2.2. The

proposed design foresees three detector banks, each composed of multiple BAND-GEM modules.
In order to demonstrate the feasibility to build large area BAND-GEM detectors, it was decided to develop one module of the middle-bank detector of LoKI, whose design is described in par 2.3.6.

Chapter 3 describes the development of the Close-Contact Neutron Emission Mapping (CNESM) diagnostic system. This is a neutron diagnostic that will be installed on the back of the beam dump structure of SPIDER, the first NBI prototype for ITER. In SPIDER a beam of deuterons accelerated up to 100 keV and carrying a current of about 40 A will impinges on two rectangular, actively cooled panels (called beam dump) producing a large amount of neutrons due to the $D(d,n)^3He$ fusion reaction. The aim of CNESM diagnostic system is the reconstruction of the deuterium beam profile from the detection of the neutron beam profile. The neutron detection in the CNESM system is done by using a nGEM detector. This is a GEM-based detector equipped with a plastic converter cathode. The nGEM was designed and produced (par 3.3 and 3.4) following the results of the simulations described in par 3.2: its converter cathode is made of a 2 mm thick polypropylene foil that acts as neutron-proton converter, followed by a 50 µm thick aluminum foil used to enhance the spatial resolution of the detector. The nGEM was tested under neutron irradiation at the ROTAX beam line at ISIS and at the Frascati Neutron Generator (FNG) facility (par 3.5). The tests have shown that the detector meets the requirements in terms of response uniformity, time stability and spatial resolution found in par 3.2.

All the results obtained during this thesis period gave the possibility to realize a system whose final installation and integration in SPIDER started in 2017 and will be completed in 2018 when first deuterium campaigns are foreseen.

List of figures

References

[1] Glenn F Knoll. Radiation detection and measurement. John Wiley & Sons, 2010

[2] F. Sauli. *"Gem: A new concept for electron amplification in gas detectors".* Nucl. Instr.& Methods A386 (1997) 531.

[3] ENDF/B-VII.1 Neutron Cross Section Data

[4] A. Oed. *"Position -Sensitive Detector With Micro-strip Anode for Electron Multiplication with Gases".* Nucl. Instr.& Methods A263 (1988) 351.

[5] Y. Giomataris et al. "*Micromegas: a highgranularity position-sensitive gaseous detector for high particle-flux environments*". Nucl. Instr.& Methods A376 (1996) 29.

[6] Kapton polyimide film. Trademark of DuPont USA (www.dupont.com)

[7] S Bachmann et al. "Charge amplification and transfer processes in the gas electron multiplier". Nucl. Instrum. Methods A 438 (1999) 376.

[8] W.Shockley. "*Currents to Conductors Induced by a Moving Point Charge*". Journal of Applied Physics 9 (1938) 635.

[9] S. Ramo.*"Currents Induced by Electron Motion".* Proceedings of the I.R.E. 27 (1939) 584.

[10] Fabio Sauli. The Gas Electron Multiplier (GEM): Operating principles and applications. Nucl. Instrum. Methods A 113 (2016) 805.

[11] M. Alfonsi et al. "High-rate particle triggering with triple-GEM detector". Nucl. Instrum. Methods A 518 (2004) 106.

[12] G. Croci et al. "nGEM fast neutron detectors for beam diagnostics. Nucl. Instrum. Methods A 720 (2013) 144.

[13] D. A. Shea et al. *"The helium-3 shortage: supply, demand, and options for Congress".* Congressional Research Service, Library of Congress, 2010.

[14] R. T. Kouzes. *"The helium-3 supply problem".* Technical report, Pacific Northwest National Laboratory (PNNL), Richland, WA (US), 2009.

[15] Gordon Leslie Squires. *"Introduction to the theory of thermal neutron scattering"*. Cambridge university press, 2012.

[16] AJ Allen et al. *"Neutron diffraction methods for the study of residual stress fields"*. Advances in Physics, 34 (1985) 445.

[17] R. Cubitt et al. *"Advances in the Study of Interfaces with Neutron Reflection"*. Langmuir (2003), 19, 7685

[18] A. J. Jackson. *"Introduction to Small-Angle Neutron Scattering and Neutron Reflectometry".* NIST Center for Neutron Research, 2008

[19] S.M. King. *"Small Angle Neutron Scattering"*. Technical report, ISIS Facility, STFC Rutherford Appleton Laboratory, 1995.

[20] K. Kanaki et al. *"ESS construction proposal. LoKI a broadband SANS Instrument"*. Technical report, European Spallation Source.

[21] *ESS Home Page: https://europeanspallationsource.se*

[22] Colin G. Windsor. *"Pulsed neutron scattering"*. Taylor & Francis, 1981

[23] A. J. Jackson et al. *"LoKI - a broad band high flux SANS instrument for the ESS".* Proceedings ICANS XXI, 2015.

[24] ESS Analysis Report. *"Analysis of requirements for the LoKI detector system",*ESS-0099544, 2017

[25] Mildner, D. F. R., & Carpenter, J. M. *"Optimization of the Experimental Resolution for Small-Angle Scattering"*. Journal of Applied Crystallography, 17(1984), 249–256

[26] *Interactive Data Language (IDL)*

[27] G. Croci et al.," *Diffraction measurements with a boron-based GEM neutron detector".* EPL Volume 107, Number 1, July 2014

[28] E. Perelli Cippo et al. *"A GEM-based thermal neutron detector for high counting rate applications".* Journal of Instrumentation, October 2015

[29] C. Höglund et al., *"B4C thin films for neutron detection ", J*. Appl. Phys. 111 (2012) 104908

[30] IENI (Istituto per l'Energetica e le Interfasi), www.ieni.cnr.it

[31] B. Ketzer et al., "A Time Projection Chamber for High-Rate Experiments: Towards an Upgrade of the ALICE TPC", Nucl. Instrum. Meth. A 732 237,2013

[32] D.Moraes et al., *"Development of the CARIOCA front-end chip for the LHCb muon detector".* Nucl. Instrum. Meth. A 491 (2002) 233.
[33] http://www.infn.it/csn5/joomla/GEMINI/.
[34] https://web.infn.it/GEMINI/index.php/hvgem
[35] ROTAX, http://www.isis.stfc.ac.uk/instruments/rotax/.
[36] ISIS-STFC, http://www.isis.stfc.ac.uk/
[37] IMAT, http://www.isis.stfc.ac.uk/Instruments/Imat/.
[38] H. Tietze-Jaensch et al., "The ROTAX/DIFF time-of-flight diffractometer at ISIS", Physica B 234–236 (1997) 1149.
[39] ANSYS software pakage, http://www.ansys.com/
[40] Garfield++,https://garfieldpp.web.cern.ch/garfieldpp/
[41] Amptek Mini-x Tube, http://www.amptek.com/pdf/minix.pdf
[42] Ortec 142IH preamplifier, http://www.ortec-online.com/-/media/ametekortec/brochures/142ih.pdf
[43] http://www.ortec-online.com/products/electronics/amplifiers/579
[44] http://www.ortec-online.com/products/application-software/maestro-mca
[45] G. Croci, "Development and Characterization of Micro-Pattern Gaseous Detectors for HEP applications and beyond" PhD thesis, 2010
[46] Y.Assran et al., "*Transport Properties of operational gas mixtures used at LHC*", arXiv:1110.6761
[47] http://www.isis.stfc.ac.uk/instruments/het/
[48] http://www.isis.stfc.ac.uk/instruments/het/
[49] http://www-llb.cea.fr/en/web/hpr web/hprweb1.php.
[50] A. Menelle, Description des fascieaux blancs pour irradiation, LLB Technical Report (2011).
[51] https://www.iter.org/
[52] https://www.igi.cnr.it/
[53] R. Pasqualotto et al., "A suite of diagnostics to validate and optimize the prototype ITER neutral beam injector", Journal of Instrumentation, Volume 12, October 2017
[54] M. Rebai,"Fast neutron instrumentation for beam diagnostics", PhD thesis, 2011

[55] ENEA, Appendix H Report RTI ION-IRP, 2004. Safety Analysis for the First ITER NB.

[56] J. Ziegler. http://www.srim.org/.

[57] W. Moller and F. Roth, “Implantation, retention and release of hydrogen isotopes in solids”. Physics of Plasma-Wall Interactions in Controlled Fusion, 1986.

[58] http://www.isis.stfc.ac.uk/instruments/rotax/.

[59] M. Martone et al. *“The 14 MeV Frascati neutron generator”,* Journal of Nuclear Materials, Volumes 212-215, Part B, September 1994, Pages 1661-1664.

[60] Design Criteria for In-vessel Components (SDC-IC) Appendix C, section IC 3800

[61] http://www.mlz-garching.de/neutron-optics

Synopsis of attached papers

1. Neutron radiography as a non-destructive method for diagnosing neutron converters for advanced thermal neutron detectors.

A. Muraro,G. Albani,E. Perelli Cippo, G.Croci,G. Angella,J. Birch, C. Cazzaniga, R. Caniello, F. Dell'Era, F. Ghezzi, G. Grosso, R. Hall-Wilton, C. Höglund, L. Hultman, S. Schimdt, L. Robinson, M. Rebai, G. Salvato, D. Tresoldi, C. Vasi and M. Tardocchi

Journal of Instrumentation, March 2016

Due to the well-known problem of ^{3}He shortage, a series of different thermal neutron detectors alternative to helium tubes are being developed, with the goal to find valid candidates for detection systems for the future spallation neutron sources such as the *European Spallation Source* (ESS). A possible ^{3}He-free detector candidate is a charged particle detector equipped with a three dimensional neutron converter cathode (3D-C). The 3D-C currently under development is composed by a series of alumina (Al_2O_3) lamellas coated by 1 µm of ^{10}B enriched boron carbide (B_4C). In order to obtain a good characterization in terms of detector efficiency and uniformity it is crucial to know the thickness, the uniformity and the atomic composition of the B_4C neutron converter coating. In this work a non-destructive technique for the characterization of the lamellas that will compose the 3D-C was performed using neutron radiography. The results of these measurements show that the lamellas that will be used have coating uniformity suitable for detector applications. This technique (compared with SEM, EDX, ERDA, XPS) has the advantage of being global (i.e. non point-like) and non-destructive, thus it is suitable as a check method for mass production of the 3D-C elements.

2. Performance of the high efficiency thermal neutron BAND-GEM detector

A.Muraro, G.Croci, E. Perelli Cippo, G. Grosso, C. Höglund, G. Albani, R. Hall-Wilton, K. Kanaki, F. Murtas, D. Raspino, L. Robinson, N. Rodhes, M. Rebai, S. Schmidt, E. Schooneveld, M. Tardocchi and G. Gorini

Accepted for publication on Progress of theoretical and experimental physics, in press

New high count rate detectors are required for future spallation neutron sources where large areas and high efficiency (>50%) detectors are envisaged. In this framework, GEM is one of the explored detector technologies since they feature good spatial resolution (<0.5 cm) and timing properties, have excellent rate capability (MHz/mm^2) and can cover large areas (some m^2) at low cost. In the BAND-GEM (Boron Array Neutron Detector GEM) approach a 3D geometry for the neutron converter cathode was developed that is expected to provide an efficiency > 30% in the wavelength range of interest for SANS instruments. A system of aluminium grids with thin walls coated with 0.59 μm layer of $^{10}B_4C$ has been built and positioned in the first detector gap, orthogonally to the cathode. By tilting the grid-system with respect to the beam, there is a significant increase of effective thickness of the borated material crossed by the neutrons. As a consequence, both interaction probability and detection efficiency are increased. This paper presents the results of the performance of the BAND-GEM detector in terms of efficiency and spatial resolution.

3. Performance of the full size nGEM detector for the SPIDER experiment

A. Muraro, G.Croci, G.Albani, G.Claps, M.Cavenago, C.Cazzaniga, M. DallaPalma, G.Grosso, F.Murtas, R.Pasqualotto, E.PerelliCippo, M.Rebai, M. Tardocchi, M.Tollin, G.Gorini

Nuclear Instruments and Methods in Physics Research A 813(2016)147–152

The ITER neutral beam test facility under construction in Padova will host two experimental devices: SPIDER, a 100 kV negative H/D RF beam source, and MITICA, a full scale, 1 MeV deuterium beam injector. SPIDER will start operations in 2016 while MITICA is expected to start during 2019. Both devices feature a beam dump used to stop the produced deuteron beam. Detection of fusion neutrons produced between beam-deuterons and dump-implanted deuterons will be used as a means to resolve the horizontal beam intensity profile. The neutron detection system will be placed right behind the beam dump, as close to the neutron emitting surface as possible thus providing the map of the neutron

emission on the beam dump surface. The system uses nGEM neutron detectors. These are Gas Electron Multiplier detectors equipped with a cathode that also serves as neutron–proton converter foil. The cathode is designed to ensure that most of the detected neutrons at a point of the nGEM surface are emitted from the corresponding beamlet footprint (with dimensions of about 40×22 mm^2) on the dump front surface. The size of the nGEM detector for SPIDER is 352 mm×200 mm. Several smaller size prototypes have been successfully made in the last years and the experience gained on these detectors has led to the production of the full size detector for SPIDER during 2014. This nGEM has a read-out board made of 256 pads (arranged in a 16×16 matrix) each with a dimension of 22 mm×13 mm. This paper describes the production of this detector and its tests (in terms of beam profile reconstruction capability, uniformity over the active area, gamma rejection capability and time stability) performed on the ROTAX beam-line at the ISIS spallation source (Didcot-UK).

4. A GEM-based thermal neutron detector for high counting rate applications

E. Perelli Cippo, G. Croci, **A. Muraro**, A. Menelle, G. Albani, M. Cavenago, C. Cazzaniga, G. Claps, G. Grosso, F. Murtas, M. Rebai, M. Tardocchi and G. Gorini

Journal of Instrumentation, October 2015

Among other neutron detector systems proposed as a possible substitute for 3He tubes, GEM-based ones have shown appealing characteristics, when coupled with suitable neutron-converter cathodes. In this paper, we present the results of a GEM-based neutron detector in a high-flux environment (the ORPHÉE reactor in Saclay), especially in terms of maximum rate capability and linearity. Recorded data show that the detector can manage neutron counting rates in the order of 50 × 106 counts/sec cm2 while maintaining a reasonable linearity and with no sign of instability.

5. A new thermal neutron detector based on 3D 10B converters for high rate applications

G. Croci, **A. Muraro**, E. Perelli Cippo, M. Tardocchi, C. Hoglund, R. Hall-Wilton, and G. Gorini

Submitted at Applied Physics Letter

A novel 3D $^{10}B_4C$ converter has been designed and realized to combine a high neutron conversion via the $^{10}B(n,\alpha)7Li$ reaction together with an efficient collection of the produced charged particles. The developed 3D converter is based on aluminum thin grids realized using a micro-waterjet technique and when it is coupled to a GEM detector has allowed reaching thermal neutron detection efficiency as a high as 50% and sustaining counting rates in excess of 1 MHz/cm2. The newly developed neutron detector will enable high-rate neutron scattering experiments at high flux spallation sources as well as other applications where large areas and custom geometries of thermal neutron detectors are foreseen.

6. Status of the CNESM diagnostic for SPIDER

A. Muraro, G. Croci, G. Albani, C. Cazzaniga, G. Claps, M. Cavenago, G. Grosso, M. Dalla Palma, M. Fincato, F. Murtas, R. Pasqualotto, E. Perelli Cippo, M. Rebai, M. Tollin, M. Tardocchi and G. Gorini

Fusion Engineering and Design Volumes 96–97, October 2015, Pages 311-314

The ITER neutral beam test facility under construction in Padova will host two experimental devices: SPIDER, a 100 kV negative H/D RF source, and MITICA, a full scale, 1 MeV deuterium beam injector. A detection system called close-contact neutron emission surface mapping (CNESM) is under development with the aim to resolve the horizontal beam intensity profile in MITICA and one of the eight beamlet groups in SPIDER, with a spatial resolution of 1.5 and 2.5 cm respectively. This is achieved by the evaluation of the map of the neutron emission due to interaction of the deuterium beam with the deuterons implanted in the beam dump surface. CNESM uses nGEM detectors, i.e. GEM detectors equipped with a cathode that also serves as neutron–proton converter foil. The diagnostic will be placed right behind the SPIDER and MITICA beam dump, i.e. in an UHV environment, but the nGEM detectors need to operate at atmospheric pressure: in order to maintain the detector at atmospheric pressure, a vacuum sealed box, that will be mounted inside the vacuum, has been designed. The box design was driven by the need to minimize the neutron attenuation and the distance between the beam dump surface and the detector active area. This paper presents the status of the CNESM diagnostic describing

the design of the detector, the design of the sealed box and reporting the results obtained with the first full-size prototype under fast neutron irradiation.

Paper 1

Neutron radiography as a non-destructive method for diagnosing neutron converters for advanced thermal neutron detectors

2016 JINST 11 C03033

(http://iopscience.iop.org/1748-0221/11/03/C03033)

Published by IOP Publishing for Sissa Medialab
Received: *January 12, 2016*
Accepted: *February 14, 2016*
Published: *March 16, 2016*

International workshop on Imaging
7–10 September 2015
Varenna, Italy

Neutron radiography as a non-destructive method for diagnosing neutron converters for advanced thermal neutron detectors

A. Muraro,[a,1] **G. Albani,**[b] **E. Perelli Cippo,**[a] **G.Croci,**[b] **G. Angella,**[c] **J. Birch,**[d] **C. Cazzaniga,**[e] **R. Caniello,**[a] **F. Dell'Era,**[a] **F. Ghezzi,**[a] **G. Grosso,**[a] **R. Hall-Wilton,**[f] **C. Höglund,**[d] **L. Hultman,**[d] **S. Schimdt,**[d] **L. Robinson,**[d] **M. Rebai,**[b] **G. Salvato,**[g] **D. Tresoldi,**[g] **C. Vasi**[g] **and M. Tardocchi**[a]

[a] *Istituto di Fisica del Plasma "P. Caldirola", IFP-CNR, Via Cozzi 53, Milan, Italy*
[b] *Dipartimento di Fisica, Università di Milano Bicocca, Piazza della Scienza 3, Milan, Italy*
[c] *IENI-CNR, Via Cozzi 53, Milan, Italy*
[d] *Dept. of Physics, Chemistry and Biology (IFM), Thin Film Physics Division, Linköping University, SE-581 83 Linköping, Sweden*
[e] *ISIS — Rutherford Appleton Laboratory — STFC, Didcot, United Kingdom*
[f] *European Spallation Source ESS-ERIC, Tunavägen 24, 223 63 Lund, Sweden*
[g] *Istituto Processi Chimico-Fisici, IPCF-CNR, Viale Ferdinando Stagno d'Alcontres 37, Messina, Italy*

E-mail: muraro@ifp.cnr.it

Abstract: Due to the well-known problem of ^{3}He shortage, a series of different thermal neutron detectors alternative to helium tubes are being developed, with the goal to find valid candidates for detection systems for the future spallation neutron sources such as the *European Spallation Source* (ESS). A possible ^{3}He-free detector candidate is a charged particle detector equipped with a three dimensional neutron converter cathode (3D-C). The 3D-C currently under development is composed by a series of alumina (Al_2O_3) lamellas coated by 1 μm of ^{10}B enriched boron carbide (B_4C). In order to obtain a good characterization in terms of detector efficiency and uniformity it is crucial to know the thickness, the uniformity and the atomic composition of the B_4C neutron converter coating. In this work a non-destructive technique for the characterization of the lamellas that will compose the 3D-C was performed using neutron radiography. The results of these measurements show that the lamellas that will be used have coating uniformity suitable for detector applications. This technique (compared with SEM, EDX, ERDA, XPS) has the advantage of being global (i.e. non point-like) and non-destructive, thus it is suitable as a check method for mass production of the 3D-C elements.

Keywords: Inspection with neutrons; Neutron radiography; Image filtering; Data processing methods

[1] Corresponding author.

doi:10.1088/1748-0221/11/03/C03033

Contents

2016 JINST 11 C03033

1 Introduction

Due to the well-known problem of ^{3}He shortage, a series of different thermal neutron detectors alternative to helium tubes are being developed, with the goal to find valid candidates for detection systems for the future spallation neutron sources such as the *European Spallation Source* (ESS [1]). Given the expected high neutron flux at the ESS, compared with present spallation sources, there is not only a need for replacing ^{3}He, but also to develop high-rate neutron detectors. An intense R&D phase is ongoing in order to find high performing ^{3}He-free detectors which can meet the requirements imposed by ESS. One possibility is to equip charged particle detectors (such as GEM [2, 3] detectors) with three-dimensional neutron converter cathodes (3D-C). The 3D-C currently under development is composed by a series of alumina (Al_2O_3) lamellas coated by 1 μm of boron-10 enriched boron carbide ($^{10}B_4C$). A thermal neutron reaction in ^{10}B produces the detectable charged particles ^{7}Li and ^{4}He. In order to obtain a well-known characterization in terms of detector efficiency and uniformity is crucial to know the thickness, the uniformity and the atomic composition of the $^{10}B_4C$ neutron converter coatings.

While the determination of such parameters is relatively straightforward for standard two-dimensional neutron converters, this may not be the case for the complex 3D-C. In fact, given the huge number of lamellas required for the composition of the 3D-C and the relatively high cost for each lamella, it is essential to find a non-destructive method for the characterization of the $^{10}B_4C$ coatings.

In this work a series of methods for the characterization of the lamellas are presented: first of all a series of destructive tests were carried out on a limited number of samples. The techniques

used in these tests are the Scanning Electron Microscopy (SEM), the Energy Dispersive X-ray Spectroscopy (EDX), the Elastic Recoil Detection Analysis (ERDA) and the X-ray photoelectron spectroscopy (XPS). Finally a non-destructive technique for the characterization of all the lamellas that will composed the 3D-C was performed using neutron radiography.

The SEM and EDX measurements were made in the electron microscopy laboratory of the research Institute IENI-CNR [3], the ERDA analysis was performed in the Linköping University [4] and, the XPS analysis was performed in the Institute IFP-CNR [5] while the neutron radiography measurements have been performed at the *ROTAX* beamline at ISIS [6], making use of the new radiography-tomography system being developed for the next *IMAT* beamline [7]. Data treatment considering the white-spectrum measurements is described and validated through the use of a standard reference sample.

2 Sample description

Figure 1 shows an Al_2O_3 lamella coated with 1 um of $^{10}B_4C$.

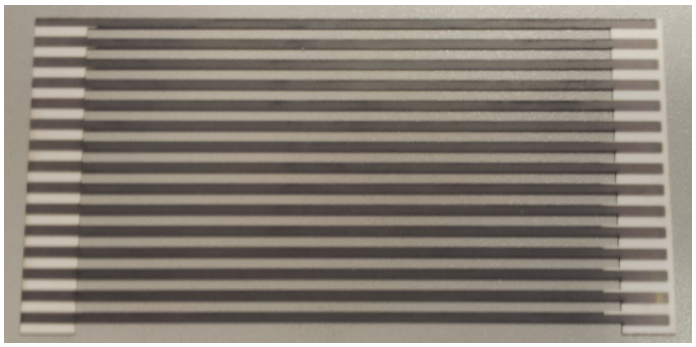

Figure 1. Coated Al_2O_3 lamella.

Each lamella has external dimensions of $120 \times 60 \times 0.25\,mm^3$ and is composed by 15 strips, each one with dimensions $100 \times 2 \times 0.25\,mm^3$. Each strip is coated on both sides with 1 μm of $^{10}B_4C$ that serves as neutron converter. $^{10}B_4C$ shows superior chemical, mechanical and electrical properties compared to pure ^{10}B. Excellent stability against neutron radiation has also been shown in [8]. The main disadvantage is the 20% lower ^{10}B concentration compared to pure ^{10}B. The coatings have been deposited using DC magnetron sputtering, as further described in [9]

The depositions were done in an industrial CC800/9 deposition system manufactured by CemeCon AG at the Linköping University in Sweden. After being cleaned in acetone followed by isopropanol in an ultrasonic bath, the alumina substrates were mounted onto a sample carousel which allows 2-axis planetary rotation and 2-sided deposition. In order to decrease the impurity level and to improve the adhesion of the coating, the lamellas where heated up to 400°C before and during the deposition process [9, 10]

3 Preliminary characterization techniques

The characterization of the lamellas proposed in this paper may give best results if some information on the deposited film are known with high precision; for the sake of this paper devoted to the

2016 JINST 11 C03033

technique development, important parameters like isotopic composition, thickness, mass density and presence of impurities have been measured and cross-checked with the techniques described in the following paragraphs.

3.1 SEM

The SEM analysis was performed with a high resolution SU70 microscope by Hitachi with Schottky electron source. This analysis gives a measurement of the coating thickness and, by repeating the measurement all along the strips length, one can obtain an estimation of the thickness uniformity. Figure 2 shows a 0.9 μm B_4C thick coating on the alumina substrate.

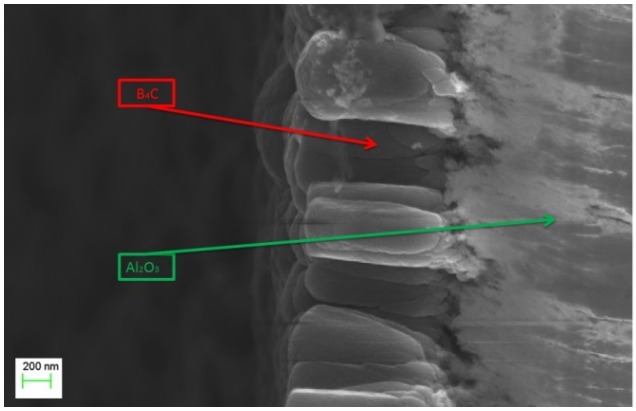

Figure 2. Result of the SEM analysis.

By repeating the measurements in different locations along the strips, it was noticed that the film thickness is not perfectly uniform. The values found lie between 0.85 μm (near the strips edges) and 0.95 μm (at the center of the lamellas): a value of 0.9 μm was taken for the successive calculations presented in this paper.

3.2 EDX, ERDA and XPS analysis

The EDS (Energy Dispersive X-Ray Spectroscopy) and the ERDA (Elastic Recoil Detection Analysis) analyses were performed in order to obtain an estimation of the impurities contained in the coating, while the XPS (X-Ray Photoelectron Spectroscopy) analysis has the scope to measure the variation of the atomic composition of the coating all along its thickness. These are standard material analysis techniques, and the detailed description of the instrumentation used to perform these analyses is beyond the scope of this paper and it will be presented in a future paper. Here we just mention that the results obtained with the different analyses are compatible (see table 1). The used techniques are intrinsically point-like, and this can easily explain small discrepancies between local values. However, the XPS analysis has shown that the atomic composition of the coating is constant all along its thickness. The averages of the found values are reported in table 1.

As one can see, not only B and C are found in the coating, but also O, Mg, Al and some heavier elements (Fe, Cr, Ni and Cu). The elemental composition found in these analyses is taken into account in the calculation of absorption coefficients for the successive non-destructive characterization method.

2016 JINST 11 C03033

Table 1. Average atomic composition found using the different analysis techniques mentioned in the paper. Values are in percentage. Typical errors associated with these estimations are in the order of a few percent. Small discrepancies between values are due to the point-like nature of the techniques. The presence of such impurities into the neutron-absorber coating is accounted for in the following calculations.

Isotopes	B	C	Fe	Cr	Ni	Cu	O	Mg	Al
EDS	73	20	4	1	1	1	/	/	/
TOF-ERDA	77	16	/	/	/	/	1	2	0.4
XPS	68	28	2	/	/	/	7	/	/

The combination of these techniques gives a complete characterization of the samples, but at the price of sectioning and sampling the lamella elements, thus making them unsuitable for further application. As a consequence, another approach must be followed in order to characterize all the samples that will compose the detector.

3.3 Neutron radiography

In order to characterize the boron carbide film deposited on all the lamellas, the neutron radiography technique was used. This is a non-invasive, non-destructive technique to obtain images of the inner parts of an object using a neutron beam to illuminate it. Neutrons transmitted through the sample are described by the following exponential law:

$$I(E) = I_0(E)e^{-\Sigma(\mathrm{E})z}$$

where $I_0(E)$ is the incoming neutron flux onto the sample, $I(E)$ is the attenuated flux after crossing the sample, z is the thickness and Σ is the total macroscopic cross section that is defined as a function of the atomic density ρ and the total neutron cross section σ of the elements which compose the sample of molecular weight PM:

$$\Sigma = \sigma\,(\mathrm{E})\,\frac{n}{V} = \sigma\,(\mathrm{E})\,\frac{\rho N_A}{PM}$$

where N_A is the Avogadro constant. For the characterization of the lamellas we were interested in the total amount of neutrons absorbed from the boron contained into the $^{10}\mathrm{B}_4\mathrm{C}$ coating. In fact, apart from the small fraction of neutrons absorbed or scattered from the nuclei of the impurities or of the alumina substrate, all the absorbed neutrons lead to the production of charged particles that can give a detectable signal in the charged particle detector equipped with the 3D-C.

In the analysis all the materials that compose the sample are taken into account, but the main contribution to the neutron absorption comes from the presence of the $^{10}\mathrm{B}$, which presents the greater cross section compared with all the other materials in the region of interest, as shown in figure 3.

The analysis for the characterization of the film uniformity is done by comparing the the expected transmitted radiation $\left(\frac{\tilde{I}}{\tilde{I}_0}\right)^{\text{expected}}$ with the measured one $\left(\frac{\tilde{I}}{\tilde{I}_0}\right)^{\text{measured}}$.

The value of the transmitted radiation is calculated by introducing the equivalent thickness t of the $\mathrm{B}_4\mathrm{C}$ film:

$$t = \frac{\rho_{B_4C} z_{B_4C}}{PM_{B_4C}}$$

2016 JINST 11 C03033

so that the expected transmitted radiation can be written as:

$$\left(\frac{\tilde{I}}{\tilde{I_0}}\right)^{\text{expected}} = \frac{\int_{E_{\min}}^{E_{\max}} I_0(E) e^{-\sigma(E) N_{\text{Av}} t^{\text{expected}}} dE}{\int_{E_{\min}}^{E_{\max}} I_0(E) dE}$$

with the expected equivalent thickness (t^{expected}) calculated using $\rho_{\text{B4C}} = 2.242\,\text{g/cm}^3$ $\rho_{\text{B4C}} = 2,242\,\text{g/cm}^3$ [2] and the value of $z_{\text{B4C}} = 0.9\,\mu\text{m}$ obtained from the SEM analysis. The measured transmitted radiation can be written as:

$$\left(\frac{\tilde{I}}{\tilde{I_0}}\right)^{\text{measured}} = \frac{\int_{E_{\min}}^{E_{\max}} I_0(E) e^{-\sigma(E) N_{Av} t^{\text{measured}}} dE}{\int_{E_{\min}}^{E_{\max}} I_0(E) dE}$$

Where t^{measured} is calculated by using the value of mass density obtained from the residuals evaluation after estimating the average of the neutrons absorbed by the lamella's strips ($\text{neutron}_{\text{abs}}$) (see par 3.3.2 for details) and the values of z and of the impurities concentration obtained in the SEM and in the EDX, ERDA and XPS analysis.

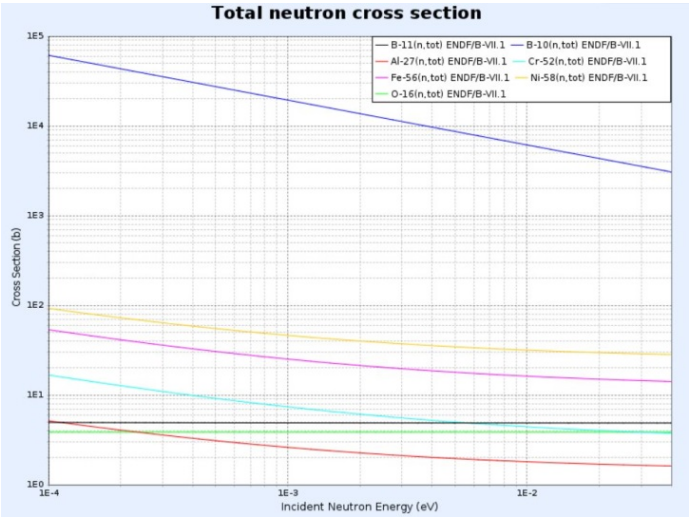

Figure 3. Total neutron cross section of the elements in the coating.

3.4 Experimental setup

The neutron radiography measurements have been performed at the *ROTAX* beamline [1] at ISIS, using the radiography-tomography system for the next *IMAT* [7] beamline at ISIS. Figure 4 shows a schematic of the experimental setup used for the characterization of the lamellas in the ROTAX beamline.

Neutrons transmitted through the sample strike a scintillator screen which converts the incoming neutrons into photons, the latter being detected, through a mirror, by a digital camera (CCD). The lamellas were positioned on a rotating sample holder, which permits to select the angle between the incoming neutron beam and the lamellas. Moreover, the neutron beam in the ROTAX beamline has

2016 JINST 11 C03033

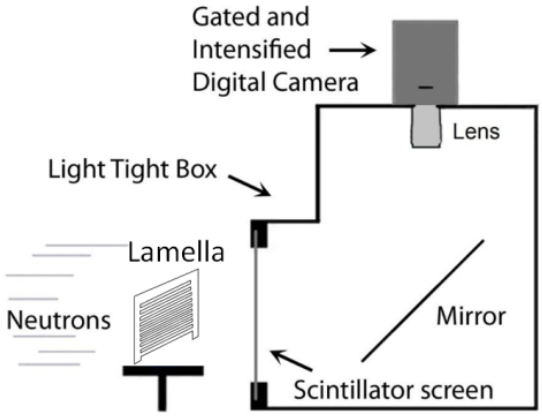

Figure 4. Schematic of the experimental setup.

dimensions of about $40 \times 35\,\mathrm{mm}^2$ therefore the rotating sample holder has been mounted on a x-y positioner, which allows to move and to enlighten all the lamella.

The neutron flux used for the irradiation had an energy spectrum cleaned of fast neutrons and gamma components thanks to an upstream t-zero chopper. This is a rotating structure that operates at the ISIS source frequency and is phased in such a way that the line of sight from the target to the sample is blocked when the proton beam hits the target. The details of operation of the chopper on the ROTAX beamline can be found in [14]. The resulting spectrum is shown in figure 5. The use of a gamma suppressing chopper is a common procedure at ISIS when transmission (i.e. *in the beam*) diagnostics are used, as in this case. In the present case, the scintillator coupled to the radiography system has a residual sensitivity to gamma rays: while this sensitivity is low (in the order of 10^{-6}) enough to make negligible the background due to activation inside the block-house and from the sample itself (see par. 3.5 for details), it may not be the case when a large flux of gammas is expected, as the one coming from the spallation target.

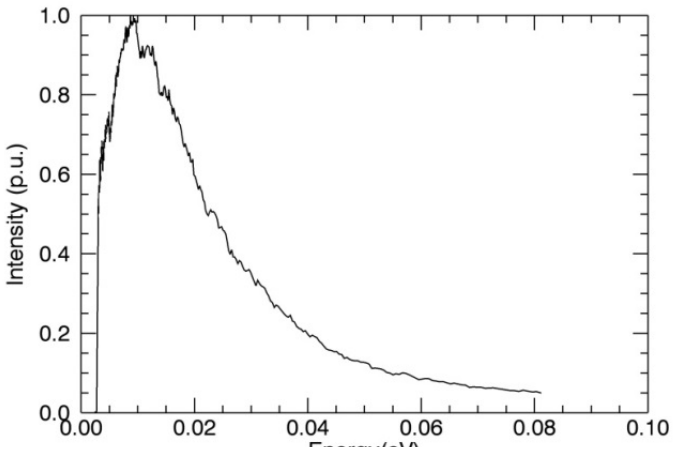

Figure 5. Neutron spectrum in the ROTAX beam line.

2016 JINST 11 C03033

The types of performed measurements are:

- measurements with the lamellas perpendicular to the neutron beam direction.
- measurements with the lamellas inclined by different angles with respect to the neutron beam.

Each measurement is composed by the following steps:

- Acquisition of the CCD "dark signal" with the neutron shutter closed.
- Acquisition of the neutron "open beam" $\tilde{I}_0$ (i.e. without sample).
- Acquisition of the lamella radiography at different positions ($\tilde{I}$). See figure 9 for details.
- Rotation of the lamella and acquisition of the neutron radiography for different angles of irradiation.

For each step, the acquisition system produces a file that contains a matrix of 512x512 16-bit pixels, subsequently analysed by an appropriate code.

3.5 Data analysis

All the images recorded by the acquisition system are processed by an IDL [12] code, whose operations are summarized in the following.

After importing the data into the IDL environment, the code selects the data useful for the analysis, discarding the parts near the sample holder, as shown in figure 6.

This operation is followed by the subtraction of the dark signal (obtained with the shutter closed), from the beam signals, without ($\tilde{I}_0$) and with ($\tilde{I}$) the lamellas. In this way the gamma-ray background due to the activation of the surrounding materials in the ROTAX block-house is subtracted from the data useful for the analysis. However the gamma-sensitivity of the scintillator used in the measurements is very low (about 10^{-6}) as shown in [15]. This is a very important feature of the neutron radiography system used, given that in 93% of the ^{10}B neutron abortion reactions,

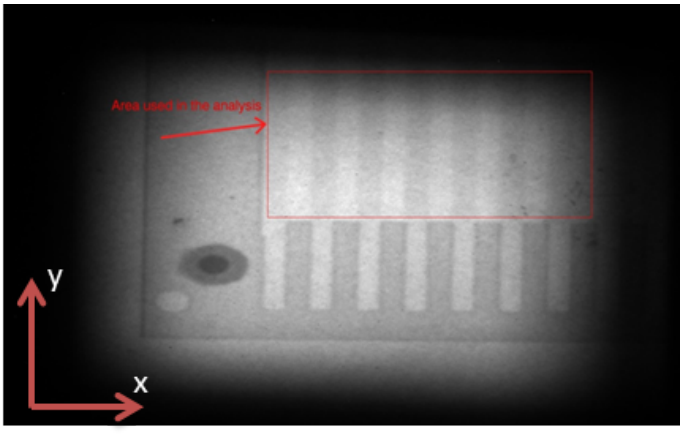

Figure 6. An example of area useful for the analysis.

the ^{7}Li nucleus is created in an excited state which relaxes through the emission of a 0.48 MeV gamma-ray [16].

The resulting data are then filtered using a low-pass digital Butterworth filter in order to reduce the noise due to the high frequency components and the contribution of the noisy pixels. The filtered data are then normalized by making the ratio between the lamella data ($\tilde{I}$) and the open beam data ($\tilde{I}_0$). In this way is possible to eliminate the beam-shape dependence (the beam is not flat but has a Gaussian profile) from the acquired data.

In order to reduce the fluctuations presented by the normalized image, all the data are averaged along the y direction (i.e. along the strips). In figure 7 is possible to see the plot of the data along an x coordinate before and after this operation.

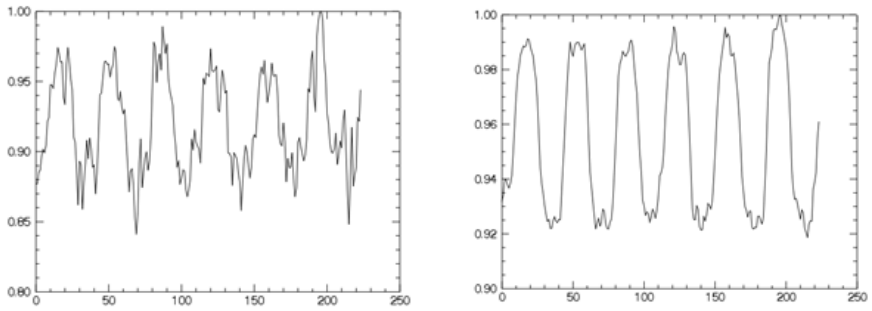

Figure 7. Plot of the data along the x coordinate before (left) and after (right) the averaging and the filtering of the normalized data. The data of the left plot are taken in the middle of the image.

Given the large number of analyzed samples and the resulting large amount of data produced by the measurements, it was necessary to implement an automatic method for the localization of the strips in the image. This method evaluates the firsts derivatives of the normalized-averaged data with respect to the x coordinate. The array of the derivatives is then filtered by a high order low-pass digital filter in order to reduce the high frequency noise, as shown in figure 8.

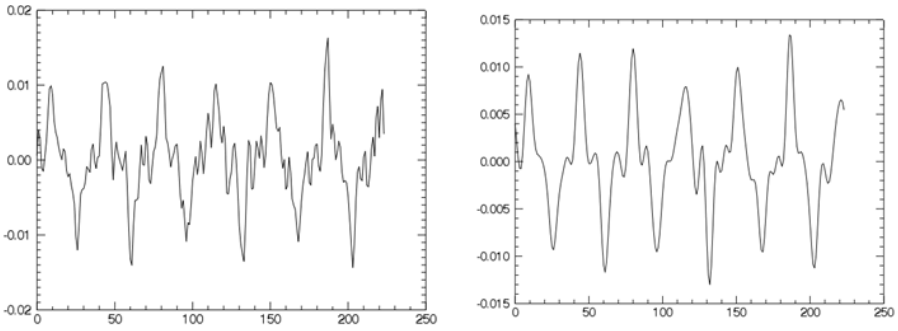

Figure 8. Plot of the first derivative first (left) and after (right) the application of the filter.

The strips of the lamella begin at the points in which the first derivative is lower than a fixed negative constant and terminate at the points in which the first derivative is greater than a fixed positive constant. The values of the constants were found after an empiric evaluation of the images. When

2016 JINST 11 C03033

the strips are localized, the data that lie on them are averaged along the y coordinate (along the strip) as well as the data that lie outside of them. The ratio between the average of the data on the strips and the average of the data outside of the strips gives an estimation of the neutron absorption ($\text{neutron}_{\text{abs}}$).

It is now possible to obtain the value of the amount of boron carbide crossed by the neutron beam in terms of equivalent mass density ρ, by implementing in the code an iterative method that minimizes the following equation:

$$\tilde{I} = (1 - \text{neutron}_{\text{abs}}) \cdot \tilde{I}_0$$

The value of ρ is found through the evaluation of the residuals:

$$\rho \rightarrow \left| \left(\left((1 - \text{neutron}_{\text{abs}}) \cdot \tilde{I}_0 \right) - \tilde{I} \right)^2 \right|_{\text{min}}$$

The value of the equivalent boron carbide mass density found is used for the calculation of the measured equivalent thickness t^{measured}:

$$t^{\text{measured}} = \frac{\rho z}{PM}$$

which is then used for the calculation of the measured transmitted radiation $\left(\frac{\tilde{I}}{\tilde{I}_0}\right)^{\text{measured}}$ that will be compared with the expected transmitted radiation $\left(\frac{\tilde{I}}{\tilde{I}_0}\right)^{\text{expected}}$

3.6 Results of the measurements with the lamellas perpendicular to the neutron beam

In order to obtain a complete characterization of the film deposit, all the lamellas (about 80 samples) was enlightened by the ROTAX neutron beam at different positions. Figure 9 shows the map of the different measurements position.

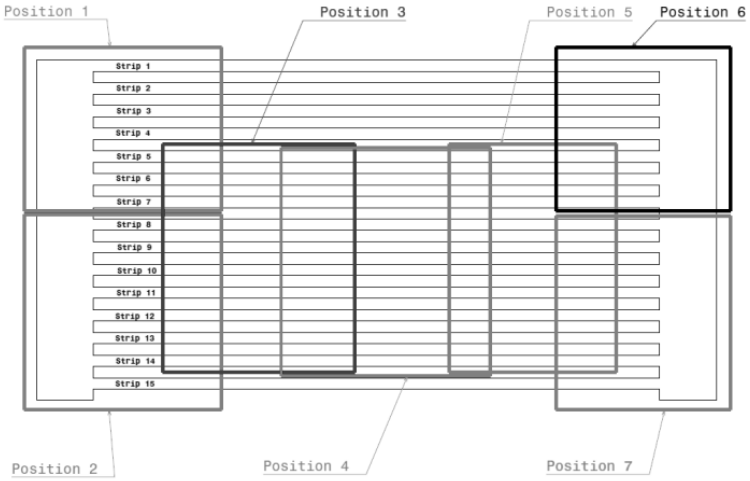

Figure 9. Schematic of the different neutron irradiation positions.

All the strips are enlightened by the beam at least twice, and the comparisons between all the different measurements give an estimate of the quality of the coating. For each measurement the code extrapolates a set of t^{measured} values (one value for each strip in the enlightened area), which

2016 JINST 11 C03033

are subsequently used for the evaluation of the $^{10}B_4C$ coating uniformity. A lamella is considered as suitable to compose the 3D-C if the coating has a value of non-uniformity less than 10% with respect to the average of all the t^{measured} values found on the entire lamella surface. Figure 10 shows a sample of accepted lamellas, with the labelling of the strips as per figure 9. For the strips 1,2,3,4 and 15 two values of t^{measured} are obtained, while for all the other strips five values of t^{measured} are obtained.

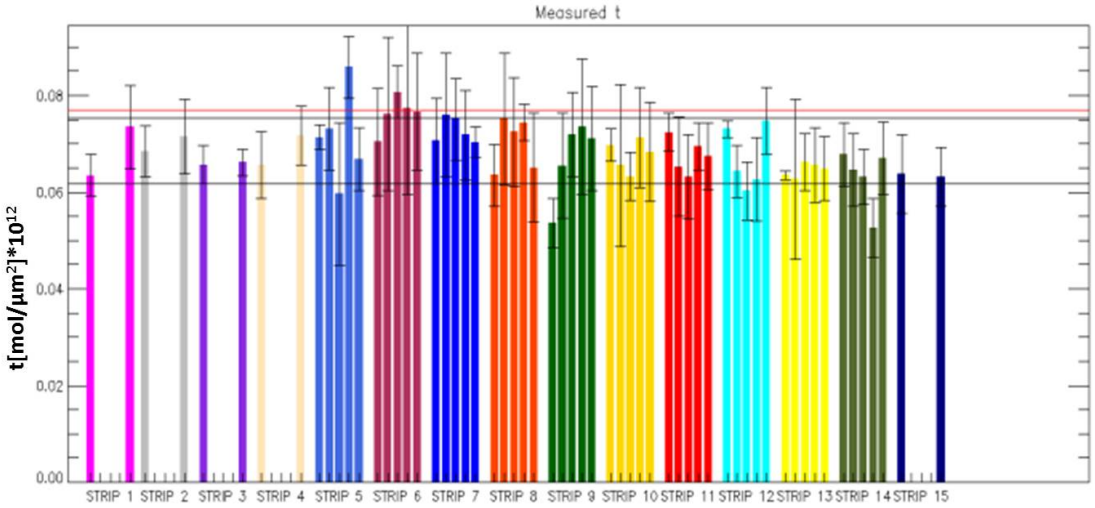

Figure 10. Example of accepted lamella. The red line indicates the t^{expected} value; the black horizontal lines indicate the acceptance criteria: if the t^{measured} values lie between these two lines the lamella is accepted.

More than the 90% of the enlightened samples satisfy the acceptance criterion. Moreover these measurements have shown that the deposition process is reasonably reproducible: therefore only a small number of samples will be checked in the future, in order to highlight possible major failures in a particular deposition run.

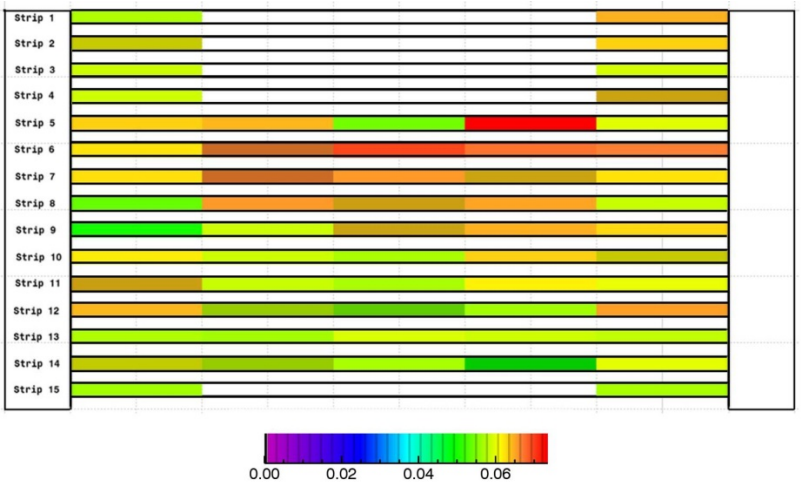

Figure 11. Bi-dimensional map of the t^{mesaured} values on an accepted lamella. The values of the legend must be multiplied by 1012 in order to get the value in mol/μm^2 units.

3.7 Results of the measurements with the lamella inclined by different angles

The envisaged detector will be inclined with respect to the incoming neutron beam, in order to increase the efficiency keeping constant the escape probability of the generated charge particles inside the neutron converter coating [13]. This behavior was confirmed by a measure taken during the ROTAX campaign. In figure 12 is shown the comparison between the expected transmitted radiation $\left(\frac{\tilde{I}}{\tilde{I}_0}\right)^{\text{expected}}$ and the measured one $\left(\frac{\tilde{I}}{\tilde{I}_0}\right)^{\text{measured}}$ for the measurements taken for a single lamella rotated from 0° to 81° in steps of 0.9°.

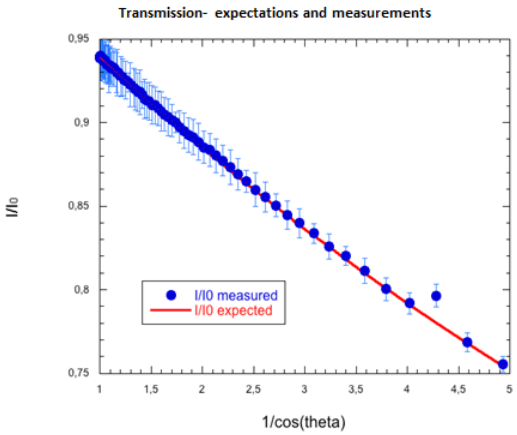

Figure 12. Comparison between the expected transmitted radiation (red line) and the measured one by varying the incidence angle of the incoming neutron beam.

By varying the angle between the coated lamella and the neutron beam, the fraction of absorbed neutron is increased, due to the longest path of the neutron inside the $^{10}B_4C$ coating. However in the $n^0+^{10}B \rightarrow ^7Li+^4He$ reaction the charged particles are emitted back-to-back, therefore the probability to escape from the coating is the same that would occur with the $^{10}B_4C$ coating placed orthogonally to the neutron beam. This means that with a good choice of the 3D-C geometry, one can obtain higher neutron absorption with respect to the standard 2D-C without paying in terms of escape probability of the generated charged particles [13].

3.8 Measurement of lamellas with different boron thickness

Ten lamellas out of 80 were by purpose coated with 1.1 μm of B_4C instead of 1 μm. The neutron radiography technique was also applied to check if it was possible to distinguish coatings that have a 10% difference in thickness. Figure 13 shows that using this technique two different values of t are obtained for the lamellas with 1.1 and 1 um of B_4C, respectively. As expected the two groups of lamellas are well separated beyond the estimated error bars. Only a small fraction of the samples is shown in figure 13.

3.9 Results validation

The analysis method was validated applying the same analysis method to a standard vanadium sample of known thickness and density.

2016 JINST 11 C03033

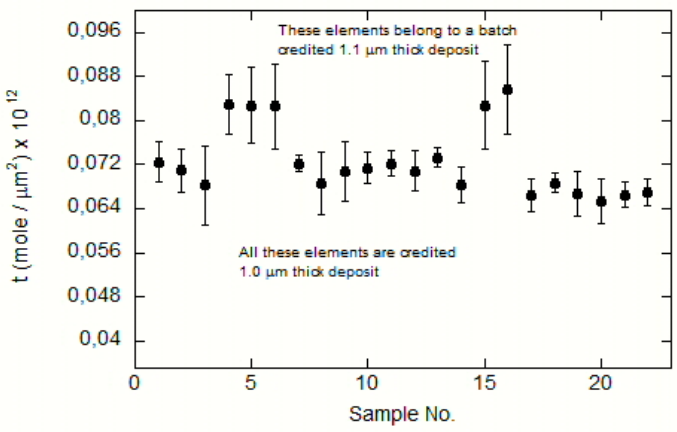

Figure 13. Comparison between the t measured for lamellas with 1 and 1.1 μm B_4C coatings. Some of the samples are shown.

The extracted and the real equivalent thickness $t$of Vanadium are:

$$t^{\text{extracted}} = 2,30 \times 10^{-4}\,\text{mol} \cdot \text{mm}^{-2}$$

$$t^{\text{expected}} = 2,35 \times 10^{-4}\,\text{mol} \cdot \text{mm}^{-2}$$

From the value of $t^{\text{extracted}}$ it is possible to extract the thickness z of the Vanadium:

$$z^{\text{extracted}} = 1,92\,\text{mm}$$

that can be compared with the real thickness of the block

$$z^{\text{real}} = 1,95\,\text{mm}.$$

4 Conclusions and future work

In this work a series of destructive and non-destructive measurements made on a series of Al_2O_3 lamellas coated with 1 μm of $^{10}B_4C$ have been presented. These tests were made in order to evaluate the suitability of the lamellas in order to realize a three dimensional cathode of a new ^{3}He-free thermal neutron detector. All the analyses have shown that the larger fraction of the measured samples (more than the 90%) are suitable to be used in the realization of the three dimensional cathode.

Acknowledgments

This work was supported within the CNR-STFC Agreement No. 01/9001 concerning collaboration in scientific research at the spallation neutron source ISIS. The financial support of the Consiglio Nazionale delle Ricerche in this research is hereby acknowledged.

2016 JINST 11 C03033

References

[1] European Spallation Source, https://europeanspallationsource.se.

[2] G. Croci et al., *GEM-Based thermal neutron beam monitors for spallation sources*, *Nucl. Instrum. Meth.* **A 732** (2013) 217.

[3] G. Croci et al., *Diffraction measurements with a boron-based GEM neutron detector*, *Europhys. Lett.* **107** (2014) 12001.

[4] IENI (Istituto per l'Energetica e le Interfasi), www.ieni.cnr.it.

[5] IFP (Istituto di Fisica del Plasma), www.ifp.cnr.it.

[6] ISIS-STFC, www.isis.stfc.ac.uk.

[7] IMAT (Imaging and Materials Science & Engineering), http://www.isis.stfc.ac.uk/Instruments/Imat/.

[8] C. Höglund et al., *Stability of $^{10}B_4C$ thin films under neutron radiation*, *Radiat. Phys. Chem.* **113** (2015) 14.

[9] C. Höglund et al., *B_4C thin films for neutron detection* , *J. Appl. Phys.* **111** (2012) 104908.

[10] J. Correa Magdalena, *$^{10}B_4C$ Multi-Grid as an alternative to 3He for Large Area Neutron Detectors*, PhD Thesis, University of Zaragoza (2012).

[11] ROTAX, http://www.isis.stfc.ac.uk/instruments/rotax/.

[12] http://www.exelisvis.com/ProductsServices/IDL.aspx.

[13] G. Croci et al., *The BAND-GEM detector: An improved efficiency GEM-based solution for thermal neutrons detection at spallation sources*, talk presented at the *4th Conference on Micro-Pattern Gaseous Detectors*, Trieste, Italy, October 12–15, 2015.

[14] H. Tietze-Jaensch et al., *The ROTAX/DIFF time-of-flight diffractometer at ISIS*, *Physica* **B 234–236** (1997) 1149.

[15] T. Nakamura et al., *High detection efficiency ZnS scintillator for a fiber-coded linear neutron detector for thermal neutron scattering instruments*, *IEEE Nucl. Sci. Symp. Conf. Rec.* (2008) 1215.

[16] D.J. Rej et al., *Neutron-capture-induced radiation treatment of polymeric materials*, *Appl. Phys. Lett.* **68** (1996) 2517.

2016 JINST 11 C03033

Paper 2

Performance of the high efficiency thermal neutron BAND-GEM detector

Andrea Muraro[1,†,*], Gabriele Croci[2,1,4,†], Enrico Perelli Cippo[1,†] ,Giovanni Grosso[1,†], Carina Höglund[5,7,†], Giorgia Albani[2,], Richard Hall-Wilton[7,8], Kalliopi Kanaki[7,], Fabrizio Murtas[3,], Davide Raspino[6,†], Linda Robinson[7,], Nigel Rodhes[6,], Marica Rebai[2,], Susann Schmidt[5,7], Erik Schooneveld[6,†], Marco Tardocchi[1,†] and Giuseppe Gorini[2,4,†]

[1]*Istituto di Fisica del Plasma "P. Caldirola", Associazione EURATOM-ENEA/CNR, Milano, 20125, Italy*
[2]*Dipartimento di Fisica "G. Occhialini", Università degli Studi di Milano-Bicocca, Milano, 20125, Italy*
[3]*Istituto Nazionale di Fisica Nucleare, Laboratori Nazionali di Frascati, Frascati, 0044, Italy*
[4]*Istituto Nazionale di Fisica Nucleare, Sezione di Milano Bicocca, Milano, 20125, Italy*
[5]*Dept. of Physics, Chemistry and Biology (IFM), Linköping University, SE-581 83 Linköping, Sweden*
[6]*STFC-ISIS Facility, Rutherford Appleton Laboratory, Didcot Uk*
[7]*European Spallation Source ESS AB, Tunavägen 24, 223 63 Lund, Sweden*
[8]*Mid-Sweden University, Sundsvall, Sweden*

[*]*E-mail: muraro@ifp.cnr.it*

[†] *These authors contributed equally to this work.*

Abstract New high count rate detectors are required for future spallation neutron sources where large areas and high efficiency (>50%) detectors are envisaged. In this framework, GEM is one of the explored detector technologies since they feature good spatial resolution (<0.5 cm) and timing properties, have excellent rate capability (MHz/mm^2) and can cover large areas (some m^2) at low cost. In the BAND-GEM (Boron Array Neutron Detector GEM) approach a 3D geometry for the neutron converter cathode was developed that is expected to provide an efficiency > 30% in the wavelength range of interest for SANS instruments. A system of aluminium grids with thin walls coated with 0.59 μm layer of $^{10}B_4C$ has been built and positioned in the first detector gap, orthogonally to the cathode. By tilting the grid-system with respect to the beam, there is a significant increase of effective thickness of the borated material crossed by the neutrons. As a consequence, both interaction probability and detection efficiency are increased. This paper presents the results of the performance of the BAND-GEM detector in terms of efficiency and spatial resolution.

Subject Index [Insert subject index codes here]

1. Introduction

Neutron diffraction and spectroscopy experiments using thermal neutrons are the core activity at spallation neutron sources. Detection systems nowadays make great use of ^{3}He-based gaseous detectors that offer the possibility to cover large areas (m^2) and have an intrinsic efficiency to thermal neutrons higher than 80%. The ^{3}He shortage [1] and its massive use in applications linked to homeland security have determined an exponential rise of its price, preventing its use for research applications including future neutron sources such as the European Spallation Source (ESS [2]). In the case of ESS, together with the need for replacing ^{3}He, it is essential to develop high-rate neutron detectors [3] able to fully exploit the increased neutron flux of ESS relative to the present neutron sources [4]. The situation calls for the development of large area and high-rate neutron detectors that do not use ^{3}He but have a comparable detection efficiency with a price ideally not exceeding 500 k€/m^2 and a spatial resolution between 1- 10 mm. This paper describes a new detector based on the GEM technology [5-8] that is able to detect beams at high rate (> 1 MHz/mm^2) and gives the possibility to cover large areas at low cost. Although GEM-based detectors are mostly used to detect charged particles, they can be adapted (typically by using a customised cathode configuration), to

detect neutral particles, such as neutrons and photons [9-12]. Several GEM detectors for fast and thermal neutron detection have been realized during the last years [13-30].

The BAND-GEM detector described in this paper aims at increasing the thermal neutron detection efficiency with respect to single layer boron based detectors such as the one described in [19] since its designed has been optimized for cold neutron energies. The strategy that has been adopted consists in the realization of a cathode with 3-dimensional structure similarly to what is described in [31-33].

2. BAND-GEM Detector construction

2.1. Principle of Operation

The Boron Array Neutron Detector based on the GEM technology (BAND-GEM) described in this paper is constituted by a Triple GEM detector equipped with a 3D converter cathode. The detector has an active area of 5x10 cm^2. Figure 1 shows a scheme of the detector layout. The first element at the bottom is a thin aluminium cathode. The 3D converter is made of a stack of twenty-four aluminium grids coated with about 0.59 µm of $^{10}B_4C$ (99% purity - see Figure 2). Each grid is 3 mm high, has an overall area of 12 x 7 cm^2 and is composed by eleven strips 10 cm long, 3 mm high and 200 µm thick. The pitch between the strips is 4 mm. All around the strips, there is an external frame that is 1 cm thick and that get also borated during the deposition. The internal side of this thick frame represents the boundary of the detector active area. Between the grids, there are 1 mm thick spacers made from fiberglass. Three standard GEM foils and an anode with pads of different dimensions are placed on top of the borated grid stack. If the full detector is inclined by few degrees (less than 10°) with respect to the incoming beam, neutrons are forced to cross the boron layers at grazing angles. As a consequence, interaction probability, as well as the detection efficiency, is augmented while keeping the beam perturbation small (due to the reduced volume of non-active material). Moreover, conservation of energy and momentum for the n(^{10}B,^{7}Li)α occurring in the layer implies that the two charged particles (^{7}Li and α) are emitted back to back with kinetic energies in the order of 1 MeV. It means that at least one of the (charged) reaction products is likely to leave the $^{10}B_4C$ layer and thus be revealed. The gas mixture used in the detector is Ar/CO_2 70%/30% and it is characterized by a mean work function of approximately 27 eV [34]. In order to get a signal the primary electrons created either by alpha particles or ^{7}Li ions must be able to move inside the grid system and reach the Triple GEM structure where they are multiplied.

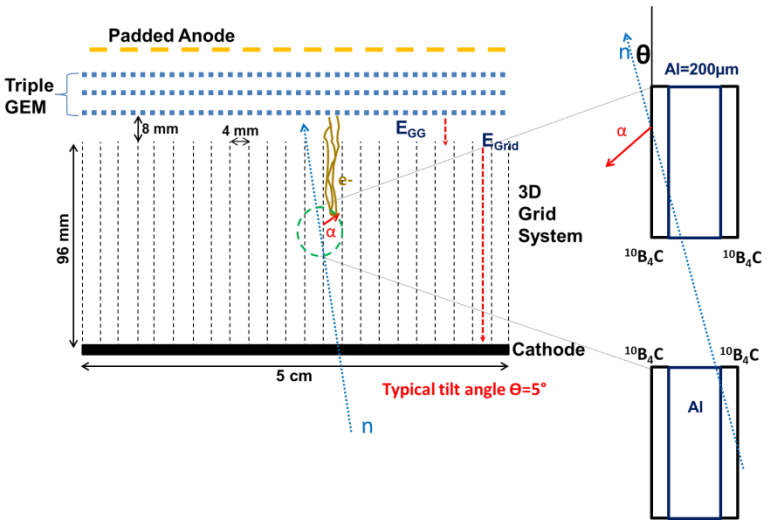

Figure 1: Detector schematics and principle of operation

2.2. The Grid System Engineering

In order to extract the primary charge, each grid is kept at a different voltage: this allows generating a drift field in the system that is as uniform as possible. A particular $^{10}B_4C$ coating procedure [35-37], performed at the ESS thin films deposition facility in Linkoping, co-located with Linkoping University [38], was studied in order to coat the thin walls of the grids that represent the active conversion area. The grid system can thus be considered as a *field cage* (similarly to what is done in [39]) and the potential to each grid is given through an external voltage divider that has the two ends connected between the planar cathode and the grid closest to the Triple GEM.

Figure 2: Example of the 3 mm thick grids used in the converter after $^{10}B_4C$ coating. The thickness of thin walls is 200 µm. The external area of the grid is 12 cm x 7 cm; the frame surrounding the thin walls is 1 cm thick.

A detailed engineering design (see Figure 3, top-left) has been performed in order to realize the full system guaranteeing that each grid is correctly positioned sustained and gets the right potential. The critical parameters for optimization of the detector performances are described in Table 2-1.

Geometrical parameter	**Value**
Strip pitch	4 mm
Grid Thickness	3 mm
Spacer Thickness	1 mm
Number of walls per grid	11
3D converter dimensions	10 cm (x) · 5 cm (y) · 9.6 cm (z)
Strip thickness	200 µm
Grid Bulk Material	Aluminium Al5754
B_4C Resisitivity	696 Ω cm
B_4C thickness on Al strips	0.55 µm
Divider Resistors	24 of 8 MΩ
Max Resistor Current	100 µA

Maximum Applied Voltage (bottom grid of the stack)	14.9 kV
Minimum Applied Voltage (top grid of the stack)	3.3 kV

Table 2-1: Geometrical and Electrical parameters of the present detector

Due to the complexity of the problem, numerical simulations using IDL [40] and Ansys+Garfield software [41] have been performed for the optimization of these parameters. These simulations are described in another paper[42].

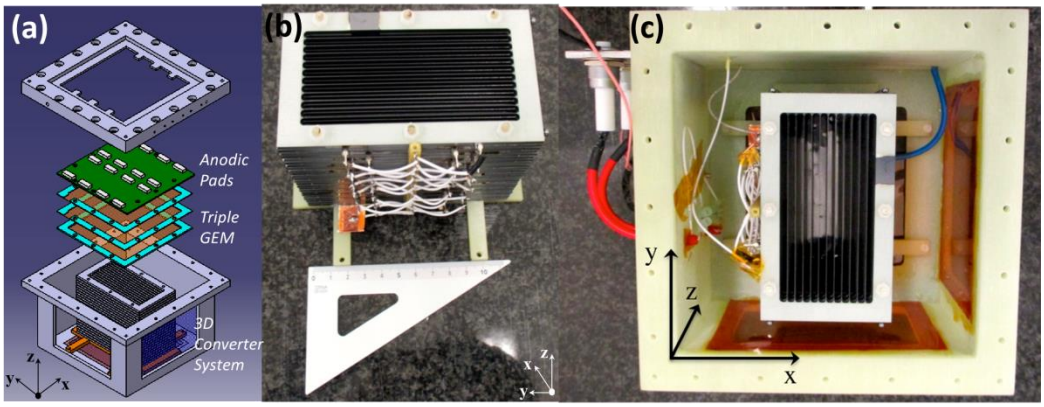

Figure 3: 3D converter system: (a) Exploded view of the detector CAD design describing the different components of the device, (b) 3D converter system completely assembled (c) 3D-converter system after its final insertion in the detector gas box. The white screws used for fixing are used also for alignment. The co-ordinate axes are described in Figure 6 relatively to the pad position. The z-axis represents the neutron direction when the detector is used at grazing angles

2.3. Detector Assembly and signals read-out.

Figure 3 and Figure 4 show a series of pictures of the detector assembly and containment box. The triple GEM box is closed on top of the grid box and the appropriate electric contacts are realized. This BAND-GEM detector is equipped with a padded anode (see Figure 4, right panel) composed of 128 pads, each with different dimensions (4 mm x 3 mm, 4 mm x 6 mm, 4 mm x 12 mm). The pads were realized with a step of 4 mm in the x-direction in order to match the strip pitch. The gap between two adjacent pads is equal to 200 µm, corresponding to the thickness of the thin strips. One of the most important procedures that were performed is the alignment of the pads with the 3D converter system. The alignment was obtained by means of centring holes positioned both in the detector box and in the detector lid were the anodic pads are located. By referring to this mechanical references, an alignment better than the centring holes tolerance (about 1/10 mm) was obtained. Out of 128 pads, only half have been read-out. The signal of each pad is routed to a different channel of a CARIOCA [43] chip whose connector is located on the back of the read-out anode board. The LVDS signals of each CARIOCA channel are then managed by a FPGA motherboard [44] that is located away from the detector and elaborates the signals in real-time thus providing the possibility of on-line monitoring of the thermal neutron beam. The high voltage is given to the three GEM foils by means of a custom designed NIM Module (HVGEM) [45]. The grid system is powered with a second module (CAEN A1526 [46]) that is able to deliver up to 15 kV.

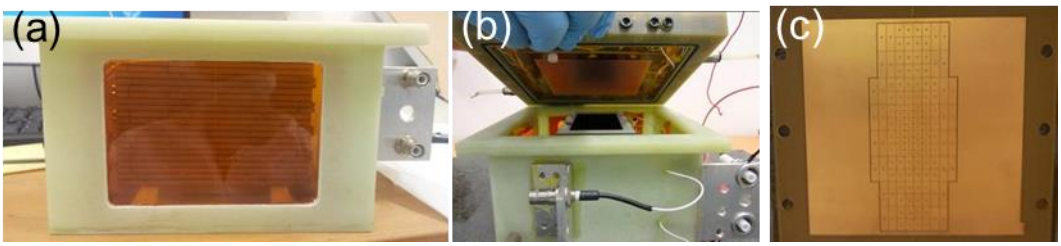

Figure 4: Final detector assembly: view from lateral diagnostic window of the 3D converter (a), mounting of the triple-GEM on top of 3D converter (b); photo of the anodic pads readout (c)

3. Performance Measurement using neutrons

3.1. Experimental Setup at the EMMA Beam-Line at ISIS

The detector was tested for the first time with a neutron beam on the EMMA instrument at on Target Station 1 at ISIS. Instruments located on Target Station 1 receive 4 pulses out of 5 coming from the source operating at a frequency of 50 Hz. The aim of the experiment was to conduct a characterisation of the detector, and measure the efficiency of the detector with respect to the tilt angle and the neutron wavelength. EMMA is a new instrument at ISIS. It is located at the place of the previous HET instrument [47]. The EMMA beam has maximum dimensions of 45 x 45 mm^2 but motorised jaws can define smaller beam sizes. The nominal beam divergence is about few mrad. The sample position is 16 m from the moderator and it is provided with a rotating and movable support. The range of available neutron wavelengths is approximately $\lambda = 1 - 4 \cdot 10^{-10}$ m corresponding to the energy range $E_n = 5 - 81$ meV. The incident beam monitor, positioned immediately behind the jaws (i. e. the beam dimension selector), is a commercial GS-20 Lithium Glass Scintillator with an efficiency at $\lambda = 1$ Å, ε_{bm} ($\lambda = 1 \cdot 10^{-10}$ m) = 0.60% ± 0.06%. The beam monitor efficiency scales linearly with λ in the range of interest of the instrument. A scheme of the EMMA setup is shown in Figure 5 and the pad layout is shown in Figure 6. The Θ angle is defined as the BAND-GEM tilting angle with respect to the incoming neutron beam and it is shown in Figure 1. Θ is set using a turn-table with a precision better than 0.1°.

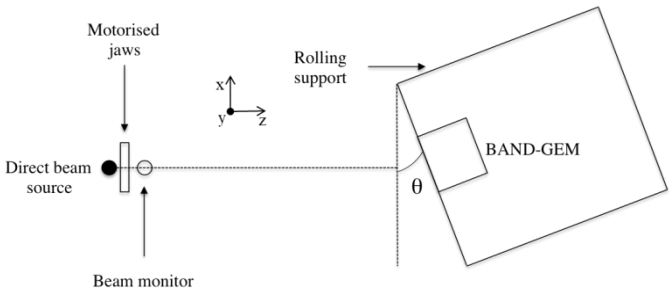

Figure 5: Scheme of the experimental setup on EMMA (Top view). The monitor to detector distance is about 40 cm and the jaws to source distance is about 16 m.

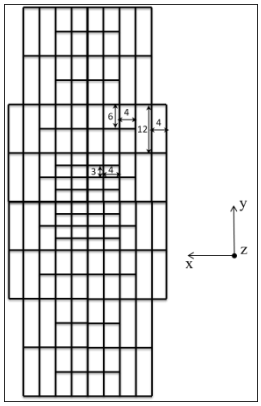

Figure 6: Pad layout with coordinate axis description and dimensions (mm).

Different setups were used for the various measurements performed, as summarised in Table 3-1.

Table 3-1: List of the measurements performed on the EMMA beamline. The definition of the coordinate x, y and z is shown in Figure 3 (c) where two diagnostic windows are also visible on the cathode plane (x-y) and along the 3D converter. Θ is the tilt angle of the movable support. The potential difference V_1, V_2 and V_3 are defined later in Figure 9.

Experimental Setup Used	Performed measurement
Θ=0°	V_1, V_2, V_3 scans (see text for details)
Θ=90°	Z scan (extraction efficiency η_C)
0°< Θ < 6°	Efficiency ε
0°< Θ < 5°	Position Resolution (FWHM)
Θ=5°, $1 \cdot 10^{-10}$ m < λ < $4 \cdot 10^{-10}$ m	Efficiency ε

The BAND-GEM detector was positioned in the beam immediately behind the beam monitor and it was mounted on the x/y/z/Θ positioner. In Figure 7 the setups for Θ=0°, with the cathode facing the beam source and Θ=90°where the beam hits the side of the 3D converter passing through a diagnostic window are shown.

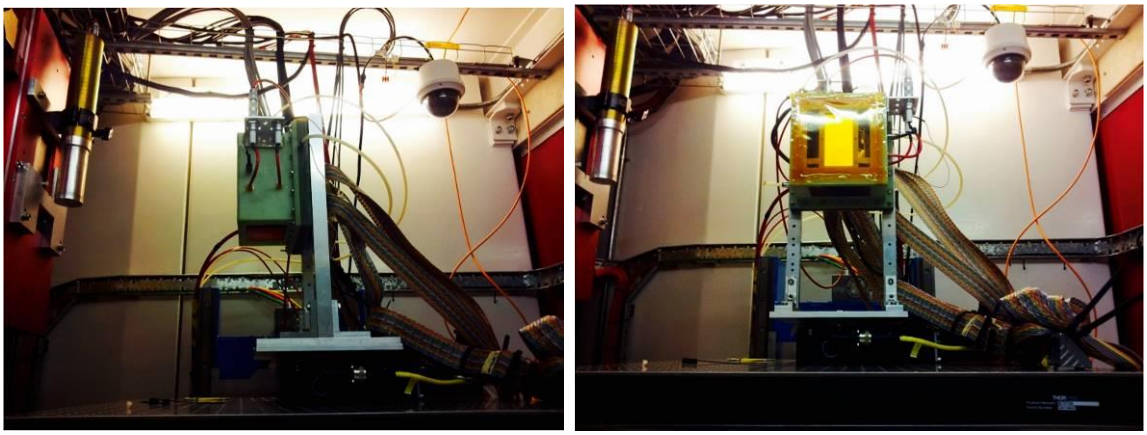

Figure 7: BAND-GEM setup on EMMA for Θ=0° (left) and Θ=90° (right).

The voltage divider of the 3D converter was biased using two channels of the 15 kV high voltage module, while the triple GEM was biased using the custom made HVGEM module. Following this configuration the maximum achievable value of electric field inside the grid system is about 1.5 kV/cm. The gas used during all the measurements is a 70%/30% Ar/CO_2 mixture with a flow rate of about 20 l/h. Since the detector volume is 4.4 l, this means that during a 24 h period, the gas was replaced about 100 times.

3.2. Time of Flight analysis

Due to the pulsed structure of the ISIS spallation source, energy-resolved measurements can be performed using the Time of Fight technique (ToF). This feature represents a crucial point in order to characterize the response of the BAND-GEM at different neutron wavelengths. The LVDS signals generated by the CARIOCAs were routed to a user-designed FPGA board that formed the interface between the front-end electronics and the standard ISIS Data Acquisition Electronics (DAE), known as DAE2 [49]. Data from the CARIOCAs were first buffered inside the FPGA, using an individual buffer per GEM pad, so that the interface electronics did not introduce any additional dead time. When the FPGA found data in one of the buffers, the position of the corresponding GEM pad that generated the signal was sent to the DAE for histogramming. The DAE performed the time stamping of these events and incremented the corresponding bin in the ToF histogram associated with this GEM pad, thereby creating a ToF spectrum $S_i(t)$ for each BAND-GEM pad. The bin width applied by DAE for ToF spectra reconstruction is 100 µs. Given that neutrons can travel up to about 96 mm in the 3D converter system, it is important to verify that the time spent by the neutron before being captured has a negligible effect on the ToF measurement. An error on the ToF measurement induces a wrong reconstruction of the neutron wavelength. Once captured, the delay introduced by the drift of the primary electrons (coming from charged neutron products ionization) in the 3D converter system can be considered negligible since the average electron velocity inside the 3D-converter system is about 7 cm/µs [48] that is much higher than the velocity of incoming neutrons. The range of neutron velocity on EMMA is approximately between v_1 = 3950 m/s ($\lambda = 1 \cdot 10^{-10}$ m) and v_2 = 990 m/s ($\lambda = 4 \cdot 10^{-10}$ m). Neutrons with such velocities can introduce a delay up to 25 µs and 100 µs respectively. Since this delay is comparable with the bin width used by the DAE, it may introduce a maximum absolute error on neutron wavelength determination that is less than $0.025 \cdot 10^{-10}$ m. The signal from the reference EMMA beam monitor was also routed to the DAE2 and a time of flight spectrum M(t) was created also for this detector. The results are shown in Figure 8. Time of flight spectra obtained with the two detectors (BAND-GEM and beam monitor) are consistent.

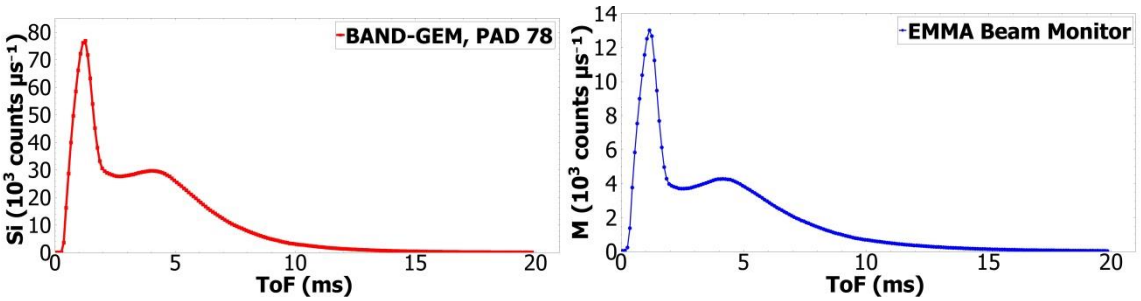

Figure 8: Time of Flight spectra recorded for one of the BAND-GEM pad (top) and for the EMMA GS20 beam monitor (bottom). The exposure time to neutron was 6 hours and 30 minutes, corresponding to a proton current of 950 µA.

The analysis for different neutron wavelengths is performed by slicing the ToF spectrum. The relation between ToF and neutron wavelength for EMMA is shown in Table 3-2.

$\lambda(10^{-10}$ m)	TOF (ms)
1	4.000
2	8.060
3	12.560
4	17.060

Table 3-2: ToF and λ relationship on EMMA

The counting rate for a certain λ interval is thus calculated for the i-th pad of the BAND-GEM and for the beam monitor respectively as

$$C_i(t=\lambda) = \int_{t1}^{t2} S_i(t)dt \quad C_M(t=\lambda) = \int_{t1}^{t1} M(t)dt$$

Where t_1 and t_2 represents the ToF interval used for the calculation and $S_i(t)$ and $M(t)$ are the ToF spectra. If more than one BAND-GEM pad is hit by the beam, the quantity

$$I_{GEM} = \sum_{i=1}^{n} C_i$$

represents the integrated counting rate for that specific λ interval over all the *n* active pads.

3.3. Working point determination

In order to establish the BAND-GEM working point, three potential difference scans have been performed for the three main voltage values (for simplicity named V_1, V_2 and V_3) shown in Figure 9

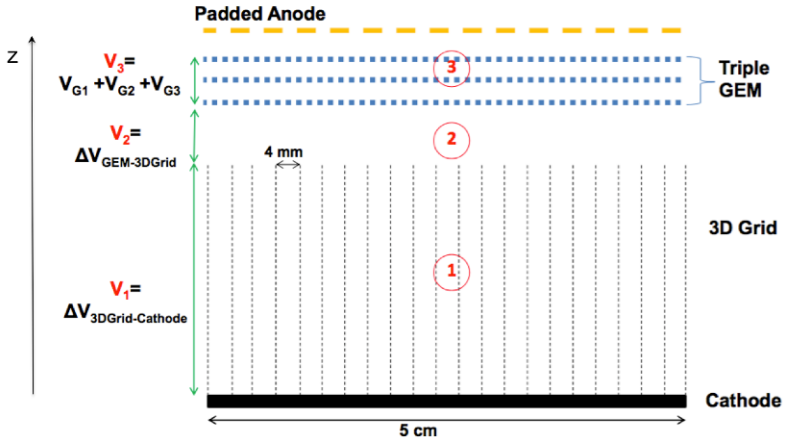

Figure 9: Definition of V_1, V_2 and V_3 parameters: V_1 is the potential difference applied across the full 3D converter, V_2 is the potential difference between the top grid and the bottom of the first GEM and V_3 is the sum of the three potential difference applied to the triple GEM stage.

All measurements for the working point determination were performed at Θ=5° and using a neutron beam with dimensions of 4 mm x 4 mm. The beam-footprint reconstructed using this setting is shown in Figure 10.

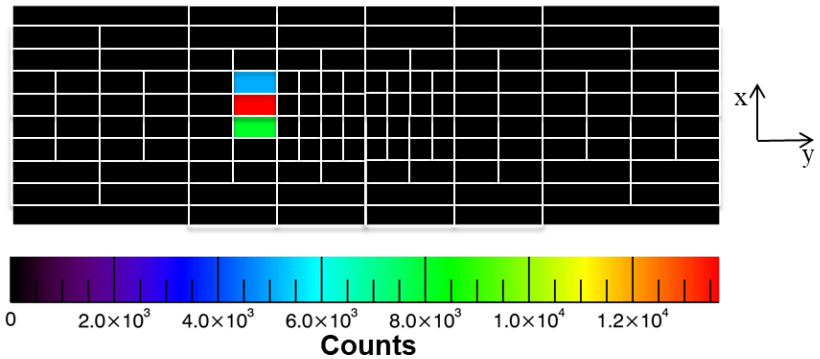

Figure 10: Beam footprint reconstructed using a beam dimension of 4 mm x 4 mm and a tilting angle Θ=5°. The colour scale represents C_i (integrated counts) normalized to the pad area calculated for 1 · 10^{-10} m < λ < 4 · 10^{-10} m . For coordinate axis definition See Figure 5 (b) – colour on-line.

V_1 Scan

The integrated counting rate I_{GEM} is an increasing function of V1 and in particular it reaches a plateau for values higher than 8 kV (see Figure 11). The occurrence of a plateau indicates that the charge extraction efficiency (see paragraph 3.4) is practically saturated. A value of V_1 = 11.1 kV was chosen as working point.

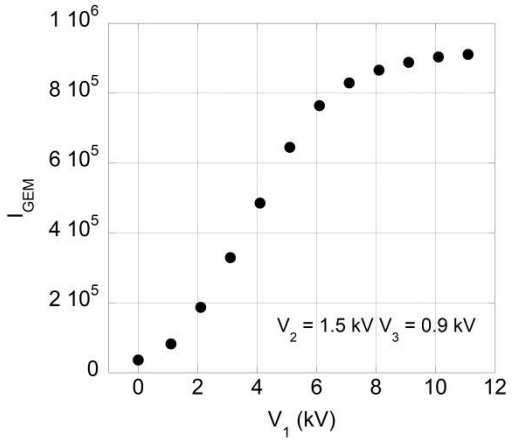

Figure 11: V_1 scan. I_{GEM} is calculated for 1 · 10^{-10} m < λ < 4 · 10^{-10} m .

V_2 Scan

The integrated counting rate I_{GEM} is a slowly increasing function of V_2 and reaches a plateau for values higher than 1.2 kV. A value of V_2 = 1.5 kV was chosen as working point.

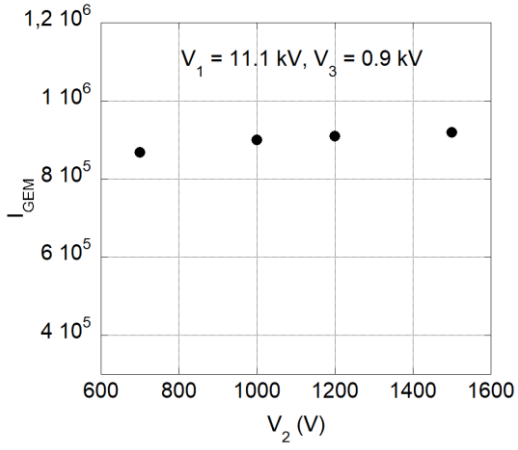

Figure 12: V_2 scan. I_{GEM} is calculated for 1 · 10^{-10} m < λ < 4 · 10^{-10} m .

V_3 Scan

The gas gain of Triple GEM based detectors depends exponentially on V_3. Due to the loss of primary charge in the 3D converter (see paragraph 3.4), it is useful to increase the gas gain. However, as

already shown in previous papers, a too high gain makes GEM-based detectors sensitive to gamma-ray background [50].

I_{GEM} for $1 \cdot 10^{-10}$ m < λ < $4 \cdot 10^{-10}$ m was measured as a function of V_3 and the results are shown in Figure 13. The two curves shown in Figure 13 represent an open/free beam measurement (circles) and a measurement with a 1 mm thick sheet of Cd interposed between the EMMA jaws and the BAND-GEM (square). The second setup has been used to measure the gamma sensitivity of the detector, since the Cd foil stops all thermal neutrons with energies lower than 0.5 eV (i.e λ > $0.4 \cdot 10^{-10}$ m) and through neutron capture generates gamma rays with energy ranging between 0.6 and 4 MeV [51]. The counting rate is an increasing function of V_3 and, as expected, the detector starts to detect thermal neutrons at a voltage V_3 = 810 V (i. e. a gain of about 50). In order to increase the counting rate, the voltage was set to 1020 V and a slight variation of the slope of the curve is observed at V_3 = 920 V. The gain corresponding to this voltage (about 300) was interpreted as the gain where the detector starts to be sensitive to gamma rays. This statement is confirmed by the Cd measurement where I_{GEM} changes slope for V_3 > 900 V that corresponds to an effective gas gain > 200. This result is compatible with what was obtained previously and described in [50]: according to the results presented in [50] the GEM detector has sensitivity to gamma rays of about 10^{-5} at this gain. A value of V_3 = 900V was chosen as working point.

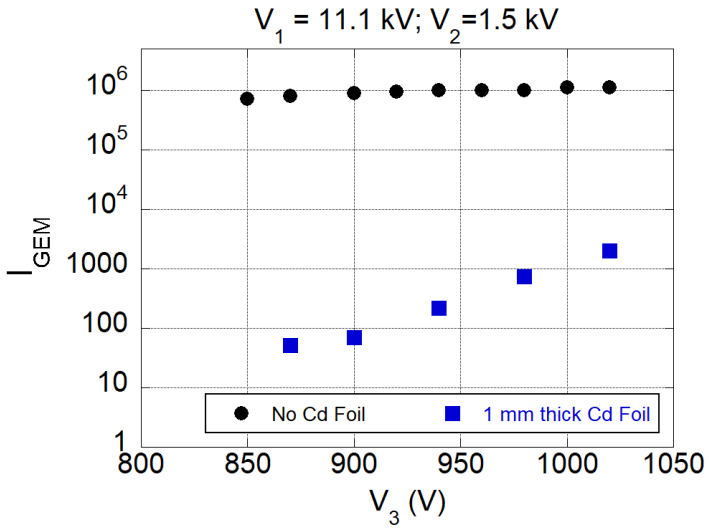

Figure 13: V_3 scan. I_{GEM} is calculated for $1 \cdot 10^{-10}$ m < λ < $4 \cdot 10^{-10}$ m .

3.4. Measurement of charge extraction efficiency η_C

One of the most important parameters to be determined when working with a 3D converter that operates also as a field cage is the capability of extracting the primary charge that is released by neutron capture products (either alphas or Li ions). In order to perform these measurement the neutron beam area was set to 4 mm x 4 mm and Θ was set to 90° so that the beam entered 3D converter from the side through a diagnostic window that has a dimension of 75 mm (z) * 100 (x) mm (see Figure 4 and Figure 7). The beam position was moved along the z axis (see Figure 3) and the measurement was repeated for different V_1 values ranging from 3.3 kV to 11.1 kV. The beam footprint for one of the measurement is shown in Figure 14.

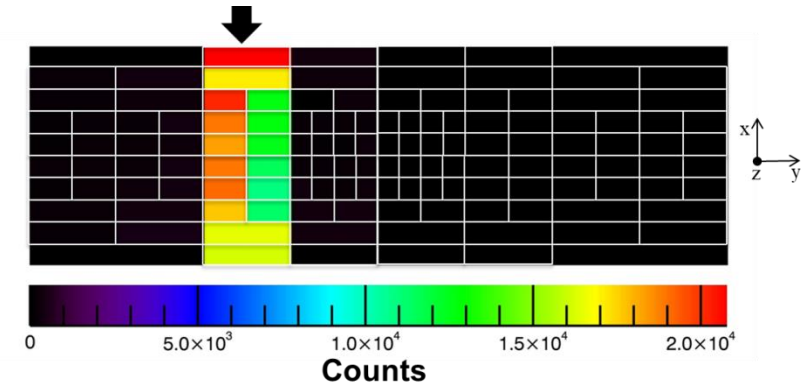

Figure 14: Beam footprint reconstructed using a beam dimension of 4 mm x 4 mm and a tilting angle Θ=90°. The colour scale represents $C_{BAND\text{-}GEM,PAD\ i}$ (integrated counts) normalized to the pad area calculated for $1 \cdot 10^{-10}$ m $< \lambda < 4 \cdot 10^{-10}$ m. The arrow indicates the incident neutron direction. For coordinate axis definition see Figure 5 (b) – colour online.

The results of z-scans for different V_1 are shown in Figure 15**.**

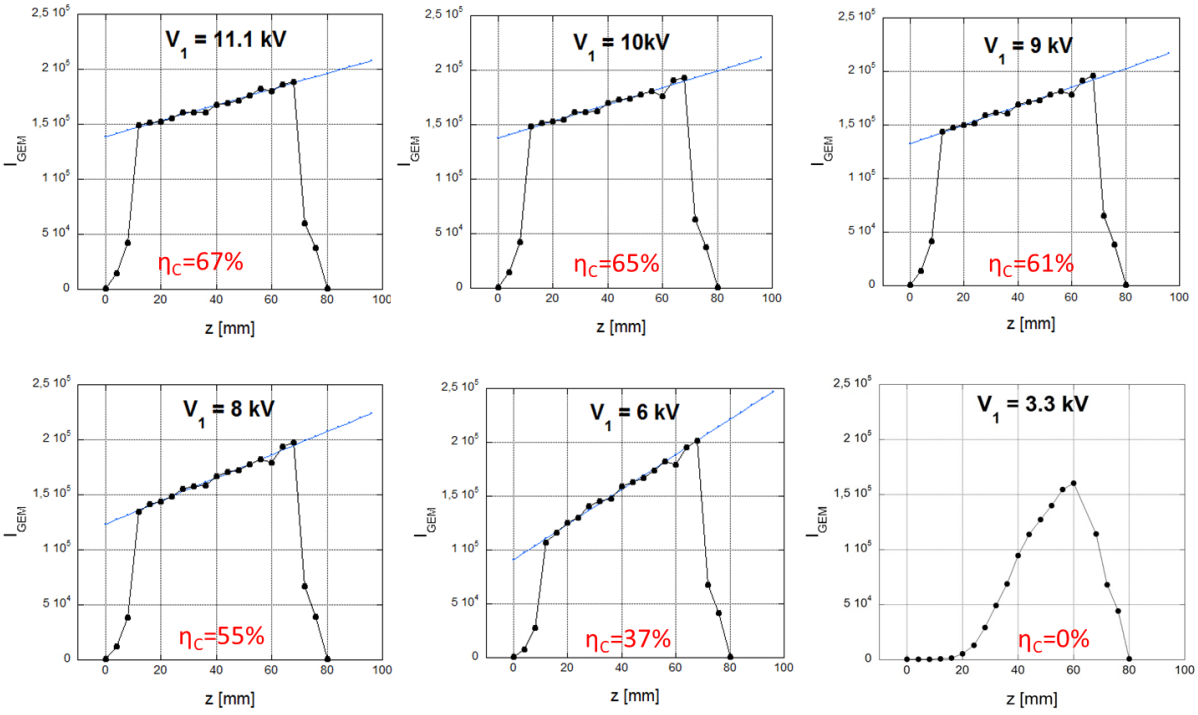

Figure 15: Measurement of the charge extraction efficiency for different V_1

In Figure 14 the plots of the z scan for six different values of V_1 are shown. The width of the lateral diagnostic window is only 75 mm meaning that the range that can be completely explored is 12 mm < z < 68 mm using a beam of 4 mm x 4 mm: in this range $I_{GEM}(z)$ is found to be linear for not too low V_1 values Outside this z range the values of I_{GEM} can be extrapolated from the measured ones as shown in Figure 14. The relative charge extraction efficiency η_C is defined as $\eta_C = I_{GEM}$ (z=0 mm)/I_{GEM}(z=96 mm) and the values for different applied V_1 are shown in the different panels of Figure 14 (z = 0 mm at the bottom and z = 96 mm is at the top of the 3D converter). Ideally one would like η_C to be as close as possible to unity which would provide uniform charge extraction efficiency. This is not the case and a fraction of charge is inside the 3D converter. The linear dependence of I_{GEM} on z suggests

that the loss is caused by a geometrical effect (physical presence of grids). The last panel of such figure however shows that at too low voltages the charge extraction is not satisfactory.

3.5. Neutron detection efficiency determination

The neutron detection efficiency was measured using a beam dimension of 4 mm x 4 mm and for Θ values ranging from 0° to 6°. In this configuration the beam footprint is similar to the one shown in Figure 10. The efficiency ε_{GEM} of the BAND-GEM detector was obtained as:

$$\varepsilon_{GEM}(\lambda) = \frac{I_{GEM}(t=\lambda)}{C_M(t=\lambda)} * \varepsilon_1$$

Where $\varepsilon_1 = \varepsilon_{bm}$ ($\lambda = 1 \cdot 10^{-10}$ m) = 0.60% ± 0.06%. The efficiency of the beam monitor was previously been measured using a well calibrated ^{3}He detector as reference. The working points values V_1=11.1 kV, V_2=1.5 kV, V_3= 0.9 kV obtained in the previous section have been used in the following measurements.

Efficiency measurement as a function of tilting angle Θ

The detector efficiency was determined as function of Θ for two wavelengths by considering the corresponding ToF periods. Figure 16 shows that for Θ > 2° the detector reaches an efficiency plateau of about 17% and 30% for $\lambda = 1$ and $2 \cdot 10^{-10}$ m respectively. The measurement is compared to a numerical simulation (using IDL, Ansys and Garfield++) that has been superimposed. Figure 16 shows that measurements and simulations results are compatible. The small dips that can be observed at Θ=2.5° in Figure 16 are due to geometrical effect related to the parameters of the 3D converter cathode. At this angle the thickness of $^{10}B_4C$ crossed by the neutrons results to be lower with respect to Θ>3°. Due to the coarser granularity of the performed scan this effect was not experimentally appreciated. A finer angular scan for 2°<Θ<3° is needed to measure this effect. Details of the simulation are provided in another paper that is presently under submission [42].

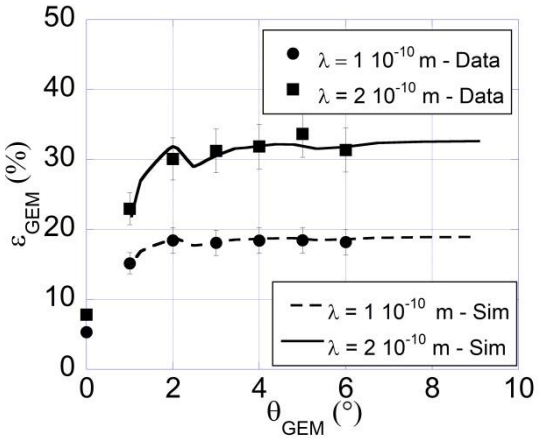

Figure 16: BAND-GEM efficiency as function of tilt angle Θ for two neutron wavelengths. Data are compared with simulations [39].

Efficiency as function of neutron wavelength λ

The efficiency of the detector was determined also as function of neutron wavelength in the range $1 \cdot 10^{-10}$ m < λ < $4 \cdot 10^{-10}$ m accessible on EMMA. The results are shown in Figure 17. A value of efficiency higher than 40% is obtained at $\lambda = 4 \cdot 10^{-10}$ m which makes this technology competitive with other detectors for small angle neutron scattering (SANS) applications. A tilt angle Θ=5° has been set for this measurement.

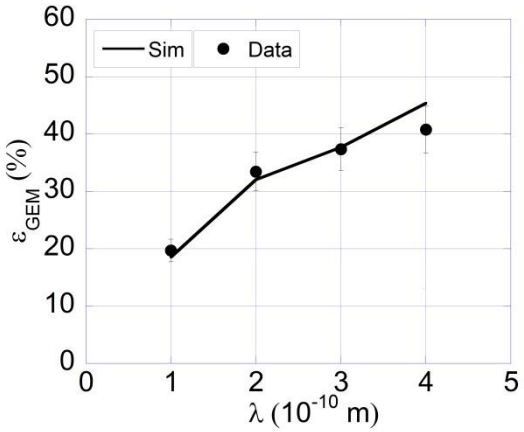

Figure 17: BAND-GEM efficiency as function of neutron wavelength and comparison with IDL+Ansys+Garfield simulation [39].

3.6. Position resolution determination

As explained in paragraph 2.1, in order to increase the detection efficiency, the BAND-GEM detector must be tilted by few degrees. Due to this feature, a neutron trajectory can give signals in 2-4 adjacent gaps and thus more than one pad per event can collect charge. This is due to the probability *p* of a neutron to be absorbed in a single strip (each made of two boron layers). If p is the absorption probability every time a neutron crosses a thin wall of a borated grid (*p* only depends on the boron capture cross section and the angle at which the strip is crossed), then a probability density function can be constructed following the description in Figure 18.The spatial resolution is therefore defined as the FWHM of the distribution of the joint probability P of a neutron to be absorbed in either one of the two strips adjacent to a specific gap and to release by-products into this specific gap.

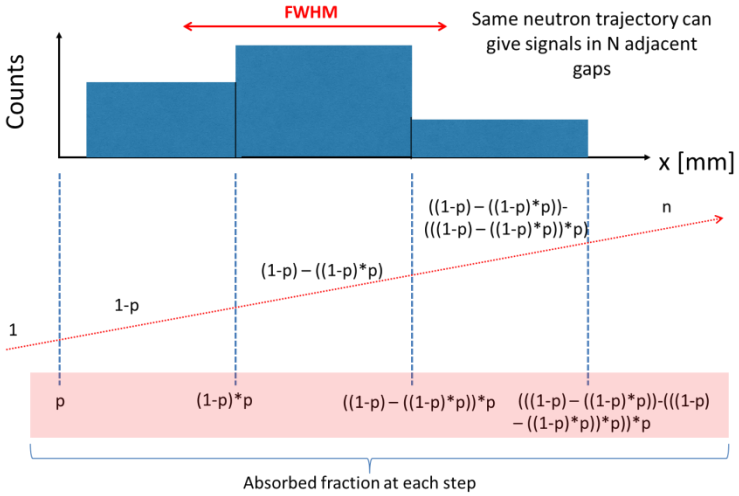

Figure 18: BAND-GEM position resolution is defined as the of FWHM of a probability density distribution of charge collection events in adjacent gaps

Analytically the probability density function p(x) [52] can be written for the first three intercepted gaps as

$$p(x)=\begin{cases} p\ (GAP\ 1) \\ p(p^2\text{-}3p+2)\ (GAP\ 2) \\ p\ (\text{-}p^3+3p^2\text{-}3p+1)(GAP\ 3) \\ \ldots..\ (GAP\ 4) \\ \ldots. \end{cases}$$

which has first and second order momenta given by

$$\boldsymbol{\mu = \frac{\int_{GAP1}^{GAPn} x * p(x)dx}{\int_{GAP1}^{GAPn} p(x)dx} = \frac{-10p^3 + 36p^2 - 48p + 24}{-p^3 + 4p^2 - 6p + 4}}$$

and

$$\boldsymbol{\sigma^2 = \frac{\int_{GAP1}^{GAPn} (x - \mu)^2 * p(x)dx}{\int_{GAP1}^{GAPn} p(x)dx}}$$

where GAP_n is the last gap that can be crossed by a neutron trajectory and depends on the incident angle. The FWHM of the p(x) distribution is

$$FWHM = 2.35\sqrt{\sigma^2}$$

and can be used as an estimate of the spatial resolution of the detector.

Results of the calculation along with measured FWHM values at different angles and for two neutron wavelengths are shown in Figure 19. These were obtained by illuminating the detector with a pencil beam of neutrons (4 x 4 mm^2). The measured resolution approaches the one defined for the ideal case and does not depend on the neutron energy. The ideal case implies a precise alignment between the pads and the 3D converter system. The method adopted in order to guarantee the alignment within certain limit was described in par 2.3. The slope variation of the curves present for Θ=3° is due to the fact that a higher number of coated strips is crossed by the neutron beam (see the scheme shown in Figure 18). Up to Θ=3°, the number of coated strips intercepted by the neutron beam is maximum one, thus maximum two gaps can give a signal (i.e. the histogram of Figure 18 would be narrower). A narrower distribution features a lower FWHM value. For Θ>3°, the number of coated strips intercepted by a neutron trajectory becomes more than one, thus implying a broader signal distribution. These results are particularly important for SANS applications.

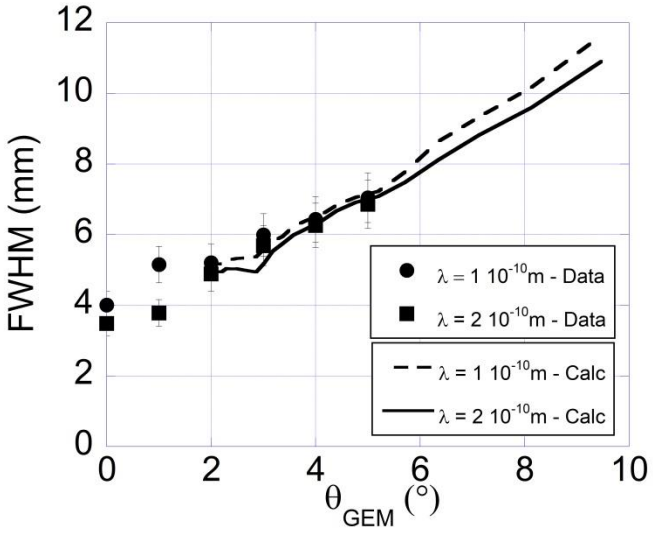

Figure 19: Measured BAND-GEM spatial resolution versus the tilt angle and comparison with calculation

Conclusions and future perspectives

The BAND-GEM detector described in this paper is one of the most recent developments of neutron detectors based on complex converters: the boron layers are distributed in a number of grids composing a 3D converter, and a proper regulation of the field inside the converter ensures good charge collection. A feature of the 3D converter is that, if the whole detector is tilted by an angle Θ with respect to the direction of incoming neutrons, the thickness of $^{10}B_4C$ crossed by the neutrons is increased by a factor $1/\sin(\Theta)$ so that the neutron "conversion" probability is enhanced and thus the detection efficiency. The detector was tested on the EMMA instrument at ISIS. A measurement of the relative charge extraction efficiency across the 3D converter resulted in values up to $\eta_C = 67\%$. The efficiency ε_{GEM} approaches 40% at $\lambda = 4 \cdot 10^{-10}$ m for a tilt angle $\Theta = 5°$. The space resolution measured for this angle is ~7 mm and is independent on neutron energy. These and other features achieved with this new technology, make it an attractive candidate for Small Angle Neutron Scattering Applications. Most of the SANS instruments (e.g. D22 at ILL and Sans2d at ISIS [53]) are nowadays equipped with ^{3}He tubes that are traditionally the most commonly used thermal neutron detectors. These detectors assure efficiency larger than 80%, spatial resolution in the order of 5 mm (depending on specific tube geometry) but their rate capability is limited to 30-50 kHz/tube. In addition, the exponential rise of the price of ^{3}He makes it prohibitive to realize new instruments entirely based on ^{3}He technology. The increase of neutron fluency expected in the future spallation sources (like ESS) required development of new detectors and the one described in this paper belong to this new detector family. The BAND-GEM technology is thus one of the candidates for installation (after further optimisation) on Small Angle Neutron Scattering instrument such as LoKI, one of the first instruments to be installed at the European Spallation Source. Further steps will be the construction of a full detector module suitable for installation on LoKI [54].

Acknowledgements

We would like to thank A. Balla, G. Corradi and D. Tagnani from the electronic group of Laboratori Nazionali di Frascati (INFN) for all the support about the design of the detector pads and electronics. This work was supported within the CNR-STFC agreement No. 01/9001 concerning collaboration in scientific research at the spallation neutron source ISIS. The financial support of *Consiglio Nazionale delle Ricerche* (CNR-Italy) is hereby acknowledged. This work was also setup in collaboration and financial support of INFN-group V. Richard Hall-Wilton and Susann Schmidt would like to acknowledge the financial support of the EU H2020 Brightness Project, grant agreement 676548.

References

1. Pacific North-west Laboratory, The ^{3}He Supply problem (available at: http://www.pnl.gov/main/publications/external/technical_reports/PNNL-18388.pdf)
2. European Spallation Source (available at http://europeanspallationsource.se/)
3. O. Kirstein et al. "Neutron Position Sensitive Detectors for the ESS", PoS (Vertex2014) 029 (2014); arXiv:1411.6194
4. S. Peggs et al., "European Spallation Source Technical Design Report", Report 2013-0001. Esss.se
5. F. Sauli, Nucl. Instrum. Meth. A, 386, 531 (1997).
6. S. Duarte Pinto et al, J. Instrum 4 P12009 (2009).
7. M. Villa et al, Nucl. Instrum. Meth. A, 628, 182 (2011).
8. M. Alfonsi et Al, Nucl. Instrum. Meth. A 617, 151 (2010)
9. M. Alexeev et Al, Nucl. Instrum. Meth. A 610, 174 (2009)
10. M. Alexeev et Al, Nucl. Instrum. Meth. A 617, 396 (2010)
11. M. Alexeev et Al, J. Instrum 5 P03009 (2010)
12. M. Alexeev et Al, Nucl. Instrum. Meth. A 623, 129 (2010)
13. M. Rebai et Al , Review of Scientific Instruments, 83, 02B721 (2012)

14. R. Pasqualotto et Al, Review of Scientific Instruments, 83, 02B103 (2012)
15. G. Croci et Al, J. Instrum 7 C03010 (2012)
16. F. Murtas et Al, J. Instrum 7 P07021 (2012)
17. G. Croci et Al, Nucl. Instrum. Meth. A 720, 144, (2013)
18. G. Croci et Al, Nucl. Instrum. Meth. A 712, 108 (2013)
19. G. Croci et Al, Nucl. Instrum. Meth. A 732, 217 (2013)
20. G. Croci et Al , EPL, 107 (2014) 12001
21. G. Croci et Al, Prog. Theor. Exp. Phys. (2014) 083H01
22. G. Albani et Al, J. Instrum 10 C04040 (2015)
23. G. Croci et Al, EPJP (2015) 130:118
24. E. Perelli Cippo, G. Croci et Al, J. Insturm 10 P10003 (2015)
25. A. Muraro et Al, Nucl. Instrum. Meth A. 813, 147, (2016)
26. D. Pfeiffer et Al, J. Instrum 10, P04004 (2015);
27. H. Oshita et al., Nucl. Instrum. Meth. A 623, 126 (2010).
28. M. Shoji et Al, J. Instrum, 7 C05003 (2012)
29. H. Oshita et Al, Nucl. Instrum. Meth. A 672, 75 (2012).
30. D. Pfeiffer et Al, J. Instrum 11, P05011 (2016)
31. G. Albani et Al, Meas. Sci. Technol. 27 115902
32. M. Köhli et al. Nucl. Instrum. Meth A 828, 242 (2016)
33. M. Henske et al. Nucl. Instrum. Meth A 686, 151 (2012)
34. F. Sauli, Principles of operation of multiwire proportional and drift chambers, CERN-77-09, CERN Yellow Report
35. C. Höglund et al., Journal of Applied Physics 111, 104908 (2012)
36. C. Höglund,K. et Al, Radiation Physics and Chemistry 113 , 14-19 (2015)
37. S. Schmidt, et Al, Journal of Materials Science 51, Issue 23 (2016)
38. https://liu.se
39. B. Ketzer Nucl Instrum A 732 , 237 (2013)
40. https://www.harrisgeospatial.com/docs/using_idl_home.html;
41. www.ansys.com; https://cern.ch/garfieldpp
42. A. Muraro et Al, BAND-GEM Detectors for Loki@ESS, Poster at 4th International Conference Frontiers in Diagnostic Technologies, LNF-INFN 30/03/2016 – 01/04/2016
43. W Bonivento et al, Nucl. Instrum. Meth. A, 491, 233 (2002).
44. A. Balla, et al, Nucl. Instrum. Meth. A, 628, 194 (2011).
45. Design of the FPGA-MB and of HVGEM Module, Gemini LNF Web Site, https://web.infn.it/GEMINI/
46. http://www.caen.it/csite/CaenProd.jsp?idmod=890&parent=20
47. T.G. Perring, The Resolution Function of the Chopper Spectrometer HET at ISIS, Journal of Neutron Research, Proceedings of the Twelfth Meeting of the International Collaboration on Advanced Neutron Sources (ICANS-XII), Cosener's House, Abingdon, UK, May 24-28, 1993, pp. I-328 to I-337
48. Y.Assran et al., "Transport Properties of operational gas mixtures used at LHC", arXiv:1110.6761
49. WCA Pulford, et Al. Institute of physics conference series, number 97, pages 537–547
50. G. Croci et Al, J. Instrum 8 P04006 (2013)
51. Reardon A. William et Al, Phisical Review, Volume 91, Number 2, (1953)
52. George W. Collins, Fundamental Numerical Methods and Data Analysis, NASA Astrophysics Data System (ADS)
53. http://www.ill.eu/instruments-support/instruments-groups/instruments/d22/description/instrument-layout/; http://www.isis.stfc.ac.uk/instruments/sans2d/sans2d3000.html
54. Jackson, A.J et Al, LoKI - A Broad Band High Flux SANS Instrument for the ESS, Proceedings ICANS XXI Conference, 10.11484/jaea-conf-2015-002

Paper 3

Nuclear Instruments and Methods in Physics Research A 813 (2016) 147–152

Contents lists available at ScienceDirect

Nuclear Instruments and Methods in Physics Research A

journal homepage: www.elsevier.com/locate/nima

Performance of the full size nGEM detector for the SPIDER experiment

A. Muraro [a,b,*], G. Croci [a,b,d], G. Albani [b], G. Claps [c], M. Cavenago [e], C. Cazzaniga [b], M. Dalla Palma [f], G. Grosso [a], F. Murtas [c], R. Pasqualotto [f], E. Perelli Cippo [a], M. Rebai [b], M. Tardocchi [a], M. Tollin [a], G. Gorini [b,d]

[a] Istituto di Fisica del Plasma "P. Caldirola" – CNR, Milan, Italy
[b] Dipartimento di Fisica "G. Occhialini", University of Milano-Bicocca, Italy
[c] Laboratori Nazionali di Frascati – INFN, Frascati, Italy
[d] Sez. INFN Milano-Bicocca, Milano, Italy
[e] Laboratori Nazionali di Legnaro – INFN, Legnaro, Italy
[f] Consorzio RFX, Padova, Italy

ARTICLE INFO

Article history:
Received 15 July 2015
Received in revised form
10 November 2015
Accepted 9 December 2015
Available online 14 January 2016

Keywords:
GEM (Gas Electron Multiplier)
Fast neutrons beam monitors
ITER
Neutral beam

ABSTRACT

The ITER neutral beam test facility under construction in Padova will host two experimental devices: SPIDER, a 100 kV negative H/D RF beam source, and MITICA, a full scale, 1 MeV deuterium beam injector. SPIDER will start operations in 2016 while MITICA is expected to start during 2019. Both devices feature a beam dump used to stop the produced deuteron beam. Detection of fusion neutrons produced between beam-deuterons and dump-implanted deuterons will be used as a means to resolve the horizontal beam intensity profile. The neutron detection system will be placed right behind the beam dump, as close to the neutron emitting surface as possible thus providing the map of the neutron emission on the beam dump surface. The system uses nGEM neutron detectors. These are Gas Electron Multiplier detectors equipped with a cathode that also serves as neutron–proton converter foil. The cathode is designed to ensure that most of the detected neutrons at a point of the nGEM surface are emitted from the corresponding beamlet footprint (with dimensions of about 40×22 mm^2) on the dump front surface. The size of the nGEM detector for SPIDER is 352 mm $\times$ 200 mm. Several smaller size prototypes have been successfully made in the last years and the experience gained on these detectors has led to the production of the full size detector for SPIDER during 2014. This nGEM has a read-out board made of 256 pads (arranged in a 16×16 matrix) each with a dimension of 22 mm $\times$ 13 mm. This paper describes the production of this detector and its tests (in terms of beam profile reconstruction capability, uniformity over the active area, gamma rejection capability and time stability) performed on the ROTAX beam-line at the ISIS spallation source (Didcot-UK).

1. Introduction

SPIDER [1,2] is the ITER beam source prototype in the neutral beam test facility hosted at Consorzio RFX in Padua, Italy, which has to demonstrate the feasibility of the deuterium beam injectors for the ITER fusion experiment [3]. SPIDER will start operation in 2016 and its main goal is to prove the capability to generate a 1 h long D^- beam pulse at the 40 A current level required by ITER but with a reduced beam energy (up to 100 keV). The 100 keV deuterons will be dumped against a target (the beam dump) tilted by 60° relatively to the beam axis (Fig. 1). The beam dump is composed of two rectangular panels made of a vertical array of CuCrZr-alloy water-cooled hypervapotrons with an elemental composition of about 99% Cu. The SPIDER D^- beam is composed of 1280 beamlets arranged in 4×4 rectangular arrays of 5 (horizontal) $\times$ 16 (vertical) beamlets each, whose axes projected on the dump panels are 40 mm and 22 mm respectively. The total beam current of 40 A is spread out over a surface of $\approx$ 1 m^2 for a reference average current density of 40 A/m^2 and deuterium flux of 2.5×10^{20} D/m^2 s. The neutron production due to fusion reactions between beam deuterons and deuterons implanted in the dump will be a few times 10^{15} neutrons per SPIDER pulse [4]. The neutron source intensity at the detector surface will be a few times 10^7 n/cm^2 s [4]. This intensity is comparable to that of several present day tokamaks and therefore suitable for diagnostic applications. The expected neutron spectrum impinging on the detector surface is shown in Fig. 2. MITICA will aim to study the

* Corresponding author at: Istituto di Fisica del Plasma "P. Caldirola" – CNR, Milan, Italy.
E-mail address: muraro@ifp.cnr.it (A. Muraro).

http://dx.doi.org/10.1016/j.nima.2015.12.015
0168-9002/

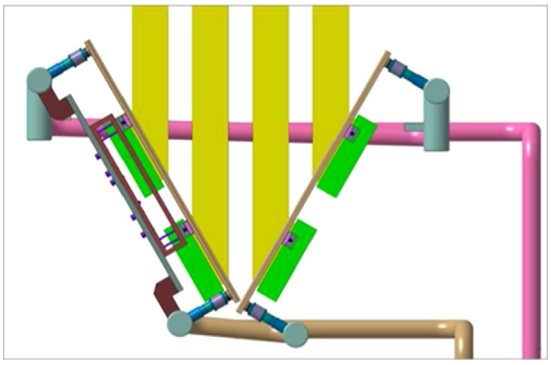

Fig. 1. Schematics of the SPIDER beam dump. The beam dump is tilted by 60° relative to the beam axis (yellow). The CNESM detectors (green) are placed right behind the beam dump. (For interpretation of the references to color in this figure caption, the reader is referred to the web version of this paper.)

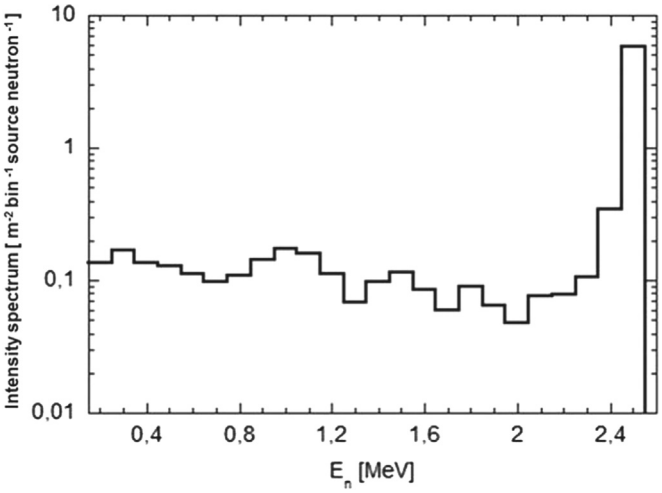

Fig. 2. Simulated neutron energy spectra on the detector surface in SPIDER.

whole injector operation, including the beam acceleration, focalization and neutralization. The ion energy will be 10 times higher than the SPIDER one (1 MeV) while the beam current and composition will be the same [5]. Due to the higher energy and the consequent increased probability of the deuterium fusion reaction, the expected neutron flux will be about 10^9 n/cm^2 s [4]. In view of neutron measurements at SPIDER, a neutron diagnostic was designed to provide the map of the beam intensity with a spatial resolution approaching the size of individual beamlets. The proposed detection system is called Close-contact Neutron Emission Surface Mapping (CNESM) and it is placed right behind the beam dump as close as possible to the neutron emitting surface (around 30 mm). The detectors employed in this diagnostic system are nGEM detectors [14]. These are Gas Electron Multiplier (GEM) detectors [6] equipped with a plastic fast neutron converter, which converts neutrons into protons via elastic scattering on hydrogen. The goal of each nGEM detector is to map the neutron emission from a group of 5×16 beamlets: populating the total beam dump surface would require a total of 16 nGEM detector units (area 35.2×20 cm^2 each) but the SPIDER experiment foresees to start the operations with just one nGEM detector installed. The full size SPIDER detector is described in the next section and its performance in the following one.

2. Detector description and construction

GEM-based detectors belong to the family of micro-pattern gaseous detectors and are typically used in high-energy physics [7] for tracking and triggering thanks to their good spatial resolution (< 5 mm) and timing properties, excellent rate capability (MHz/mm^2), radiation hardness and possibility to cover large areas (up to 1 m^2) [8–10]. Although GEM-based detectors are mostly used to detect charged particles, these detectors can be adapted (typically by using a customized cathode configuration), to detect neutral particles, such as neutrons and photons [11–13]. Several GEM detectors for fast [14–21] and thermal neutron [22–26] detection have been made during the last years.

The cathode of this nGEM detector is composed by two layers: one polypropylene (C_3H_6) foil 2 mm thick and one aluminum layer 50 μm thick.

Incident neutrons are converted into protons by elastic recoil in the polypropylene sheet. The presence of the Al layer after the polypropylene sheet gives at the detector a directional response for neutrons of 2.5 MeV energy, since the Al foil stops all protons with a recoil angle greater than 45° and/or with a recoil energy $E_p \leq 2.1$ MeV. The measurements made in order to study this directional response together with the simulations made to find the optimum thickness of the Al layer are reported in [14]. Protons leaving the conversion layer with enough energy can cross the Al foil and reach the gas, thus ionizing it. The range of the recoil protons in Ar/CO_2 70/30 (tens of cm) is larger than the drift gap (the distance between the cathode and the first GEM foil) thickness (4 mm wide), so only a fraction of their energy is deposited in the gas. Moreover the stopping power is inversely proportional to v^2, so protons of higher energy deposit a lower fraction in the gas. Ionization electrons liberated by protons energy release drift towards the GEM foils where they are multiplied. The signal generated by electron cascade is induced [28,29] on a padded anode (total of 256 pads, 22×13 mm^2 each) that is connected to the front end electronics. Considering that the gas gain of the detector is about 100 (see Section 3), protons releasing less than 100 keV are not detected. The front-end chip used to readout all the pads are the CARIOCA-GEM digital chips [30]. From the literature [31] we know that the maximum dose that a doped silicon device can stand before changing its properties is about 10^{12} n/cm^2 for 1 MeV neutrons. Considering an area of about 1 mm^2 of the silicon die of the CARIOCA chip, this means that CARIOCA chip can work fine for about 2700 h under 1 MeV neutrons irradiation. This operational time is grater than the estimation of the forseen SPIDER lifetime, that will be about 1000 h at full power. An experimental campaign is foreseen during the next year in order to investigate the effect of the 2.5 MeV neutrons on the CARIOCA chip. In MITICA the neutron flux will be about 100 times higher than the flux expected in SPIDER, but in this case the CARIOCA chip will be replaced by a new rad-hard chip (called GEMINI [32]) that is under development and will be ready by the end of 2015. Even the GEMINI chip will be tested under 2.5 MeV neutrons irradiation. All CARIOCAs are then connected to a custom made FPGA Mother Board [33] that analyzes the LVDS signal coming from the chips. The FPGAs motherboards in SPIDER will be placed outside of the vacuum vessel: they will be hosted inside a borated polyethylene neutron shielded box (borated polyethylene thickness equal to 40 cm) in a position of about 5 m away from the beam dump surface emitting neutrons. In this way the neutron flux on the FPGAs will be less than 10^2 n/cm^2 s. Since in MITICA the neutron flux will be 100 times higher, the FPGAs reading the GEMiNi chip will be located outside of the bio-shield, where the neutron flux will be negligible. The detector active area is 35.2×20 cm^2, the gap geometry is 4 mm for the drift gap and 2 mm for all the other gaps (transfer 1 and 2 and induction gaps). The high voltage configuration was generated using the HVGEM NIM module [33] and the potentials were applied to each electrode by means of passive resistive-capacitive filters properly designed for a Triple GEM detector. The construction technique

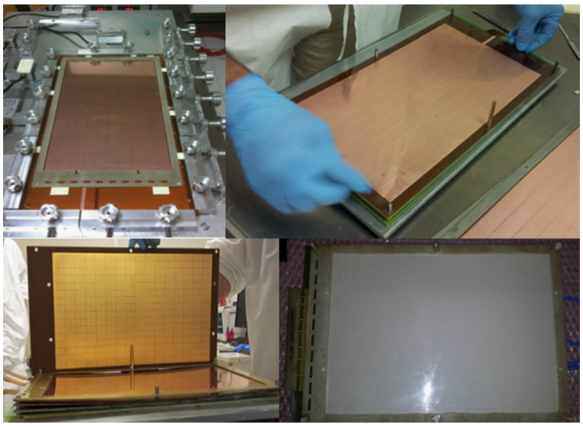

Fig. 3. Assembly of the detector. Top-left: GEM foil stretching. Top-right: the detector components are stacked together. Bottom-left: the padded anode is glued to the assembled detector structure. Bottom-right: nGEM protoype for SPIDER ready to be tested.

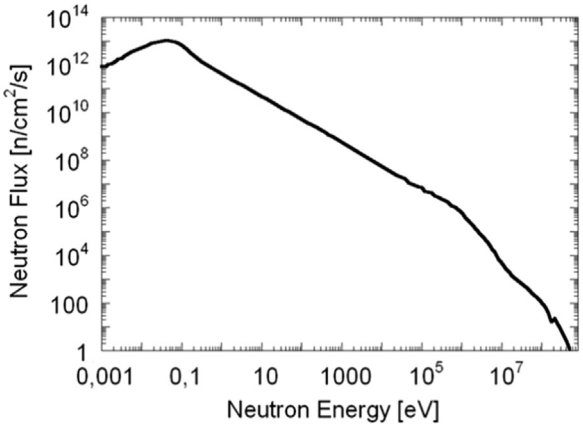

Fig. 4. The ROTAX neutron spectrum [34].

used to assemble this detector is similar to that used to make the LHCb GEM detectors [7]. Fig. 3 shows the assembly procedures that includes cathode mounting, GEM foil stretching and final assembly.

3. Detector performance

3.1. Tests on the ROTAX beam-line

The nGEM was irradiated on the ROTAX test beam line at the ISIS spallation source [34]. Neutrons are produced by a double bunch-structured proton beam, the bunches being about 70 ns wide and separated by about 300 ns. The ROTAX beam profile widths $FWHM_x$ and $FWHM_y$ are in a range between approximately 30 mm and 40 mm. The nGEM was placed in the direct beam, exiting a methane moderator at 95 K, at a distance of 15.5 m from it. The neutron energy (E_n) spectrum is known to feature a peak at about 10 meV and a $1/E_n$ tail in the epithermal/fast-neutron region, as shown in Fig. 4. The fraction of neutrons with an energy between 2 and 3 MeV is about 1.6% of the total amount of neutron. Since that the ROTAX beam line present a non-monochromatic spectrum, the nGEM detector efficiency varies as a function of the neutron energy. Fig. 5 shows the simulation (using the GEANT-4 toolkit [35]) of the nGEM detector efficiency to different neutron energies (considering only protons releasing more than 100 keV) as reported in [16].

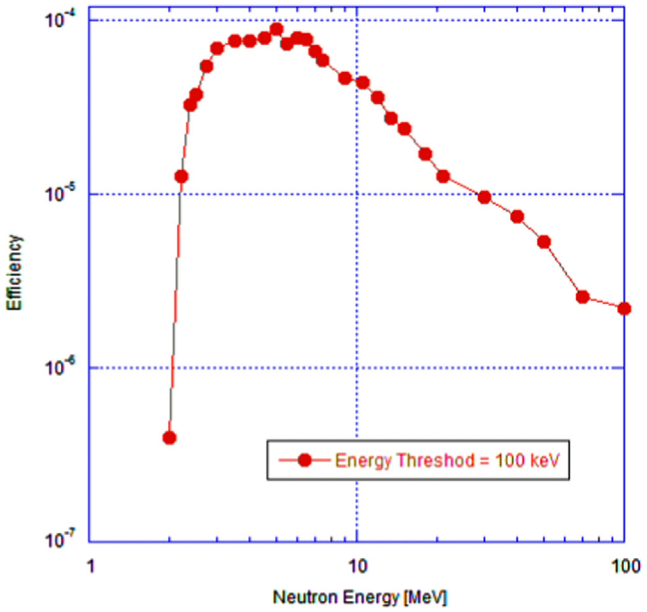

Fig. 5. Neutron detection efficiency of the GEM simulated by the GEANT4 package for neutron energies in the range 2→100 MeV and for a value of deposited energy threshold of 100 keV.

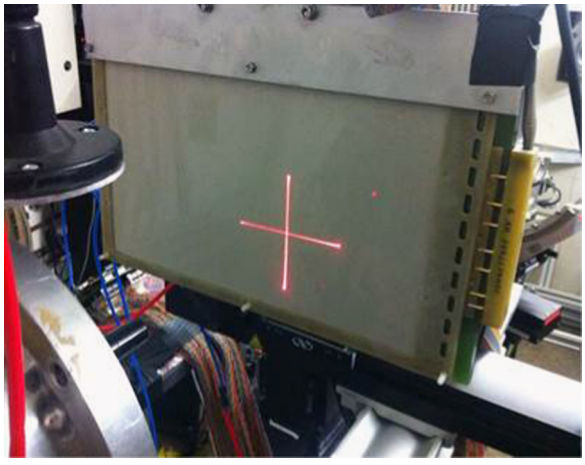

Fig. 6. The nGEM detector installed inside the ISIS-ROTAX beam-line.

Fig. 6 shows a picture of the nGEM installed inside the ROTAX beam-line. A total of 16 CARIOCA cards (32 CARIOCA chips) have been used to read-out the full detector. Two FPGA motherboards located out of the beam were used to simultaneously acquire data from all chips. The experimental setup used in this test resembles the one that will be used in SPIDER but for the length of the flat cable connecting to the FPGA that will be extended from 4 m in ROTAX to 5 m in SPIDER. The detector was mounted on a *X*–*Y* positioner, orthogonal to the beam direction, in order to center the beam in different positions on the active area. The gas mixture used for all measurements is Ar/CO2 70%/30% with a flow rate of 5 l/h.

3.2. High voltage scan and γ background rejection

The nGEM counting rate was measured as a function of the effective gain by varying the sum of voltage drops across the three GEM foils ($\Sigma\Delta V_{GEM} = V_{GEM}$). Two different measurements were performed, scanning the high voltage V_{GEM} when the neutron beam was on and off. The former is a measurement of the neutron

counting rate while the latter provides the counting rate for photons coming from surrounding activated materials (Fig. 7).

As expected [19], the detector is insensitive to gamma rays at V_{GEM} less than 900 V: for $V_{GEM} < 900$ V the gamma rays counting rate on the whole detector is about 0.1 Hz while the neutron counting rate is great than 100 kHz). As for the small area prototypes [16,19], γ rays are detected only for $V_{GEM} > 900$ V; a V_{GEM} value of 870 V was thus chosen as the working point for all the subsequent measurements. The values of the external fields used for all the subsequent measurements were E_d (electric field in the drift gap)=0.75 kV/cm, E_{T1} (electric field in the transfer 1 gap)=1.5 kV/cm, E_{T2} (electric field in the transfer 2 gap)=3 kV/cm and E_I (electric field in the induction gap)=3.865 kV/cm.

3.3. Beam profile reconstruction

Using the detector electrical settings determined in the previous paragraph, a high-statistics beam profile measurement was performed (Fig. 8). The measured $FWHM_x$=41.1 mm and $FWHM_y$=34.1 mm are compatible with the technical specifications of the beam when using pads of these dimensions [36].

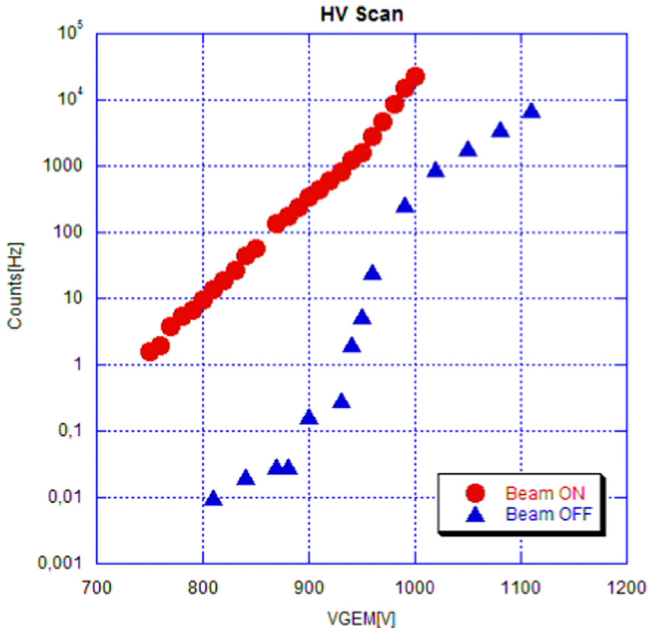

Fig. 7. nGEM counting rate as a function of V_{GEM} (applied voltage) when the beam was on (neutrons – red squares) and off (gamma rays – blue triangles). (For interpretation of the references to color in this figure caption, the reader is referred to the web version of this paper.)

3.4. Counting rate uniformity

The measurement of the detector response uniformity was performed by scanning the beam over the entire detector active area but two rows of pads at top and bottom, because the used X–Y positioner 30 cm maximum excursion does not cover the full detector height. A total of 192 neutron beam profiles (the number of PADs that we can irradiate with this positioner) were acquired for each x–y position and the scan was performed with $Step_x$=22 mm=x-dimension of the pad and $Step_y$=13 mm=y-dimension of the pad. In this way the detector response was checked pad by pad. The 192 profiles were all summed together giving a matrix of 192 elements. The average counting rate of the nGEM was determined by averaging the 192 counting rates per pad. The level of non-uniformity (per pad) was calculated by dividing the actual counting rate of each pad by the average counting rate. The resulting uniformity map is shown in Fig. 9.

In order to evaluate the uniformity of the detector (in terms of deviation from the average), an histogram of the uniformity was calculated. This histogram (shown in Fig. 10) has a bin size of 0.05 and can be fitted by a Gaussian function. The HWHM=0.12 is a measurement of the non-uniformity of the detector with respect to the average. This means that more than 70% of the pads have a non-uniformity lower than 12% with respect to the average.

3.5. Stability

An important feature that the beam profile monitor for the CNESM system must possess is the stability in time. Many factors,

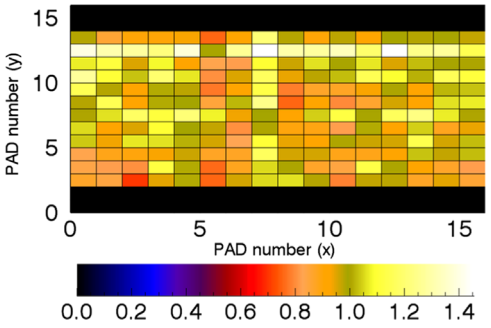

Fig. 9. nGEM uniformity map.

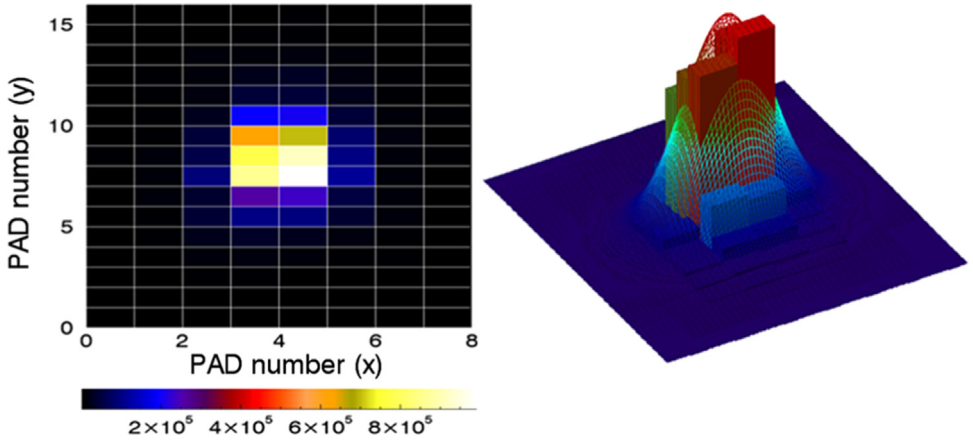

Fig. 8. Neutron beam profile reconstruction.

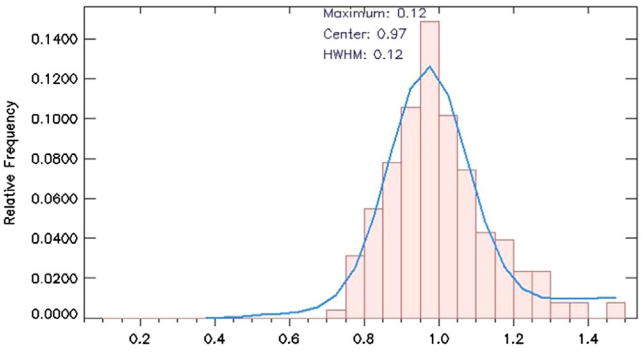

Fig. 10. Histogram of nGEM uniformity.

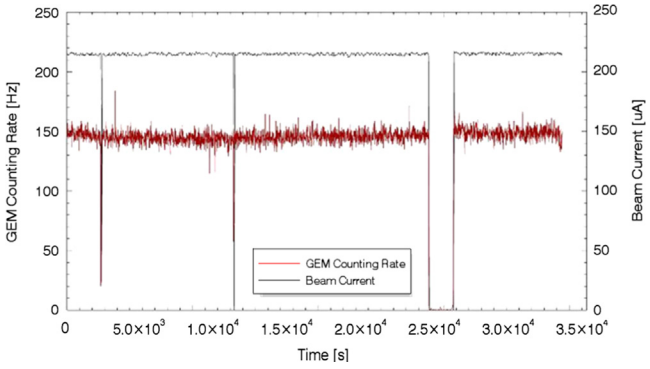

Fig. 11. nGEM counting rate as a function of time (stability in time) compared to the ISIS beam current.

including charge accumulation [38] or the variation of atmospheric parameters, can influence the behavior of the detector. In order to study this parameter the detector was irradiated in a single position for several hours and the counting rate was recorded. The counting rate was also compared to the beam current in order to prove that there is a correlation between the nGEM counting rate and the ISIS beam current. Since the FPGAs were located outside the neutron beam, they were able to run for several hours without experiencing any error due to radiation. Fig. 11 shows the nGEM counting rate as well as the ISIS proton beam current during the irradiation.

The nGEM counting rate follows the time evolution of the proton beam current demonstrating the possibility to on-line monitor the neutron beam intensity. Fig. 12 shows the histogram of the recorded counting rate, with a bin size equal to 1 s: the sigma of the fitted Gaussian divided by the most probable counting rate gives a measurement of the nGEM detector stability in time. A value of about 8% has been measured. This value should be below 10% in order to guarantee a detector time stability suitable with this application. The expected rate on the whole detector active area during a full power SPIDER pulse will be around 70 kHz, considering an efficiency of the detector of about 10^{-5} [14]. This is 500 times higher than the rate measured during the ROTAX campaign (see Fig. 11). Since the nGEM detector can easily handle rates up to tens of MHz/cm^2 [15], the expected detector performance in SPIDER should not be different from that obtained at ISIS, especially in terms of beam profile reconstruction and stability, although this should be confirmed by further experiments at higher count rates.

4. Conclusions and future perspective

The full size nGEM detector of the CNESM diagnostic system has been produced and successfully tested at the ISIS-ROTAX beam

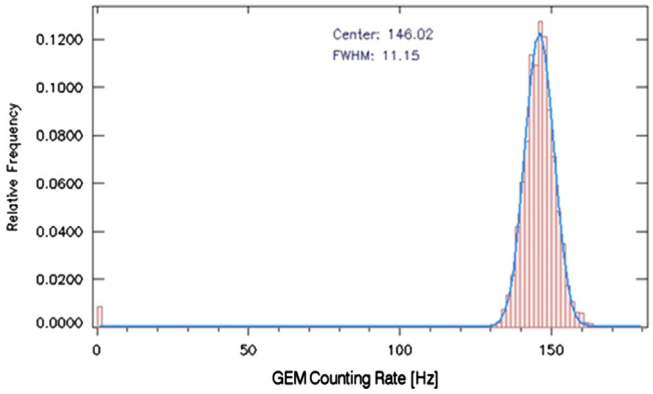

Fig. 12. Histogram of nGEM counting rate.

line using a neutron spectrum with a 1.6% fraction of neutrons with energy between 2 and 3 MeV and a count rate 500 times lower than that expected from the 2.6 MeV neutron source in SPIDER. The tests have given positive results and no significant deviation from the expected nGEM detector behavior was observed. The full-size detector has a response uniformity better than 20% and features gamma ray rejection capability, time stability and reliable on-line operation. Further experiments will allow to complete the characterization of the nGEM detector. In particular, the directionality property will be measured at FNG (Frascati Neutron Generator) [37] using 2.5 MeV neutrons in order to confirm such property, as already demonstrated for the small-scale prototype [14].

Acknowledgments

The work leading to this publication has been funded partially by Fusion for Energy under the Contract F4E-RFX-PMS-A-WP-2014. This publication reflects the views only of the author, and Fusion for Energy cannot be held responsible for any use which may be made of the information contained therein. The views and opinions expressed herein do not necessarily reflect those of the ITER Organization. This work was also setup in collaboration and financial support of INFN-Group V.

References

[1] P. Sonato, et al., Fusion Engineering and Design 84 (2009) 269.
[2] R. Pasqualotto, et al., Review of Scientific Instruments 83 (2012) 02B103.
[3] R. Hemsworth, H. Decamps, J. Graceffa, B. Schunke, M. Tanaka, M. Dremel, et al., Nuclear Fusion 49 (2009) 045006.
[4] M. Rebai, Fast neutron instrumentation for beam diagnostics (Ph.D. thesis) www.boa.unimib.it/retrieve/handle/10281/28449/37122/phd_unimib_725266.pdf.
[5] V. Toigo, et al., Nuclear Fusion 55 (2015) 083025.
[6] F. Sauli, Nuclear Instruments and Methods in Physics Research Section A 386 (February (2–3)) (1997) 531, ISSN 0168-9002, 10.1016/S0168-9002(96)01172-2.
[7] M. Alfonsi, et al., Nuclear Instruments and Methods in Physics Research Section A 518 (2004) 106.
[8] S. Duarte Pinto, et al., Journal of Instrumentation 4 (2009) P12009.
[9] M. Villa, et al., Nuclear Instruments and Methods in Physics Research Section A 628 (2011) 182.
[10] M. Alfonsi, et al., Nuclear Instruments and Methods in Physics Research Section A 617 (2010) 151.
[11] M. Alexeev, et al., Nuclear Instruments and Methods in Physics Research Section A 617 (2010) 396.
[12] M. Alexeev, et al., Nuclear Instruments and Methods in Physics Research Section A 623 (2010) 129.
[13] M. Alexeev, et al., Journal of Instrumentation 5 (2010) P03009.
[14] G. Croci, et al., Journal of Instrumentation 7 (2012) C03010.
[15] E. Perelli Cippo, et al., Journal of Instrumentation 10 (2015) P10003.
[16] F. Murtas, G. Croci, et al., Journal of Instrumentation 7 (2012) P07021.
[17] G. Croci, et al., Nuclear Instruments and Methods in Physics Research Section A 720 (2013) 144.

[18] G. Croci, et al., Nuclear Instruments and Methods in Physics Research Section A 712 (2013) 108.
[19] G. Croci, et al., Journal of Instrumentation 8 (2013) P04006.
[20] B. Esposito, et al., Nuclear Instruments and Methods 617 (2010) 155.
[21] B. Esposito, et al., Nuclear Instruments and Methods in Physics Research Section A 741 (2014) 196.
[22] G. Croci, et al., Nuclear Instruments and Methods in Physics Research Section A 732 (2013) 217.
[23] G. Croci, et al., Europhysics Letters 107 (2014) 12001.
[24] G. Croci, et al., Progress of Theoretical and Experimental Physics 2014 (8) (2014) 083H01.
[25] H. Oshita, et al., Nuclear Instruments and Methods in Physics Research Section A 623 (2010) 126.
[26] H. Oshita, et al., Nuclear Instruments and Methods in Physics Research Section A 672 (2012) 65.
[28] W. Shockley, Journal of Applied Physics 9 (1938) 635.
[29] S. Ramo, Proceedings of the I.R.E. 27 (1939) 584.
[30] W. Bonivento, P. Jarron, D. Moraes, W. Riegler, F. dos Santos, Nuclear Instruments and Methods in Physics Research Section A 491 (September (1–2)) (2002) 233.
[31] R. Wunstorf, A Systematic investigation of the radiation hardness of silicon detectors for high-energy physics experiments, DESY FH1K 92-01.
[32] A. Pezzotta, et al., GEMINI: a triple-GEM detector read-out mixed signal AISC in 180 nm CMOS, in: ISCAS 2015 IEEE International Symposium, 10.1109/ISCAS.2015.7168984.
[33] ⟨http://www.infn.it/csn5/joomla/GEMINI/⟩.
[34] H. Tietze-Jaensch, et al., Physica B: Condensed Matter 234236 (1997) 1149.
[35] ⟨https://cern.ch/geant4⟩.
[36] G. Albani, et al., Journal of Instrumentation 10 (2015) C04040.
[37] M. Martone, M. Angelone, M. Pillon, Journal of Nuclear Materials 1661 (1994) 212.
[38] M. Alfonsi, et al., Nuclear Instruments and Methods in Physics Research Section A 671 (2012) 6.

Paper 4

A GEM-based thermal neutron detector for high counting rate applications

2015 JINST 10 P10003

(http://iopscience.iop.org/1748-0221/10/10/P10003)

JINST

PUBLISHED BY IOP PUBLISHING FOR SISSA MEDIALAB

RECEIVED: *May 18, 2015*
REVISED: *August 25, 2015*
ACCEPTED: *September 7, 2015*
PUBLISHED: *October 5, 2015*

A GEM-based thermal neutron detector for high counting rate applications

E. Perelli Cippo,[a,1] **G. Croci,**[b,a,c] **A. Muraro,**[a] **A. Menelle,**[d] **G. Albani,**[b] **M. Cavenago,**[e] **C. Cazzaniga,**[b] **G. Claps,**[f] **G. Grosso,**[a] **F. Murtas,**[f] **M. Rebai,**[b] **M. Tardocchi**[a] **and G. Gorini**[c]

[a] *Istituto di Fisica del Plasma "P. Caldirola", Associazione EURATOM-ENEA/CNR, Milano, Italy*

[b] *Dipartimento di Fisica "G. Occhialini", Università degli Studi di Milano-Bicocca, Milano, Italy*

[c] *INFN – Sezione di Milano-Bicocca, Piazza della Scienza 3, 20125 Milano, Italy*

[d] *Laboratoire Léon Brillouin, CEA-Saclay, 91191 Gif sur Yvette Cedex France*

[e] *INFN Laboratori Nazionali di Legnaro, Viale dell'Università 2, 35020 Legnaro, Italy*

[f] *INFN – Laboratori Nazionali di Frascati, Via Fermi 40, 00044 Frascati, Italy*

E-mail: perelli@ifp.cnr.it

ABSTRACT: Among other neutron detector systems proposed as a possible substitute for ^{3}He tubes, GEM-based ones have shown appealing characteristics, when coupled with suitable neutron-converter cathodes. In this paper, we present the results of a GEM-based neutron detector in a high-flux environment (the ORPHÉE reactor in Saclay), especially in terms of maximum rate capability and linearity. Recorded data show that the detector can manage neutron counting rates in the order of 50×10^6 counts/sec cm^2 while maintaining a reasonable linearity and with no sign of instability.

KEYWORDS: Micropattern gaseous detectors (MSGC, GEM, THGEM, RETHGEM, MHSP, MICROPIC, MICROMEGAS, InGrid, etc); Neutron detectors (cold, thermal, fast neutrons)

[1] Corresponding author.

doi:10.1088/1748-0221/10/10/P10003

2015 JINST 10 P10003

Contents

2015 JINST 10 P10003

1 Introduction

The R&D activity about neutron detectors has had a sensible rise in recent times due to the somehow sudden shortage of ^{3}He. The search for substitutes of ^{3}He tubes as thermal neutron detectors is paramount for the implementation of present and especially next generation neutron sources such as the European Spallation Source (ESS [1]). In order to make a full use of the intense ESS neutron beam, an optimised detector should have high-rate capability and (especially for SANS and NR instruments) cover a large area. GEM (Gas Electron Multiplier) -based detectors fulfil such requirements: in particular, they have proven very high-rate capabilities for X-rays (up to 1 MHz/mm^2 [2], coverage of up to 1 m^2 area and spatial resolution better than 0.5 mm [3–5]. GEMs are intrinsically charged-particles detectors for tracking and triggering but if coupled to a proper converter can be used to detect neutral particles such as photons [6–9] and neutrons [10–14].

GEMs can be made sensitive to thermal neutrons by coupling with a neutron converter cathode (for instance enriched in ^{10}B) able to let the neutrons generate electrically charged particles (for instance Alpha particles or Lithium ions) to be revealed by the GEM [15]. Present R&D activity is concentrated on the optimisation of such cathodes (the present authors group them under the common name of 3-D cathodes), of which many examples exist [20, 21]. Other approaches followed for the development of gas counters as neutron detectors are, for instance, optimisation for fast neutrons [23], or the CASCADE detectors [24]. All of these detectors present some advantages and disadvantages, depending on the expected applications and, consequently, the different characteristics that are either improved (for instance efficiency, resolution etc.) or, on the opposite, neglected. Thus, not a single kind of detector can be considered as the "perfect" substitute for ^{3}He tubes.

The present authors are involved in the development of a series of detectors, the envisaged application of which is low-angle scattering and diffraction in the future spallation source ESS, with

typical neutron wavelength range 1 to 12 Å (thus extending from "thermal" to "cold" neutrons) and high neutron flux. In this paper, we present the results obtained with a triple-GEM detector with a natural B_4C neutron converter cathode tested at the G3-2 irradiation station of the 14 MW ORPHÉE reactor in Saclay [16]. The G3-2 beamline provides a flux of 7.88×10^8 n/s cm^2, and it thus constitutes a very valuable test bed for counting rate capability, radiation hardness and other detector properties requiring a high neutron flux. Moreover, the G3-2 flux distribution, peaked at about 3.5 meV energy, is reasonably representative of the thermal/cold neutron field expected at ESS. The presented results show that the GEM-based detector can achieve counting rates in the order of 50 MHz/cm^2 with a reasonable loss of linearity. Moreover, the used GEM electronics has worked continuously in the neutron beam for about 9 hours without appreciable loss of performances.

2 Experimental setup

2.1 The G3-2 station

The G3-2 irradiation station is located at about 20 m from the ORPHÉE reactor core; it provides a white neutron beam of peak energy of about 3.5 meV with a 25×50 mm^2 spot and 0.4° divergence. The expected thermal neutron flux at the measurement position is $\Phi = 7.88 \times 10^8$ n/cm^{2}s [22].

2.2 The GEM-based detector

The detector used in the present experiment was a triple-GEM based one, equipped with a 400 μm Al cathode covered with a 1 μm thick boron carbide layer. Such a cathode/converter exploits the ^{10}B(n, α)^{7}Li reaction in order to convert thermal neutrons into charged particle to be detected through the GEM multiplication stages. The choice of the converter layer thickness is determined by two competing effects, and namely the probability of neutron capture from ^{10}B nuclei (higher for higher thicknesses) and probability of escape of reaction products from the layer (lower for higher thickness). In fact, only reaction products emerging from the layer into the gas may be detected. Both previous tests and analytical calculations have shown that 1 μm is very close to the optimum thickness [25]. The relevant parameters of such a detector [17] were:

a) GEM gaps (*Drift, Transfer* 1, *Transfer* 2 and *Induction*): 13 mm, 2 mm, 3 mm and 1 mm, respectively. The choice of a triple-GEM configuration is linked to discharge probability: a triple-GEM has a discharge probability that is many order of magnitude lower than a single one with the same total gain. Thus the triple-GEM represents a safer and more robust option for a detector that has to work at high rates for long measurement times [26].;

b) padded anode composed by 124 8×8 mm^2 pads plus 4 L-shaped angular pads for a total area of 192 mm^2 on 128 independent channels (see figure 1, left panel).

c) read-out performed through CARIOCA chips [18] and a FPGA motherboard with real-time recording capability [17]. The "working point", i.e. total applied voltage (shared by the three GEM foils) is nominally 870 V (see further for details). Previous measurements had shown, for such an applied voltage and the Ar 70%/CO_2 30% gas mixture used in this setup, a gain G = 100 [13].

The conversion efficiency of the borated cathode may be written as:

$$1 - e^{-\Sigma z_{\text{eff}}} \tag{2.1}$$

where Σ is the macroscopic cross-section for neutron capture in ^{10}B nuclei and z_{eff} is the effective thickness of such nuclei into the converter material. Considering the cross-section of the neutron capture reaction in boron and the mentioned parameters, a 5% conversion efficiency estimated for a cold/thermal beam as the one of G3-2. The number of detected counts in the detector depends of course on other parameters, such as for instance the settings of the electronic read-out; however, taking the previous figure as a rough indication of the overall efficiency of the detector, thus the expected count rate with the G3-2 station flux was estimated to be of 39.4 MHz/cm^2.

3 Results and discussion

3.1 Measurement of the thermal neutron 2D map

The detector operated with the electrical parameters described in the previous paragraph was exposed to the neutron beam and figure 1 shows the reconstruction of the 2D beam image using 128 pads with 8×8 mm^2 area. The shape of the beam is rectangular as expected from the shape of the G3-2 beam-line collimator [22].

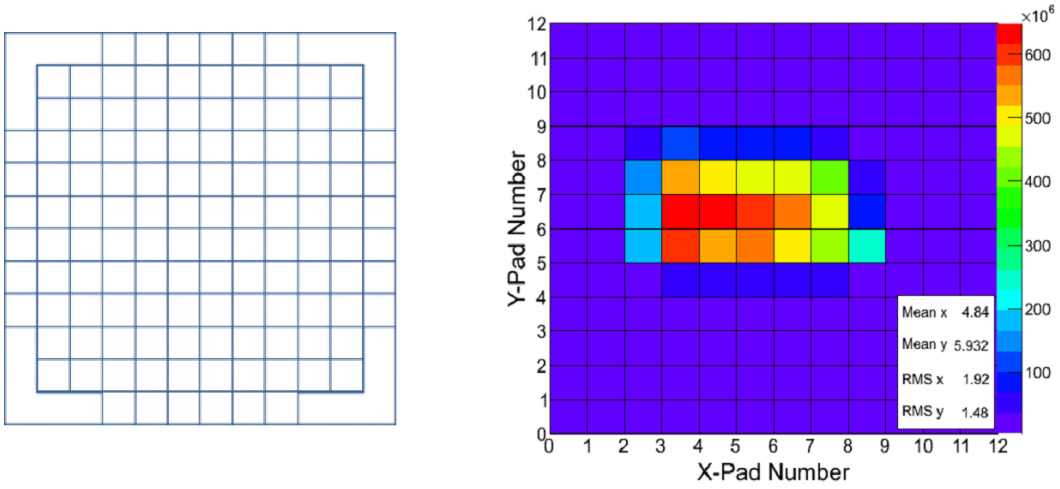

Figure 1. Left panel: a scheme of the padded anode of the GEM used in these measurements. The square pads dimensions are 8×8 mm^2. Right panel: 2D Neutron Map reconstructed with the GEM.

3.2 Maximum rate capability and linearity test

The GEM counting rate capability as well as its linearity were compared with a fission chamber (FC) detector (a well-proven neutron flux monitor) constituted of a 4 mm diameter gas proportional counter with a 2 cm section internally coated with a ^{235}U deposit. The FC was positioned in front of the GEM detector and simultaneous measurements were taken. A series of 1.8 mm thick polyethylene slabs were placed in the neutron beam in order to attenuate, via multiple scattering,

the flux impinging on both detectors. As a rule of thumb, such polyethylene slabs are credited to reduce the G3-2 neutron flux of about a factor 2 for every mm of thickness. For sake of clarity, we have to underline that a precise estimation of the flux reduction through moderation typically would require long and complex simulations; however, for the present purposes, it is not necessary to exactly quantify the flux on the detectors, provided that the flux investing the two systems is the same. For that reason, the data presented in figure 2 are just labelled with the total thickness of plastic interposed.

Due to the behaviour of the electronic system, our detector setup can be modelled using a *non-paralizable* model. We consider the FC as the reference detector so that its measured interaction rate is strictly linked to the real interaction rate. The non-paralizable model leads to the following relation between GEM and the real counting rates:

$$N_{\mathrm{Real}} - N_{\mathrm{GEM}} = \tau N_{\mathrm{GEM}} N_{\mathrm{Real}} \tag{3.1}$$

where N_{Real} and N_{GEM} are the true and GEM detector count rates and τ is the saturation time.

Since the FC is taken as reference detector we can say that $N_{\mathrm{Real}} = aN_{\mathrm{FC}}$ and we rewrite the saturation time τ as b/a, where b and a are parameters that can be determined through a fitting procedure.

By applying the described changes to formula (2.1) we can obtain the saturation formula that links the GEM counting rate to the FC counting rate:

$$N_{\mathrm{GEM}} = a \quad N_{\mathrm{FC}}/(1 + bN_{\mathrm{FC}}) \tag{3.2}$$

where N_{FC} and N_{GEM} are the reference detector and GEM detector count rates. Assuming the reference detector is perfectly linear in its whole dynamic range, the b/a ratio assumes as expected the physical meaning of the saturation time of the (non-paralizable) system constituted by the GEM detector and its front-end electronics.

Fitting of the data in figure 2 with formula (3.1) gives the values $a = 3.519$ MHz/pad and $b = 0.028$, thus resulting in an estimated saturation time τ of about 8 ns/pad. The GEM system non-linearity measured in correspondence of the dashed-line in figure 2 (that is when the beam is attenuated by one polyethylene slab) is about 9% while this values increases up to 20% if the full beam (no absorber) is considered.

The value of the GEM counting rate per pad where the non-linearity starts to appear is around 10MHz/pad which represents the limit value for the CARIOCA linearity [17].

3.3 HV-scan and threshold-scan

The rate achieved in full beam conditions with the GEM detector with the present settings, and in particular with the present applied voltage, was of about 40 MHz/cm^2. However, the overall count rate depends upon a) the gas gain of the detector, and thus the applied voltage, and b) the *low level discrimination* (LLD) threshold applied. A suitable LLD is in fact necessary to cut thermal electronic noise. Previous measurements [15] had shown an ideal applied HV ("working point") of 870 V divided on the three GEM foils: tests showed that at such working point the sensitivity of the detector to the (ever present) gamma-ray background is negligible [13].

2015 JINST 10 P10003

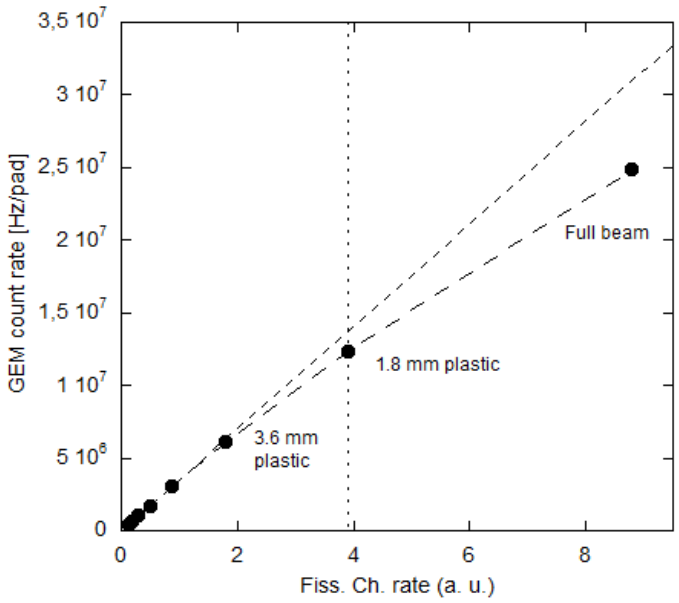

Figure 2. GEM counting rate per pad vs Fission chamber counting rate for different thickness of plastic absorbers interposed in the beam before both detectors.

The present digital electronics does not allow to obtain a pulse eight spectrum (in order to precisely determine the exact relationship between LLD threshold and energy deposit in the gas); however, it had been observed [15] that a 900 mV LLD threshold is high enough to reject most of the noise, even if it is usually set higher to be on the safe side. So called "HV-scan" and "threshold-scan" were performed in order to study the dependence of count rate upon the previous parameters and to check the maximum realistic count rates achievable with the present detector setup. Figure 3 shows such measurements in the left and right panel, respectively. In this case the counting rate was normalized to the pad dimensions that are $8 \times 8\,\mathrm{mm}^2$. As already seen from previous measurements, it may be noted that the counting rate dependence *vs* applied HV shows a sort of plateau for $V > 850\,\mathrm{V}$, corresponding to a rate of about $40\,\mathrm{MHz/cm}^2$, in good agreement with the estimated value. The rate may be even raised while lowering the LLD threshold down to 900 mV. The HV-scan and threshold-scan suggest that, in appropriate conditions, the thermal neutron count rate may be as high as about $50\,\mathrm{MHz/cm}^2$, thus overtaking the theoretical upper limit of linearity of the CARIOCA chips.

3.4 Counting stability

Among other aspects, counting rate stability is a major requirement for high-rate neutron detectors, expected to work properly for the sake of many-hours long experimental runs. Most concerns about detector stability involve the detector itself (possibility of discharges between GEM foils) and especially the CARIOCA chips board. We have to note that, due to the configuration of the detector, with the chips right behind the padded anode, the chips themselves were irradiated by the neutron beam, thus enhancing the possibility of the rise of so-called "soft-errors" [19]. To check the detector stability, the integrated number of events detected in 0.4 seconds intervals was recorded

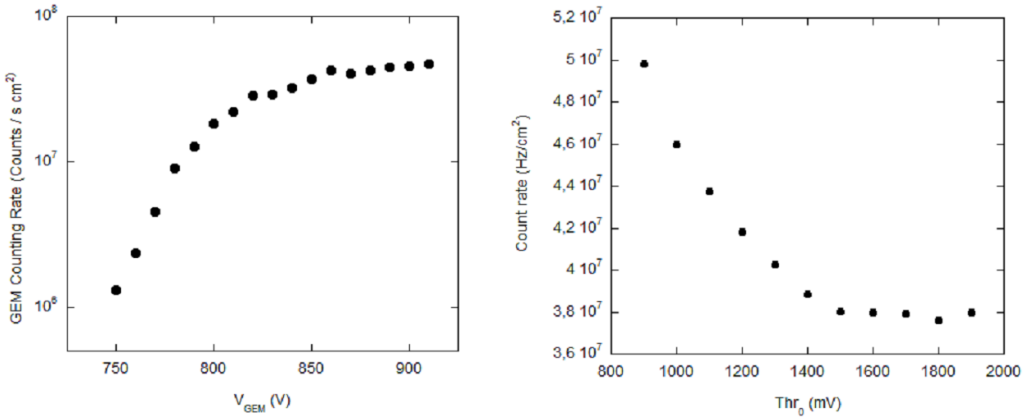

Figure 3. Left: HV-scan measurement. The scan was performed with a LLD threshold of 1300 mV, in order to avoid any possible signal from unwanted gamma-rays. Right: threshold-scan measurement. The quantity on the X axis is the common threshold applied to the CARIOCA chips. In both panels, the count rate is normalized to a conventional $8 \times 8\,\mathrm{mm}^2$ detector surface.

for a 9-hours long run (see figure 4), and the distribution of the recorded values analysed. A mean and median value of 3.6604×10^7 counts/s and 3.6603×10^7 counts/s, respectively as well as a standard deviation of 1.4×10^5 counts/s were measured. Assuming the latter value as an indication of the detector count rate stability, we can conclude that, in the present, very high-flux conditions, the detector was stable within a 0.5% level.

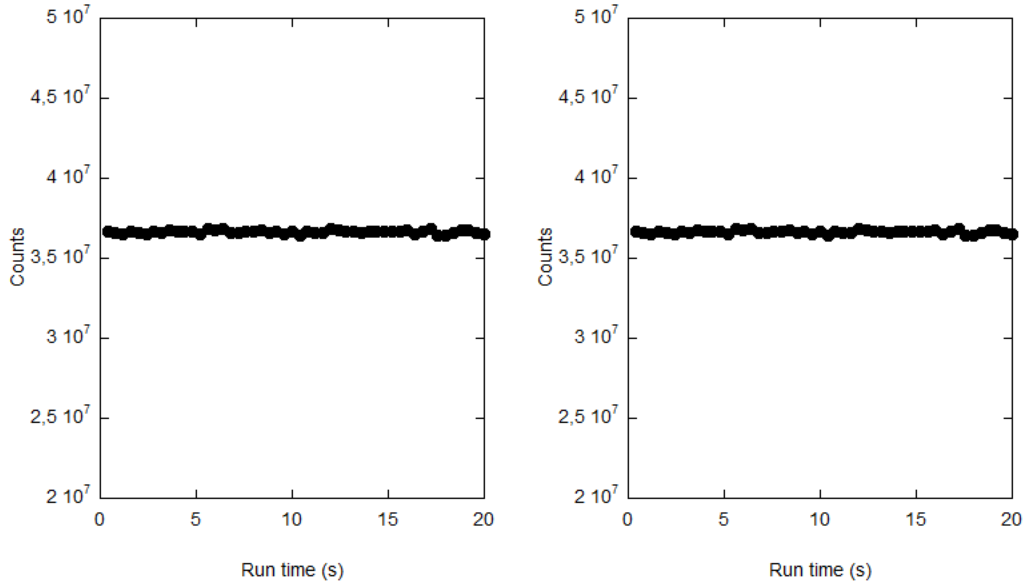

Figure 4. Integrated counts in a series of 0.4 s time intervals for a 9-hours long run. Left panel: the first 20 seconds of the measurement. Right panel: the last 20 seconds.

2015 JINST 10 P10003

4 Conclusions

In this paper, results from tests on a GEM-based thermal neutron detector have been presented. The tests were especially devoted to the investigation of the possibilities offered by GEMs in terms of count rate. High count rate, in fact, is a paramount for the detectors envisaged in next-generation neutron sources like ESS. The application of the GEM detector to the realistic conditions (very high neutron flux) available at ORPHÉE has shown that the GEM-based detector coupled with a boron cathode/converter may easily reach count rates of the order of 50 MHz/cm^2, with good linearity. The count rate appears to be limited by the associated read-out electronics only. The CARIOCA chips used in the present setup are in fact characterised by a range of linearity up to about 10 MHz per channel. New chips based on 180 nm CMOS technology are being developed in order to overcome this problem. Moreover, the detector offers the additional advantage of a good long-term (several hours) stability in a harsh environment.

The present results add up to the good characteristics already shown by the detector in terms of spatial and Q resolution when applied as a neutron diffraction detector [14], resolution that may also be further improved by mean of a proper focussing procedure.

Acknowledgments

The authors warmly acknowledge Dr. C. Alba-Simionesco of Laboratoire Léon Brillouin in providing the neutron research facilities used in this work. This work was set up in collaboration and financial support of INFN Group 5 (Technology Research).

References

[1] European Spallation Source, http://europeanspallationsource.se/.

[2] M. Alfonsi et al., *Activity of CERN and LNF groups on large area GEM detectors*, *Nucl. Instrum. Meth.* **A 617** (2010) 151.

[3] S. Duarte Pinto et al., *Progress on large area GEMs*, 2009 *JINST* **4** P12009.

[4] F. Sauli, *GEM: A new concept for electron amplification in gas detectors*, *Nucl. Instrum. Meth.* **A 386** (1997) 531.

[5] M. Villa et al., *Progress on large area GEMs*, *Nucl. Instrum. Meth.* **A 628** (2011) 182 [arXiv:1007.1131].

[6] M. Alexeev et al., *The quest for a third generation of gaseous photon detectors for Cherenkov imaging counters*, *Nucl. Instrum. Meth.* **A 610** (2009) 174.

[7] M. Alexeev et al., *THGEM based photon detector for Cherenkov imaging applications*, *Nucl. Instrum. Meth.* **A 617** (2010) 396.

[8] M. Alexeev et al., *Development of THGEM-based photon detectors for Cherenkov Imaging Counters*, 2010 *JINST* **5** P03009.

[9] M. Alexeev et al., *Micropattern gaseous photon detectors for Cherenkov imaging counters*, *Nucl. Instrum. Meth.* **A 623** (2010) 129.

[10] G. Croci et al., *nGEM neutron diagnostic concept for high power deuterium beams*, 2012 *JINST* **7** C03010.

2015 JINST 10 P10003

[11] F. Murtas et al., *Triple GEM gas detectors as real time fast neutron beam monitors for spallation neutron sources*, 2012 *JINST* **7** P07021.

[12] G. Croci et al., *nGEM fast neutron detectors for beam diagnostics*, *Nucl. Instrum. Meth.* **A 720** (2013) 144.

[13] G. Croci et al., *Measurements of ?-ray sensitivity of a GEM based detector using a coincidence technique*, 2013 *JINST* **8** P04006.

[14] G. Croci et al., *Diffraction measurements with a boron-based GEM neutron detector*, *Eur. Phys. Lett.* **107** (2014) 12001.

[15] G. Croci et al., *GEM-based thermal neutron beam monitors for spallation sources*, *Nucl. Instrum. Meth.* **A 732** (2013) 217.

[16] http://www-llb.cea.fr/en/web/hpr_web/hprweb1.php.

[17] G. Croci et al., *Characterization of a thermal neutron beam monitor based on gas electron multiplier technology*, *Prog. Exp. Phys.* **2014** (2014) 083h01.

[18] D.Moraes et al., *Development of the CARIOCA front-end chip for the LHCb muon detector*, *Nucl. Instrum. Meth.* **A 491** (2002) 233.

[19] C. Andreani et al., *Facility for fast neutron irradiation tests of electronics at the ISIS spallation neutron source*, *Appl. Phys. Lett.* **92** (2008) 114101.

[20] G. Claps et al., *^{3}He-free triple GEM thermal neutron detector*, *Europhys. Lett.* **105** (2014) 22002.

[21] F. Piscitelli et al., *Study of a high spatial resolution 10B-based thermal neutron detector for application in neutron reflectometry: the Multi-Blade prototype*, 2014 *JINST* **9** P03007.

[22] A. Menelle, *Description des fascieaux blancs pour irradiation*, LLB Technical Report (2011).

[23] V. Dangendorf et al., *Detectors for energy resolved fast neutron imaging*, *Nucl. Instrum. Meth.* **A 535** (2004) 93 [nucl-ex/0403051].

[24] M. Klein and C.J. Schmidt, *CASCADE, neutron detectors for highest count rates in combination with ASIC/FPGA based readout electronics*, *Nucl. Instrum. Meth.* **A 628** (2011) 9.

[25] J. Birch et al., *$^{10}B_4C$ Multi-Grid as an Alternative to ^{3}He for Large Area Neutron Detectors*, *IEEE Trans. Nucl. Sci.* **60** (2013) 871.

[26] S. Bachmann et al., *Discharge mechanisms and their prevention in the gas electron multiplier (GEM)*, *Nucl. Instrum. Meth.* **A 479** (2002) 294.

2015 JINST 10 P10003

Paper 5

A new thermal neutron detector based on thin 3D $^{10}B_4C$ converters for high rate applications

G. Croci[1,2,a),*], A. Muraro[2,*], E. Perelli Cippo[2,*], M. Tardocchi[2,*], G. Albani[1], G. Angella[3], I. Defendi[4], G. Grosso[2], R. Hall-Wilton[5,6], C. Höglund[5,7], D. Raspino[8], N. Rhodes[8], L. Robinson[5], S. Schmidt[5], E. Schooneveld[8], K. Zeitelhack[4] and G. Gorini[1,2]

[1]*Dipartimento di Fisica "G. Occhialini," Università degli Studi di Milano-Bicocca, Italy*
[2]*Istituto di Fisica del Plasma "P. Caldirola", Consiglio Nazionale delle Ricerche, Milano*
[3]*IENI-CNR, Consiglio Nazionale delle Ricerche, Milano*
[4]*Heinz Maier-Leibnitz Zentrum (MLZ), Technische Universität München, Lichtenbergstr. 1, 85748 Garching, Germany*
[5]*European Spallation Source ERIC (ESS), Tunavägen 24, 221 00 Lund, Sweden*
[6]*Mid-Sweden University, Sundsvall, Sweden*
[7]*Dept. of Physics, Chemistry and Biology (IFM), Linköping University, SE-581 83 Linköping, Sweden*
[8]*STFC-ISIS Facility, Rutherford Appleton Laboratory, Didcot UK*

a) Corresponding author: gabriele.croci@unimib.it
* *These authors contributed equally to this work*

Abstract

A new position sensitive thermal neutron detector based on boron coated converters has been developed as an alternative to today's standard ^{3}He based technology for application to thermal neutron scattering. The key element of the development is a novel 3D $^{10}B_4C$ converter which has been ad hoc designed and realized with the aim of combining a high neutron conversion probability via the $^{10}B(n,\alpha)^7Li$ reaction together with an efficient collection of the produced charged particles. The developed 3D converter is composed of thin aluminum grids made by a micro-waterjet technique and coated on both sides with a thin layer of $^{10}B_4C$. When coupled to a GEM detector this converter allows reaching neutron detection efficiencies close to 50% at neutron wavelengths equal to 4 Å. In addition, the new detector features spatial resolution of about 5 mm and can sustain counting rates well in excess of 1 MHz/cm^2. The newly developed neutron detector will enable time resolved measurements of fast evolving biological samples in neutron scattering experiments at high flux spallation sources and can find use in other applications where large areas and custom geometries of thermal neutron detectors are foreseen.

Letter

The recent ^{3}He shortage, which is due to a progressive nuclear disarmament started in 2000, has resulted in reduced availability of this noble gas and a consequent high increase in its price. Nowadays the world's most important suppliers (USA and Russia) are keeping the residual amount of ^{3}He mainly for homeland security and nuclear safeguards applications [1]. As a consequence, the availability of ^{3}He gas for thermal neutron detectors (in the form of high pressure single-wire proportional counter tubes [2]) has been severely reduced. On the other hand, the scientific community is experiencing the need to realize new large area position sensitive devices able to fully exploit the increase of neutron flux offered by new spallation neutron sources like ESS [3]. These two reasons led to the development of new ^{3}He-free position sensitive neutron detectors capable of detection efficiencies comparable with ^{3}He tubes [4], but being able to sustain much higher counting rates than the 30-50 kHz typical for single ^{3}He tubes [5]). A possible approach relies on the use of solid neutron converters (such as Boron or Lithium) combined to charged particle detectors. The efficiency (ε) of these detectors is the result of the product of three factors: the neutron conversion probability (p), the escape probability (ξ) of the charged products generated by the neutron nuclear reaction and the extraction efficiency (η) of the primary charge liberated by the charged reaction products. The challenge in the design of novel detectors relies on finding a geometrical and electrical configuration able to simultaneously optimize these three parameters (p, ξ and η). Optimization of the charge extraction probability η is the key element in achieving high neutron detector efficiency and represents the main challenge.

The detector described in this paper is called BAND-GEM (Boron Array Neutron Detector) [6] and it is made of a novel 3D $^{10}B_4C$-based active converter coupled to GEM (Gas Electron Multiplier [7]) technology. The converter is formed by a stack of aluminum grids consisting of 200 μm thin strips realized using an ultra-precise (<10 μm) micro-waterjet [8] cutting machine. The strips of each grid are coated on both sides with an electrically conductive layer of $^{10}B_4C$ using a magneto-sputtering technique [9, 10, 11]. The converter stack is built by alternating one grid with one insulating spacer (see Figure 1). High voltage is applied to each individual grid via resistor chain The neutron conversion happening in the $^{10}B_4C$ layers gives rise to the creation of charged products that, depending on their energy, may be able to escape from the $^{10}B_4C$ layer and ionize the gas in the detector. The liberated primary electrons then drift inside the 3D converter that acts as a drift field cage; in addition depending on their origin along z (see Figure 2), they can be also multiplied by the middle GEM foil. When they leave the 3D

converter region, they enter a Triple GEM [7] amplifying structure where they are multiplied by a factor of about 100. The signal is then induced on a padded anode equipped with front-end electronics (128 pads, 4 x 3 mm^2 area, arranged in a square matrix).

This new detector design allows the neutron conversion probability *p* to be increased by operating the detector at grazing incident angles (θ=5-10°) [12] with respect to the incoming neutron direction. ξ and η are then optimized by a suitable choice of the geometrical and electrical parameters. These are the numbers of grids composing the stack, the height and spacing of the grids, the thin strip pitch, the $^{10}B_4C$ layer thickness and the voltage values applied to each grid. The design of the 3D converter leading to the values that maximize ε was performed using a numerical model that is able to simultaneously simulate: i) the neutron absorption in the $^{10}B_4C$ layers, ii) the capability of charged particle products to escape from these layers, iii) the ionization of the active gas (a mixture of Ar-CO_2 70-30% in volume), iv) the efficiency in extracting the charge out of the 3D converter. This complex simulation involves the integrated exploitation of IDL, Ansys, Garfield++ and SRIM codes [13].

A key feature of the BAND-GEM is the angular tilting which increases the neutron conversion probability *p* by augmenting the thickness of the borated material crossed by the neutrons (see Figure 2). Several geometrical parameters influence the effective boron thickness seen by a neutron: the height and number of grids and their relative spacing between each other, the pitch between the thin strips, the angle between the incoming neutrons and the strips and the thickness of the $^{10}B_4C$ layer. The cross-section view of the $^{10}B_4C$ coating on an aluminum strip performed using a Scanning Electron Microscope (SEM, see Figure 1) shows that its thickness is about 1.0 µm. This thickness was chosen in order to optimize the detection efficiency at 4 Å. In the nuclear reaction $^{10}B(n,\alpha)^7Li$ the two charged particles are produced with kinetic energies K_α= 1.47 MeV

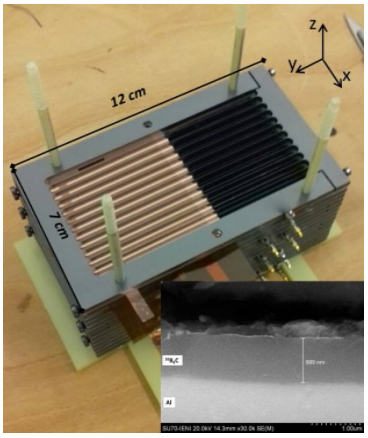

Figure 1: Picture of the 3D-converter. The GEM foil in the middle of the converter is also visible. Small rectangle: SEM image of the cross-section view of the $^{10}B_4C$ coating on the aluminum grids.

and K_{7Li} = 0.84 MeV for the most probable (96%) reaction with ^7Li left in the excited state, or with K_α= 1.78 MeV and K_{7Li} = 1.01 MeV for the least probable (4%) reaction with ^7Li left in the ground state. In either case, the *Q-value* of these two reactions (2.31 and 2.79 MeV, respectively) is very large compared with the incoming energy of the thermal neutron and as a consequence the two charged particles are emitted back-to-back since the incoming neutron momentum can be neglected. The α and ^7Li ions are produced isotropically along the $^{10}B_4C$ layer thickness and one or other

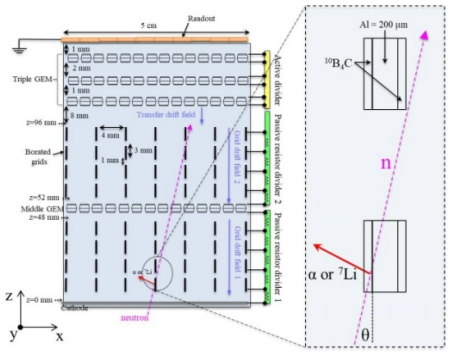

Figure 2: Schematics and operation principle of the BAND-GEM detector. A zoom of the coated aluminum grids is shown on

the right. See text for details..

of these particles may leave the $^{10}B_4C$ layer and ionize the gas volume. Therefore the charge escape probability ξ depends on: i) the neutron interaction point along the thickness of the $^{10}B_4C$ layer; ii) the direction of emission of the charged particles, iii) the $^{10}B_4C$ layer thickness. The charged particles escaping from the layer will feature a continuous energy spectrum ranging from 0 to K_α and $K_{7Li.}$ The signal due to a neutron interaction is thus registered if the primary electrons generated by the charged products ionizing the gas volume are efficiently collected. In order to extract the primary charge, the 3D converter acts as a field cage [14]. The charge extraction efficiency η depends on the detailed grid geometry as well as on the voltage values applied to each grid and on the gas mixture used. The presence of the 3 mm high strips spaced by 4 mm separated by 1 mm (due to presence of insulating frames) and each put at a different potential, leads to a periodic electrostatic solution of the Poisson equation such as the one depicted in Figure 3. The electric field lines present in the region between two grids show that the field is highly non-uniform even when the potential difference between two grids is kept constant. Even if this represents an optimized solution, it is clear that unavoidable losses of the primary electrons occur, either if the primary charge is generated into regions where the electric field lines close on a grid strip, or due to transverse diffusion that can deflect the electron paths towards these loss regions. The resulting effect is that the charge extraction efficiency η features a strong dependence along the converter z axis (see Figure 4). In order to restore part of the primary charge lost due to the geometrical configuration of the field a single GEM foil was inserted in the middle of the grid stack and operated with an approximate gas gain of 2. The resulting advantage is to further improve η and consequently the overall detection efficiency ε.

The detector prototype was tested at the neutron beamline TREFF of the FRM2 research reactor in Garching (Germany) and at the EMMA beamline of the ISIS spallation neutron source in Didcot (United Kingdom). The aim of these measurements was to determine the charge extraction efficiency η, the overall detection efficiency ε and the spatial resolution. During the measurement at TREFF, the detector was irradiated with a 2 x 2 mm^2 monochromatic beam of 4.74 Å [**Error! Reference source not found.**] neutrons entering orthogonally with respect to the strips (θ=90°).

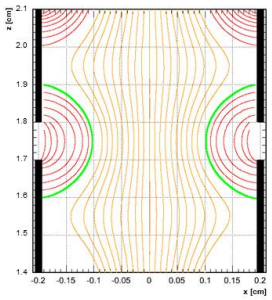

Figure 3: Electric field lines in the region between two grids. Electrons entering the area delimited by the thick green lines follow the red lines and are lost.

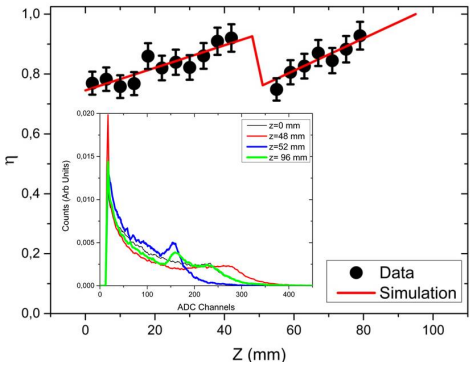

Figure 4: Measurement and simulation of the charge extraction efficiency η as a function of converter depth, for a neutron beam incoming at Θ=90°.Small Rectangle Pulse Height spectra acquired with the neutron beam incident at different z (see Figure 2)

By scanning this beam along the 23 grids, the charge extraction was measured (see Figure 4) and it was found to vary as a piecewise linear curve along z (the converter depth). The presence of the GEM in the middle of the stack divides the converter into two regions that show approximately the same charge extraction efficiency, meaning that the amplifying foil is able to restore part of the primary charge lost during the drift in the field cage. This is also confirmed by the pulse height

spectra (see Figure 4) collected at four different positions along the converter depth z. This plot shows that losses of primary electrons generated in region far from the triple GEM are compensated by the amplification of the GEM in the middle of the stack.

The second important aspect of the detector physics lies in the response in terms of detection efficiency ε and spatial resolution at grazing incident angles. Measurements with a 4 x 4 mm^2 monochromatic neutron beam ($\lambda = 4.74$ Å) entering as depicted in Figure 2 allowed to determine the efficiency of the BAND-GEM detector by comparison to an absolutely calibrated ^{3}He tube. Efficiency values of about 47% at $\lambda = 4.74$ Å were found and a plateau is reached if the detector is inclined by at least 3.5°. This feature guarantees that above an incident angle of about 4° the same detector efficiency can be obtained, regardless of the exact arrangement of the detector with respect to the incoming neutron beam. The spatial resolution (in terms of Full Width at Half Maximum of the spatial distribution of the signals in two directions, orthogonal and horizontal to the thin strips) was also studied as a function of the tilting angle. The spatial resolution in the direction orthogonal to the strips increases with the tilting angle up to about $FWHM_x = 6$ mm at 5° while in the other direction it remains constant at a $FWHM_y = 4.5$ mm. This behavior is well reproduced by the integrated numerical simulation and it is due to the geometrical configuration of the 3D model and the potential difference applied to the GEM positioned in the middle of the grid structure.

In addition to the measurements performed at TREFF, the response of the detector was also studied as a function of neutron wavelengths between 1 Å and 4 Å by performing measurements at EMMA [16,17].

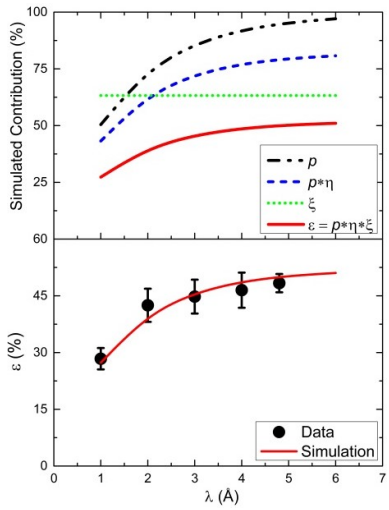

Figure 5: Top: Different contributions to the overall efficiency as a function of neutron wavelength Bottom - BAND-GEM measured and simulated detection efficiency as a function of neutron wavelength.

The efficiency of the BANDGEM detector (see Figure 5-bottom) was determined by comparison with a neutron beam monitor [17] at EMMA and with a standard calibrated ^{3}He tube for the TREFF measurement. The error bars represent the statistical uncertainties in the inferred efficiency values. It was found that the efficiency increases as a function of neutron wavelengths and it is higher than 40% at λ values above 2 Å, approaching values higher than 45% for longer wavelengths. The obtained result was found in good agreement with the expected values from numerical calculations. The specific shape of the detector efficiency curve is due to the complex 3D converter structure and can be explained with contributions of the three curves shown in Figure 5-top: the absorption probability *p*, the charge escape probability ξ and the charge extraction efficiency η.

Since the detector described in this paper is based on the GEM technology, it intrinsically owns the high count rate capability of the micro-pattern gaseous detector family. This capability was demonstrated by irradiating the detector with a neutron flux higher than 10^8 n/(cm^2 s) at the G3-2 beamline of the Orphee reactor in Saclay [19]. The detector counting rate was shown to be linear with the neutron flux up to 4 MHz/cm^2 where a deviation less than 10% from the expected linear behavior was observed. The details of this measurement will be published in a separate paper [20]. Another advantage of thermal neutron detectors based on the GEM technology is that it features the low gamma sensitivity typical for gas based detectors [21,22]. This property is crucial when detecting thermal neutrons since most of the expected background is often induced by gamma-rays.

The BAND-GEM detector described in this paper represents one of the new detector technologies that can be used as an alternative to ^{3}He-based detectors. The achieved BAND-GEM detection efficiency represents an optimum value for detectors based on solid boron converters [23]. The main advantage compared to standard ^{3}He single wire proportional tubes is that it features a counting rate about two orders of magnitude higher, together with a 2D imaging capability.

This detector may find applications in high rate experiments at future spallation neutron sources like ESS. Due to its performance it is presently considered as one of the detector options for the Small Angle Neutron Scattering (SANS) instrument at ESS [24,25]. A significant advantage of this detector technology is that it can be custom designed to match the specific detector area requirements of a neutron beam line. For instance, the BAND-GEM detector under development for SANS instruments features a modular structure with trapezoidal shapes which approximates the ideal spherical geometry better than the present square detector arrangement used on SANS instruments [26]. The second important advantage of the BAND-GEM detector is that it can reliably sustain counting rates in the region up to 10 MHz. This will open up new possibilities for exploring rapidly changing large biological samples like proteins. For instance, although protein assembly [27], orientation of molecules in cellular membranes and thin polymeric films [28] have typical evolution in the 10-30 s range, there are some protein fast-folding times in the 100 µs-1 s temporal range. The BAND-GEM technology will allow time resolved measurements of these fast evolving biological samples. Finally, other applications such as homeland security and nuclear safeguard could profit from this technology in order to realize fast and large area neutron detectors.

Acknowledgements

Richard Hall-Wilton and Susan Schmidt would like to acknowledge the support of EU BrightnESS project, grant #676548.

References

1. Pacific North-west Laboratory, The 3He Supply problem (http://www.pnl.gov/main/publications/external/technical_reports/PNNL- 18388.pdf)
2. G. F. Knoll Radiation Detection and Measurement, 4th Edition. John Wiley and Sons, Inc,
3. S. Peggs et al., "European Spallation Source Technical Design Report", Report 2013-0001. esss.se
4. S. Mühlbauer et Al, The new small-angle neutron scattering instrument SANS-1 at MLZ—characterization and first results, NIMA, Volume 832, 1 October 2016, Pages 297-305
5. M. Titov, Gaseous Detectors: recent developments and applications, arXiv: 1008.3736
6. A. Muraro et Al, Performance of the high efficiency thermal neutron BAND-GEM detector, Accepted for publication in Progress of Theoretical and Experimental Physics
7. Fabio Sauli, The gas electron multiplier (GEM): Operating principles and applications, NIMA Volume 805, 2016, Pages 2-24
8. Watajet - Precision cut Water Jet – www.watajet.com
9. C. Höglund et al., Journal of Applied Physics 111, 104908 (2012)
10. S. Schmidt, C. Höglund, J. Jensen, L. Hultman, J. Birch, R. Hall-Wilton. "Low-temperature growth of boron carbide coatings by direct current magnetron sputtering and high-power impulse magnetron sputtering", Journal of Materials Science 51, Issue 23 (2016); doi:10.1007/s10853-016-0262-4.
11. C. Höglund,K. Zeitelhack, P. Kudejova, J. Jensen, G. Greczynski, J. Lu, L. Hultman, J. Birch, R. Hall-Wilton. "Stability of $^{10}B_4C$ thin films under neutron radiation", Radiation Physics and Chemistry 113 , 14-19 (2015); doi:10.1016/j.radphyschem.2015.04.006.
12. F. Piscitelli et al., "Analytical modeling of thin film neutron converters and its application to thermal neutron gas detectors", JINST 8, P04020 (2013), arXiv:1302.3153
13. https://www.harrisgeospatial.com/docs/using_idl_home.htm; wwww.ansys.com; https://cern.ch/garfieldpp; www.srim.org
14. B. Ketzer Nucl Instrum A 732 , 237 (2013)
15. Journal of large-scale research facilities, 3, A121 (2017)
16. http://www.isis.stfc.ac.uk
17. T.G. Perring, The Resolution Function of the Chopper Spectrometer HET at ISIS, Journal of Neutron Research, Proceedings of the Twelfth Meeting of the International Collaboration on Advanced Neutron Sources (ICANS- XII), Cosener's House, Abingdon, UK, May 24- 28,1993, pp. I-328 to I-33
18. http://quantumdetectors.com/neutrons/
19. E. Perelli Cippo, G. Croci et Al, J. Insturm 10 P10003 (2015)
20. G. Albani et Al, High rate performance of the BAND-GEM detector, to be submitted to JINST
21. G. Croci et Al, J. Instrum 8 P04006 (2013)
22. Richard T.Kouzes, Neutron detection gamma ray sensitivity criteria, NIM A, Volume 654, Issue 1, 21 October 2011, Pages 412-416
23. M.Köhli et Al, Efficiency and spatial resolution of the CASCADE thermal neutron detector, NIM A Volume 828, 21 August 2016, P. 242-249
24. ESS Construction Proposal : LoKI - A broad-band SANS Instrument. Zenodo. http://doi.org/10.5281/zenodo.13302
25. Jackson, A.J.; Kanaki, K.; Lopez, C.I, LoKI - A broad band high flux SANS instrument for the ESS, Proceedings of the 21st meeting of the international collaboration on advanced neutron sources (ICANS-21). 'Dawn of high power neutron sources and science applications', http://dx.doi.org/10.11484/jaea-conf-2015-002
26. http://www.isis.stfc.ac.uk/instruments/sans2d/sans2d3000.html
27. D. M. Warshaw *et al., Proc. Natl. Acad. Sci. U.S.A.* 1998 , 95 , 8034 - 8039
28. G. Zhang *et al. Phys.Chem.Chem.Phys.,* 2010, 12 2308–2

Paper 6

Fusion Engineering and Design 96–97 (2015) 311–314

Contents lists available at ScienceDirect

Fusion Engineering and Design

journal homepage: www.elsevier.com/locate/fusengdes

Status of the CNESM diagnostic for SPIDER

A. Muraro[a,*], G. Croci[a,b], G. Albani[f], C. Cazzaniga[b,f], G. Claps[c], M. Cavenago[d], G. Grosso[a], M. Dalla Palma[e], M. Fincato[e], F. Murtas[c], R. Pasqualotto[e], E. Perelli Cippo[a], M. Rebai[f,b], M. Tollin[e], M. Tardocchi[a], G. Gorini[f,b]

[a] IFP-CNR, Via Cozzi 53, Milano, Italy
[b] Sez. INFN Milano-Bicocca, Piazza della Scienza 3, Milano, Italy
[c] INFN-LNF, Via Enrico Fermi 40, Frascati, Italy
[d] INFN-LNL, Viale dell'Università 2, Legnaro, Italy
[e] RFX Consortium, Corso Stati uniti 4, Padova, Italy
[f] University of Milano-Bicocca, Piazza della Scienza 3, Milano, Italy

HIGHLIGHTS

- We have finished the design of the detector box of the CNESM diagnostic for SPIDER.
- We have constructed the GEM detector of the CNESM detector for SPIDER.
- We have tested the detector under fast neutron irradiation.

ARTICLE INFO

Article history:
Received 4 October 2014
Received in revised form 8 June 2015
Accepted 17 June 2015
Available online 3 July 2015

Keywords:
Neutron detectors
GEM (gas electron multiplier)
Fast neutron
NBI diagnostic

ABSTRACT

The ITER neutral beam test facility under construction in Padova will host two experimental devices: SPIDER, a 100 kV negative H/D RF source, and MITICA, a full scale, 1 MeV deuterium beam injector. A detection system called close-contact neutron emission surface mapping (CNESM) is under development with the aim to resolve the horizontal beam intensity profile in MITICA and one of the eight beamlet groups in SPIDER, with a spatial resolution of 1.5 and 2.5 cm respectively. This is achieved by the evaluation of the map of the neutron emission due to interaction of the deuterium beam with the deuterons implanted in the beam dump surface. CNESM uses nGEM detectors, i.e. GEM detectors equipped with a cathode that also serves as neutron–proton converter foil. The diagnostic will be placed right behind the SPIDER and MITICA beam dump, i.e. in an UHV environment, but the nGEM detectors need to operate at atmospheric pressure: in order to maintain the detector at atmospheric pressure, a vacuum sealed box, that will be mounted inside the vacuum, has been designed. The box design was driven by the need to minimize the neutron attenuation and the distance between the beam dump surface and the detector active area. This paper presents the status of the CNESM diagnostic describing the design of the detector, the design of the sealed box and reporting the results obtained with the first full-size prototype under fast neutron irradiation.

1. Introduction

Additional heating will be provided to the ITER [1] project by two beam injectors resulting from the neutralization of accelerated negative ions. To study production and extraction of negative ions, a beam test facility called SPIDER (source for production of ion of deuterium extracted from Rf plasma) is under construction at the Consorzio RFX site in Padova, Italy. SPIDER's main goal is the optimization of the source operation and the test of the beam properties through the production of 1 h long D-beam pulse accelerated up to 100 keV, carrying a current of 50 A spread out over a surface of about 1 m^2 for a resulting deuterium flux of about 2.5×10^{20} D/m^2 s [2]. The SPIDER beam is composed by 1280 beamlets arranged in 4×4 beamlet groups and they will hit a target (the beam dump) that is tilted by 60° relative to the beam axis, such that the dimensions of the beamlet footprint is about 40 mm × 22 mm. The beam dump is composed by a rectangular panel made of CuCrZr-alloy, with an elemental composition of about 99% Cu,

* Corresponding author.
E-mail address: muraro@ifp.cnr.it (A. Muraro).

http://dx.doi.org/10.1016/j.fusengdes.2015.06.081
0920-3796/

water-cooled with the hypervapotrons technique. The interactions between the beam deuterons and deuterons implanted in the dump lead to fusion reaction, with the consequent emission of neutrons with a flux of few times 10^{15} neutrons per SPIDER pulse (lasting 3600 s). One of the diagnostics of the SPIDER beam [3] will be CNESM (close-contact neutron emission surface mapping), a neutron detector based on GEM (gas electron multiplier) technology especially designed to provide the 2D intensity profile of a beamlet group with a spatial resolution approaching the size of individual beamlets by detecting 2.5 MeV neutrons coming from the D–D nuclear reaction [4,5]. GEM based detectors [6–8] were invented at CERN as charged particle tracking detectors [9] but, if properly adapted, they can be used also as neutral particles detectors [10–13]. This paper presents the status of the CNESM diagnostic and shows the design of the detector and of the sealed box, describing in particular the analysis carried out to define its parameters, the necessary pumping and leak test procedures to ensure the compatibility of the box with the UHV environment and the proposed installation/removal procedure.

2. CNESM principle

The CNESM detection system is placed right behind the beam dump panels (Fig. 1 left), as close as possible to the front neutron emitting surface. In order to provide the map of neutron emission on the beam dump surface with a spatial resolution sufficient to resolve the individual beamlets, it is very important that the distance between the detection surface and the emitting surface is less than 30 mm. The CNESM diagnostics uses nGEM [14,15] as neutron detectors. These are flat gas electron multiplier (GEM) detectors equipped with a cathode foil that also serves as neutron–proton converter. The principle of operation of the nGEM cathode is shown in Fig. 1 right. Incoming neutrons have an energy En between 2.45 and 2.85 MeV, depending on the emission angle. They are converted into protons by elastic recoil in a polythene (CH_2) film. Protons leaving the CH_2 film with enough energy can cross the Al foil and reach the gas. The proton recoil energy is equal to $E_p = E_n \cos^2\theta_p$, where θ_p is the proton recoil. By interposing a thin film of aluminium between the polythene film and the gas layer, it is possible to exploit this relation to improve the spatial resolution of the detector. In fact since the planar neutron source to be mapped is at some distance from the detection surface, better spatial resolution is achieved if the trajectory of the detected neutrons is not too far from being perpendicular to the cathode surface. An Al foil with a thickness of 50 μm stops all the protons with an energy $E_p < 2.2$ MeV, thus implying that all the protons emitted with an angle greater than 45° are not detected by the CNESM system. The induced signal in the padded anode is due to the motion of the electrons created by the protons that ionize the GEM gas. Operating the nGEM detector at a total gain of 100 (corresponding to an applied voltage for each GEM foil equal to 290 V) allows a complete discrimination of neutrons from gamma background [16].

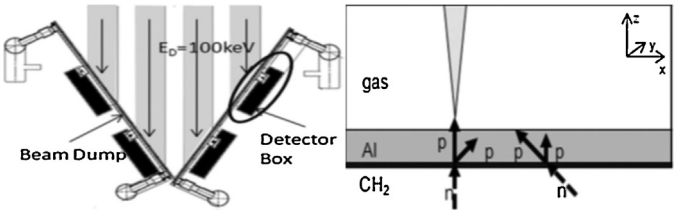

Fig. 1. (Left) Schematics of the SPIDER beam dump. The beam dump is tilted by 60° relative to the beam axis. The CNESM detectors (black) are placed right behind the beam dump panels. (Right) Illustration of how the Al cathode thickness can be used to suppress detection of neutrons with oblique incidence. Neutrons are converted into protons in the polythene foil (black). Only one of the four protons in the figure crosses the Al foil (grey) and produces a discharge in the GEM gas.

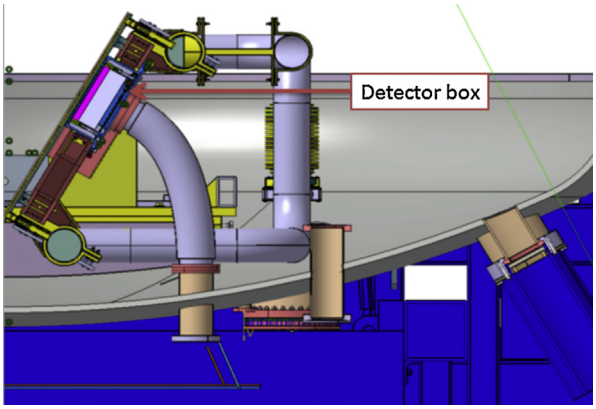

Fig. 2. Top view of the SPIDER beam dump cross section, showing the detector box (blue). One flexible pipe is used to connect the inside of the detector box to the outside through a flange on the rear port of the SPIDER vacuum tank. (For interpretation of the references to color in this figure legend, the reader is referred to the web version of this article.)

2.1. Design of detector box

Since the nGEM detector operates at room pressure, it will be placed inside a steel containment box (detector box) connected to the off-vacuum environment outside of the SPIDER vacuum vessel by one flexible pipe (Fig. 2) used to keep the neutron detector at atmospheric pressure and to provide access for electric cables and for two thin pipelets needed to keep a constant flow of Ar/CO_2 gas inside the nGEM detector. The chosen flexible pipe is a convoluted bellow, and this type of pipe was preferred to the edge welded bellow since it guarantees a lower leakage risk and is self supporting.

The spatial resolution of the CNESM diagnostic critically depends on the distance between the nGEM detector and the beam dump front surface. The front side of the detector box was designed in order to minimize this distance, taking into account the steady state load due to the pressure difference between the internal side (1 bar) and the vacuum environment inside the SPIDER vacuum vessel. Mechanical design rules for monotonic type damage have been applied as well as those specified in the ASME boiler and pressure vessel code and in the ITER structural design criteria for in-vessel components [17].

The general requirements imposed by ITER are:

$$\begin{cases} \dfrac{L_m}{d} > 0.5 + 1.43\dfrac{p}{S_u} & (1) \\ \dfrac{L_m}{d} > 1.2 & (2) \\ \dfrac{p}{S_u} < 1.5 & (3) \end{cases}$$

where L_m is the minimum distance of the bolt axis from the free edge; d is the bolt diameter; p is the nominal contact pressure and S_u is the ultimate tensile strength. At a temperature of 150 °C, the ultimate tensile strength of the AISI 304L is about 437 MPa, so by imposing a nominal contact pressure of 600 MPa, one can obtain the geometrical parameters and the number of bolts necessary for the design of the detector box (Fig. 3). With these geometrical parameters, a mechanical verification was carried out by limiting the local primary stresses to the maximum allowable stress value set at half the AISI 304L material yield stress, which is about 200 MPa. In order to keep the equivalent stress within the set limit, the front side of the detector box was designed with a thickness of 4 mm and with a

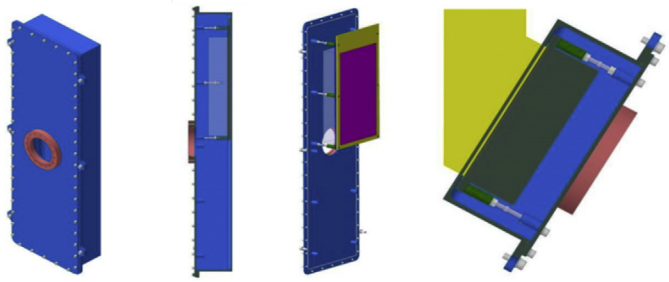

Fig. 3. Details of the CAD model of the detector box. From left to right: (i) detector box with flange; (ii) side view showing the detector supports; (iii) isometric view of the box lid with the detector supports and (iv) top view showing detector, supports and flange and footprint of the beamlet group.

rib in the middle across the width. The junction between the front side and the lateral walls and between the front side and the rib was designed with a 10 mm radius fillet, in order to improve the stress distribution and to reduce the stress peak present along the rib. The results of the static structural mechanical analysis show that the stress does not exceed the value of 120 MPa, which can be still considered acceptable. The analysis provides also an estimate of the deflection on the front side of the neutron box, which must be less than about 2 mm in order to avoid interference with the beam dump back panel face, 5 mm apart. The maximum deflection on the front side of the detector box was found to be about 1.2 mm, a value that can be considered acceptable. Finally this analysis gives information about the deflection of the lid, which could lead to air leakage. In order to investigate this deflection, a simplified model has been studied.

In this model the area that hosts the bolts was assumed in bonded contact while the area near the bolts was assumed as free contact. The results of this analysis show that the deflection of the lid leads to a gap between lid and box less than 0.1 mm, which is not enough to produce a leakage, given the presence of the O-ring.

2.2. Pumping and leak test procedure of the detector box

The CNESM diagnostic requires three vacuum connections: two at the two ends of the tombak and one at the lid of the detector box. The first two are copper gaskets, the third one is a Viton O-ring and it is the most critical one. In order to reduce the leakage risk due to mispositioning of the Viton O-ring gasket, the detector box will be closed before the installation on the dump and not further opened or closed in situ, thus avoiding the risk of a weak vacuum tightness which otherwise could only be verified after the closure of the SPIDER vacuum vessel. To further reduce the risks of an unverified vacuum connection, also the tombak will be connected to the detector box before installation on the dump. Thus only the connection of the tombak to the vacuum port of the lid will be done during installation. In order to test the O-ring vacuum tightness between the lid and the detector box, three tests will be carried out:

1. Pump the box and tombak system without GEM to UHV. A leak detector will be installed at the exit of the vacuum pump connected to the box. The leak detection will be done by spraying helium on the box from the outside. Although this is not the operational condition, with vacuum outside and 1 bar inside, this test is used to validate the tightness of the box.
2. In an environment at a pressure of 1 bar, the box and tombak system without GEM are filled with helium at a pressure up to 2 bars. The leak test is then done using a sniffer. This test is equivalent to the next one (the force exerted on the walls of the box turns out to be always 98 kPa, in the same direction), but without the need to install the box in a large vacuum chamber. Since this test must be done without detector inside, it is only planned for the first acceptance test of the box and will be used to verify its deformations. The disadvantage presented by this test is the presence of the atmospheric air, which increases the background noise and does not allow the detection of losses lower than 10^{-5} mbar l/s.
3. After pumping the box and tombak system to UHV, thus desorbing the internal surfaces, the detector is installed. Subsequently the sealed box is installed in a vacuum chamber, with a connection to the outside pressure, like in SPIDER, through which it is filled with helium at known He partial pressure. The leakages are measured by means of a leak detector positioned at the exit of the vacuum pump of the chamber. This last test would exactly reproduce the operational conditions of the box installed in SPIDER.

3. Design of the detector

The first full-size nGEM prototype was built in May 2013. This detector was built following the construction method developed and used for the Triple GEM of the LHCb experiment at CERN [18]. The detector has an active area of 32.5 cm × 20 cm and its cathode is composed of two layers: one 150 μm thick polythene (CH_2) film and one 50 μm thick aluminium layer. The detector gap configuration (drift/transfer1/transfer2/induction gap) was 4/2/2/2 mm. The padded read-out anode is composed of 256 pads, each with an area of 22 mm × 13 mm. The front-end chips used to read all the pads are the CARIOCA-GEM digital chips [19]. A system of patch panel + cables carry the LVDS signals to a custom made FPGA Mother Board [20] that analyzes the LVDS signals coming from the chips. This configuration allows to protect the FPGA chip from neutron irradiation and thus reducing the rate of soft errors. The high voltage configuration is generated using the HVGEM [21] NIM module and the potentials are applied to each electrode by means of passive resistive–capacitive filters properly designed for a Triple GEM detector.

4. Test of the full-size prototype

The test on the full-size prototype were performed with the detector placed in the neutron beam of the ISIS-VESUVIO [22] beam line with a flight path of about $L = 12.5$ m from the target.

Fig. 4 shows a 2D map of the VESUVIO neutron beam profile reconstruction obtained by exposing the detector to the neutron beam. The first reconstruction of the beam width using pads of this

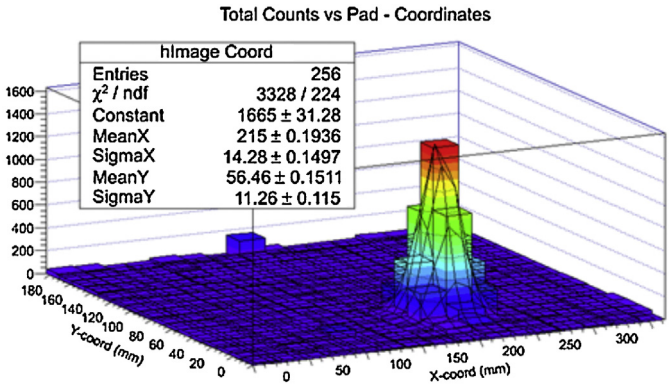

Fig. 4. 2D map of the Vesuvio fast neutron beam fitted by a bi-Gaussian function. The reconstructed σ_x and σ_y are respectively 14.28 mm and 11.26 mm. The detector parameters used are E_d (drift field) = 2.25 kV/cm; E_{T1} (transfer 1 field) = 1.5 kV/cm, E_{T2} (transfer 2 field) = kV/cm, E_{Ind} (induction field) = 1.5 kV/cm and V_{GEM} = 870 V.

dimension (area $22\,(x)\,\text{mm} \times 13\,(y)\,\text{mm}$) and a Gaussian fit gives $\sigma_x = 14.28 \pm 0.15$ mm and $\sigma_y = 11.26 \pm 0.12$ mm. These values are compatible both with the technical specification of VESUVIO and with previous results [15].

5. Conclusions

The engineering design of the CNESM detector box, and its integration within the beam dump structure has been finalized. The first full-size nGEM prototype for SPIDER has been realized and successfully tested at ISIS. The CNESM system for SPIDER can now be built and will be the basis for the realization of an even larger area detector that will be used in the MITICA NBI prototype for ITER that represents the evolution of SPIDER.

Acknowledgments

This work was set up in collaboration and financial support of Fusion for Energy and of INFN Group 5 (Technology Research). This publication reflects the views only of the author, and Fusion for Energy cannot be held responsible for any use which may be made of the information contained therein. The views and opinions expressed herein do not necessarily reflect those of the ITER Organization.

References

[1] R. Hemsworth, et al., Nucl. Fusion 49 (2009) 045006.
[2] P. Sonato, et al., Fusion Eng. Des. 84 (2009) 269.
[3] R. Pasqualotto, et al., Diagnostics of the ITER neutral beam test facility, Rev. Sci. Instrum. 83 (2012) 02B103.
[4] G. Croci, et al., nGEM neutron diagnostic concept for high power deuterium beams, JINST 7 (2012) C03010.
[5] M. Rebai, et al., A new diagnostic concept for high power deuterium beams, Rev. Sci. Instrum. 83 (2012) 02B721.
[6] F. Sauli, GEM: a new concept for electron amplification in gas detectors, Nucl. Instrum. Methods A 386 (1997) 531.
[7] S. Duarte Pinto, et al., Progress on large area GEMs, JINST 4 (2009) P12009.
[8] M. Villa, et al., Progress on large area GEMs, Nucl. Instrum. Methods A 628 (2011) 182–186.
[9] M. Alfonsi, et al., Activity of CERN and LNF groups on large area GEM detectors, Nucl. Instrum. Methods A 617 (2010) 151–154.
[10] M. Alexeev, et al., Micropattern gaseous photon detectors for Cherenkov imaging counters, Nucl. Instrum. Methods A 623 (2010) 129–131.
[11] M. Alexeev, et al., Development of THGEM-based photon detectors for Cherenkov imaging counters, JINST 5 (2010) P03009.
[12] M. Alexeev, et al., THGEM based photon detector for Cherenkov imaging applications, Nucl. Instrum. Methods A 617 (2010) 396–397.
[13] G. Croci, et al., GEM-based thermal neutron beam monitors for spallation sources, Nucl. Instrum. Methods A 732 (2013) 217–220.
[14] G. Croci, et al., nGEM fast neutron detectors for beam diagnostics, Nucl. Instrum. Methods Phys. Res. A 720 (August) (2013) 144–148.
[15] F. Murtas, et al., Triple GEM gas detectors as real time fast neutron beam monitors for spallation neutron sources, JINST 7 (2012) P07021.
[16] G. Croci, et al., Measurements of γ-ray sensitivity of a GEM based detector using a coincidence technique, JINST 8 (2013) P04006.
[17] Design Criteria for In-vessel Components (SDC-IC) Appendix C, section IC 3800.
[18] G. Bencivenni, et al., A triple GEM detector with pad readout for high rate charged particle triggering, Nucl. Instrum. Methods A 488 (2002) 493–502.
[19] W. Bonivento, et al., Development of the CARIOCA front-end chip for the LHCb muon detector, Nucl. Instrum. Methods A 491 (2002) 233–243.
[20] http://www.infn.it/csn5/joomla/GEMINI/
[21] F. Murtas, et al., Applications in beam diagnostics with triple GEM detectors, Nucl. Instrum. Methods A 617 (2010) 237.
[22] C. Andreani, et al., Appl. Phys. Lett. 92 (2008) 11401.

Acknowledgments

Giunti alla fine di questo lavoro, arriva il momento di ringraziare tutte le persone che lo hanno reso possibile. Non posso che iniziare ringraziando per primi il mio supervisore Dr. Marco Tardocchi, e il mio “co-supervisore” (se così si può dire) Prof. Giuseppe Gorini, per aver creduto nel mio lavoro e per aver permesso il mio inserimento in un gruppo di ricerca molto affiatato e produttivo.

Un ringraziamento particolare va dedicato ai miei colleghi Gabriele, Enrico e Giovanni, con i quali ho lavorato a stretto contatto in questi anni e dai quali ho imparato davvero molto. E’ con loro che ho discusso la maggior parte dei risultati scientifici ottenuti, migliorandoci di volta in volta fino ad arrivare alla realizzazione di un progetto (quello del full-module) in cui pochi al di fuori del nostro gruppo credevano quando abbiamo iniziato. Inoltre mi hanno aiutato a migliorare il mio lavoro di tesi, portando ottimi consigli scientifici e traducendo in inglese ciò che da me era stato scritto in una sorta di inglese-veneto. Grazie mille!

Ringrazio poi tutti gli altri miei colleghi per le lunghe conversazioni (scientifiche e non) che mi hanno fatto crescere sia in ambito lavorativo che in ambito umano.

Per ultimi, ma non certo per grado di importanza, devo un grande grazie ai miei genitori, ai miei fratelli e a Veronica, i quali mi hanno dato ogni sorta di sostegno in questi anni rendendo possibile la riuscita del mio percorso.

A Veronica devo un grazie davvero speciale: oltre a supportarmi (e sopportarmi) per tutti questi anni, ha reso possibile il mio percorso seguendomi senza indugi fino a Milano. Senza di lei di certo non sarei arrivato a questo punto.